Berkeley Seismological Laboratory

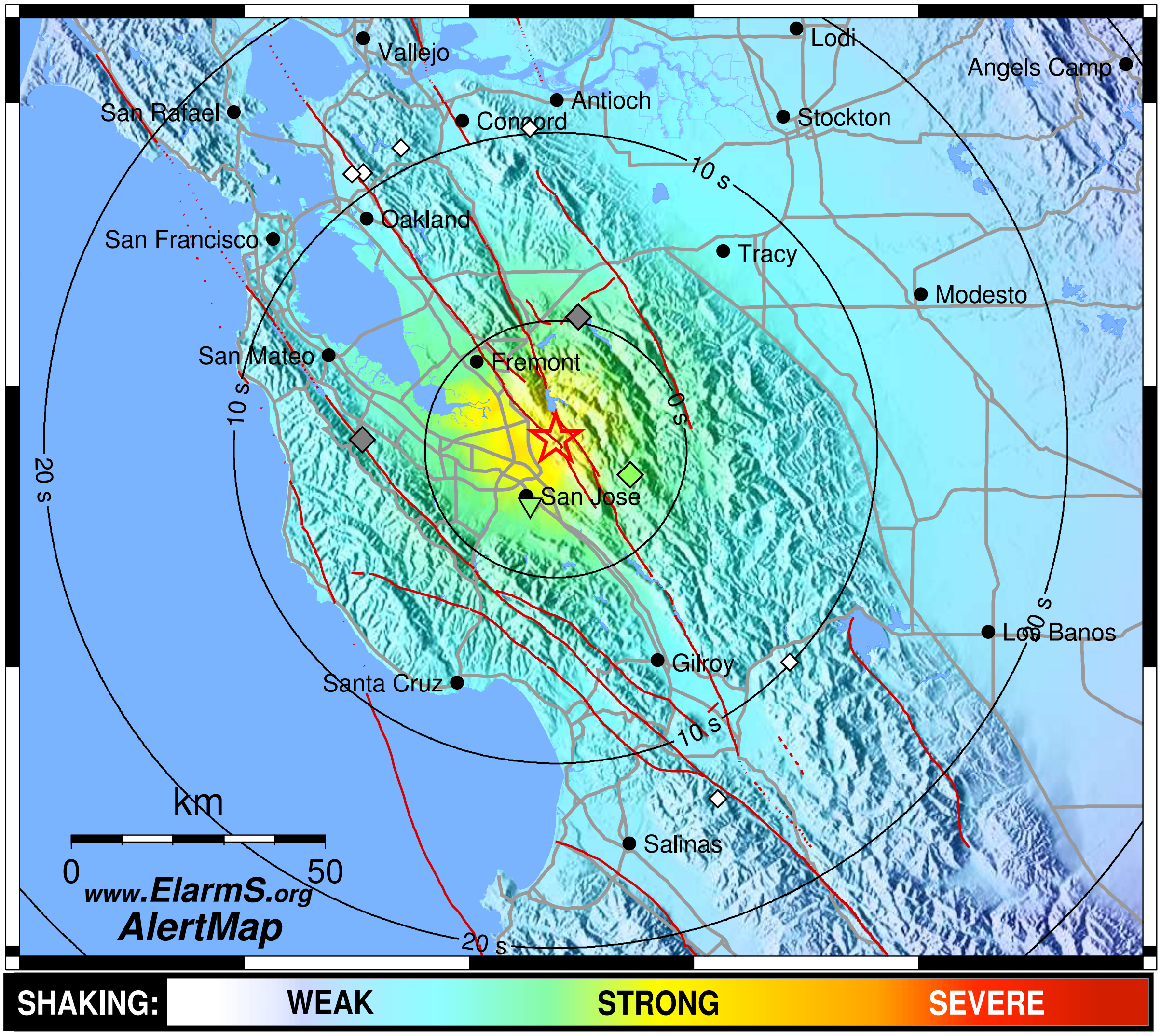

Annual Report
July 2007 - June 2008

Berkeley Seismological Laboratory
Annual Report
July 2007 - June 2008

Cover Picture

Alum Rock AlertMap: On October 30, 2007 the magnitude 5.4 Alum Rock earthquake rippled across the San Francisco Bay Area. The largest earthquake in the region since the 1989 Loma Prieta earthquake, it was felt by most people but caused little damage. The CISN early warning test system named ElarmS caught the earthquake. This map shows the distribution of ground shaking intensity predicted using the first few seconds of data recorded by seismometers near the epicenter in San Jose. The epicenter is shown as a star and the estimated magnitude is 5.2. The warmer colors show where the stronger shaking was predicted near the epicenter and the cooler colors show weaker shaking at greater distances. The predicted ground shaking is very accurate. The data used to generate this map was available a few seconds before the shaking was felt in San Francisco. (This picture is a simplified version of Figure 2.59 in Research Study 26.)

Contents

Chapter 1

Director's Report

1. Introduction

During the year 2007-2008, we experienced the largest earthquake in the San Francisco Bay Area since the M 6.9 1989 Loma Prieta earthquake. The M_w5.4 Alum Rock earthquake occurring in the evening of October 30, 2007, local time, was felt widely. It caused surprisingly little damage, however, because its epicenter lay to the southeast of the population centers, and it ruptured southward, away from them. This was a gentle reminder that we live in earthquake country, as well as a good opportunity to test the performance of the Northern California earthquake notification system which we operate jointly with the US Geological Survey in Menlo Park, and that of the Early Warning System currently being tested at the BSL. In contrast, this past year was also marked by the tragic M_w7.8 Sichuan Earthquake (May 12, 2008), which caused 70,000 deaths and 4.8 million homeless, the largest earthquake in China since the 1976 Tangshan earthquake. This earthquake occurred at the eastern boundary of the Tibet Plateau. It is now the subject of intense geophysical study, as it is thought to hold some important keys to the nature of the tectonics and crustal structure of this remarkable region of the world. Researchers at the BSL are actively studying this earthquake.

For those of you familiar with our Annual Report, please skip the background section, which provides a historical introduction to the BSL and has not changed significantly from past years.

2. Background and Facilities

The Berkeley Seismological Laboratory (BSL), formerly the Berkeley Seismographic Stations (BSS), is the oldest Organized Research Unit (ORU) on the UC Berkeley campus. Its mission is unique in that, in addition to research and education in seismology and earthquake-related science, it is responsible for providing timely information on earthquakes (particularly those that occur in Northern and Central California) to the UC Berkeley constituency, the general public, and various local and state government and private organizations. The BSL is therefore both a research center and a facility/data resource, which sets it apart from most other ORUs. A major component of our activities is focused on developing and maintaining several regional observational networks, and participating, along with other agencies, in various aspects of the collection, analysis, archival, and distribution of data pertaining to earthquakes. At the same time, we maintain a vigorous research program on earthquake processes and Earth structure. In addition, the BSL staff spends considerable time on public relations activities, including tours, talks to public groups, responding to public inquiries about earthquakes, and, more recently, World-Wide-Web presence (`http://seismo.berkeley.edu/`).

UC Berkeley installed the first seismograph in the Western Hemisphere at Mount Hamilton (MHC) in 1887. Since then, it has played a leading role in the operation of state-of-the-art seismic instruments and in the development of advanced methods for seismic data analysis and interpretation. Notably, the installation, starting in 1927, of Wood-Anderson seismographs at 4 locations in Northern California (BKS, ARC, MIN and MHC) allowed the accurate determination of local earthquake magnitude (M_L). This was the beginning of a unique historical catalog of regional earthquakes, which continues to grow, providing crucial input to earthquake probabilities studies.

Over the years, the BSS continued to keep apace of technological improvements. The first centrally telemetered network using phone lines in an active seismic region was installed by the BSS in 1960. The BSS was the first institution in California to operate a 3-component "broadband" system (1963). Notably, the BSS played a major role in the early characterization of earthquake sources using "moment tensors" and source-time functions, and made important contributions to the early definitions of detection/discrimination of underground nuclear tests and to earthquake hazards work, jointly with UCB Engineering. Starting in 1986, the BSS acquired 4 state-of-the-art broadband instruments (STS-1), while simultaneously developing PC-based digital telemetry, albeit with limited resources. As telecommunication and computer technologies made rapid progress, in parallel with broadband instrument development, paper record reading was soon completely abandoned in favor of largely automated digital data analysis.

The current facilities of the BSL have been progressively built over the past two decades, initiated by significant "upgrade" funding from UC Berkeley in 1991-1995. The BSL currently operates and acquires data, continuously and in real-time, from over 60 regional observatories, which house a combination of broadband and strong motion seismic instrumentation installed in vaults, borehole seismic instrumentation, permanent GPS stations of the Bay Area Regional Deformation (BARD) network, and electromagnetic sensors. The seismic data are fed into the BSL real-time processing and analysis system and are used in conjunction with data from the USGS NCSN network in the joint earthquake notification program for Northern California, started in 1996. This program capitalizes on the complementary capabilities of the networks operated by each institution to provide rapid and reliable information on the location, size and other relevant source parameters of regional earthquakes. In recent years, a major emphasis in BSL instrumentation has been in densifying the state-of-the-art seismic and geodetic networks. A second important focus of research has been the development of robust methods for quasi-real time, automatic determination of earthquake source parameters, and predicting strong ground motion, using a sparse network combining broadband and strong motion seismic sensors, as well as permanent geodetic GPS receivers. A recent emphasis has been the development of "earthquake early warning" capabilities.

The backbone of the BSL operations is a regional network of 32 digital broadband and strong motion seismic stations, the Berkeley Digital Seismic Network (BDSN), with continuous telemetry to UC Berkeley. This network provides the basic regional data for the real-time estimation of location, size and rupture parameters for earthquakes of M 3 and larger in Central and Northern California, within our Rapid Earthquake Data Integration (REDI) program. It is the Berkeley contribution to the California Integrated Seismic Network (CISN). It also provides a fundamental database for the investigation of three-dimensional crustal structure and its effects on regional seismic wave propagation, which is ultimately crucial for estimating ground shaking for future earthquakes. Most stations also record auxiliary temperature/pressure channels, valuable in particular for background noise quality control. Complementing this network is a $\sim$ 25 station "high-resolution" network of borehole seismic sensors located along the Hayward Fault (HFN) and under the Bay Area bridges, operated jointly with the USGS/Menlo Park and linked to the Bridge Safety Project of the California Department of Transportation (Caltrans). The latter has facilitated the installation of sensor packages at 15 bedrock boreholes along 5 East Bay bridges in collaboration with Lawrence Livermore National Laboratory (LLNL). A major science goal of this network is to collect high signal-to-noise data for micro-earthquakes along the Hayward Fault to gain insight into the physics that govern fault rupture and its nucleation. The BSL is also involved in the operation and maintenance of the 13 element Parkfield borehole seismic array (HRSN), which is providing high quality data on micro-earthquakes, clusters, and, most recently, tremors, and provides an important reference for the San Andreas Fault Observatory at Depth (SAFOD). Since April 2002, the BSL is also involved in the operation of a permanent broadband ocean bottom station, MOBB, in collaboration with the Monterey Bay Aquarium Research Institute (MBARI).

In addition to the seismic networks, the BSL archives and distributes data for the permanent geodetic BARD Network as well as operating and maintaining 30 sites and processing the data from them. Whenever possible, BARD sites are collocated with BDSN sites in order to minimize telemetry costs. In particular, sites continue to be upgraded to 1 Hz sampling. This benefits the development of analysis methods which combine seismic and geodetic data for the rapid estimation of the source parameters of significant earthquakes, which is one focus of BSL research.

Finally, two of the BDSN stations (PKD, SAO) also share data acquisition and telemetry with 5-component electromagnetic sensors installed with the goal of investigating whether tectonic signals can be detected. In 2002-2003, automated quality control software was implemented to monitor the electromagnetic data.

Data from these and other regional networks are archived and distributed at the Northern California Earthquake Data Center (NCEDC), operated at the BSL in collaboration with USGS/Menlo Park. The data reside on a mass-storage device (current holdings $\sim$ 30 TerraBytes), and are accessible "on-line" over the Internet (`http://www.ncedc.org`). Among others, data from the USGS Northern California Seismic Network (NCSN), are archived and distributed through the NCEDC. The NCEDC also compiles, maintains, archives and distributes the ANSS earthquake catalog. Core University funding to our ORU currently provides salary support for 2 field engineers, one computer expert, 2 data analysts, 1 staff scientist and 2 administrative staff. This supports a diminishing portion of the operations of the BDSN and provides seed funding for our other activities. All other infrastructure programs are supported through extra-mural grants primarily from the USGS, NSF, and the State of California, through its Office of Emergency Services (OES). We acknowledge valuable recent contributions from other sources such as Caltrans and PEER, as well as our Earthquake Research Affiliates.

3. Highlights of 2007-2008

3.1 Research Accomplishments

Chapter 2 documents the main research contributions of the past year. Research at the BSL spans a broad range of topics, from the study of microseismicity at the local scale to global deep earth structure, and includes the use of seismological, geodetic, and remote sensing (InSAR) techniques. Productivity continues to be high: over forty papers in refereed journals have been authored or co-authored by BSL researchers in the last year, a steady number compared to previous years.

Once again, the data provided by the borehole stations of the HRSN (Parkfield) network have led to important and exciting results. Following the discovery two years ago of non-volcanic tremors in the Parkfield area, a highlight of this past year's research is the use of a noise correlation approach to document seismic velocity changes correlated with fault zone deformation as measured by GPS, as well as with tremor activity, following the M6.5 San Simeon and M6.0 Parkfield earthquakes (Research Study 32.). This study is a powerful illustration of the successful continuing collaboration between BSL and IPG (Institut de Physique du Globe de Paris) researchers. The collaboration started with a workshop in Paris in January 2007 and is supported on the French side by funding from CNRS through a PICS (Projet international de Coopération Scientifique) and, on the Berkeley side, through a combination of BSL core funds and two France Berkeley Fund awards. A second workshop was held at BSL in December 2007, and a third one is being planned for January 2009 in Paris.

Monitoring of tremor activity at Parkfield continues with new intriguing observations, such as the occurrence of quasi-periodic bursts of tremor activity (Research Study 21.), or the identification of several classes of tremors with different locations (Research Study 28.). On the other hand, acceleration of the recurrence of repeating microseisms since the early 1990's has been confirmed (Research Study 25.).

BSL researchers made important contributions to the analysis of the data in the wake of the tragic 08/06/07 Crandall Canyon mine collapse. Through the use of seismic broadband waveform inversion tools developed at BSL, Sean Ford and Doug Dreger, with LLNL collaborator Bill Walter, demonstrated that the recorded seismic signals could not be due to a tectonic earthquake, but rather the collapse itself (Research Study 30.).

The occurrence of the 10/30/07 M_w 5.4 Alum Rock earthquake, widely felt in the San Francisco Bay Area, provided an opportunity to demonstrate the capabilities of both the Northern California real time systems (Research Study 22.) and the ElarmS earthquake Early Warning methodology (Research Study 26.). It also highlighted the possibility of slip transfer between the Hayward and Calaveras faults (Research Study 3.).

The comparison of low frequency noise at the ocean floor broadband station MOBB and the island station FARB has provided important constraints on the generation of this noise and its relation to infragravity waves in the ocean (Research Study 14.).

BSL researchers continue to investigate the recently widely advertised Accelerated Moment Release hypothesis (AMR) and have documented the high sensitivity of "observed" AMR to the choice of free parameters considered (Research Study 4.).

On the global seismology front, a new method has been developed to separate the effects of depth dependence and intrinsic frequency dependence on seismic attenuation as measured using free oscillations (Research Study 20.) and progress is being made in the construction of tomographic models at global and regional scales, using 3D numerical wave propagation computations (Research Studies 12. and 17.).

Finally, the development of new electronics for the STS-1 seismometer has been completed. BSL researchers and engineers have been involved in the testing and evaluation of these successful new electronics (Chapter 3, Section 9.) and in particular, have already utilized their convenient remote calibration capabilities at several BDSN stations.

3.2 Infrastructure and Earthquake Notification

As in previous years, BSL's infrastructure development efforts have centered around several major projects:

- operation and enhancement of the joint earthquake notification system with USGS/Menlo Park.
- the continuing development of the California Integrated Seismic Network
- participation, at various levels, in two components of the national Earthscope program: archival of borehole strainmeter data in the framework of the Plate Boundary Observatory (PBO), and the preparation for archival of the data from the San Andreas Fault Observatory at Depth (SAFOD). The USArray Transportable Array has now moved out of California.
- development of borehole networks at Parkfield and along the Hayward Fault
- operation and further enhancements of the BARD network of continuous GPS
- operation of the Northern California Earthquake Data Center

The main goal of the CISN (see Chapter 3, Section 2.) is to ensure a uniform system for earthquake monitoring and reporting in California. The highest priority, from the point of view of emergency responders in California, is to improve the robustness of statewide real-time notification and to achieve a uniform interface across the State to the California OES and other emergency responders. This represents a major challenge, as the CISN started as a heterogeneous collection of networks with disparate instrumentation, software systems, and cultures. Over the past few years, much effort has gone into developing coordinated software between Southern and Northern California and, in Northern California, between Berkeley and USGS/Menlo Park. These two institutions are joined together in the Northern California Earthquake Management Center (NCEMC). A highlight of the past year has been the re-installation of five sites (SUTB, RAMR, HATC, HAST, HELL) previously occupied by USArray Travelling Array, with permanent broadband equipment acquired through FEMA grants and OES funds. In particular, BSL engineers improved the installation design to remove condensation inside the vaults, an important issue for long term deployments. One other site is awaiting transfer of permit to BSL, while two additional former USArray sites are awaiting funding to acquire permanent seismic equipment.

2007-2008 is the last year of the 3 year funding cycle for CISN from the Office of Emergency Services (OES). In the past year, progress has been made on unifying the way leap seconds are treated in Southern and Northern California, and on magnitude calibration across the state. The `Jiggle` analysis software has been modified and installed in Northern California in November 2006 and will be offered to other regions of the Advanced National Seismic System soon. Data from the Northern Hayward Fault Network have been integrated into the Northern California Seismic System.

BSL staff continue to spend considerable efforts in organizational activities for CISN, notably by participating in the CISN Project Management Group (Neuhauser and Hellweg), which includes weekly 2 hour phone conferences, and the Standards Committee (Neuhauser-chair, Hellweg, Lombard), which strives to define and coordinate software development tasks. Romanowicz and Hellweg serve on the CISN Steering Committee. The CISN also represents California as a designated region of ANSS (Advanced National Seismic System) and the BSL is actively involved in planning activities for the ANSS.

The Parkfield borehole network (HRSN, see Chapter 3, Section 4.) continues to play a key role in support of the Earthscope SAFOD (San Andreas Fault Observatory at Depth) drilling project, by providing low noise waveforms for events in the vicinity of the target drilling zone. Efforts have been started this year to minimize the costs of this network, in particular the land fees, by moving key elements of the telemetry away from a very costly site.

The BARD continuous GPS (C-GPS) network (see Chapter 3, Section 5.) has focused its efforts on the development of local collaborations to densify the network and reduce telemetry costs associated with the installation of new stations. Also, BSL engineers have been working on the design of meteorological sensors to be installed at GPS sites. Corrections using data from these sensors will help minimize the effects of the troposphere on BARD solutions.

Finally, the NCEDC has continued to expand its data holdings and enhance access to the data; in particular, we have made progress in archiving continuous seismograms read from NCSN tapes, to satisfy numerous requests from researchers interested in looking for non-volcanic tremors in the background noise, as well as for the study of teleseisms, and have ported the entire NSCN earthquake catalog into the CISN database schema.

4. BSL staff news

Changes in BSL staff in 2007-2008 are as follows.

The following graduate students associated with BSL completed their PhD's in the past year: Mei Xue, now a faculty member at Tongji University in Shanghai, and Karl Kappler, who is still around. Eileen Evans obtained her MS in May 2008 and worked through the summer before starting a PhD at Harvard this fall.

In the global seismology group, Aimin Cao, graduate student and later post-doc left for Rice University, and Fabio Cammarano left for ETH (Zurich). There have been several new arrivals: Laurent Stehly joined the global seismology group as a post-doc in January, and Paul Cupillard in June. Laurent obtained his PhD at the Universite Joseph Fourier in Grenoble, and Paul, at IPG in Paris. They bring expertise on the use of noise cross-correlations for structure studies, and on the Spectral Element Method, respectively. Zhao Zheng (Allen), from Peking University and Sanne Cottaar, from Utrecht University, have joined the group as graduate students.

Bob Uhrhammer, who started working at the Berkeley Seismographic Stations in 1975, retired in January 2008, and has come back to work part time as a retiree appointee. His help in training Taka'aki Taira, our new staff seismologist who arrived in August, is invaluable. Dr. Taira obtained his PhD at Hokkaido University in Japan, followed by post-docs at Carnegie and the Univ. of Utah. His research interests include earthquake nucleation and rupture processes, as well as fault rheology and time dependent phenomena in fault zones.

BSL hosted the following visiting scientists in 07-08: Jean Pierre Vilotte (IPG Paris), Georges Poupinet (Grenoble, France), Hui-Hsuan (Kate) Chen (National Taiwan Normal University, Taiwan), DV Chandrasekhar

(National Geophysical Research Institute, Hyderabad India), Luca Malagnini (Istituto Nazionale di Geofisica e Vulcanologia, Italy), Paramesh Banerjee (Newcastle University, England), Fabian Walter (ETH Zurich), Shweta Sangewar (Indian Institute of Technology, India), Andrea Cannata (University of Catania, Italy), Stefano Gresta (University of Catania, Italy), and the following summer 07 interns: Jake Lippman, from UC Davis, and Andrew Tran, from Cal Poly.

Alexey Kireev left BSL in early April. Oleg Khainovski, a 2006 UCB engineering Physics graduate, was hired in August as a programmer to work on the CISN and Early Warning projects. Angela Chung left the BSL in June to pursue a PhD in geophysics at Stanford University.

5. Acknowledgements

I wish to thank our technical and administrative staff, scientists and students for their efforts throughout the year and their contributions to this Annual Report. Individual contributions to activities and report preparation are mentioned in the corresponding sections, except for the Appendix section, prepared by Kate Lewis (Conner), Kristen Jensen and Jennifer Taggart.

I also wish to specially thank the individuals who have regularly contributed to the smooth operation of the BSL facilities: Mario Aranha, Rich Clymer, Angela Chung, Doug Dreger, John Friday, Jarrett Gardner, Peggy Hellweg, Nicolas Houlié, Bill Karavas, Alexei Kireev, Rick Lellinger, Pete Lombard, Kevin Mayeda, Rick McKenzie, Bob Nadeau, Doug Neuhauser, Charley Paffenbarger, Jennifer Taggart, Bob Uhrhammer, and Stephane Zuzlewski, and in the administrative office, Kristen Jensen, Kate Lewis (Conner), Tina Barber-Riggins, and Yolanda Andrade. I also wish to thank our undergraduate assistants, Eileen Evans, Sarah Minson, Eric Winchell, and Jozef Matlak for their contributions to our research and operations activities.

I am particularly thankful to Jennifer Taggart and Peggy Hellweg, for their help in putting together this Annual Report.

The Annual Report of the Berkeley Seismological Laboratory is available on the WWW at `http://seismo.berkeley.edu/annual_report`.

Barbara Romanowicz
September 30, 2008

Chapter 2

Research Studies

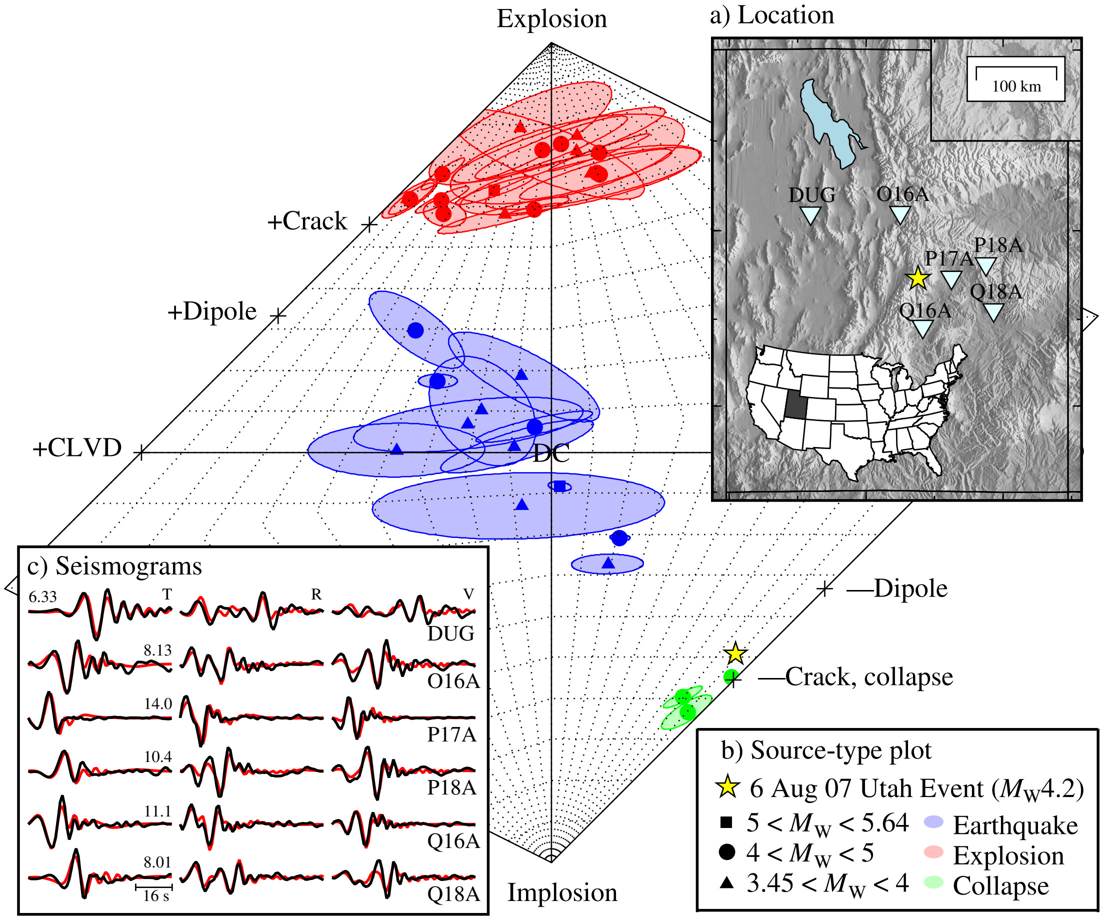

Figure 2.1: a) Locations of the August 6, 2007 event and 6 of the closest USArray and ANSS stations. b) Source type plot from the method of *Hudson et al* (1989) shows clear separation of populations of earthquakes, explosions and collapses. The yellow star shows the solution for the August 6, 2007 seismic event. c) Observed seismograms (black) are compared to synthetics (red) for the non-double-couple solution, which is dominated by a horizontal closing crack (b). The maximum displacement (10^{-7} m) of each set of tangential (T), radial (R), and vertical (V) observations is given. (Figure from Section 30.)

1. Stress preconditioning and magma chamber pressure evolution at Piton de la Fournaise

Nicolas Houlié, J.C. Komorowski, and J. Dufek

1.1 Introduction

The pressure in upper crustal magma reservoirs is a key parameter for understanding pre-eruptive surface deformation and the governing processes leading to an eruptive crisis. Although much progress has been made in documenting pre-eruptive measurements, it remains difficult to incorporate measurements that span the full range of temporal scales of deformation (from seconds to years) using existing geophysical networks.

Instrumental limitations constitute a significant difficulty in the study of processes occurring over large frequency domains. Each geophysical measurement has its own sensitivity and thus is able to describe aspects of particular source mechanisms (Figure 2.2a). For instance, short period seismic monitoring is able to track magma motion (typically $1Hz$ range) during seismic crises. However, the use of microseismic observations is limited during quiescence of volcanic activity. Broadband seismometers ($Period < 60s$) have been successfully used to constrain magma flow in secondary conduits, dyke vibration and dyke propagation (*Chouet*, 1996). Deformation survey networks (GPS, InSAR, extensometers, and tiltmeters) typically describe inter-crisis periods and highlight that the volcanic edifice is active between main flank eruptive events when the seismicity level is low. Deformation monitoring is thus complementary to seismic instrumentation. Despite the use of all techniques available from GPS to short-period seismometers, the period domain from 100 to 1000 seconds remains unfortunately inaccessible to all but very broadband seismometers (corner period > 200 seconds). These instruments require high quality installations that are complex to complete in volcanic areas. Also, the integration of velocity into displacement time-series remains challenging, and distinguishing tilt from horizontal motion (*Wielandt et al.*, 1999) is not always possible. As a consequence, theoretical numerical models that simulate continuous magmatic injection cannot be fully tested. This limits the reliability of the prediction (both time and location) of eruptive events and explains why our understanding of processes is typically restricted to pressure drops assuming single geometries (location and shape) for the source.

The creation of a physical model of a whole edifice will not be achieved until the unaccounted magma volumes injected in the volcano can be quantified properly. Most techniques (deformation, CO_2/SO_2 concentration drops, etc.) evaluate the change in pressure and not the pressure relative to lithostatic pressure. We estimate the absolute pressure in the magma chamber as a reference pressure for the whole edifice. In order to achieve this goal, we need to estimate the volumes intruded into or extruded from the magma chamber. We propose to address both instrumental and theoretical limitations by defining a geophysical model centered on the upper magma reservoir.

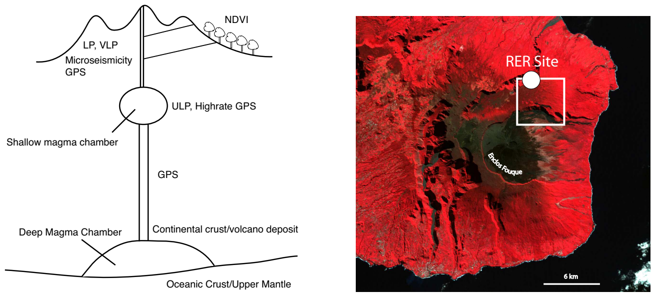

Figure 2.2: a) General sketch of the Piton de la Fournaise. Already successfully applied techniques are indicated on the sketch. b) Near infrared composite (432) of the Piton de la Fournaise volcano. Vegetated areas are red. The NDVI methodology cannot be applied on the upper part of the volcano, as there is a lack of vegetation. BAND 4 (Near infra-red, $760 - 900nm$) is the color red, BAND 3 (Visible red, $630 - 690nm$) is the color green, BAND 2 (Visible Green, $520 - 600nm$) is the color blue.

Here, we integrate seismic data, supported by geodetic observations, in a multi-scale model of the pressure in the magma chamber over the last two decades for the Piton de la Fournaise. We set up a physical model able to integrate various techniques which is consistent with the wide range of length and time scales of signals recorded on the field. As an example, we present an application (included in this framework) made at different time and space scales for different magmatic sources with different characteristic periods.

We reconstruct the pressure-history at Piton de la Fournaise (PdF) over the past two decades based on a collection of pressure drops to describe upper-crustal magma injection processes in relation to eruptive events. The choice of PdF as a study case is four-fold: First, this volcano is one of the few volcanic edifices with a very-broadband seismometer located within 10 km of the summit. Second, PdF volcano is minimally affected by tectonic stress or continental deformation. The maximal extension across the magmatic edifice was estimated at $3\,mm/yr$ (*Houlié*, 2005). The upper magma chamber lo-

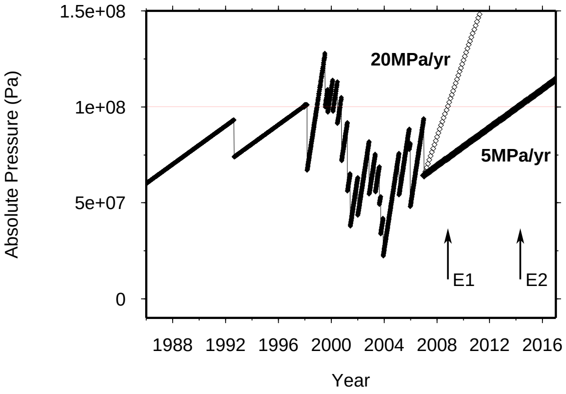

Figure 2.3: When will the next flank eruption occur at Piton de la Fournaise? Projection of the Pressure during the next decade ($I2/I1 = 8$). Assuming the pressurization rate would decrease to 20MPa/yr (period 1998-2000) or possibly to 5MPa/yr (back to the pre-1998 injection rate), the next eruptive flank event would occur between 2009 (E1) and 2012 (E2).

cated at sea-level is thus not affected by a large flank deformation of the volcano. Third, it has been one of the most active volcanoes during the last decade, with more than fifteen eruptions since 1998. And lastly, this volcano is vegetated enough (Figure 2.2b) to test the Normalized Difference Vegetation Index (NDVI) (*Richardson*, 1977) following guidelines defined previously (*Houlié et al.*, 2006).

1.2 Discussion

By proposing to model each event in the framework of the absolute pressure in the magma chamber, we hope to integrate models/datasets from various origins in order to set up a physical model of the volcano. The estimates provided in this work can be scaled according to any new available dataset (tiltmeters, degassing monitoring, etc.).

As a first step, we show that the injection rate in the upper magma chamber increased by at least a factor of 8 in two years (1999-2001), following the 1998 flank eruption. This result demonstrates the ability of the absolute pressure parameter to describe eruptive activity over decades using simple geometry reservoirs.

Additionally, computed amplitudes of the 2-year periodic magma bursts are consistent with previous long-term intrusion estimates and justify our choice of pressure of the magma chamber. The observed periodicity suggests an interaction between magma reservoirs and the changing stress state of the crust. This interaction was previously suggested (*Aki and Ferrazzini*, 2001). Representation of the volcano edifice mainly generated by monitoring habits that emphasize isolated events may be at odds with the physical model presented here.

The increased activity since 1998 may be preparing the next flank event along the fractures left open by the 1998 dyke injections. According to NDVI results, we encourage the community to also monitor the fractures formed by the 1998 eruption that have not emitted any magma yet.

References

Aki, K., and V. Ferrazzini (2001), Comparison of Mount Etna, Kilauea, and Piton de la Fournaise by a quantitative modeling of their eruption histories, *J. Geophys. Res.*, *106*(B3), 4091–4102.

Chouet, B. (1996), Long-period volcano seismicity: its source and use in eruption forecasting, *Nature*, *380*, 309–316.

Houlié, N. (2005), Mesure et Modélisation de données GPS de volcans. Applications à des études de déformation à diverses échelles et à la tomographie des panaches atmosphériques., Ph.D. thesis, Institut de Physique du Globe de Paris.

Houlié, N., J.-C. Komorowski, M. de Michele, M. Kasereka, and H. Ciraba (2006b), Early detection of eruptive dykes revealed by Normalized Difference Vegetation Index (NDVI) on high-resolution satellite imagery., *Earth & Planet. Sc. Lett.*, *246*(3-4), 231–240, doi:10.1016/j.epsl.2006.03.039.

Richardson, A. J., and C. Wiegand (1977), Distinguishing vegetation from soil background information, *Photogramm. Eng. Remote Sens.*, *43*, 1541–1552.

Wielandt, E., and T. Forbriger (1999), Near-field seismic displacement and tilt associated with the explosive activity of stromboli, *Ann. Geofis.*, *42*(3), 407–416.

2. Rigid Block Motion, Interseismic Strain, and Backarc Deformation in the Aegean

Edwin (Trey) Apel, Roland Bürgmann, and Enrico Serpelloni (INGV - Bologna, Italy)

2.1 Introduction

We combine available GPS data in and around the Aegean region to model plate boundary deformation and earthquake cycle effects in the observed velocity field. Typically, GPS data in the region have been used as evidence that a southern Aegean block behaves coherently and rigidly (e.g. *Nyst and Thatcher*, 2004; *Reilinger et al.*, 2006). These first-order models match the observed data quite well, suggesting little intra-plate or plate-boundary deformation. There has been little suggestion that the GPS data record anything other than rigid plate motion. However, the M_w ∼8.4 (*Shaw et al.*, 2008) Crete earthquake of AD 365 (Figure 2.4) and some other historic earthquakes likely occurred along the Hellenic subduction zone (*Burton et al.*, 2004), which implies that a substantial portion of the subduction thrust may be locked. Depending on the locking required to generate earthquakes of this magnitude, a measureable elastic strain signal reaching far into the overriding plate should be evident in the surface velocity field. Alternatively, slow accumulation of elastic strain and dominantly aseismic creep on the subduction thrust may generate a signal different from the pattern commonly observed along subduction zones. It is also possible that the surface velocities generated by convergence at a locked subduction zone are masked by simultaneous back-arc extension, creating the illusion of rigid block motion. We consider multiple possibilities in an attempt to interpret the current geodetic signal in the region and its implications for earthquake hazard assessment. We use a block modeling approach that considers both rigid rotations of plates and elastic strain fields along plate boundary faults to examine the possible trade-off between these components. As many of the observations are located away from the plate boundaries in question, it is difficult to constrain boundary parameters, such as locking depth and dip, using only the GPS data. We generate multiple models to explore the solution space of all reasonable parameters. Our modeling suggests that it is possible for coeval extension and convergence to occur at opposite ends of a plate masquerading as rigid block motion. Eventually, precisely determined vertical motions of GPS stations above the Hellenic subduction zone are needed to resolve this important question.

2.2 GPS Velocities

Our primary data in this study is a solution of 166 stations, concentrated primarily in Western Europe, processed by Enrico Serpelloni. Processing details can be found in (*Serpelloni et al.*, 2007). Selected, globally distributed IGS sites were used to define an ITRF00 reference frame.

In addition to our own analysis, we integrate GPS-station velocities from published work in Africa, Central Greece, and Turkey. We integrate these published solutions (*Stamps et al.*, 2008; *Reilinger et al.*, 2006; *Hollenstein et al.*, 2008; *Clarke et al.*, 1998) with our own solution. These velocities were combined with our solutions by rotating them into a common reference frame. We combine velocities published in an ITFR00 reference frame into our own solution by minimizing the misfit at co-located stations. After the combination, we compare our combined solution the published values to estimate misfit. For most sites the RMS is ∼1-2 mm/yr, well within the 95% confidence intervals for these sites.

2.3 Plates and Blocks

Plate boundary locations are critical for characterizing GPS velocities and the plate kinematics of a particular region. While some plate boundaries in the Aegean region are well defined by active fault traces, youthful geomorphology, and abundant local seismicity, others appear more diffuse and ambiguous. We draw on the distribution and kinematics of 20th century seismicity, local geology, and mapped faults, and the GPS velocity itself to define our block model boundaries. Within this paper the term plate (and microplate) refers to the rigid, coherent, lithospheric entity defined by faults, seismicity etc. The term block is the specific implementation of these data into a parameterized set of variables within our block model (e.g. *Apel et al.*, 2006).

We define our blocks as rigid entities on a spherical earth bounded by dislocations in an elastic halfspace and invert for poles and rates of rotation that minimize the misfit to the GPS velocities using the block modeling code by *Meade and Hager* (2005). Because our inversion combines rigid block rotation with elastic strain accumulation effects, the parameterization of the block boundary geometry is critical. Geometry of the block boundaries is based heavily on seismicity and adopted from prior analyses (*Nyst and Thatcher* 2004; *Reilinger et al.*, 2006) or adjusted as indicated by the geodetic data.

2.4 Results

Some block motions are well defined and vary little within our model. The Eurasian block and Nubian block

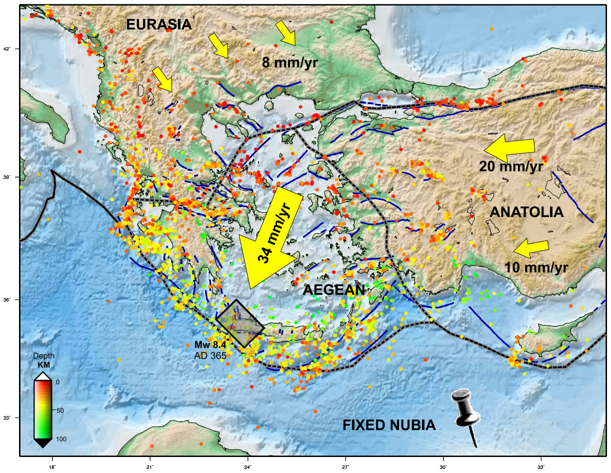

Figure 2.4: Seismicity of the Aegean region for depths less than 100km. Arrows show relative block motions in a fixed Nubian reference frame.

rotation parameters are defined primarily by the sites that lie within the stable interior and are affected very little by plate boundary strain. The inferred motion of smaller blocks (Aegean and Anatolian) can change based the parameterization of the boundaries of these blocks. The stability of the major blocks provides robust constraints on far-field motions and allows us to test variable segment geometries along those boundaries used develop our preferred model.

Figure 2.5 shows observed and predicted velocities through a model of simultaneous extension and contraction within the Aegean block. We model the subduction zone with variable locking dips which generate a series of non-unique fits to our data. It remains unclear whether or not the rigid block model with no elastic boundaries actually fits the horizontal GPS data better than models that include elastic block boundaries. At present, our models suggest that it possible to accumulate some amount of elastic strain along the subduction zone. Our continuing research includes incorporating vertical uplift rates in models to fully capture and constrain any amount of elastic strain that is accumulating along the Hellenic subduction zone.

2.5 References

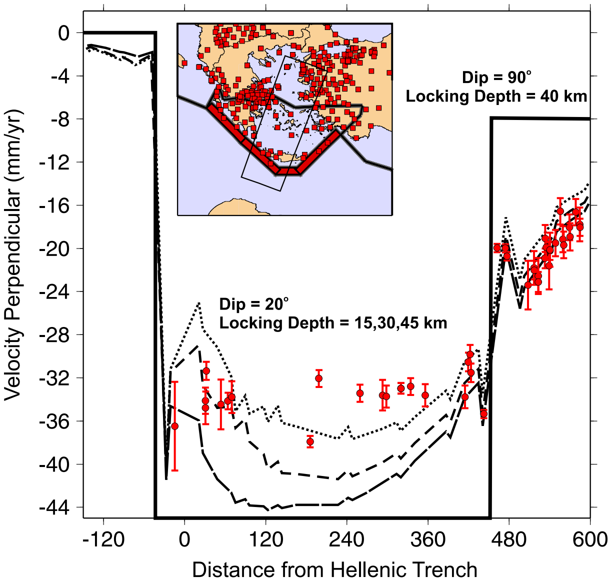

Figure 2.5: Velocity profile of measured (circles) and predicted velocities (dashed lines) through the Aegean region. The inset figure shows the block configuration used in the inversion.

Apel, E. V., R. Bürgmann, G. Steblov, N. Vasilenko, R. King, and A. Prytkov, Independent active microplate tectonics of northeast Asia from GPS velocities and block modeling, *Geophysical Research Letters*, 33, L11303, doi:10.1029/2006GL026077, 2006.

Burton, P., X. Yebang, C. Qin, G. Tselentis, and E. Sokos, A catalogue of seismicity in Greece and the adjacent areas for the twentieth century, *Tectonophysics*, Vol 390, pg. 117127, 2004.

Clarke, P. et al., Crustal strain in central Greece from repeated GPS measurements in the interval 1989-1997, *Geophysical Journal International*, Vol 135, pg. 195-214, 1998.

Hollenstein, Ch., M. Müller, A. Geiger, and H.-G. Kahle, Crustal motion and deformation in Greece from a decade of GPS measurements, 19932003, *Tectonophysics*, Vol 449, pg. 1740, 2008.

Meade, B. J., and B. H. Hager, Block models of crustal motion in southern California constrained by GPS measurements, *Journal of Geophysical Research*, 110, B03403, 10.1029/2004JB003209, 2005.

Nyst, M., and W. Thatcher, New constraints on the active tectonic deformation of the Aegean, *Journal of Geophysical Research*, 109, B11406, doi:10.1029/2003JB002830, 2004.

Reilinger R., et al., GPS constraints on continental deformation in the Africa-Arabia-Eurasia continental collision zone and implications for the dynamics of plate interactions, *Journal of Geophysical Research*, 111, B05411, doi:10.1029/2005JB004051, 2006.

Shaw B., et al., Eastern Mediterranean tectonics and tsunami hazard inferred from the AD 365 earthquake, *Nature - Geoscience*, Vol 1, doi:10.1038/ngeo151, 2008.

Stamps, S., E. Calais, E. Saria, C. Hartnady, J.-M. Nocquet, C. Ebinger, and R. Fernandes, A kinematic model for the East African Rift, *Geophysical Research Letters*, 35, L05304, doi:10.1029/2007GL032781, 2008.

3. Linking faults: Subsurface creep directly connecting the Hayward and Calaveras faults

Eileen Evans and Roland Bürgmann

3.1 Introduction

Identifying and understanding the geometry of the Hayward and neighboring faults is crucial for determining the earthquake hazard of the San Francisco Bay Area. Although creeping along most of its surface trace, the Hayward fault can and does produce major earthquakes; the last rupture occurred in 1868. Slip on the Calaveras and Hayward faults may be transferred directly between the two faults through a contiguous stepover, requiring reassessment of potential earthquake scenarios on both faults. Seismicity on the fault shows that the near-vertical Hayward Fault dips to the east towards the southern end of its trace (*Waldhauser and Ellsworth*, 2002). Characteristic repeating earthquakes through the stepover provide an estimate of subsurface creep through the juncture. Incorporating InSAR and updated GPS campaign data into an elastic dislocation model of the East Bay, we evaluated the validity of the seismically proposed geometry and explored the kinematics of a contiguous structure linking the Hayward and Calaveras faults.

3.2 Seismic Stepover

A seismic trend east of the southernmost trace illuminates a possible contiguous structure linking the Hayward Fault with the Calaveras Fault to the east (*Manaker et al.*, 2005). Accurate hypocenter locations in the seismic trend between the Hayward and Calaveras faults begin to reveal the structure of this stepover region. A tomographically derived velocity structure of the eastern Bay Area, combined with hypo-dd relocations of clustered events, made better absolute relocations of microseismicity possible (*Hardebeck et al.*, 2007). We used these relocations to define the geometry of fault planes in our dislocation model. The relative relocations of the hypo-dd method, (*Waldhauser and Ellsworth*, 2002) sharpen fault structures and clearly show the eastward dip of the Hayward fault (Figure 2.6). Additionally, characteristic repeating earthquakes (*Nadeau et al.*, 1994) exist through the stepover (Figure 2.6), identifying a relatively narrow band of seismicity within the background seismicity. We consider these repeaters as a proxy for creep, confirming aseismic slip through the stepover.

3.3 Modeling GPS and InSAR data

GPS campaigns, conducted over the last year in the Grant network in Halls Valley and the Calaveras network surrounding the Calaveras reservoir, give updated surface velocities for the region, demonstrating deformation consistent with a dipping Hayward Fault. In our slip inversion, we also include GPS data from the Bay Area's permanent network and PS-InSAR (Permanent scatter-interferometric synthetic aperture) data. We use an elastic dislocation model (*Okada*, 1985) of Bay Area faults (*Bürgmann et al.*, 2006), incorporating several shallow rectangular dislocations to model the stepover (constructed to be as contiguous as rectangles will allow)(Figure 2.6). We then perform a joint inversion to solve for slip on these dislocations, finding high slip rates near Fremont and towards the Calaveras. Slip inversions on the step-over structure were robust between InSAR and GPS. In the final inversion, the InSAR data are weighted at 20%. Modeled surface velocities (in gray) and observed velocities (black) are shown in Figure 2.7. As the stepover patches dive underground, modeled slip increases towards the Calaveras fault, which is conistent with creep rates on that section on the Calaveras (*Manaker et al.*, 2003) and with the slip estimates from the repeaters (*Nadeau*, 1994). Indeed, the existence of characteristic repeating earthquakes through the stepover indicates that creep actively contributes to the direct transfer of slip from the central Calaveras fault to the southern Hayward fault.

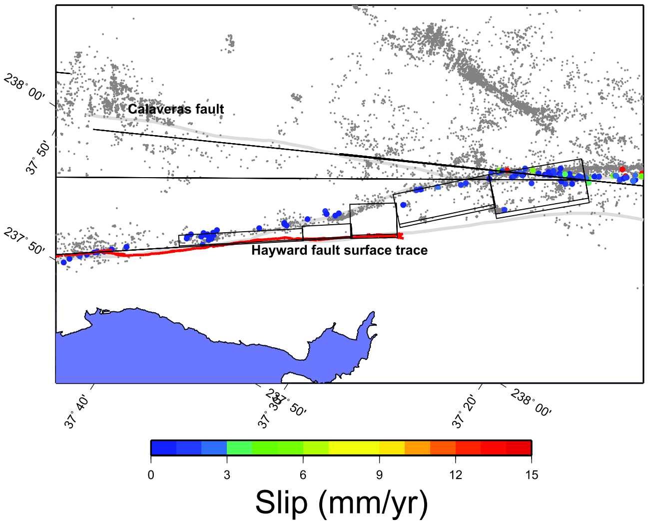

Figure 2.6: The Mission trend between the Hayward and Calaveras faults is well defined in the background seismicity. Characteristic repeating earthquakes are superimposed on seismicity and color coded by slip rate. Rectangles are the surface projections of model faults.

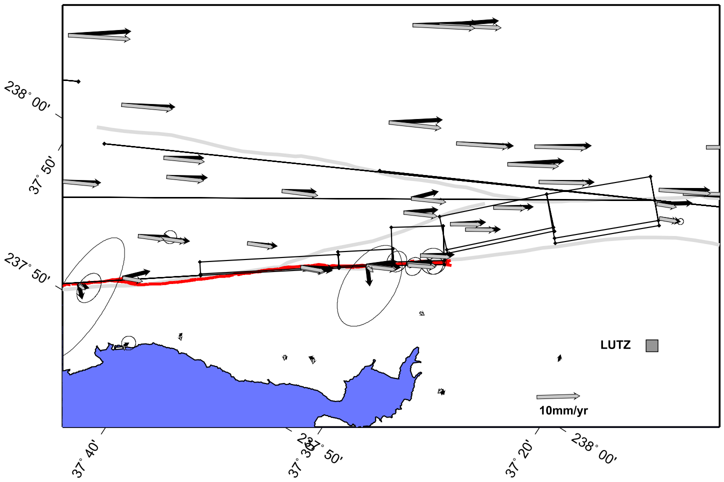

Figure 2.7: Modeled velocities based on our slip inversion are shown in gray. Observed velocities are black. All velocity vectors are shown in reference to station LUTZ

3.4 Alum Rock Earthquake

On October 30, at 8:04 local time, a M_w 5.4 earthquake nucleated just south of the Calaveras Reservoir. The epicenter was located on the central Calaveras fault between the Calaveras network to the north and the Grant network to the south. Aftershocks to the south extended into the Grant network, which had been surveyed only two weeks before. Following the earthquake, we set up GPS recievers in the Grant network. Additionally, several nearby continuous GPS sites observed this earthquake. Coseismic offsets following the Alum Rock earthquake are consistent with right lateral slip. Offsets in the Grant network indicate compression across the fault, although the measurements have large error. Aftershocks continued for several days, and the signal continued to develop for months following the earthquake. Unfortunately, the postseismic signal is too small relative to noise to quantify postseismic deformation.

3.5 Conclusions

The Hayward Fault dips into and merges with the Calaveras Fault at depth, affecting hazard scenarios on both faults. This contiguous step-over appears to directly transfer slip between the two faults. Characteristic repeating earthquakes outline this geometry and confirm subsurface creep through the juncture. GPS velocities and PS-InSAR range change rates verify this geometry and constrain slip rates. Additionally, the 2007 Alum Rock earthquake demonstrated that this region is seismogenic. This implies that a large earthquake on the Hayward or Calaveras fault may transfer slip through the step-over, in previously unanticipated rupture scenario.

3.6 Acknowledgements

Special thanks to Isabelle Ryder, Romain Jolivet, David Shelly, and Rob Porritt for their invaluable field assistance. This project was made possible by NSF grant EAR-0337308.

3.7 References

Bürgmann, R., G. Hilley, A. Ferretti and F. Novali, Resolving vertical tectonics in the San Francisco Bay Area from permanent scatterer InSAR and GPS analysis, *Geology, 34* no. 3; p. 221-224, 2006.

d'Alessio, M.A., I.A. Johanson, R.Bürgmann,, D.A. Schmidt, M.H. Murray, Slicing up the San Francisco Bay Area: Block kinematics and fault slip rates from GPS-derived surface velocities, *J. Geophys. Res., 110*, 2005.

Hardebeck, J. L., A.J. Michael, and T.M. Brocher, Seismic Velocity Structure and Seismotectonics of the Eastern San Francisco Bay Region, California, *Bull. Seism. Soc. Am., 97,* 826-842, 2007

Manaker, D.M. A.J. Michael, and R. Bürgmann, Subsurface Structure and Kinematics of the Calaveras-Hayward Fault Stepover from Three-Dimensional Vp and Seismicity, San Francisco Bay Region, California, *Bull. Seism. Soc. Am., 95,* 446-470

Manaker, D.M., R. Bürgmann, W.H. Prescott, and J. Langbein, Distribution of interseismic slip rates and the potential for significant earthquakes on the Calaveras fault, central California, *J. Geophys. Res., 108*, 2287, 2003.

Okada, Y., Surface Deformation due to shear and tensile faults in a half-space, *Bull. Seism. Soc. Am., 75,* 1135-1154, 1985

Waldhauser, F., W.L. Ellsworth, Fault structure and mechanics of the Hayward Fault, California, from double-difference earthquake locations, *J. Geophys. Res., 107*, B32054, 2002

4. No Apparent Accelerating Moment Release in Areas of High Stress

Aurélie Guilhem and Roland Bürgmann

4.1 Introduction

The search for spatio-temporal interactions between earthquakes is fundamental in order to understand the stress evolution in the lithosphere as well as the earthquake mechanism. Many studies have been conducted to analyze the evolution of seismicity in relation to the stress field, with the idea that continuous plate motion needs to be accommodated on faults by the occurrence of earthquakes releasing the accumulated stress. This earthquake cycle theory, first developed by Reid in 1910, introduced the relation between elastic stress accumulated along the fault zone and occurrence of earthquakes. The Accelerating Moment Release (AMR) idea was developed by *Bowman et al.* (1998) and is based on the hypothesis that prior to a large earthquake the stress field in the vicinity of the next rupture increases in such a way that one can observe an acceleration of the background seismicity following a power-law function. The change in the seismicity rate produces a regional increase in the cumulative Benioff strain, which is a measure of the cumulative seismic energy of the seismic events considered prior to a mainshock. To quantify the AMR, one examines the ratio, called c-value, between the root-mean-square of a power-law time-to-failure function versus a linear fit to the cumulative energy of the events. A strong case for AMR would be for c less than 0.5. Previous works (*Guilhem et al.*, 2007; *Hardebeck et al.*, 2008) showed that AMR, observed for all M6.5+ earthquakes in Southern California of recent times (*Bowman et al.*, 1998; *Bowman and King*, 2001), is very sensitive to three free parameters: magnitude range of the pre-seismicity, area surrounding the events (considering a circular search) and the time period prior to a large earthquake. Because of the large dependence on the choice of the free parameters, doubts about the validity of the analysis have emerged (*Hardebeck et al.*, 2008).

4.2 AMR search in Parkfield region

Mignan et al. (2007) suggested that if AMR exists, one should in theory observe it over an entire earthquake cycle. The Parkfield region is an excellent example for studying AMR where M6.0 earthquakes, since 1857, repeat over a relatively short earthquake cycle (22 years on average). We studied the AMR during the last two earthquake cycles, from 1935 to 1966 and 1967 to 2004, using the ANSS seismicity catalog ($2.0 \leq M \leq 7.0$ in a 5-by-5 degree region centered on the nucleation zone). Computation of the AMR in the area was performed using various magnitude and distance ranges. The lowest c-values noticed during the first earthquake cycle (about 32 years, from 1934 to 1966) was 0.65 for a search area radius of 85 km, indicating that no AMR was objectively observed during the time period. The second earthquake cycle (1967 to 2004) did not show any case of AMR; the c-value is equal to 1 over all radii considered (0 to 200 km) (Figure 2.8). The AMR results appeared to be very sensitive to the occurrences of the 1983 M6.5 Coalinga and 2003 M6.5 San Simeon earthquakes and in particular to their aftershock sequences. Declustering the earthquake catalog to remove most of the aftershocks was performed, but still no change was detected in the AMR.

AMR appears to be biased by the occurrence of large earthquakes during the studied period (Figure 2.8). A large event in the beginning of a chosen observation period tends to dominate the analysis and to increase the c-value, compared to a mainshock at the end of the time period that would significantly decrease the c-value and support the case for AMR (small c-value).

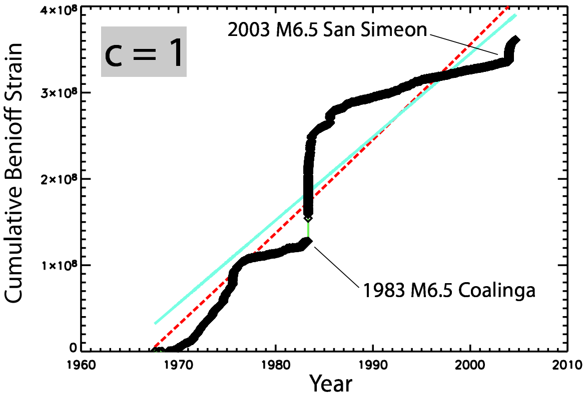

Figure 2.8: AMR in the Parkfield region in a 60-km radius region. The c-value for the 1967-2004 period does not show any AMR, with a c-value equal to 1. The red dashed line shows the power-law function, and the blue line shows the best-fit linear trend of the cumulative Benioff strain. The occurrences of the 1983 M6.5 Coalinga and 2003 M6.5 San Simeon earthquakes, and their aftershock sequences, dominate the signal.

4.3 AMR and Stress

In order to complete the analysis of AMR in Southern California, we evaluated AMR in apparent high stress regions. Maps of stress changes were computed by Andrew Freed at Purdue University considering the coseismic, postseismic and interseismic stress changes of all M7+ earthquakes in Southern California for the last 200 years (*Freed et al.*, 2007). We tested for AMR in the areas of high stress (Figure 2.9), using the hypothesis that the high stress regions represent the places of eventual future events, compared to the regions of low stress, and where we would expect to detect significant AMR if the AMR idea is correct. We studied the AMR for the two high stress regions presented in Figure 2.9 over various time ranges, starting in 1950 to 2008. The test was performed for an eventual mainshock in the region on June 1st, 2008, about 6 months after the end of the analyzed earthquake catalog. We considered all seismic events occurring in the high stress regions ($\Delta\sigma \geq 10$ bars), excluding events in lower stress areas, and we computed the AMR in such way that we considered the entire high stress regions. No AMR was detected in those two regions (c-values remained between 0.8 and 1.0). We performed an AMR search in the area of low stress resulting from the occurrence of the great Fort Tejon earthquake, and we did not find evidence of AMR. No difference is observed in the AMR between high and low stress areas. Also, we performed an AMR study over the entire region, considering all events in regions where the stress exceeds 10 bars as well as all events with no condition on the stress field, and again no significant variation was observed.

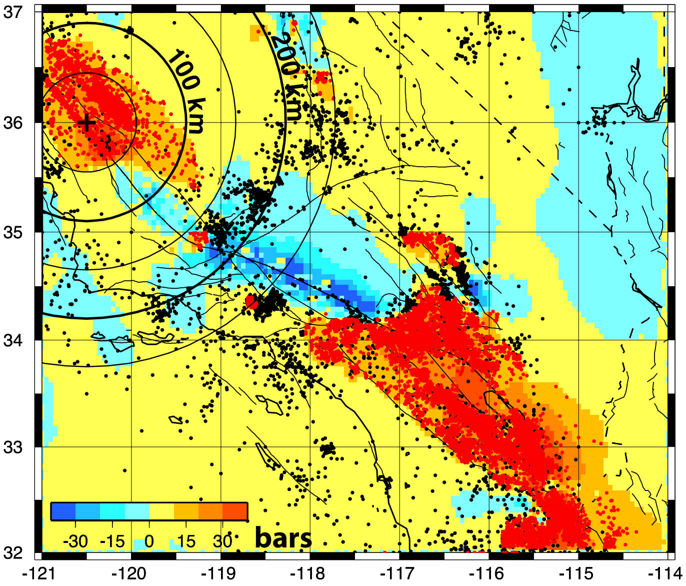

Figure 2.9: AMR study in the northern high stress region. The circles materialize the distance every 50 km from a possible epicenter (black cross). The red dots are the M2.5+ earthquakes located in a high stress region (stress larger than 10 bars), and the black dots show other M2.5+ events in the study region. The background colors show the stress field computed by Andrew Freed for 2005.

4.4 Conclusions

Recent AMR studies (Guilhem *et al.*, 2007; Hardebeck *et al.*, 2008) emphasize the high sensitivity to the choice of free parameters considered in the AMR idea, which becomes a data-fitting exercise with no real power in earthquake forecasting. No evidence of AMR was noticed in the Parkfield region where periodic M6.0 earthquakes occur. AMR, which should be related to high stress regions, is not observed in Southern California, even considering various time, magnitude and distance ranges. Finally we noticed the significant impact of the timing of large events during the pre-mainshock period on the AMR calculations. A large earthquake occurring in the early time period will cancel an eventual AMR case by adding a significant cumulative Benioff strain in a very short time. The contrary is observed when the large shock occurs at the end of the time analysis, forcing to an AMR case.

4.5 References

Bowman, D.D., G. Ouillon, C.G. Sammis, A. Sornette, and D. Sornette (1998), An observational test of the critical earthquake concept, *Journ. of Geophys. Res., 103, B10*, 24,349-24,372.

Bowman, D.D. , and G.C.P. King (2001), Accelerating seismicity and stress accumulation before large earthquakes, *Geophys. Res. Lett., 28*, 4039-4042.

Freed, A.M., S.T. Ali, and R. Bürgmann (2007), Evolution of stress in Southern California for the past 200 years from coseismic, postseismic and interseismic stress changes, *Geophys. Journ. Intern., 169*, doi: 10.1111/j.1365-1246X.2007.03391.x.

Guilhem, A., R. Bürgmann, A.M. Freed, and T. Ali (2007), Accelerating Moment Release in Areas of High Stress? Preliminary Results, *2006-2007 Berkeley Seismological Laboratory Annual Reports.*

Hardebeck, J.L., K.R. Felzer, and A.J. Michael (2008), Improved Tests Reveal that the Accelerating Moment Release Hypothesis is Statistically Insignificant,*Journ. of Geophys. Res., in press.*

Mignan, A., D.D. Bowman, and G.C.P. King (2007), A Mathematical Formulation of Accelerating Moment Release Based on the Stress Accumulation Model, *Journ. of Geophys. Res., 111*, B11304.

5. Probing the Rheology of Tibet using Postseismic Motion from Large Earthquakes

Isabelle Ryder and Roland Bürgmann

5.1 Introduction

For the last three decades, a rather vigorous debate has been going on about the most fundamental aspects of the style of continental deformation in the India-Eurasia collision zone. While one school of thought envisions Tibet to be a thickened, weak and fluid-like zone (e.g. *Cook and Royden*, 2008), others consider the tectonics in the region as that of essentially rigid microplates bounded by major lithospheric faults (e.g. *Thatcher*, 2007). Until this issue is resolved, it will be difficult to gain a clear idea of what forces drive the deformation of the upper crust in this region. Large earthquakes initiate rock mechanics experiments of lithospheric dimensions in which a sudden stress change leads to stress relaxation at depth. Surface measurements of the resulting deformation provide a basis for testing structural and rheological models of the lithosphere.

Our main objective in this project is the elucidation of lithospheric rheological structure in northern Tibet, chiefly through InSAR investigation of postseismic motion following three recent major earthquakes. These events are the 1997 M_w 7.6 Manyi earthquake (*Funning et al.*, 2007; *Ryder et al.*, 2007), the 2001 M_w 7.9 Kokoxili earthquake (*Lasserre et al.*, 2005) and the 2008 M_w 7.2 Yutian earthquake. By analysing the spatio-temporal characteristics of the postseismic signals, and testing the data against various candidate models, we hope to determine whether deformation in the mid to lower crust is localized or distributed, and constrain rheological parameters associated with our preferred model. Our broader objective is to inform the geophysical debate concerning the nature of the Tibetan Plateau: specifically, whether it behaves more like a viscous fluid or a series of rigid blocks.

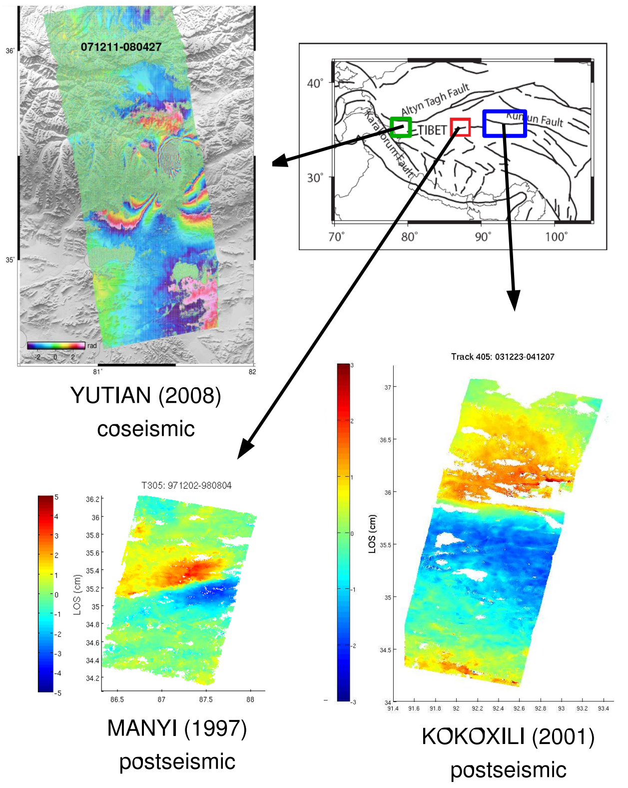

Figure 2.10: Interferograms for the three earthquakes considered in this study. Postseismic interferograms are shown for the 1997 Manyi earthquake and the 2001 Kokoxili earthquake. For the Manyi case, ERS-2 SAR data covering an 8-month time interval are used, and for the Kokoxili case, Envisat data covering a 1-year time interval are used. A coseismic interferogram is shown for the 2008 Yutian earthquake, with each fringe representing about 12 cm of line-of-sight displacement.

5.2 InSAR Observations

We use the satellite geodetic technique of Interferometric Synthetic Aperture Radar (InSAR) to observe postseismic deformation for several years following each of the three major earthquakes. For the Manyi case, we use data from the European Space Agency's (ESA) ERS-2 satellite, and for the Kokoxili case we use radar scenes from ESA's Envisat. The Yutian earthquake occurred after the launch of Japan's L-band ALOS satellite, so we will be able to utilize postseismic data from this as well as the C-band Envisat. Postseismic interferograms for both the Manyi and Kokoxili earthquakes reveal several centimeters of line-of-sight transient displacement in both cases (Figure 2.10). The wavelength of the postseismic signal suggests that relaxation processes occur at a depth of 15-20 km, which is approximately the seismogenic depth in this area. A deformation time series for the Manyi event can be constructed from multiple interferograms, and yields a relaxation time of 0.7 years. It is not possible to make early postseismic interferograms for the Kokoxili case, and so making a time series is difficult, but GPS data from a network of 65 sites either side of the rupture will ultimately give temporal information about the postseismic transient. We are currently waiting for postseismic data for the Yutian earthquake; cosesismic interferograms have been processed, and show clear deformation fringes despite the ice cover in the area. Figure 2.10 shows interferograms for each of the three events.

5.3 Viscoelastic Models

In order to interpret the observed surface deformation in terms of sub-surface rheological structure, we implement models of postseimic stress relaxation in a viscoelastic medium. The idea here is that stress changes near the fault induced during the earthquake are relaxed due to viscous flow beneath an elastic upper crust. The thickness and viscosity of a Maxwell viscoelastic layer are varied in the models, and we seek parameters which best fit the data. For both the Manyi and Kokoxili cases, the best-fit viscosity is between 5×10^{18} and 1×10^{19} Pa s; a single thick viscoelastic layer is preferred, suggesting that the entire mid to lower crust flows, with no stratification in viscous properties.

5.4 Future Work

A Maxwell viscoelastic medium is the simplest type of linear viscoelastic rheology, and it is reasonable to run initial models using such a rheology. However, the Manyi time series is not fit consistently throughout the entire 3.5 year observation period by a single Maxwell viscosity; rather, the effective viscosity increases over time. Another linear rheology which could produce this effect is a Burgers body, which consists of a Maxwell and a Kelvin element in series. We are currently running further models, varying the transient and steady-state viscosities as well as the ratio of Maxwell and long term shear moduli. Another candidate relaxation mechanism is localized afterslip on an extension of the coseismic rupture plane at depth. The data will also be tested against models simulating this mechanism. For strike-slip earthquakes such as Manyi and Kokoxili, surface deformation due to distributed viscous flow and localized afterslip can look very similar. The postseismic signature of the normal-faulting Yutian earthquake should be particularly useful for distinguishing between mechanisms, since the surface deformation from the two processes looks very different for dip-slip events.

5.5 Acknowledgements

This project is funded by NSF grant number EAR-0738298. All SAR data are from the European Space Agency (ESA), obtained through Category-1 Proposal No. 5119.

5.6 References

Cook K.L. and L.H. Royden, The role of crustal strength variations in shaping orogenic plateaus, with application to Tibet. *J. Geophys. Res., 112,* doi: 10.1029/2007JB005457, 2008.

Funning, G., B. Parsons and T. Wright, Fault slip in the 1997 Manyi, Tibet earthquake from linear elastic modelling of InSAR displacements, *Geophys. J. Int., 169,* 988–1008, 2007.

Lasserre, C., G. Peltzer, F. Crampé, Y. Klinger, J. Van der Woerd and P. Tapponnier, Coseismic deformation of the 2001 Mw = 7.8 Kokoxili earthquake in Tibet, measured by synthetic aperture radar interferometry, *J. Geophys. Res., 110,* B12408, 2005.

Ryder, I., B. Parsons, T. Wright and G. Funning, Post-seismic motion following the 1997 Manyi (Tibet) earthquake: InSAR observations and modelling, *Geophys. J. Int., 169,* 1009–1027, 2007.

Thatcher, W., Microplate model for the present-day deformation of Tibet, *J. Geophys. Res., 112,* B01401, 2007.

6. Automated Time-Domain Spike Identification for MT Data

Karl N. Kappler

6.1 Introduction

A method of automatic time domain spike identification for magnetotelluric array data is outlined. The algorithm exploits the simultaneous nature of geomagnetic variations at sites far (100's of km) away from one another. Data time series for instruments of the same field-type at various locations are windowed and condensed into time series of variances over the windows. Time series of the ratios of these variances are then scanned for outliers, where the definition of outlier is defined by an adaptive threshold. Examples are shown applying the method to a pair of MT stations in Central California, each with orthogonal electric dipoles and induction coil magnetometers. The method successfully identifies windows contaminated by spikes, DC offsets, and other strange variations. Only days where less than 10% of the data are contaminated are treated. A separate, but similar method not discussed here is employed to eliminate days where more than 10% of the data are contaminated.

6.2 Spike Identification

Magnetotellurics (MT) relies upon the recording of tiny variations in the earth's magnetic field. The spike identification is predicated on the assumption that these variations are horizontally polarized (spatially uniform) over 100's of km. In the absence of overwhelming noise, this implies that sensors at different sites will be strongly correlated, with the magnetic fields being nearly identical and the electric fields differing by a scale factor which depends on the local conductivity structure. This scale factor is approximately stationary as evidenced by the stability of intersite transfer functions [*Eisel and Egbert* 2002]. Figure 2.11 shows orthogonal electric and magnetic field data sampled at the earth's surface at two sites a distance of 120km apart. For a detailed description of the sites see [*Kappler* 2005]. Note the similarity in variations between channels of same orientation and field type, as well as identical scaling of the magnetic components, compared to the scale factor difference in the electric channels. This similarity can be seen to extend from periods of hours to seconds as shown by repeatedly zooming in on the data in Figures 2.12, 2.13, and 2.14.

This inherent similarity in the fields is exploited to identify windows in time when the array is not functioning correctly. Magnetotelluric data is prone to sudden sharp variations in signal of natural origin. These variations can be differentiated from variations whose origins are local noise by comparing channels at different sites, and flagging sharp variations which are not present arraywide. A variety of statistics can be used to identify spikes. The statistic used here is simply the variance of each array channel over short time windows. The variance can be calculated directly in each time window, or alternatively, the variance of the first difference data can be calculated. The ratio of the variance in channels which record the same field type at the same orientation should be stationary about some typical value; in the case of magnetic fields, this value should be 1. In the case of electric fields, the value will be approximately stationary around some value, which reflects site effects such as local field distortion phenomena. The stationarity is only approximate because the observed fields' ratios will vary as a function of frequency, and hence electric field variance ratios will wander somewhat with the frequency content of the incident radiation. We approximately account for this by scaling the electric field data by a 'site factor' s_i which scales the i^{th} channel such that non-contaminated windows of channel i data have variance nearly equal to the variance of the same time window at a reference site. Formally, with the electric field data scaled in V/m and the magnetic field data still in instrument counts (effectively dB/dt), the time series of data collected by the i^{th} sensor S_i is represented as an N-point time series $\mathbf{x}_i(\mathrm{t})$. The N-point time series is chopped into windows of length L and overlap V, resulting in a total of k=floor(N/(L-V)) windows. Thus $\mathbf{x}_i(\mathrm{t})$ is represented as $\mathbf{X}_i(\mathrm{t})$, a KxL array, whose j^{th} row is the contiguous stream of data centered at t=j*(L-V). The last row of $\mathbf{X}$ is taken as the final L points of $\mathbf{x}$ in order to avoid zero-padding. The array $\mathbf{X}$ is then contracted to a vector $\mathbf{v}$ whose j^{th} element is the variance of the j^{th} row of $\mathbf{X}$. We thus obtain a windowed variance time series $\mathbf{v}_i(\mathrm{t})$ for each sensor, where the time increment for $\mathbf{v}$ is (L-V) times the sampling period of $\mathbf{x}$. In our example, we use day-long time series, sampled at 1Hz (hence N=86400), and set L=256, V=64, thus k=450.

The choice of window length should be sufficiently wide to account for possible intersite timing errors and FIR filter noise convolved on top of spikes, but sufficiently narrow that moderate sized spikes drive the window variance well above the value it would have without a spike. To apply the electric field scale factors, we look at the ratios of the $\mathbf{v}_i$ for approximately parallel electrodes at the different sites. In our example, we use SAO as the reference site, and point-by-point ratios of $\mathbf{v}_{ExSAO}$ to $\mathbf{v}_{ExPKD}$ are examined together with point-by-point ratios of $\mathbf{v}_{EySAO}$ to $\mathbf{v}_{EyPKD}$. Each cardinal sensor orientation is examined separately because of possible site distortion effects. Figure 2.15 shows the variance ratios over a four-year

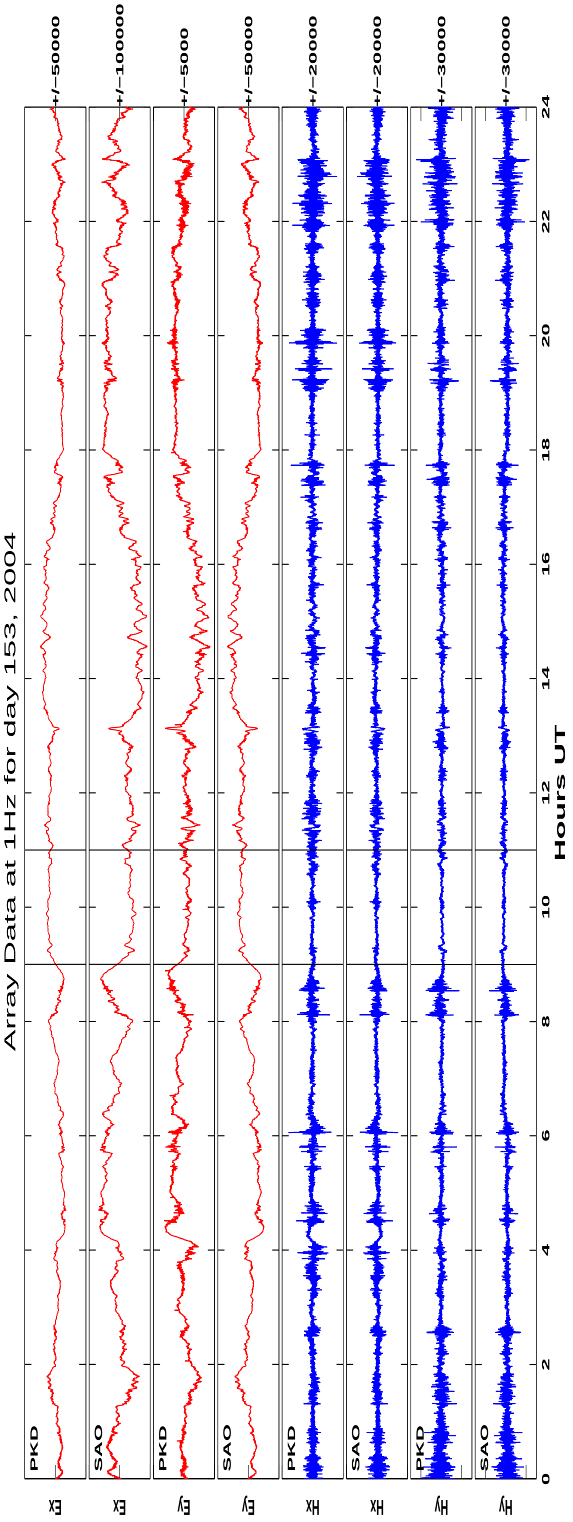

Figure 2.11: A plot of mean-subtracted array data for a full day in 2004. Electric fields are shown in red and magnetic fields in blue. Plots alternate between PKD and SAO at each field polarity. Y values are in counts with axis limits shown to the left. The vertical lines mark the domain boundaries of Figure 2.12.

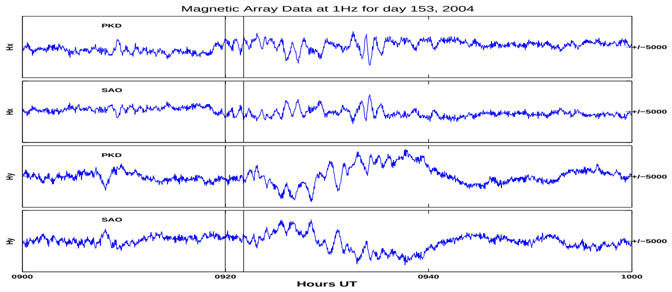

Figure 2.12: Detrended magnetic array data for one hour of the day shown in Figure 2.11. Plots alternate between PKD and SAO at each field polarity. The vertical lines mark the domain boundaries of Figure 2.13.

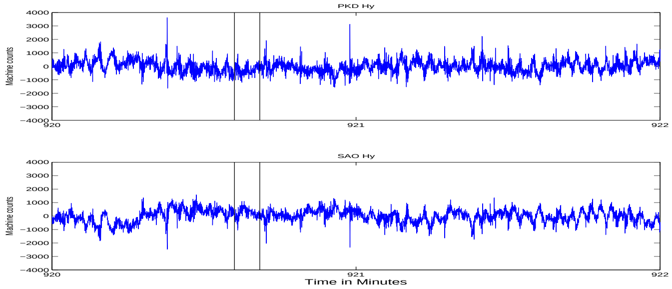

Figure 2.13: Detrended time series of y-polarity magnetic channels for two minutes within the hour shown in Figure 2.12. The vertical lines mark the domain boundaries of 2.14

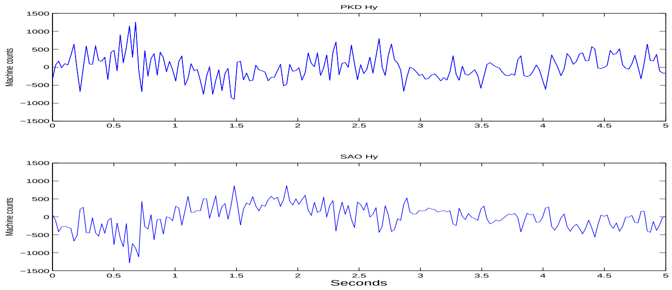

Figure 2.14: Detrended time series of y-polarity magnetic channels for 5 seconds within the window shown in Figure 2.13.

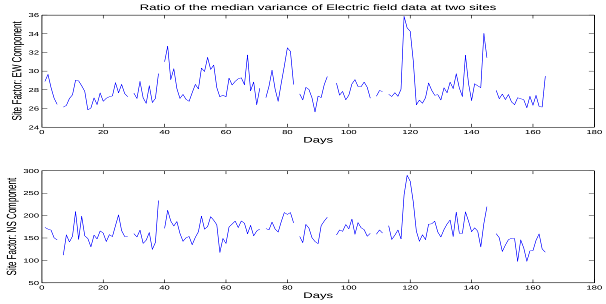

Figure 2.15: Each day, 450 windows of 256s length are input to calculate variance ratios. The daily median is shown above. Note the relative anisotropy between sites.

window. Note that there is a significant difference in the ratio amplitudes between the two cardinal orientations, a median of 28 for EW and 148 for NS, implying a relative electrical anisotropy between the two sites. Some seasonal effects are also apparent, as are offsets due to instrument swaps, or times when sites were not functioning properly. In general however, the ratio is reasonably stable, and stationary on a day-to-day basis. The EW electric field at PKD is thus scaled by $\sqrt{28}$ or equivalently $\mathbf{v}_{EewPKD}$ is scaled by 28, and similarly for the NS component. With E field data appropriately scaled, we recalculate the $\mathbf{v}_i(\mathrm{t})$, but this time the rows of $\mathbf{X}_i$ are first-differenced before variances are calculated. Windows of anomalous variance can now be flagged. Each $\mathbf{v}(\mathrm{t})$ is associated with a two digit code, one digit for field type (E or H) and one for orientation. Channels with the same codes are grouped together (we assume that sites are not significantly rotated w.r.t one another). Within each pairing, the log ratio $\mathbf{r}$ of the variance time series is calculated:

$$\mathbf{r}_{i,j}(t) = log_{10}(\frac{\mathbf{v}_i(t)}{\mathbf{v}_j(t)})\forall t \qquad (2.1)$$

For each grouping, the median-subtracted time series $\mathbf{r}(\mathrm{t})$ is searched independantly over each day. An anomalous window at time t is flagged if $\mathbf{r}(\mathrm{t})$ is greater than a threshold. The threshold is chosen adaptively each day as M times the two-sided α-trimmed standard deviation of $\mathbf{r}$. The two-sided α-trimmed standard deviation of a time series $\mathbf{r}(\mathrm{t})$ is defined as the standard deviation of the collection of all elements of $\mathbf{r}$ which are larger than the $\alpha/2^{th}$ percentile and less than the $(100\text{-}\alpha/2)^{th}$. Using this measure prevents a few very large spikes from driving the standard deviation up so high that smaller spikes are not caught. Practically speaking, n=5 works well for magnetic fields, and n=6 for electrics, with α set to 0.03. Plotted in Figure 2.16 are some examples of the spike ID method. On the left are shown one day's worth of $\mathbf{r}(\mathrm{t})$. The horizontal lines denote the M α-trimmed standard deviation thresholds. The vertical dashed line coincides with a time-window where a channel has been flagged as having a spike. The corresponding plot on the right shows the channel with spike and its 'sister channel' at the other site. The channels used for the numerator of the ratio are shown in blue, and the denominator channels are shown in green. The algorithm described only identifies windows where the variance ratio between two channels is anomalous. Deciding which of the two channels corresponds to non-physical data is another matter. For spikes and sharp offsets, the channel with more energy in the scaled time series is selected as the offending data. One need beware that a malfunctioning amplifier in some system component could result in a channel with a signature smaller than average variance. In this case, the algorithm will flag a normally functioning channel as spikey.

6.3 Conclusions

The method seems to work well. It has application in the monitoring of array health, and possibly in other mutichannel systems where channels typically record stationary time series. There are a very few cases where the method misidentifies data as being a spike. Addition of a hard threshold insisting that spikes be ID-ed as windows having **v** greater than 0.3 or M alpha trimmed stds, whichever is greater, seems to protect agianst this.There are several parameters which control the algorithm; these are: initial time series lengths (N), window length (L), window overlap (V), whether or not to 'first-difference the data' (boolean), α (percent of data to reject when calculating thresholds), and M, the threshold multiplier. A code has been written which incorporates these variables into a few simple scripts. Four years of data at 1Hz can be rapidly despiked in a short amount of time.

6.4 References

Egbert, G.D., Booker, J.R., Multivariate Analysis of Geomagnetic Array Data 1. The Response Space, *Journal of Geophys. Res.*, V94 No.B10 pp14227-14247, 1989

Eisel M., Egbert G.D., (2001), On the stability of magnetotelluric transfer function estimates and the reliability of their variances, *Geophys. J. Int.*, 144, pp65-82, 2001

Kappler, K.N., Morrison, H.F., Egbert, G.D., Parkfield-Hollister Electromagentic Monitoring Array, *BSL Annual Report*, 2005-06

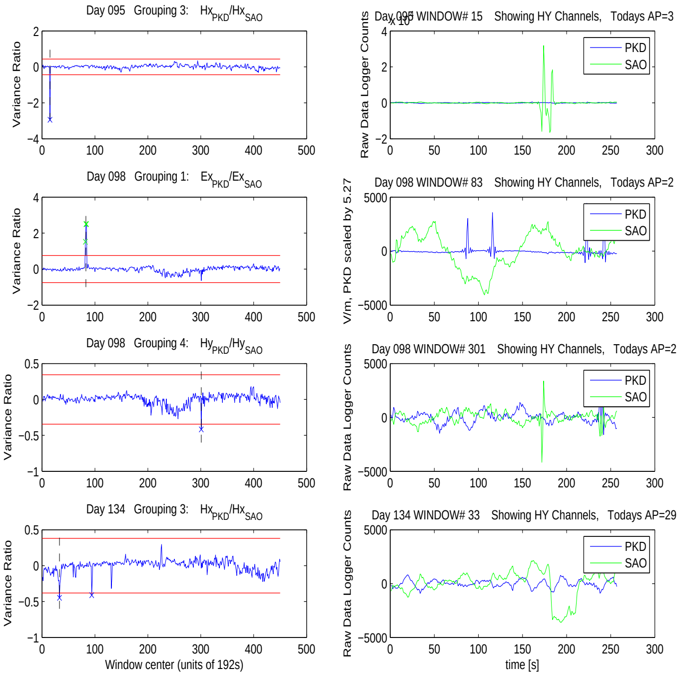

Figure 2.16: Variance ratio time series, together with adaptive threshold bars (left) raw time series (right) for window in time denoted by vertical line on left.

7. Stress Changes on the Sunda Megathrust Preceding the M_w 8.4 2007 Earthquake

Kelly Grijalva, Roland Bürgmann, and Edwin (Trey) Apel

7.1 Introduction

The M_w 8.4 September 12, 2007 Sumatra earthquake's occurrence, close in time and space to the 2004 Sumatra-Andaman and 2005 Nias megathrust events, suggests that it could be a triggered earthquake. The 2007 earthquake initiated ~750 km south of the 2005 epicenter, in the southern portion of the historic 1833 rupture zone. Earlier studies of vertical motion, derived from coral growth histories, suggest that interseismic strain accumulating along the 1833 segment had approached levels relieved in the historic earthquake (*Natawidjaja et al.*, 2006). We investigate why the portion of the Sunda subduction zone between the 2005 and 2007 rupture patches, which previously slipped in 1797, did not rerupture or rupture with the 2007 event.

7.2 Coulomb Failure Stress Models

We model the coseismic and viscoelastic postseismic deformation from the 2004-2005 earthquake sequence in order to quantify its influence on the hypocentral region of the 2007 earthquake. The elastic coseismic deformation is calculated in a layered spherical geometry using the method of *Pollitz* (1996) and previously published source parameters (*Banerjee et al.*, 2006; *Konca et al.*, 2007; *Zhou et al.*, 2002). Viscoelastic relaxation is calculated using the method of *Pollitz* (1992), with a bi-viscous rheology in the asthenosphere that includes an initial short-term viscosity of 5×10^{17} Pa s and a long-term viscosity of 1×10^{19} Pa s (*Pollitz et al.*, 2006). We use the deformation calculations to model the Coulomb failure stress (CFS) changes along the Sunda megathrust. Previous studies have shown that CFS increases of 1-3 bars are generally sufficient to trigger seismicity and sometimes even a few tenths of a bar appear sufficient to advance (or retard) the occurrence of large earthquakes (e.g. *Rydelek and Sacks*, 1999; *Lin and Stein*, 2004). We use a CFS function given by CFS $= \Delta\tau + \mu' \Delta\sigma_n$, which defines CFS as a sum of the change in shear stress τ and the change in normal stress (clamping is negative) σ_n, multiplied by an effective coefficient of friction. We assume low frictional fault strength and use an effective coefficient of friction, $\mu' = 0.1$. CFS changes are resolved onto the down-going Sunda slab, with dips increasing at depth, and rake varying along strike.

Although the 2004 event was a M_w9.2, the ~950 km separation distance prevented the coseismic and postseismic CFS changes at the 2007 hypocenter from being $>$ 0.1 bars. The 2005 earthquake was also too far from the 2007 hypocenter to produce significant CFS changes. The 2004-2005 sequence did produce a slightly negative CFS change in the 1797 rupture patch. Notably, the largest contributor to positive CFS change at the southern portion of the 2007 rupture zone was the M_w7.9 2000 earthquake. However, the 2000 earthquake still did not produce > 0.1 bars CFS changes at the 2007 hypocenter (Figure 2.17).

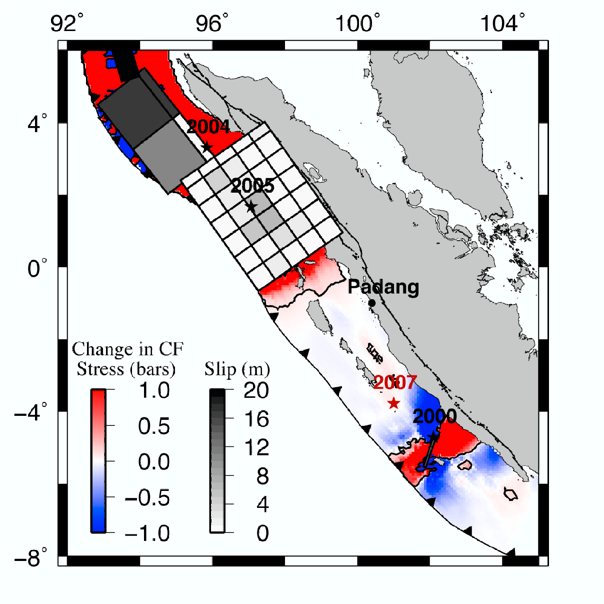

Figure 2.17: Total CFS changes resulting from the combination of the 2000, 2004, and 2005 coseismic and postseismic deformation on the Sunda megathrust. The 0.1 bar contour is plotted in black and the earthquake source models overlay the CFS changes.

7.3 Seismicity Rate Changes

We investigated seismicity changes following the 2004 earthquake using the standard beta-statistic approach (*Hough*, 2005). Beta is defined as $\beta = (N_a - N_e)/\sqrt{variance}$, where N_a is the number of earthquakes occurring after a major event and N_e is the expected number of earthquakes. Beta will be large and positive when there is increased seismic activity. We compare the annual seismicity $M \geq 4.5$ following the 2004 event with the previous fifteen years of earthquakes. Figure 2.18 shows the beta values for the Sumatra region at the

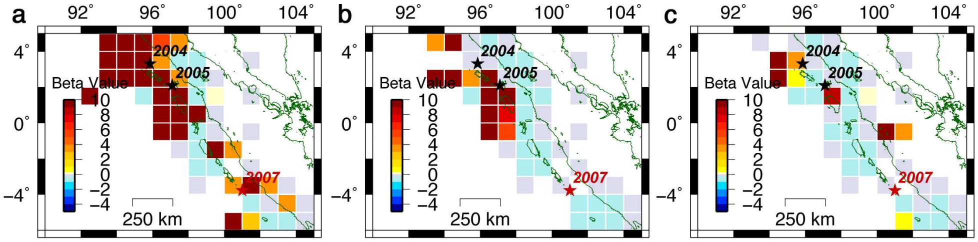

Figure 2.18: Beta values showing the relative change in seismicity following the 2004 earthquake in a) 2005, b) 2006, c) 2007 up to the September earthquake. All beta values are based on seismicity between 15-30 km depth.

depth range of 15-30 km, which includes the depth of the 2007 earthquake. Based on the high beta values, seismicity increased in the vicinity of the 2007 event during the months following the 2004 and 2005 megathrust earthquakes. In 2005, seismicity also increased near Siberut Island, at the northern end of the 2007 rupture patch. This increased seismicity may be related to aseismic slip on the Sunda megathrust, which could have further stressed the 2007 hypocentral region. During 2006 and 2007, the seismicity level dropped off to average conditions at the 2007 hypocenter location.

7.4 Discussion and Future Work

CFS change at the 2007 hypocenter, resulting from the combined 2004-2005 coseismic and postseismic deformation, is likely too small to have triggered the recent earthquake. The slightly negative CFS change in the northern 1797 rupture patch, resulting from the 2004-2005 earthquake sequence, may have delayed the recurrence of the 1797 earthquake. The smaller 2000 earthquake turns out to have had the largest CFS change at the 2007 hypocenter and may help to explain the southern location of the 2007 earthquake. Furthermore, increasing the oblique component to the slab receiver fault geometry, as observed with the larger than average 114° slip direction for the 2007 earthquake, amplifies this positive CFS change. Investigations of the beta-statistic, for the years following the 2004 earthquake, show that there was increased seismic activity during 2005 on the ends of the 2007 rupture patch. We are starting to analyze geodetic data for the years 2005-2007 in order to assess whether accelerated aseismic slip contributed significantly to the timing and location of the 2007 earthquake.

7.5 Acknowledgments

This work is supported by the National Science Foundation grant EAR 0738299.

7.6 References

Banerjee, P. B., F. F. Pollitz, B. Nagarajan, and R. Bürgmann, Coseismic slip distributions of the 26 December 2004 Sumatra-Andaman and 28 March 2005 Nias earthquakes from GPS static offsets, *Bull. Seism. Soc. Am.*, *97*, S86-S102, 2006.

Hough, S. E., Remotely triggered earthquakes following moderate mainshocks (or, why California is not falling into the ocean), *Seism. Res. Lett.*, *76*, 58-66, 2005.

Konca, A. O., V. Hjorleifsdottir, T. A. Song, J. Avouac, D. V. Helmberger, C. Ji, K. Sieh, R. Briggs, and A. Meltzner, Rupture kinematics of the 2005 M_w 8.6 Nias-Simeulue earthquake from the joint inversion of seismic and geodetic data, *Bull. Seism. Soc. Am.*, *97*, S307-S322, 2007.

Lin, J.and R. S. Stein, Stress triggering in thrust and subduction earthquakes and stress interaction between the southern San Andreas and nearby thrust and strike-slip faults, *J. Geophys. Res.*, *109*, 10.1029/2003JB002607, 2004.

Natawidjaja, D. H., K. Sieh, M. Chlieh, J. Galetzka, B. W. Suwargadi, H. Cheng, R. L. Edwards, J. Avouac, and S. N. Ward, Source parameters of the great Sumatran megathrust earthquakes of 1797 and 1833 inferred from coral microatolls, *J. Geophys. Res.*, *111*, 10.1029/2005JB004025, 2006.

Pollitz, F. F., Postseismic relaxation theory on the spherical earth, *Bull. Seism. Soc. Am.*, *82*, 422-453, 1992.

Pollitz, F. F., Coseismic deformation from earthquake faulting on a layered spherical earth, *Geophys. J. Int.*, *125*, 1-14, 1996.

Pollitz, F. F., P. Banerjee, R. Bürgmann, M. Hashimoto, and N. Chhoosakul, Stress changes along the Sunda trench following the 26 December 2004 Sumatra-Andaman and 28 March 2005 Nias earthquakes, *Geophys. Res. Lett.*, *33*, 10.1029/2005GL024558, 2006.

Rydelek, P. A. and I. S. Sacks, Large Earthquake occurrence affected by small stress changes, *Bull. Seism. Soc. Am.*, *89*, 822-828, 1999.

Zhou, Y. H., L. S. Xu, Y. T. Chen, Source process of the 4 June 2000 Southern Sumatra, Indonesia, Earthquake, *Bull. Seism. Soc. Am.*, *92*, 2027-2035, 2002.

8. GPS exploration of the elastic properties across and within the Northern San Andreas Fault zone and heterogeneous elastic dislocation models

Romain Jolivet (Ecole Normale Superieure de Paris), Roland Bürgmann and Nicolas Houlie

8.1 Introduction

The Northern San Francisco Bay Area (hereafter "North Bay") is sliced by three major right-lateral strike-slip faults: the northern San Andreas Fault (SAF), the Rodgers Creek Fault (RCF) and the Green Valley Fault (GVF). The RCF represents the North Bay continuation of the Hayward Fault Zone, and the GVF is the northern extension of the Concord Fault. North of the juncture with the San Gregorio Fault, geodetic and geologic data suggest a SAF slip rate of 20-25 *mm/yr* (*d'Alessio et al*, 2007, *Lisowski et al.*, 1991). Geodetically determined slip rates range from 20.2 ± 1.4 *mm/yr* (*d'Alessio et al.*, 2007) to 23 ± 3 *mm/yr* (*Freymueller et al.*, 1999). The remainder of the 40 *mm/yr* of Pacific plate to Sierra Nevada Great Valley microplate motion is primarily accomodated by the RCF and the GVF.

Earthquake cycle deformation is commonly modeled assuming lateraly homogeneous elastic properties in the Earth's crust. First-order variations in rock elastic strength both across and within fault zones can, however, strongly impact inferences of fault slip parameters and earthquake rupture characteristics. Near Point Reyes, the SAF separates two different geologic terranes. On the east side of the fault is the Franciscan Complex, made of a mixture of Mesozoic oceanic crustal rocks and sediments, which were accreted onto the North American continent during subduction of the Farallon plate. On the west side of the SAF is the Salinian terrane, which is composed of Cretaceous granitic and metamorphic rocks, overlain by Tertiary sedimentary rocks and Quaternary fluvial terrasses. *Prescott and Yu* (1986) and *Lisowski et al* (1991) describe an asymmetric pattern along a geodetically measured surface velocity profile across to SAF at Point Reyes, which can be explained by higher rigidities to the SW of the fault. *Le Pichon et al.*, 2005, also describes an asymmetric pattern further north along the SAF, at Point Arena, but not at Point Reyes. *Chen & Freymueller*, 2002, rely on near-fault strain rates determined from trilateration and GPS measurements to infer a 2-*km*-wide near-fault compliant zone (with 50% reduced rigidity) near Bodega Bay and Tomales Bay. Here we use densily spaced GPS velocities across the SAF to evaluate changes in elastic properties and within the SAF zone.

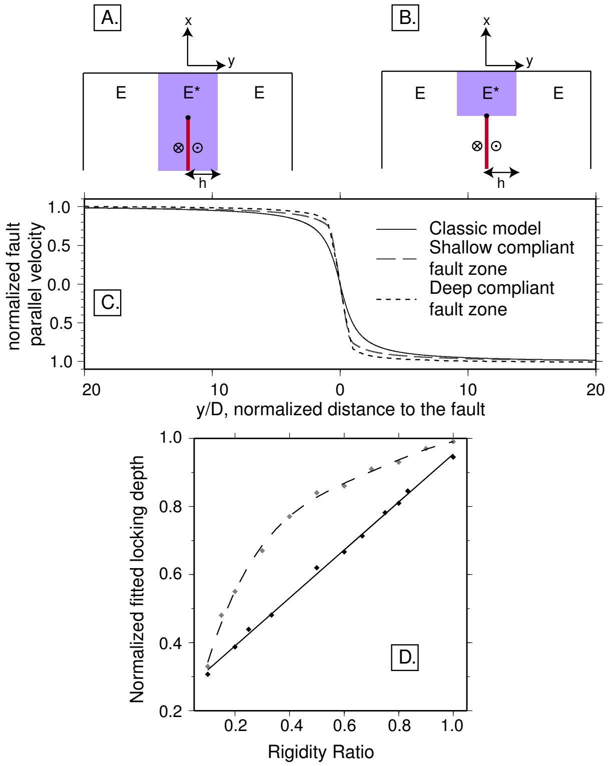

Figure 2.19: Model geometry of A. deep and B. shallow CFZM. The shaded area is the weak fault zone. C. Comparison between a 10 km locking depth classic screw dislocation model (continuous line), a 10 km locking depth Shallow CFZM (long-dashed grey line) and a 10 km locking depth Deep CZFM (dashed black line) with rigidity in the 2-km-wide fault zone being reduced by 80%. D. Locking depth determined by fitting velocity profiles (400 km long with a point spacing of 0.5 km) calculated with the CFZMs with the half-space equation 2.2. The grey dots are the best-fit locking depth for the deep CFZM and the dashed line is the corresponding polynomial fit. The black dots are the fitted locking depth for the shallow CFZM and the continuous line is the corresponding linear fit.

8.2 Heterogeneous Elastic Models

The classic way to interpret a GPS-derived velocity profile across a strike-slip fault is, assuming that the movement is only horizontal, to use the screw dislocation model (*Savage and Burford*, 1973):

$$v(y) = \frac{v_{max}}{\pi} atan(\frac{y}{D}) \tag{2.2}$$

Where v is the predicted fault-parallel velocity of a surface point at distance y from the fault and v_{max} is the far field velocity. v_{max} is also the slip rate on the dislocation below the locking depth D. This model assumes an infinite dislocation burried in a semi-infinite elastic medium. Next we consider laterally heterogeneous models that account for variation of elastic properties across and within the fault zone.

We first consider the model developed by *Le Pichon et al.*, 2005, where the fault separates two elastic media, with different Young's modulus E_1 and E_2. They consequently use a rigidity ratio, K, in the following equations:

$$\begin{aligned} y < 0 \quad &\Rightarrow \quad V(y) = KV_{max} + (\frac{2KV_{max}}{\pi}) atan(\frac{y}{D}) \quad (2.3) \\ y > 0 \quad &\Rightarrow \quad V(y) = KV_{max} + (\frac{2(1-K)V_{max}}{\pi}) atan(\frac{y}{D}) \end{aligned}$$

Where $V(y)$ is again the velocity at a distance y from the fault, V_{max} is the far field velocity, D the locking depth, and $K = \frac{E_2}{E_1+E_2}$ is the asymmetry ratio.

We also evaluate the deep Compliant Fault Zone Model (CFZM) developed in *Chen & Freymueller*, 2002, following *Rybicki and Kasahara*, 1977. A low rigidity fault zone is introduced between two elastic blocks (Figure 2.19).

This model (A. in Figure 2.19) is based on an infinitely deep weak fault zone. If we consider that the fault zone is weak because of damage caused by repeated earthquakes, this zone should not extend deeper than the locking depth. Therefore, we developed, using Finite Element Modeling (*Chéry et al.*, 2001), a shallow CFZM (B. in Figure 2.19). Both models tend to localize the deformation close to the fault trace, but the shear is more localized in the shallow CFZM.

We tried to fit the computed velocity profiles obtained with both CFZMs with the classic screw dislocation model, to evaluate the trade-off between the rigidity ratio and the obtained best-fit locking depth. For both models, there is an inverse relationship between the rigidity ratio and the fitted locking depth (linear for the deep CZFM and curved for the shallow CZFM). As the difference between the CFZMs and the fitted classic models is smaller than the typical error obtained with geodetic data (typically 1 *mm/yr*), we cannot distinguish between a shallow locking depth and a compliant fault zone, relying only on geodetic data. Thus it is important to have independent constraints on the locking depth, for instance, from the depth extent of microseismicity.

8.3 GPS velocities along the Northern San Andreas Fault

We collected GPS data in Bodega Bay and Tomales Bay, using 1996-2000 GPS measurements from *Chen & Freymueller* (2002) to calculate the velocities. We also used data from the Point Reyes profile, provided by the Bay Area Velocity Unification (BAVU), a compilation of the San Francisco bay area GPS velocities (*d'Alessio et al.*, 2005). The data are processed using the GAMIT/GLOBK GPS analysis software. The site velocities are shown with respect to BARD continuous GPS station LUTZ in Figure 2.20.

A first analysis with a simple screw dislocation model, based on three parallel faults (SAF, RCF and GVF) provides a 23 ± 1 *mm/yr* slip rate on the SAF, with a 14 ± 2 *km* locking depth, while the whole system is accomodating 40 *mm/yr* of fault parallel displacement (we find a 8 ± 1 *mm/yr* slip rate on the RCF and 9 ± 1 *mm/yr* on the GVF)(Figure 2.20). *d'Alessio et al.* (2007) show that the velocity of the Farallon islands with respect to the Pacific plate is about 2.9 *mm/yr*, consistent with our modeled velocity field. But the half-space model velocity for the Farallon Island station is 4 to 5 *mm/yr* faster than the actual measured velocity. We next consider asymmetric models with a rigidity contrast across the SAF, fitting the data with equation 2.3. We find that the modeled velocity profile better matches the Farallon Islands velocity with a 0.41 K ratio. Thus, we infer that the Salinian terrane has a rigidity 1.4 times higher than the Franciscan complex to the east of the SAF. Our results suggest an 18 *mm/yr* slip rate on the SAF, with a 10 *km* locking depth. There is a significant trade-off between the inferred slip rate on the SAF and the rigidity contrast across the fault, with smaller rigidity contrasts leading to higher inferred slip rates.

The two networks across the SAF located further north, one in Tomales Bay and one in Bodega Bay, allow us to consider if the SAF represents a low-rigidity fault zone. Our preferred model for the Tomales Bay profile is a classic dislocation, with a 21 *mm/yr* slip rate on the SAF, with a 12 *km* locking depth. We did not explore the corresponding trade-off, but, as our data set doesn't extend far away on both side of the fault, even using the PS-SAR data from *Funning et al.*, 2007, the determined parameters are not well constrained. In Bodega Bay, our preferred model is based on a deep CFZM, with a 28 *mm/yr* slip rate on the SAF, with a 15 *km* locking depth. The compliant zone is 40% weaker than the surrounding medium. But a classic homogeneous model with a 24 *mm/yr* slip rate and a 7 *km* locking depth on the SAF satisfies the near-field data as well, as shown by the first-order trade-off between locking depth and the compliant fault zone rigidity contrast we found in the previous section. We prefer a 15 *km* locking depth and, consequently, introducing this deep CFZM because of the microseismicity near the Point Reyes profile, assuming that there is no significant change in the locking depth.

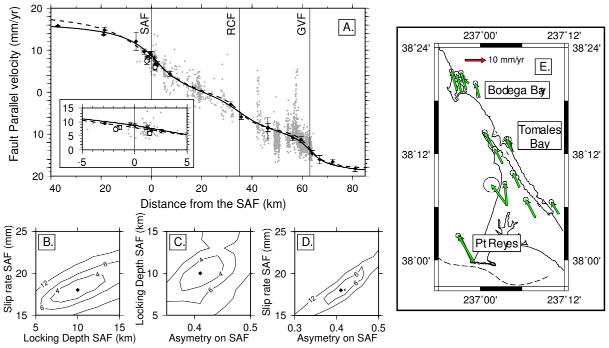

Figure 2.20: A. Best fit dislocation models for the Point Reyes profile. The black dots are the fault-parallel projected GPS velocities with their associated error bars. The grey dots are the PS-SAR data from (*Funning et al.*, 2007). The dashed line is the best classic (elastic half-space) dislocation model. The continuous line is our preferred asymmetric model with a K ratio of 0.41 that better matches the observed velocity of the westernmost GPS site on the Farallon Islands. B. Trade off between the Locking Depth and the Slip Rate on the SAF. Contoured values are the sum of the weighted squared residuals divided by the number of data points C. Trade off between the Asymmetry Ratio and the Locking Depth on the SAF. D. Trade off between the Asymmetry Ratio and the Slip Rate on the SAF.

8.4 Acknowledgements

This project was funded by the USGS National Earthquake Hazard Reduction Programm (NEHRP). We would like to thank J. Freymueller for his help during the GPS survey. Thanks to R. Bürgmann for having me in his team during 6 months and to all the Berkeley Active Tectonics Group.

8.5 References

d'Alessio, M. A., Johanson, I. A., Bürgmann, R., Schmidt, D. A. and Murray, M. H., Slicing up the San Francisco Bay Area: Block kinematics and fault slip rates from GPS-derived surface velocities, *J. Geophys. Res.*, *110*, B0640, 2007.

Chen, Q. and Freymueller, J. T., Geodetic evidence for a near-fault compliant zone along the San Andreas Fault in the San Francisco Bay Area, *J. Geophys. Res.*, *92*, 2002.

Chéry, J., Zoback, M. and Hassani, R., Rheology, strain and stress of the San Andreas Dault in Central and Northern California: A 3-d thermomechanical modeling study, *J. Geophys. Res.*, *106*, , B08406, 2001.

Freymueller, J. T., Murray, M. H., Segall, P. and Castillo, D., Kinematics of the Pacific-North America plate boundary zone, Northern California, *J. Geophys. Res.*, *104*, 7419-7442, 1999.

Funning, G. J., Bürgmann, R., Ferretti, A. and Fumagalli, A. Creep on the Rodgers Creek Fault, northern San Francisco Bay Area, from 10 year ps-insar dataset. *submitted*, 2007.

Le Pichon, X., Kreemer, C. and Chamot-Rooke, N., Asymmetry in elastic properties and the evolution of large continental strike-slip faults, *J. Geophys. Res.*, *110*, B03405, 2005.

Lisowski, M., Savage, J. C. and Prescott, W. H., The Velocity Field Along the San Andreas Fault in Central and Southern California, *J. Geophys. Res.*, *96*, 8369-8389, 1991.

Prescott, W. H. and Yu, S. B., Geodetic measurement of horizontal deformation in the northern San Francisco Bay region, California, *J. Geophys. Res.*, *91*, 7475-7484, 1986

Savage, J. and Burford, R., Geodetic determination of relative plate motion in Central California, *J. Geophys. Res.*, 1973

9. A look in the eyes of hurricanes by Global Positioning System

Nicolas Houlié and Gaetano Festa

9.1 Introduction

The landfall of Hurricanes Frances, Charley, Jeanne, and, more recently, Katrina caused billions of dollars in damage to structures and property, the loss of thousands of lives, and displaced millions of people during the summers 2004 and 2005.

In order to mitigate the risk associated with hurricanes and tropical storms, several studies attempted to predict their occurrence, estimate their number and understand their behavior from birth to death (*De Pondeca and Zou*, 2001; *Powers and Davis*, 2002; *Wang and Wu*, 2004; *Larcombe and Carter*, 2004; *McConochie et al.*, 2004; *Xu et al.,* 2005; *Tolman and Alves,* 2005; *Lu and Garrido,* 2005; *Emanuel*, 2005). Accuracy in the prediction strongly depends on observations such as the temperature and pressure vertical profiles that constrain the modelling of thermodynamic processes involved inside the convection cell. Due to high-speed wind in the outer part of the turbine, however, actual operational tools are limited to measurements at the Earth surface, above and inside the eye of the hurricane. There is thus a need for an instrument capable of scanning the entire hurricane. In order to scan the outer part of the hurricane, which is the most humid and windy, several instruments are limited because they need light (i.e. LASER system) or because the wind velocity is too high (balloons). GPS is strongly attached to the ground and can work in extreme conditions, night and day. The particular sensitivity of the GPS to water vapour in the atmosphere allows us to constrain the temperature profile in the wet part of a hurricane. Indeed, the radio waves emitted by each GPS satellite are delayed by the water vapor contained in the troposphere and can therefore be used as a powerful scanner of the lower atmosphere (*Baby et al.*, 1988; *Bevis et al.*, 1992; *Rocken et al.*, 1993; *Brunner et al.,* 1993; *Bevis et al.*, 1994; *Rocken et al.*, 1995; *Bevis et al.,* 1996; *Rocken et al.,* 1997; *Coster et al.,* 1998; *Ruffini et al.,* 1999; *Pany et al.,* 2001). These studies encourage the use of GPS in order to determine the atmosphere state by using both GPS and ground based measurements. However, GPS has not yet been used to investigate hurricanes.

The paths of Hurricanes Charley, Frances, Jeanne, and Katrina have crossed the GPS network in the Southeast United States (Figure 2.21), allowing us to explore perturbations in pressure, temperature and relative humidity due to the passage of hurricanes in the troposphere.

In this paper, we specifically quantify the change of the vertical temperature profile in the wet part of Katrina during its passage over the Lousiana coast.

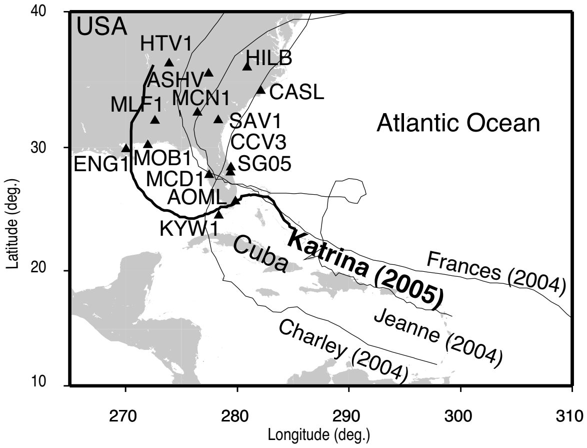

Figure 2.21: The GPS network used in this study. The sites belong to the GPS-MET and IGS networks. Superimposed on the picture, we also plot the paths of the hurricanes that hit the Southeast United States during the summers of 2004 and 2005. The trajectories are derived from MODIS Observation.

9.2 Results

Since we fix the ground temperature at $25\,^oC$, the increase in the wet tropospheric delay can be interpreted as an average increase of the temperature along the whole air column above the station. We quantified the vertical gradient increase to be $1\,^oC/km$. An analogous increase of the temperature vertical gradient has been observed in the central part of the hurricane by dropsonds and Microwave Imager Sounder, with a maximum difference comparable with results presented here.

9.3 Discussion

GPS networks, dedicated to tectonic and geodynamic problems in the US-Caribbean area, could be densified by adding instrumentation on boats or/and islands and could become a forecast tool to study the hurricanes, remotely, in 3D, by night and by day.

Our results suggest that we could evaluate the radial variations of the vertical temperature profile in the wet part of the hurricanes using GPS, improving the real-time state of the hurricanes and allowing for short-term prediction of the trajectory of hurricanes. These profiles would be directly related to the distance between the GPS receivers, the position of which is known, and the eye of the hurricanes, the location of the latter being accurately computed by remote sensing imagery (e. g.

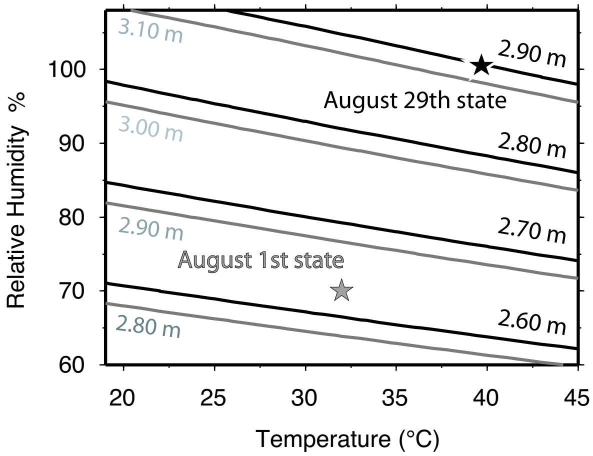

Figure 2.22: Abacus presenting the increase of the tropospheric delay as a function of the temperature T and the relative humidity H. Gray lines represent the tropospheric delay contours for the pressure value of 1.013 *bar*, as measured on August 1, while black lines are drawn for the pressure value of 916 *mbar*, as measured on August 29.

MODIS, SPOT). Non-linearity in the hurricane trajectories is owed to sharp changes in the temperature at the sea surface and to the presence of sparse islands. Indeed, the use of GPS measurements could also help describe the air column's state above the starting areas of hurricane, better constraining the prediction of its future path.

The integration of 2D or 3D effects that may not be secondary for the evaluation of the tropospheric delays will be the next step of GPS applications to hurricanes.

References

H. Baby, P. Golé, and A. Lavergnat, J. Model for tropospheric excess path length of radio waves from surface meteorological measurements. *Radio Science*, 22:1023–1038, 1988.

M. Bevis, S. Businger, T. A. Herring, C. Rocken, R. A. Anthes, and R. H. Ware. GPS Meteorology: Remote Sensing of Atmospheric Water Vapor Using the Global Positioning System. *J. Geophys. Res.*, 97(16):15787–15801, October 1992. doi: 10.1029/92JD01517.

M. Bevis, S. Businger, S. Chiswell, T.A. Herring, R.A. Anthes, C. Rocken, and R.H. Ware. Gps meteorology: Mapping zenith wet delays onto precipitable water. *Journal of Applied Meteorology*, 33(3):379–386, 1994. doi: 10.1175/1520-0450(1994)033⟨0379:GMMZWD⟩2.0.CO;2.

M. Bevis, S. Chiswell, S. Businger, T. T. Herring, and Y. Bock. Estimating Wet Delays Using Numerical Weather Analyses and Predictions. *Radio Sci.*, 31(3):477–487, 1996.

A.J. Coster, A.E. Niell, F.S. Solheim, V.B. Mendes, P.C. Toor, R.B. Langley, and C.A. Upham. The Westford Water Vapor Experiment: Accuracy issues involving the use of GPS to measure total precipitable water vapor. In *Preprints of the 10th Symposium on Meteorological Observations and Instrumentation*, pages J70–J75. 78th Annual Meeting of the American Meteorological Society, 1998.

M. S. F. V. De Pondeca and X. Zou. A case study of the variational assimilation of gps zenith delay observations into a mesoscale model. *Am. Meteo. Soc.*, 40:1559–1576, 2001.

K.A. Emanuel. Increasing destructiveness of tropical cyclones over the 30 years. *Nature*, 436, 2005.

R. Hanssen. Atmospheric heterogeneities in ERS tandem SAR interferometry, Chapter 2. *DEOS Report*, 98.1:8–24, 1998.

P. Larcombe and R.M. Carter. Cyclone pumping, sediment partitioning and the development of the great barrier reef shelf system: a review. *Quaternary Science Reviews*, 23: 107–135, 2004.

Y. Lu and J. Garrido. Doubly periodic non-homogeneous Poisson models for hurricane data. *Statistical Methodology*, 2:17–35, 2005.

J.D. Mc Conochie, T.A. Hardy, and L.B. Mason. Modelling tropical cyclone over-water wind and pressure fields. *Ocean Engineering*, (31):1757–1782, 2004.

T. Pany, P. Pesec, and G. Stangl. Atmospheric GPS slant path delays and ray tracing through numerical weather models, a comparison. *Physics and Chemistry of the Earth A*, 26:183–188, January 2001.

J. Powers and C.A Davis. A cloud-resolving regional simulation of tropical cyclone formation. *Atmospheric Science Letters*, 3(1):15–24, 2002.

C. Rocken, T. Van Hove, J. Johnson, F. Solheim, R. Ware, M. Bevis, S. Chiswell, and S. Businger. GPS/STORMGPS sensing of atmospheric water vapor for meteorology. *Jour. of Atmos. and Ocean. Tech., 1995*, 12 (3):468–478, 1995.

C. Rocken, T. Van Hove, and R. Ware. Near real-time GPS sensing of atmospheric water vapor. *Geophys. Res. Lett.*, 24:3221–3224, December 1997. doi: 10.1029/97GL03312.

Rocken, C. and Ware, R. and Van Hove, T. and Solheim, F. and Alber, C. and Johnson, J. . Sensing atmospheric water vapor with the global positioning system. *Geophys. Res. Lett.*, 20:2631–2634, 1993.

G. Ruffini, L.P. Kruse, A. Rius, B. Burki, L. Cucurull, and A. Flores. Estimation of Tropospheric Zenith Delay and Gradients over the Madrid Area Using GPS and WVR Data. *Geophys. Res. Lett.*, 26:447–450, 1999.

H.L. Tolman and J-.H. G.M. Alves. Numerical modeling of wind waves generated by tropical cyclones using moving grids. *Ocean Modelling*, 9:305–323, 2005.

Y. Wang and C.C. Wu. Current understanding of tropical cyclone structure and intensity changes a review. *Meteorol. Atmos. Phys.*, 87:257–278, 2004. doi: 10.1007/s00703-003-0055-6.

X. Xu, L. Xie, X. Zhang, and W. Yao. A mathematical model for forecasting tropical cyclone tracks, Nonlinear Analysis. *Real World Applications*, In Press, Corrected Proof, Available online 20 April, 2005.

.

10. Observations of Infragravity Waves at the Endeavour Ocean Bottom Broadband Seismic Station (KEBB)

David Dolenc (U of Minnesota), Barbara Romanowicz, Paul McGill (MBARI), and William Wilcock (U of Washington)

10.1 Introduction

Infragravity (IG) waves are long-period (20-500 s) ocean surface gravity waves. The pressure fluctuations that they create at the ocean bottom result in seafloor deformation, which is the main source of the long-period noise observed at the ocean-bottom seismic stations. Understanding the properties of the IG waves as well as their coupling to the solid earth is important for the study of the earth's hum and structure using non-seismic sources. Also, modeling of their spatial variability could help with the selection of the most quiet locations for future ocean-bottom seismic deployments.

In our previous work, we found that IG waves are generated in the nearshore region from the shorter-period ocean waves and are observed at the ocean-bottom station KEBB only after they propagate from the shelf into the deeper water and pass over the station. In our recent work (*Dolenc et al.*, 2008), we further studied the IG waves at KEBB to identify the nearshore region where the IG waves are generated.

Station KEBB was installed 247 km offshore Vancouver Island at a water depth of 2376 m in August 2003. It comprised a 3-component broadband seismometer Guralp CMG-1T, a recording, and a battery package. The seismometer was completely buried in the ocean floor sediments and the station was recording the data continuously.

10.2 Results

The analysis of the horizontal velocity ground motions at KEBB throughout the deployment shows that motions are strongly polarized in NW-SE direction (Figure 2.23). Assuming that the IG waves propagated to KEBB as freely propagating waves, we can approximate them as plane waves. In this case we expect the horizontal motions at KEBB to be primarily in the direction of the IG wave propagation. This suggests that the IG waves arrived from the SE direction.

To identify the origin of the IG waves independently of the above observation, we took advantage of their tidal modulation. Tidal modulation of the IG waves has previously been observed at the ocean-bottom seismic stations and can be explained by a mechanism proposed by *Thomson et al.* (2006), in which it results from changes in the beach profile from convex at low-tide to concave at high-tide. To identify the origin of the IG waves we used two parameters. First, the tidal phase changes along the shore. Second, the distance from the nearshore region to KEBB changes as we move along the shore. Since the freely traveling surface waves are dispersed, the difference between the arrivals of the longer- and shorter-period IG waves at KEBB is a function of distance that IG waves have to travel. We first calculated the predicted traveltime for the IG waves from every buoy to KEBB (Figure 2.24b, solid lines). We then measured the phase delay between the tidal modulation observed at KEBB and tidal phase at individual buoys within different period bins. The comparison with the modeled traveltimes suggests that the IG waves observed at KEBB originated from the nearshore region close to buoy 46041.

10.3 Conclusions

The strong polarization of the horizontal motions at KEBB as well as the analysis of the phase of the tidal modulation observed at KEBB both suggest that IG waves originate from the nearshore region in southern Washington and not from the nearshore regions further to the north that are closer to KEBB. This suggests that long sandy beaches in southern Washington, and not the rocky and rugged coast to the north, play an important role in the IG wave generation.

10.4 Acknowledgements

This work was partially supported by NSF (grant OCE-0648302) as well as BSL funds. The KEBB was deployed as part of the 3-year multidisciplinary prototype NEPTUNE experiment supported by a grant from the W. M. Keck Foundation to the University of Washington. The seismic component of the project was a collaboration between the University of Washington, the University of Oregon, and the Monterey Bay Aquarium Research Institute.

10.5 References

Dolenc, D., B. Romanowicz, P. McGill, and W. Wilcock, Observations of infragravity waves at the ocean-bottom broadband seismic stations Endeavour (KEBB) and Explorer (KXBB), *Geochem., Geophys., Geosys., 9*, Q05007, doi:10.1029/2008GC001942, 2008.

Thomson, J., S. Elgar, B. Raubenheimer, T. H. C. Herbers, and R. T. Guza, Tidal modulation of infragravity waves via nonlinear energy losses in the surfzone, *Geophys. Res. Lett., 33*, L05601, doi:10.1029/2005GL025514, 2006.

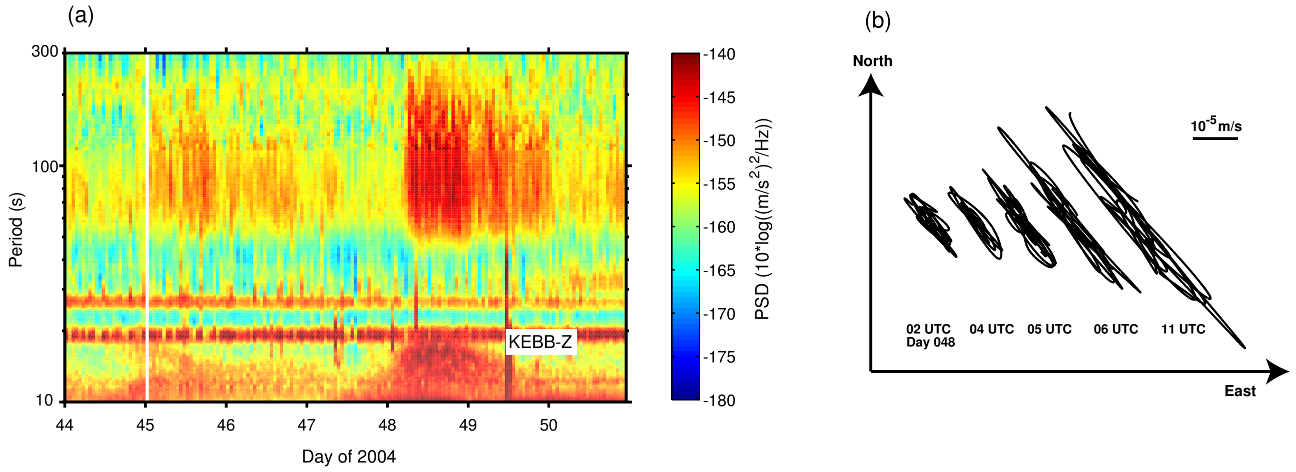

Figure 2.23: (a) Power spectral density for the vertical KEBB component as a function of time and period. A sudden change of the IG peak width and amplitude is observed on day 2004.048 after the storm approaching from the WSW direction reached the coast. (b) Horizontal velocity ground motion at KEBB just before and after the observed change of the IG peak on day 2004.048. The data shown in (b) were filtered in the period band from 40 to 200 s.

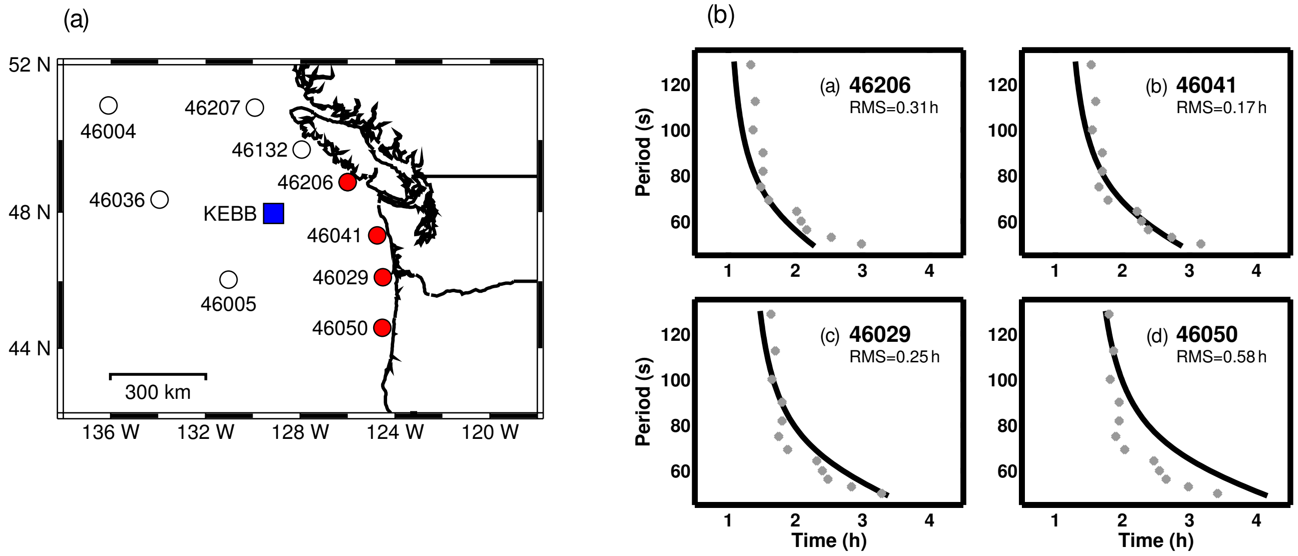

Figure 2.24: (a) Map showing the location of the ocean-bottom station KEBB and ocean buoys. (b) The predicted traveltime for the IG waves from each buoy to KEBB (solid lines) is compared to the measured phase delay between the tidal modulation observed at KEBB and tidal phase at each buoy for different period bins.

11. Western USA mantle structure and its implications for mantle convection processes

Mei Xue and Richard M. Allen

11.1 Introduction

The western USA is on the margin of the North American plate and has complicated and active tectonics. The Juan de Fuca plate, the Pacific plate, and the North American plate meet in this region and form the Mendocino Triple Junction just offshore Northern California. In addition to these primary tectonic objects, many other complicated geologic features are also observed (Figure 2.25). Their corresponding velocity structures have not been well resolved so far and many are still under debate, e.g., the depths the Juan De Fuca plate reaches and the Yellowstone plume originates (*e.g., Humphreys, et al.*, 2000; *Jordan, et al.*,2004; *Yuan and Dueker*, 2005; *Waite, et al.*, 2006; *Geist and Richards*, 1993).

Here we incorporate the Transportable Array data with all other available networks, resulting in an unprecedented dense distribution of stations in the western USA. This allows us not only to fill the gaps in the resolution of previous studies, but also to see deeper into the mantle, revealing new features. We refer to our seismic velocity models as DNA07-P for P-wave and DNA07-S for S-wave, where DNA07 represents the Dynamic North America model of 2007. Due to the limited space, we only show DNA07-S here, which reveals an extremely heterogeneous mantle structure and provides important clues to mantle convection processes in this tectonically active region.

11.2 Data and Method

The total number of stations we used is 809, and most are from the Transportable Array, with an average station spacing of 70 km (Figure 2.26). The 26 permanent networks are composed of the following: (1) 2 Global Seismograph Networks: (IRIS/IDA and IRIS/USGS); (2) 5 Federal Digital Seismic Networks: the Canadian National Seismograph Network (CNSN), GEOSCOPE (GEO), International Miscellaneous Stations (IMS), Leo Brady Network (LB), and the United States National Seismic Network (USNSN); (3) 14 regional networks: the ANZA Regional Network (ANZA), Berkeley Digital Seismograph Network (BDSN), Cascade Chain Volcano Monitoring (CC), Caltech Regional Seismic Network (CRSN), Montana Regional Seismic Network (MRSN), Northern California Seismic Network (NCSN), Western Great Basin/Eastern Sierra Nevada (WGB/ESN), Princeton Earth Physics Project-Indiana (PEPP), US Bureau of Reclamation Seismic Networks (USBR), Southern California Seismic Network TERRAscope (TERRA), University of Oregon Regional Network (UO), University of Utah Regional Network (UURN), Pacific Northwest Regional Seismic Network (PNSN), and the Yellowstone Wyoming Seismic Network (YWSN); (4) 3 temporary networks: the North Bay Seismic Experiment (NBSE), DELTA LEVY Northern California (DLNC), and the

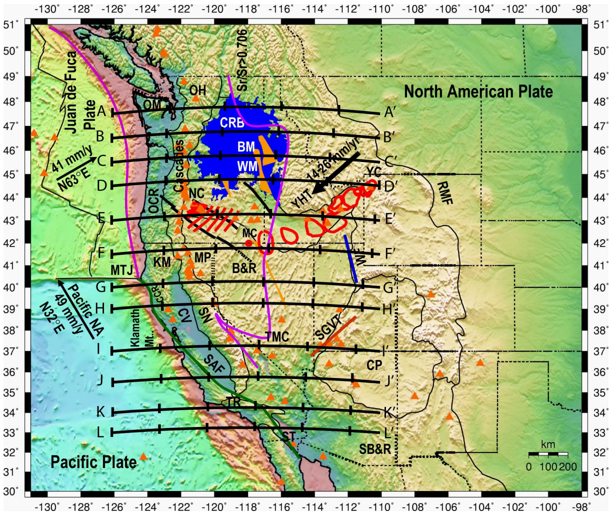

Figure 2.25: Tectonic map for the study region. Labeled features (*Humphreys and Dueker*, 1994b) are OH, Okanogan Highlands; OM, Olympic Mountains; OCR, Oregon Coast Ranges; CCR, California Coast Ranges; KM, Klamath Mountains; MP, Modoc Plateau; MTJ, Mendocino Triple Junction; CV, Central Valley; SN, Sierra Nevada; SAF, San Andreas Fault; TR, Transverse Ranges; ST, Salton Trough; CRB, Columbia River Basalts; BM, Blue Mountains; WM, Wallowa Mountains; NC, Newberry Caldera; MC, McDermitt Caldera; YC, Yellowstone Caldera; YHT, Yellowstone hotspot track along the eastern Snake River Plain; B&R, Basin and Range; SB&R, southern Basin and Range; TMC, Timber Mountain Caldera; SGVT, Saint George Volcanic Trend; CP, Colorado Plateau; WF, Wasatch Front; RMF, Rocky Mountain Caldera. Black lines trending northwest across Oregon indicate right-lateral strike-slip faults. Dike swarms associated with the 17 Ma basaltic outpourings are shown in gold (*Christiansen, et al.*, 2002). Plate motions from HS3-NUVEL 1A are shown as black arrows (*Gripp and Gordon*, 2002). Horizontal black lines indicate the locations of the vertical slices shown in Figure 2.28

Wallowa TA 2006-2008 (WTA); and (5) 2 other networks: the Laser Interferometer Gravitational-Wave Experiment (LIGO) and the Network of Autonomously Recording Seismographs (NARS).

We use a technique of teleseismic body wave travel-time tomography and follow the procedure of (*Allen, et al.*, 2002). To correct for source effects and crustal structures, event and station corrections are included in the inversion as a set of free parameters. Rather than leave the station corrections unconstrained, we use corrections calculated from the crustal model of CRUST2.0 as a reference (*Bassin, et al.*, 2000). Station elevations are also corrected. The initial RMS residual is 1.83 sec and is reduced to 0.49 sec after inversion, corresponding to a variance reduction of 73%.

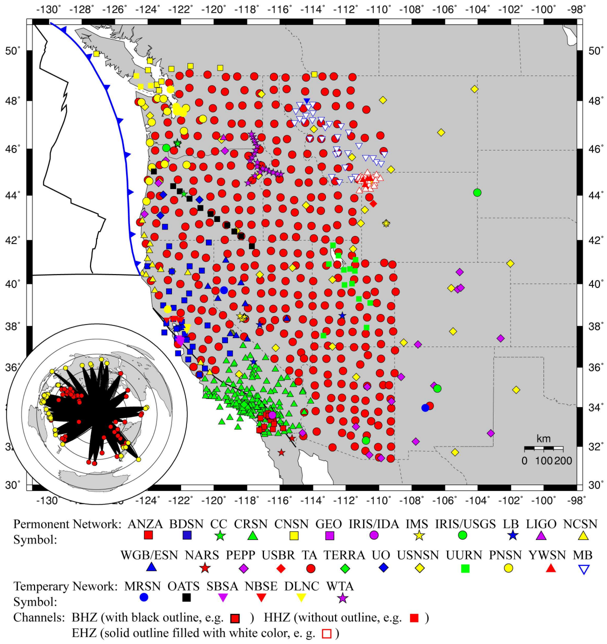

Figure 2.26: The seismic stations used in this study, with a total number of 809. The inset shows the distribution of 88 events and 23233 rays used in the DNA07-S model inversion. The red and yellow dots indicate events providing good direct S phases and SKS phases, respectively.

11.3 Tomographic results and interpretation

Perhaps one of the most striking observations is just how heterogeneous mantle structure is beneath the western USA. Despite this heterogeneity, there is a very strong correspondence with the complicated tectonics of the region. The main features of the velocity models and their implications, shown in Figure 2.27 and Figure 2.28, are listed as follows:

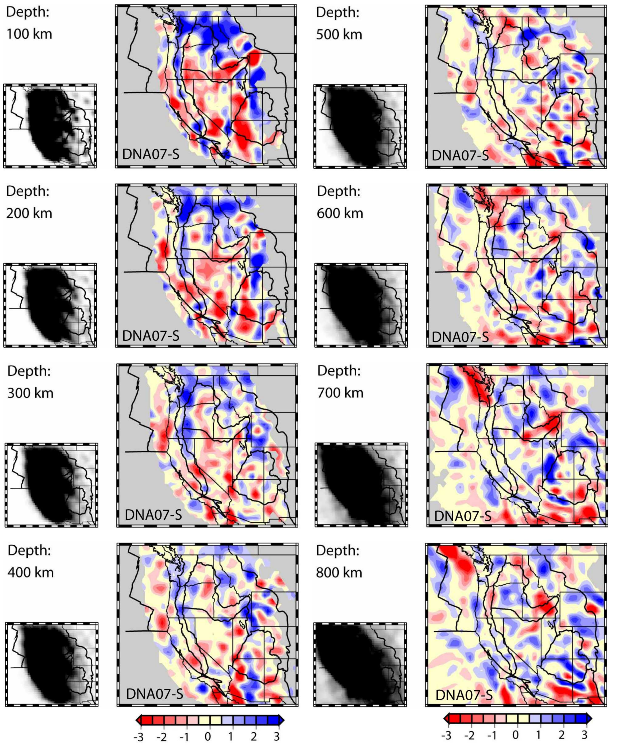

Figure 2.27: Depth slices through the DNA07-S model from 100 km to 800 km depth with an interval of 100 km. Areas with ray hits smaller than 10 are shaded gray. On the right side of each velocity slice is the corresponding ray density plot, where white indicates zero hits and black indicates 100+ hits

North of the Mendocino Triple Junction: (1) The Juan de Fuca subduction system stops at ∼ 400 km, and is disrupted in Oregon, which we interpret as being due to interaction with the Yellowstone plume head. (2) West of the Cascades the forearc is imaged as a low velocity zone beneath the Coastal Ranges with the strongest velocity anomaly beneath the Olympic Mountains and Northern California. (3) East of the Cascades and above the Juan de Fuca slab, a north-south trending low velocity zone is imaged from southern Washington to northern Nevada. (4) A high velocity region is imaged from central Washington, through northern Oregon, and into Idaho. Beneath Washington the anomalies reach 250 to 300 km depth and deeper, extending to ∼ 400 km, beneath the Wallowa Mountains of northeast Oregon. These are likely due to a combination of a cold and thick lithosphere and melt extraction during the eruption of the Columbia River Basalts. (5) The low velocity anomaly beneath Yellowstone dips towards the northwest and stops at 500 km depth. (6) A shallow low velocity zone to ∼ 200 km depth lies beneath the Eastern Snake River Plain and does not appear connected to a deeper low velocity zone at the top of the lower mantle. (7) We do not detect a

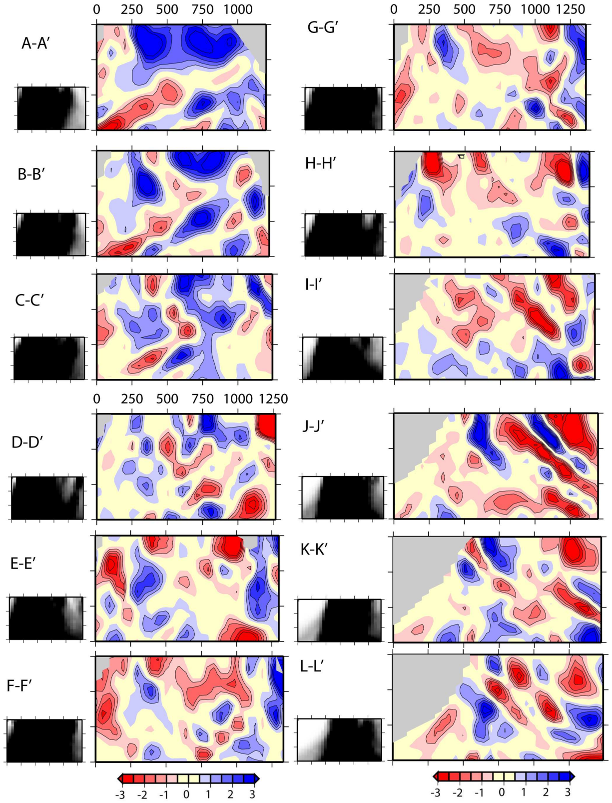

Figure 2.28: Vertical slices through the DNA07-S models. The locations of the cross-sections are shown in Figure 2.25. The color scale is the same as in Figure 2.27

low velocity conduit reaching greater than 500 km depth beneath Yellowstone implying that either (a) any plume was short-lived; or (b) the conduit is < 50 km in diameter and/or the velocity perturbation is less than 1.5% for S and 0.75% for P and therefore unresolved; or (c) there was no deep mantle plume. We prefer the short-lived plume model as it best explains many of the imaged features the Pacific Northwest. (8) There are only shallow low velocity anomalies (<150 km depth) along the Newberry hotspot track indicate no deep source.

South of the Mendocino Triple Junction: (1) In California, the high velocities of the Pacific plate are imaged abutting against the low velocity North American plate. (2) We image the "slab gap" as low velocity anomalies extending to 400 km depth from the southern end of the Juan de Fuca subduction system to the southern end of the Sierra Nevada. These anomalies are particularly strong just south of the Mendocino Triple Junction. (3) High velocity bodies are imaged beneath the southern tip of the Central Valley/Sierra Nevada and the Transverse Ranges with dips to the east. These may be part of a fossil Farallon subduction system. (4) The Basin and Range is a region of low velocities to a depth of $\sim$ 300 km. In the middle of the Basin and Range, in central Nevada, a high velocity feature is imaged extending to 300 km depth. (5) A zone of low velocity is observed to 200 km depth under the Salton Trough consistent with ongoing rifting and small scale convection in the region.

While the upper $\sim$ 400 km of the DNA07 models correlate well with surface tectonics and geologic provinces, the deeper structure (400-750km) is equally complex and not easily explained in terms of either existing geologic or geodynamic models. Further investigation is therefore warranted.

11.4 Acknowledgements

We thank Ana Luz Acevedo-Cabrera for preprocessing some of the data and thank Greg Waite for providing crust correction codes. We thank Doug Dreger, Barbara Romanowicz, and Ved Lekic for beneficial discussions/suggestions. The IRIS DMC provided seismic data. This work was supported by the NSF (EAR-0539987). The figures were produced with SAC and GMT (*Wessel and Smith*, 1995).

11.5 References

Bassin, C., Laske, G. and Masters, G., The Current Limits of Resolution for Surface Wave Tomography in North America, *EOS Trans AGU, 81,* F897, 2000.

Christiansen, R. L., et al., Upper-mantle origin of the Yellowstone hotspot, *Geological Society of America Bulletin, 114,* 1245-1256, 2002.

Geist, D. and M. Richards, Origin of the Columbia Plateau and Snake River Plain - Deflection of the Yellowstone Plume, *Geology, 21,* 789-792, 1993.

Gripp, A. E. and R. G. Gordon, Young tracks of hotspots and current plate velocities, *Geophysical Journal International, 150,* 321-361, 2002.

Hales, T. C., et al., A lithospheric instability origin for Columbia River flood basalts and Wallowa Mountains uplift in northeast Oregon, *Nature, 438,* 842-845, 2005.

Humphreys, E. D. and K. G. Dueker, Western United-States Upper-Mantle Structure, *Journal of Geophysical Research-Solid Earth, 99,* 9615-9634, 1994b.

Humphreys, E. D., et al., Bemeath Yellowstone: Evaluating Plume and Noneplume Models Using Teleseismic Images of the Upper Mantle, *GSA Today, 10,* 1-7, 2000.

Jordan, B. T., et al., Geochronology of age-progressive volcanism of the Oregon High Lava Plains: Implications for the plume interpretation of Yellowstone, *Journal of Geophysical Research, 109,* doi:1029/2003JB002776, 2004.

Waite, G. P., et al., V-pp and Vs structure of the Yellowstone hot spot from teleseismic tomography: Evidence for an upper mantle plume, *Journal of Geophysical Research-Solid Earth, 111,*, 2006.

Yuan, H. Y. and K. Dueker, Teleseismic P-wave tomogram of the Yellowstone plume, *Geophysical Research Letters, 32,* 2005.

12. A simple method for improving crustal corrections in waveform tomography

Vedran Lekic and Barbara Romanowicz

12.1 Introduction

Recordings of surface waves and overtones provide excellent constraints on the structure of the Earth's crust, upper mantle, and transition zone. This is because they provide good global coverage, and are sensitive to elastic and anelastic structure in both the crust and the mantle. Yet, in order to determine the seismic velocities and anisotropy in the mantle, we must separate the effects of the crust from those due to the sought-after mantle structure. Despite recent improvements in the global mapping of crustal structure (e.g. CRUST2.0: *Bassin et al.*, 2000), the difficulties associated with accurately modeling the effects of the crust seismic on waves mean that these improvements do not automatically translate into better corrections for crustal effects.

Crustal corrections in long period waveform modeling were first applied in a linear fashion, by calculating the effects of perturbations in Mohorovicic depth and surface topography on the (eigen)frequencies of Earth's free oscillations (*Woodhouse and Dziewonski*, 1984). However, variations in crustal thickness are often large enough to produce non-linear effects on the eigenfrequencies. In order to account for this non-linearity, Montagner and Jobert (1988) proposed a two-step approach in which the eigenfunctions and eigenfrequencies are calculated exactly for a set of tectonic settings (thereby capturing the non-linear effects), while perturbations away from these canonical 1D profiles are handled using linear corrections. This approach has recently been implemented in full-waveform analyses (*Marone and Romanowicz*, 2007). However, when applied to higher modes and to high frequencies, these non-linear crustal corrections can be computationally very expensive.

Here, we present an alternative method for performing crustal corrections. Like the aforedescribed methods, we calculate exactly the eigenfunctions and eigenfrequencies for a set of tectonic settings, but instead of using these directly, we solve for scaling coefficients, which, when applied to standard linear crustal corrections, mimic the non-linear effect. The main advantage of this approach is that, once the correction factors have been calculated, it requires no additional computational costs aside from those associated with linear corrections. This allows it to be more easily applied to overtones and to higher frequencies than the standard quasi-non-linear approach.

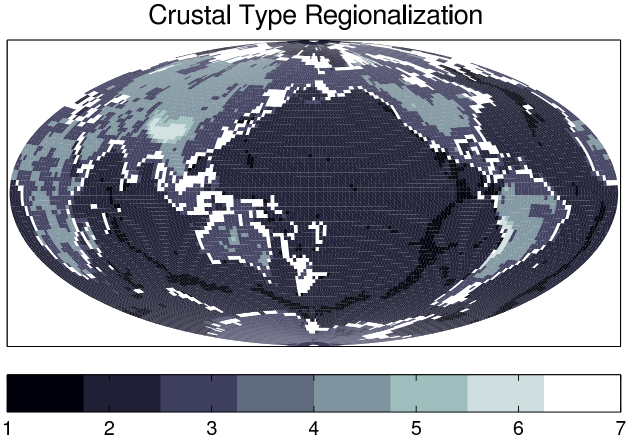

Figure 2.29: Map showing geographical distribution of the 7 crustal types used in this study.

12.2 Modified linear crustal corrections

The effects of lateral heterogeneity, such as variations in crustal velocities and thicknesses, can be approximated by considering how this heterogeneity shifts the frequencies of Earth's free oscillations, compared to their frequencies in a spherically symmetric reference model such as PREM (*Dziewonski and Anderson*, 1981). For the case relevant to this study, in which only the radii of discontinuities in the Earth are perturbed by δr_d, for an isolated mode branch, local frequency shifts can be calculated in a linear fashion through the use of sensitivity kernels H_k, the expressions for which can be found in Woodhouse and Dahlen (1978). Note that these kernels are calculated for the spherically symmetric reference model:

$$\delta\omega_k^2 = \sum_d r_d^2 \delta r_d H_k^d. \tag{2.4}$$

In order to quantify the inadequacy of linear crustal corrections, we divide the Earth's surface into 7 regions with similar crustal thicknesses and ocean depths. We base this regionalization on Mohorovicic depth from CRUST2.0, with the first 6 regions characterized by Moho depth range of 10-25km, 25-40km, 40-50km, 50-60km, and >60km. The 7th region is introduced to capture the strong effect of a shallow (< 2km) ocean layer that characterizes the continental shelves. Figure 2.29 shows the geographical extent of the 7 regions. For each region, we calculate an average radial profile of density (ρ) and shear (V_S) and compressional (V_P) wave velocity. Armed with a set of radial models that define 7 canonical crustal types, we proceed to calculate the frequencies ω_k of the fundamental modes for each model. These frequencies are then compared with those of PREM, and frequency shifts between PREM and each of the 7 regional models are calculated as

$$\delta\omega_k^{NL} = \omega_k^{(i)} - \omega_k^{PREM}, \tag{2.5}$$

where the superscript i is an index representing the frequency of mode k in the canonical crustal model i. Since these frequency shifts capture some of the non-linear effects of crustal structure, we identify them with a superscript NL. Figure 2.30 shows the $\delta\omega_k^{NL}$ plotted (solid lines) for spheroidal and toroidal fundamental modes.

We can use the kernels H_k^d that we obtained for the reference spherically symmetric model, in this case PREM, to predict the linearized effects of the canonical crustal structures on the normal mode frequencies. To do this, we only consider the differences in the radii of the discontinuities between each canonical crustal model and PREM, neglecting the differences in crustal velocities and density. This is an often used approximation of the true linear crustal effect, and is appropriate because crustal velocities have been shown to have minimal effect on long period waves (e.g. *Stutzman and Montagner*, 1994). Henceforth, which shall refer to the frequency shifts calculated in this standard, linear fashion as ω_k^{SL}. The dotted lines in Figure 2.30 show the $\delta\omega_k^{SL}$ for each of the canonical crustal structures.

A comparison of the approximate terms $\delta\omega_k^{SL}$ with the $\delta\omega_k^{NL}$ calculated before (and displayed as solid lines) confirms that linear crustal corrections are inadequate, even at long periods. Therefore, we are interested in ways of correcting the $\delta\omega_k^{SL}$ so that they better track $\delta\omega_k^{NL}$. In order to accomplish this task, we are confronted with a crucial choice.

We must decide which term or terms in equation 2.4 to correct. Since H_k^d needs to be calculated for each mode, correcting this term can be computationally expensive. This is what is done in the aforedescribed non-linear corrections. Correcting δr_d, on the other hand, does not increase computational costs. The gradual change with frequency of the differences between $\delta\omega_k^{NL}$ and $\delta\omega_k^{SL}$ change gives us hope that modifying δr_d might significantly improve the accuracy of $\delta\omega_k^{SL}$.

We start the procedure by rewriting equation 2.4 in matrix notation, where we only consider N fundamental modes and identify perturbations relating to the Mohorovicic with a subscript m and those pertaining to the surface with t:

$$\begin{pmatrix} \delta\omega_1^{SL} \\ \delta\omega_2^{SL} \\ \vdots \\ \delta\omega_N^{SL} \end{pmatrix} = \begin{pmatrix} r_m H_1^m & r_t H_1^t \\ r_m H_2^m & r_t H_2^t \\ \vdots & \vdots \\ r_m H_N^m & r_t H_N^t \end{pmatrix} \begin{pmatrix} \delta r_m \\ \delta r_t \end{pmatrix} \tag{2.6}$$

We attempt to improve standard linear corrections by introducing factors $c_{m,t}$, calculated for each canonical crustal type and mode type, that are added to $\delta r_{m,t}$ before being multiplied by the kernel matrix (relabeled $\mathbf{H}$). Written in vector notation, we seek $\mathbf{c}$ that minimises:

$$\mathbf{w} - \mathbf{H}(\delta\mathbf{r_{m,t}} + \mathbf{c_{m,t}}), \tag{2.7}$$

where the vector $\mathbf{w}$ contains the non-linear frequency shifts $\delta\omega_k^{NL}$. The least-squares solution to this minimisation problem is given by:

$$\mathbf{c_{m,t}} = (\mathbf{H}'\mathbf{H})^{-1}\mathbf{H}'(\mathbf{w} - \mathbf{H}\delta\mathbf{r_{m,t}}), \tag{2.8}$$

where the apostrophe indicates the transpose.

We could have introduced a multiplicative correction term, instead of the additive one described above. However, solving for such a term becomes unstable when the δr_d's are small. Given that discontinuity topography is likely to vary both above and below its depth in the reference model, the accompanying zero-crossings of δr_d might have adverse effects.

Because the non-linearity of crustal effects depends strongly on both crustal and mode type, we perform the minimisation in equation 2.8 for spheroidal and toroidal modes separately for each crustal type. Once the set of factors $\mathbf{c_{m,t}}$ appropriate for a given mode type are obtained, we modify the surface and Mohorovicic topography of CRUST2.0 at each point on the surface by the correction factor appropriate for the relevant crustal type (obtained from Figure 2.29). Therefore, the crustal type and correction factor information is fused into a single file that specifies a modified discontinuity topography for each mode type.

The dashed lines in Figure 2.30 show the frequency shifts predicted by our modified discontinuity radii. Henceforth, we label them $\delta\omega_k^{CL}$. The improvement in fit to $\delta\omega_k^{NL}$ is significant, and good for a large frequency range. When only long period waves ($T > 60s$) are considered, excellent agreement between $\delta\omega_k^{CL}$ and $\delta\omega_k^{NL}$ can be achieved by only correcting the Mohorovicic topography.

12.3 Conclusions

We propose and validate a new method for improving linear crustal corrections. By considering a set of 7 crustal types, we quantify the inadequacy of standard linear corrections at accounting for the effects of the crust on the fundamental mode surface waves. Then, we improve the accuracy of linear corrections by introducing additive factors to the discontinuity topographies. Incorporating an additive correction factor to the discontinuity topography as opposed to the kernels, results in no additional computation costs, compared to standard linear corrections. The correction factors depend on the local crustal type, on the discontinuity considered, and on the reference model used for calculating the sensitivity kernels, as well as mode type.

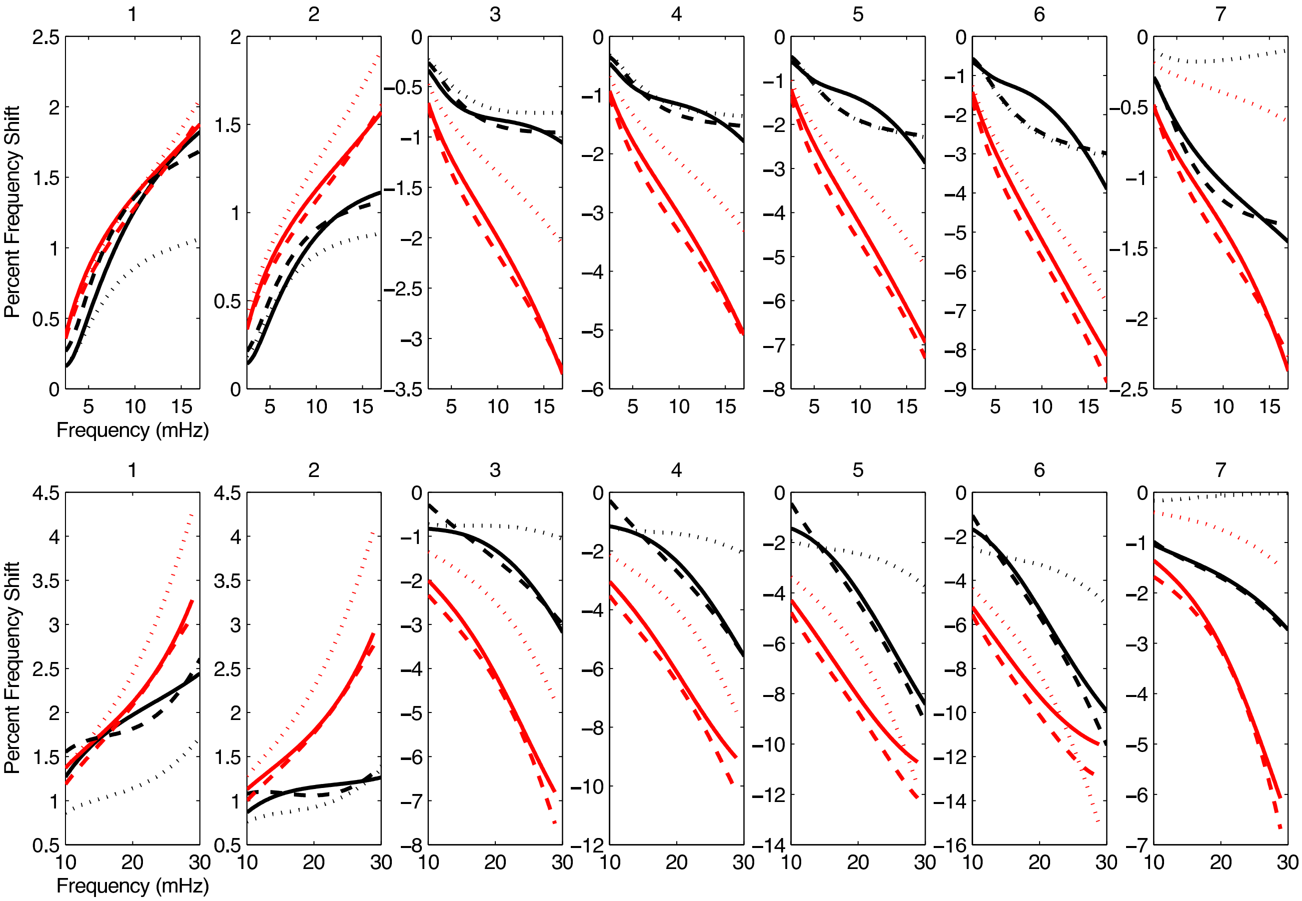

Figure 2.30: Frequency shifts of the fundamental toroidal (grey) and spheroidal (black) modes with respect to PREM anisotropic due to differences in crustal structure between each of the canonical crustal types shown in Figure 2.29. Solid lines denote non-linear corrections ($\delta\omega_k^{NL}$), dotted lines indicate linear corrections($\delta\omega_k^{SL}$), and the dashed lines indicate linear corrections improved using the method outlined in this paper. Only Mohorovicic corrections are applied in the upper row, while corrections for both surface and Mohorovicic topography are required by the broader frequency range of the bottom row.

12.4 Acknowledgements

This research was supported by National Science Foundation grant NSF/EAR-0308750 and an National Science Foundation Graduate Fellowship held by VL.

12.5 References

Bassin, C., Laske, G. and G. Masters, The Current Limits of Resolution for Surface Wave Tomography in North America. *EOS Trans AGU 81,* F897, 2000.

Dziewonski, A.M. and D.L. Anderson, Preliminary reference Earth model. *Phys. Earth and Planetary Int., 25,* 297-356, 1981.

Marone, F. and B. Romanowicz, Non-linear crustal corrections in high-resolution regional waveform seismic tomography. *Geophys. J. Int., 101* 22245-22272, 2007.

Montagner, J.-P. and N. Jobert, Vectorial tomography, II, Application to the Indian Ocean. *Geophys. J. R. Astron. Soc. 94,* 309-344, 1988.

Stutzmann, E. and J.P. Montagner, Tomography of the transition zone from the inversion of higher-mode surface waves. *Phys. Earth and Planetary Int., 86*, 99-115, 1994.

Woodhouse, J.H. and F.A., The effect of a general aspherical perturbation on the free oscillations of the earth, *Geophys. J. Int., 53*, 335-354, 1978.

Woodhouse, J.H. and A.M. Dziewonski, Mapping the upper mantle: three dimensional modeling of Earth structure by inversion of seismic waveforms. *J. Geophys. Res. 89,* 5953-5986, 1984.

13. Effects of water on seismic attenuation

Fabio Cammarano and Barbara Romanowicz

13.1 Introduction

A trace amount of water may be present in the upper mantle and would strongly affect the rheological properties of mantle rocks. Theoretically, this can be explained by the role of hydrogen in enhancing the kinetics of defect motion (for more details, see *Karato*, 2006 and *Kohlstedt*, 2008), thus significantly weakening olivine and olivine-rich rocks. A similar behaviour has been predicted for viscoelastic relaxation at seismic frequencies. Geochemical estimates on mid-ocean ridge basalts (MORB) indicate about ~0.1 *wt*% water. Assuming that MORB is the product of ~10-20% melting of peridotite (*Hirth and Kohlstedt*, 1996), the primitive mantle rock should thus have ~0.01 *wt*% H_2O, which is distributed between the individual mineralogical phases according to the partitioning coefficient of each mineral (*Hirth and Kohlstedt*, 1996). In complex tectonic areas and mantle wedges, the amount of water should increase potentially. For the first time, recent laboratory experiments (*Aizawa et al.*, 2008) allow the estimation of the effects of water on seismic attenuation. These data, together with previous data on dry olivine (*Faul and Jackson*, 2005), provide values for seismic attenuation to be expected in the upper mantle and can be used to build radial profiles of seismic attenuation based on temperature, grain size and water content, which are able to fit seismic observations (*Cammarano and Romanowicz*, 2008).

13.2 Methods and results

In general, it is reasonable to assume that $Q^{-1} \propto W^{\alpha r}$, where Q^{-1} is attenuation (i.e. $1/Q_S$), W is the water content, α is the frequency dependence, and r is a constant which depends on the process. The value of this constant has been estimated to be between ~1 for dislocation mechanisms and ~2 in case of grain boundary mechanisms (*Karato*, 2006). To model effects of water, we consider a positive contribution added to the dry attenuation. We define the total attenuation as:

$$Q^{-1} = Q^{-1}_{dry}(P,T,d,\omega) + Q^{-1}_{wet}(P,T,W) \tag{2.9}$$

where Q^{-1}_{dry} is here assumed to be the *Faul and Jackson* value and Q^{-1}_{wet} is the water contribution. The reason for using such an expression is to preserve the knowledge of the T and grain-size dependence of the *Faul and Jackson* (2005) model for dry olivine and to include an empirical correction for water based on recent experimental results at high temperature (*Aizawa et al.*, 2008). In spite of large uncertainties, we know that this correction is always positive (higher attenuation) (see Figure 2.31). The effects on pressure due to the addition of water must also be considered. Therefore,

$$Q^{-1}_{wet}(P,T,W) = A(T,P)W^{\alpha r} \tag{2.10}$$

where α is assumed to be the one from *Faul and Jackson* (i.e. 0.27). The estimated temperature dependence of Q^{-1}_{wet} at low pressure (0.2 GPa) is based on the recent experiments by Aizawa et al (2008). We compared the T-dependent attenuation for two natural dunite samples which are characterized by different amounts of water (Figure 2.31a). The "wet" sample probably retains the entire inventory of water (~2 *wt*%) during the high-T experiments, including 0.0187 wt% of molecular water. The "dry" sample, conversely, has lost most of the water and behaves similarly to anhydrous material (Figure 2.31). The effect of water on enhancing viscoelastic relaxation processes has been clearly observed for the first time with these experiments. However, a precise formalism describing the water dependence of solid-state viscoelastic relaxation is hampered because of the structural (and compositional) complexity of the natural samples; the marginal, but not negligible, role of partial melt; and, last but not least, the role of the fluid phase (*Aizawa et al.*, 2008). Further studies on simpler material will better characterize the effects of water. At the moment, we can use the available indications to give a rough estimate of the possible effects of water on absolute Q^{-1}. The difference in observed attenuation between the "dry" and "wet" (saturated) samples increases exponentially with temperature, consistent with an enhanced activated process.

Pressure effects can be modeled by multiplying $A(T, P_0)$ with the exponential factor $\exp(PV^*_W/RT)$, where V^*_W is the contribution to activation volume due to water content. Note that P dependence of the dry case is already included in attenuation predicted with *Faul and Jackson's* model (2005). In the absence of direct constraints on V^*_W, we rely again on information from rheology. If $V^*_W = 1.06 \times 10^{-5} m^3 mol^{-1}$, attenuation for a constant 0.01 *wt*% water is much larger than for the dry case, both at low and high pressure (Figure 2.31b). With this constant amount of water and the described P-T dependent model, we do not find any attenuation profile that is able to satisfactorily fit the data for any reasonable T and GS profile. For example, assuming isothermal structures for given grain sizes, we found that the best-fit model always has a value > 0.13 for surface wave observations. This is due to the very high values of attenuation around 100 km. When using a much larger activation volume ($V^* = 2.4 \times 10^{-5} m^3 mol^{-1}$), we find that interpretation in terms of average T does not change much (*Cammarano and Romanowicz*, 2008). However, only models with $GS <= 1\ mm$ and $< T >= 1500\ K$ are able to obtain a similar fit to the dry case. In this case, Q^{-1} values at 100 km (3 GPa) are sensibly lower than before and values at higher P are very similar to the dry case (see Figure 2.31b). We point out that our "water-contribution" to Q^{-1} is independent of grain size, but it does become larger as temperature increases. For example, at a GS of 1 cm and assuming isothermal structure, a $< T >= 1600\ K$ is required for both the dry and the 0.01 $wt\%$ wet case. However, values of Q^{-1} for the wet case are significantly higher, especially at shallow depths, and the misfit is not as low as in the dry case. On the other hand, for a given 1 mm GS, seismic observations are best explained with a 1500 K isotherm. In this case, the dry and wet profiles are more similar, as the effect of water on absolute attenuation is less important at lower temperatures.

Finally, we note that when modeling water effects, we should consider the feedback with all the other parameters and not only P and T. We decided to neglect the effect of water on frequency dependence. The Aizawa experiments seem to support such an assumption, not showing any systematic variation of α with water content. In particular, the "wet" sample has a very similar frequency dependence (~0.26) to the *Faul and Jackson* (2005) value. We also assume that there is no feedback between the grain-size dependence and water dependence. In conclusion, water enhances attenuation and trade-offs with temperature. Based on the available constraints, it is likely, however, that water will have a secondary effect on global attenuation measurements. Indeed, Q_S values due solely to a dry mechanism are already low enough compared to what is required seismically in the upper mantle.

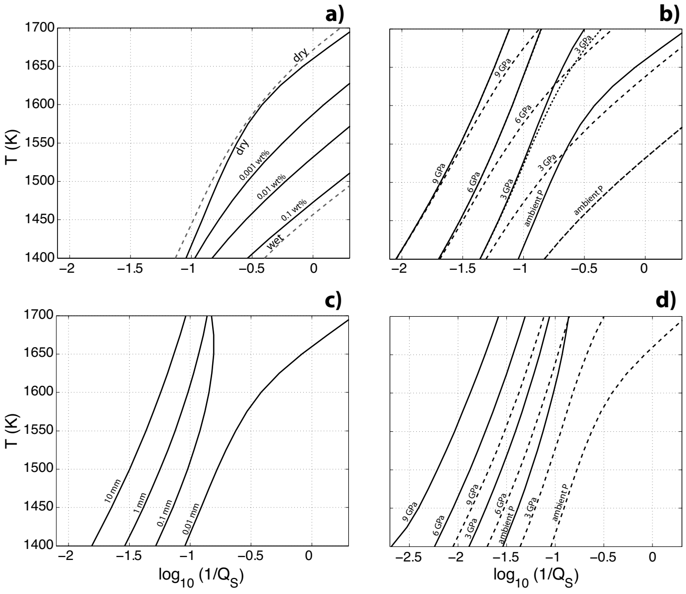

Figure 2.31: Modeled effects of water on P-T dependent attenuation. a) T-dependent attenuation as function of water content at ambient P, period = 150 s and for a GS of 0.01 mm (solid lines). The "wet" and "dry" samples (dashed lines) are, respectively, the attenuation values for two natural dunite samples (1093 and 1066 of Aizawa et al., 2008). The original laboratory data have been interpreted with Burgers model (same formalism as *Faul and Jackson*, 2005), but in this case, without the (unconstrained) grain size dependence. Both samples have an average grain size around 0.02 mm. b) Modeled T-dependent attenuation at different pressures for the dry case (solid) and with 0.01 wt% water, period = 150 s and grain size of 0.01 mm. Dashed lines are for $V^*_W = 1.06 \times 10^5 m^3 mol{-}1$. Dotted lines are with $V^*_W = 2.4 \times 10^5 m^3 mol{-}1$. For comparison, c) and d) show, respectively, variations of Q^{-1} with grain size and effects of pressures for two given grain sizes (solid lines for 1mm and dashed for 0.01mm) computed with the *Faul and Jackson* model at a period of 150 s.

13.3 References

Aizawa Y., A. Barnhoorn, U. Faul, J.F. Gerald and I. Jackson, The influence of water on seismic wave attenuation in dunite: an exploratory study, *J. Petrol.*, 49, 841-855, 2008.

Cammarano F. and B. Romanowicz, Radial profiles of seismic attenuation in the upper mantle based on physical models. *GJI*, in press, 2008.

Faul, U.H., and I. Jackson, The seismological signature of temperature and grain size variations in the upper mantle, *Earth Planet. Sci. Lett.*, 234, 119-134, 2005.

Hirth, G. and D. Kohlstedt, Water in the oceanic upper mantle: implications for rheology, melt extraction and evolution of the lithosphere, *Earth Planet. Sci. Lett.*, 144, 93-108, 1996.

Karato, S., Influence of hydrogen-related defects on the electrical conductivity and plastic deformation of mantle minerals: A critical review, in Earth's Deep Water Cycle, pp. 113-130, AGU, Washington DC, 2006.

Kohlstedt, D., Constitutive equations, rheological behavior, and viscosity of rocks, *Treatise on Geophysics*, Elsevier, 2008.

14. Analysis of Long-Period Noise at the Farallon Islands Broadband Seismic Station FARB

David Dolenc (U of Minnesota), Robert Uhrhammer, and Barbara Romanowicz

14.1 Introduction

We present a preliminary analysis of the long-period noise observed at the broadband seismic station FARB (Streckeisen STS-2) located on the South Farallon Island, 43 km off the coast of San Francisco, CA. Results from our previous work (*Dolenc et al.*, 2005) showed that long-period noise (20-500 s) observed at the ocean-bottom broadband station MOBB, located offshore Monterey Bay, CA, is mainly due to seafloor deformation under the pressure forcing by infragravity waves (IG; long-period ocean surface gravity waves). A similar type of long-period noise is observed on vertical and both horizontal components of the Farallon Islands station FARB, but not on the nearby mainland stations.

14.2 Results

The long-period noise at FARB is best observed on stormy days when it extends all the way to 1000 s and is even stronger than at MOBB (Figure 2.32). The long-period noise at FARB is stronger on the E-W than on the N-S component, suggesting that it results from the IG waves that propagate from the nearshore region into the deeper ocean.

The comparison of the power spectral density (PSD) at FARB and spectral wave density (SWD) at the nearby buoys for the 2004-2008 period showed that IG waves are generated in the nearshore region close to FARB from the shorter period ocean waves (*Dolenc et al.*, 2008). The energy in the IG wave band at FARB is, as previously observed at MOBB, modulated in phase with tides. The phase of the modulation observed at FARB agrees with the phase of the local tides, suggesting that IG waves observed at FARB are generated locally (*Dolenc et al.*, 2008).

An example of long-period signal observed at FARB and MOBB following the arrival of a dispersed swell on days 2006.037-039 is shown in Figure 2.33. The swell arrived from the NW direction and it can be observed in the 10-30 s period band at FARB and MOBB, as well as the two nearby ocean buoys. The swell signal at the buoys can be seen only when the swell periods fall below ~25 s, suggesting that buoys can only record ocean waves with shorter periods. The PSD of the swell signal at MOBB ends once the periods fall below ~20 s. Since MOBB is in 1000 m water depth, the 20 s is the short-period cutoff due to hydrodynamic filtering.

The observations at FARB in the 30-500 s period band show that IG waves are generated following the arrival of the swell. Since the incoming swell is dispersed and has a very narrow period band, it generates IG waves that also appear dispersed. A more detailed analysis reveals that IG waves are generated only once the period of the ocean swell falls below 23 s. The comparison of the incoming swell dispersion and the frequency of the resulting IG waves observed at FARB further shows that nonlinear interaction between a pair of swell components with frequencies f1 and f2 results in an infragravity wave with the difference (f2-f1) frequency.

Strong horizontal noise observed at FARB in the IG wave band suggests that passing IG waves tilt the island. The swaying of islands and underwater mounds driven by tilting due to infragravity waves could contribute to the recently observed horizontal hum of the Earth (*Kurrle and Widmer-Schnidrig*, 2008).

14.3 Conclusions

The IG waves are the main source of the long-period noise at FARB. They are generated locally and result from nonlinear interactions between the ocean waves with periods shorter than 23 s. Strong long-period horizontal noise at FARB is probably due to tilting of the island due to passing of IG waves as they propagate away from the shore. The swaying of the islands due to IG waves could contribute to the horizontal hum of the Earth.

14.4 Acknowledgements

The MOBB observatory instrumentation and deployment were supported by funds to the Monterey Bay Aquarium Research Institute from the Lucile and David Packard Foundation, the NSF (grant OCE-9911392), and UC Berkeley funds to the BSL.

14.5 References

Dolenc, D., B. Romanowicz, D. Stakes, P. McGill, and D. Neuhauser, Observations of infragravity waves at the Monterey ocean bottom broadband station (MOBB), *Geochem. Geophys. Geosys., 6*, Q09002, doi:10.1029/2005GC000988, 2005.

Dolenc, D., R. Uhrhammer, and B. Romanowicz, Analysis of long-period noise at the Farallon Islands broadband seismic station FARB, *Seism. Res. Lett., 79*, 293, 2008.

Kurrle, D. and R. Widmer-Schnidrig, The horizontal hum of the Earth: A global background of spheroidal and toroidal modes, *Geophys. Res. Lett., 35*, L06304, 2008.

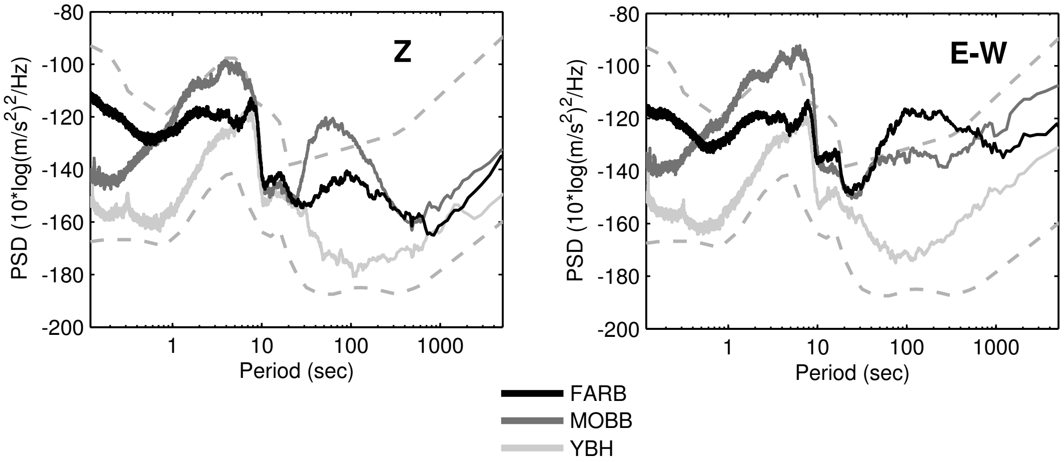

Figure 2.32: Power spectral density (PSD) at FARB, MOBB (Monterey Bay ocean-bottom seismic station), and YBH (560 km north of MOBB, one of the quietest BDSN stations) for the vertical (left) and horizontal (right) component. Results for a stormy day (2005.027) are shown. The USGS high- and low-noise models for land stations are shown as dashed.

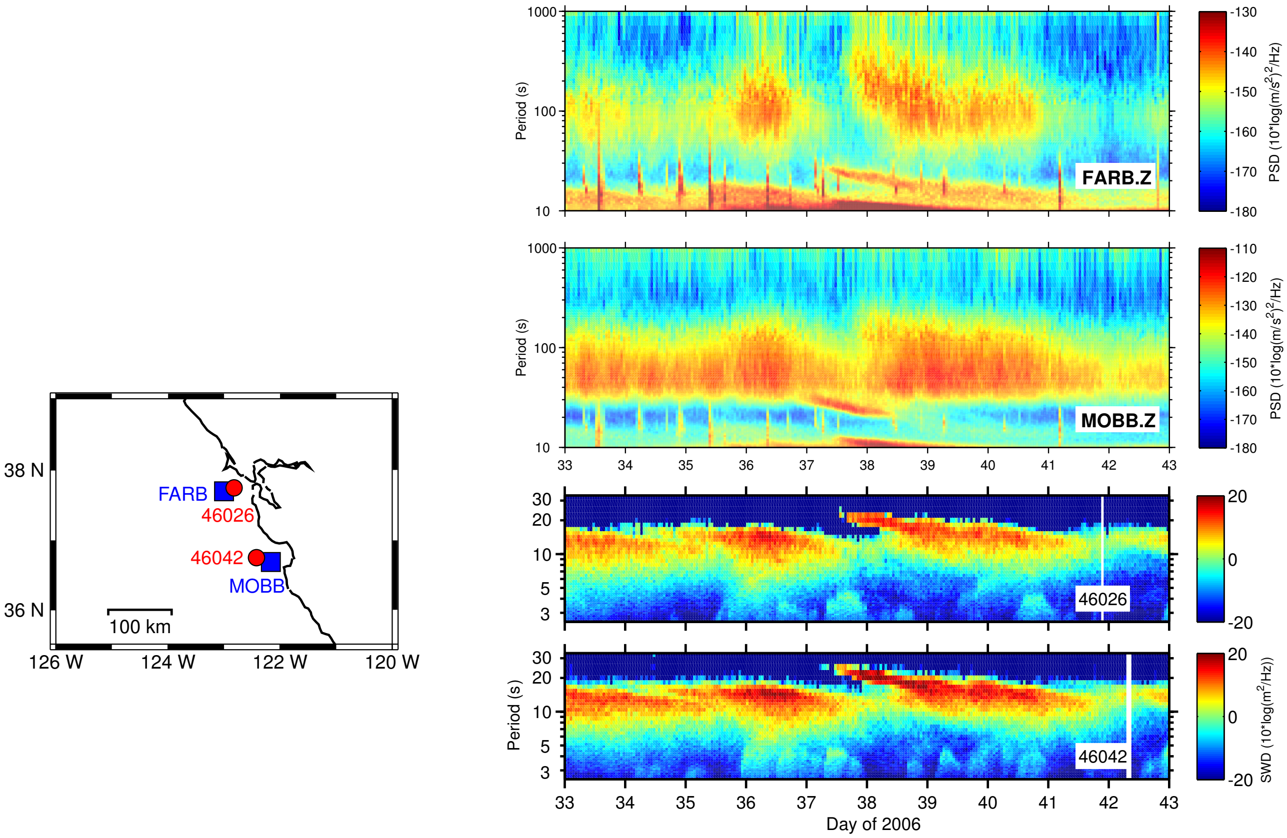

Figure 2.33: PSD for the vertical FARB and MOBB channels as a function of period and time. Bottom panels show spectral wave density (SWD) of the ocean waves calculated at the nearby buoys. The arrival of a dispersed swell on days 037-039 is observed in all 4 panels in the 10-30 s period band. The signal due to infragravity waves generated in the nearshore region following the arrival of a dispersed swell can be seen in the top panel in the 30-500 s period band.

15. Tomography of the Alpine Region from Observations of Seismic Ambient Noise

L. Stehly, B. Fry, M. Campillo, N.M Shapiro, J. Guilbert, L. Boschi and D.Giardini

15.1 Introduction

We use correlations of the ambient seismic noise to study the crust in western Europe (*Shapiro et al*, 2005). Cross correlation of one year of noise recorded at 150 3-component broadband stations yields more than 3000 Rayleigh and Love wave group velocity measurements. These measurements are used to construct Rayleigh and Love group velocity maps of the Alpine region and surrounding area in the 5-80s period band. Finally, we invert the resulting Rayleigh wave group velocity maps to determine the Moho depth.

15.2 Method

We used one year of continuous records from October 2004 to October 2005 from 150 3-component broadband European stations. Our aim is to focus on the Alps, where we have a particularly high density of stations All the records are processed day by day. First the data are decimated to 1 Hz and corrected for the instrumental response. North and East horizontal components are rotated to get radial and transverse components with respect to the inter-station azimuth. The records are then band-pass filtered and their spectrum whitened between 5 and 150 s. We correlated signals recorded on the components that correspond to Rayleigh and Love waves (ZZ, ZR, RZ, RR, and TT). Correlations of one-day records are stacked.

15.3 Group velocities maps

Rayleigh and Love wave dispersion curves are evaluated from the emerging Green's function using frequency-time analysis (*Levshing et al*, 1989, *Ritzwoller and Levshin*, 1998) for the 11,000 inter-station paths. For each path, we get eight evaluations of the Rayleigh-wave dispersion curves by considering four components of the correlation tensor (ZZ, RR, RZ and ZR) and both the positive and the negative part of the NCF. Similarly, we get two estimates of the Love-wave dispersion curves from positive and negative parts of TT correlations.

We reject waveforms 1) with S/N (ratio between Rayleigh wave's amplitude and noise variance after it) lower than seven; 2) with group velocities measured on the positive and negative correlation time differing by more than 5 percents, and 3) with paths shorter than two wavelengths at the selected period for the group velocity map. This results in about 3,500 paths over the initial 11,000 inter-station paths at 16 s. We then apply a tomographic inversion following (*Barmin et al*, 2001) to this data set to obtain group velocity maps on $100 \times 100 = 10{,}000$ cells of 25×25 km across Europe (Fig. 2.34). Several geological features can be seen on those maps. At 16s, low velocity anomalies are associated with sedimentary basins, such as the Po basin (Northern Italy), the North Sea basin and the Pannonian basin (Slovakia and Hungary). Both Rayleigh and Love waves exhibit smaller values below the molassic sediments (Southern Germany and Austria) than in the surrounding area.

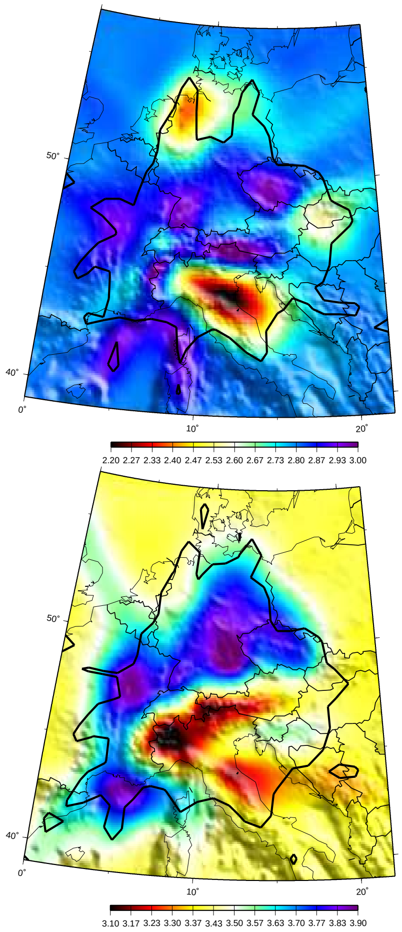

Figure 2.34: Rayeigh group velocity maps at 16s (left) and 35s (right).

15.4 Moho map of the alpine region

At each cell of our model, we extracted Rayleigh wave dispersion curves from our group velocities map, and

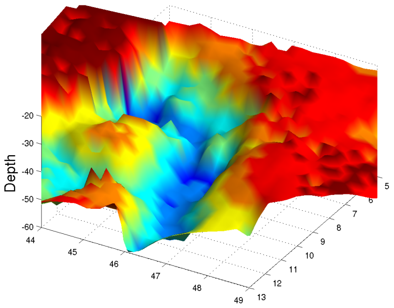

Figure 2.35: 3D view of the Moho depth.

inverted them using a Monte Carlo algorithm in order to determine the depth of the Moho in the Western Alps (Switzerland, Austria, southern Germany). Our results clearly show thickening of the crust below the Alps (Fig2.35). Our map of Moho depth shares striking similarities with the compilation of (*Waldhauser et al*, 1998) in the region where we have a high density of paths. This comparison confirms that seismic noise can be efficiently used to obtain high resolution Love and Rayleigh wave group velocity maps at periods up to 80s and 3D images of the crust and the upper mantle. This method provides spatially continuous seismic velocity distributions on large areas. The resolution of the obtained model depends mostly on the density of stations and is not limited by the uneven distribution of earthquakes. At period less than 10s, the resolution length is not isotropic as the noise is strongly directional.

15.5 References

M. P Barmin, M. H. Ritzwoller, and A. L. Levshin, A fast and reliable method for surface wave tomography, *Pure and Applied Geophysics*, 158:1351–1375, 2001.

A.L Levshin, T. B. Yanocskaya, A. V. Lander, B. G. Bukchin, M. P. Barmin, L. I. Ratnikova, and E. N. Its, *Seismic surface waves in a laterally inhomogeneous Earth*, Kluwer Academic Publishers, 1989.

M. Ritzwoller and A. L. Levshin, Eurasian surface wave tomography: group velocities, *Journal of Geophysical Research*, 103(4839-4878):4839, 1998.

N. M. Shapiro, M. Campillo, L. Stehly, and M. H. Ritzwoller, High-resolution surface wave tomography from ambient seismic noise, *Science*, 307:1615–1618, march 2005.

F. Waldhauser, E. Kissling, J. Ansorge, and St. Mueller, Three-dimensional interface modelling with two-dimensional seismic data: the Alpine crust mantle boundary, *Geophysical Journal International*, 135:264–278, 1998.

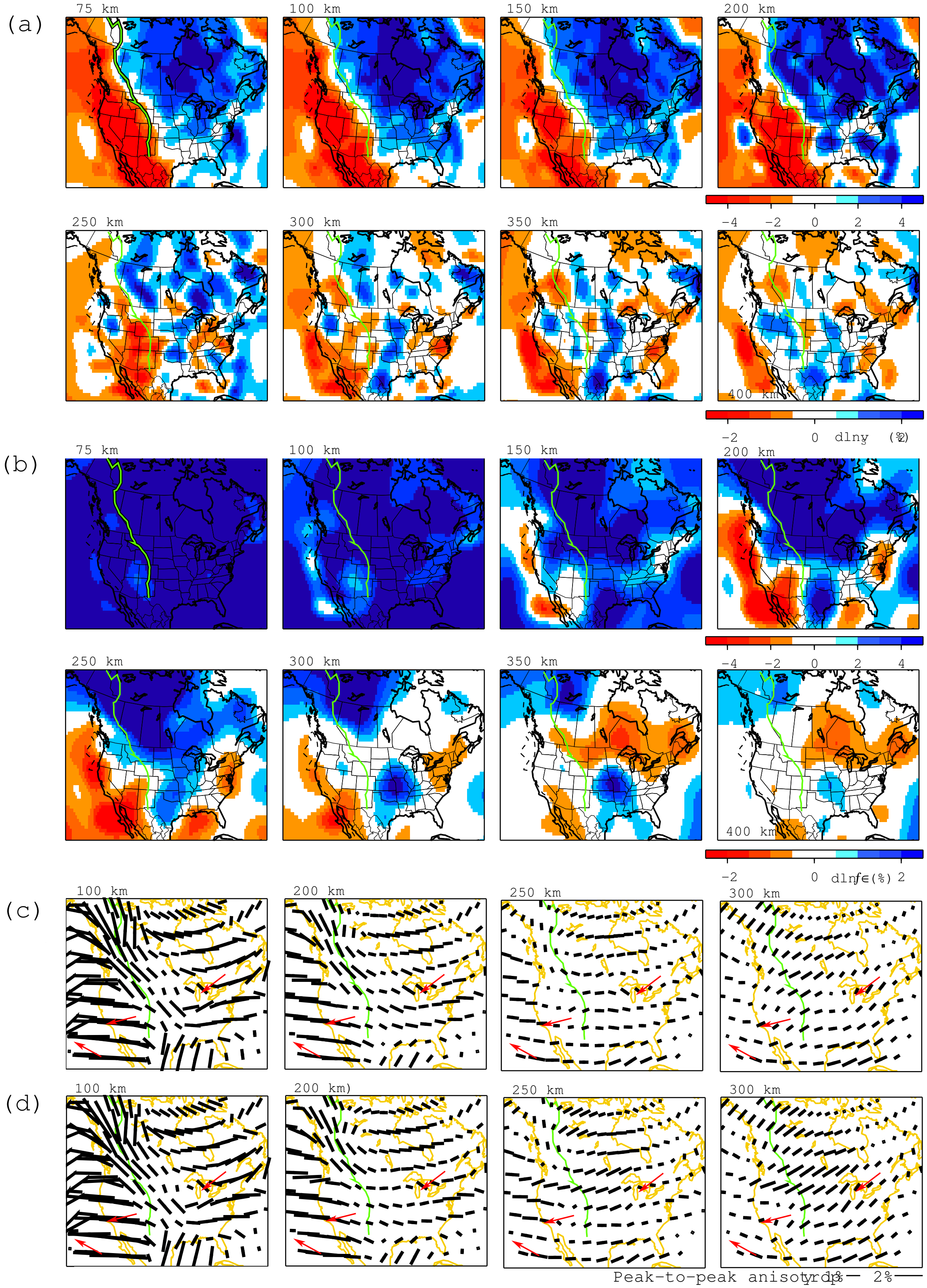

Figure 2.36: Updated isotropic S velocity (a), radial anisotropy (b) and azimuthal anisotropy (c and d) model of the North America upper mantle. Horizontal resolution is 200-km, 400-km, and 400-km for (a), (b) and (c), respectively. (c) and (d) show two azimuthal anisotropy models by surface waveforms only and by surface waveforms and SKS splits, respectively.

16. 3-D Isotropic and Anisotropic S-velocity Structure in North America

Huaiyu Yuan, Federica Marone (Paul Scherrer Institut, Switzerland), Kelly Liu (Univ. of Missouri-Rolla), Steve Gao (Univ. of Missouri-Rolla), and Barbara Romanowicz

16.1 Introduction

The tectonic diversity of the North American continent makes it an ideal region to investigate the structure and dynamics of the continental upper mantle. Investigations of timely geophysical questions, such as the relation to geological age of the variations in the lithospheric thickness, the relation of upper-mantle anisotropy to present day asthenospheric flow and past tectonic events, the nature and strength of the lithosphere/asthenosphere coupling and the driving mechanisms of plate motions, are contingent upon obtaining high-resolution 3-D tomographic models of the isotropic and anisotropic mantle structure of the continent.

In the framework of non-linear asymptotic coupling theory (NACT; *Li and Romanowicz*, 1995), we had developed a regional 3-D tomographic model of the upper mantle beneath North America that includes both isotropic S velocity structure as well as radial and azimuthal anisotropy (*Marone et al.*, 2007; *Marone and Romanowicz*, 2007). This model was constructed from a joint inversion of fundamental and higher mode surface waveforms together with constraints on azimuthal anisotropy derived from SKS splitting measurements. The model showed evidence for the presence of two layers of anisotropy beneath the stable part of the North American continent: a deeper layer with the fast axis direction aligned with the absolute plate motion, and a shallower lithospheric layer with north pointing fast axis likely showing records of past tectonic events. Under the tectonically active western US, where the lithosphere is thin, the direction of tomographically inferred anisotropy is stable with depth and compatible with the absolute plate motion direction.

16.2 Updated 3-D regional tomographic model of North America

Our published regional 3-D tomographic model (*Marone et al.*, 2007; *Marone and Romanowicz*, 2007), however, is based on pre-EarthScope data (before 2003). And since it was our first regional tomographic attemp using NACT, the model has large horizontal resolution, i.e., 400- and 800-km for the isotropic (S) and anisotropic (X) models, respectively. Therefore, during last year, we concentrated mostly on improving the model horizontal resolution by filling the station and event distribution gaps, i.e., adding newly deployed permanent and temporary stations and selectively collecting data from the NE and South back-azimuthal quadrants. Our first set of updated models, with horizontal resolution of 200- and 400-km for S and X respectively, has been presented at 2007 Fall AGU meeting and 2008 IRIS workshop (Figure 2.36).

Our isotropic and anisotropic shear-wave images are consistent with our published model, but show greater details beneath the cratonic upper mantle, benefitting from the augmented waveform datasets from the US array and newly deployed IRIS PASSCAL and Canadian arrays. For example, our isotropic shear-wave velocity model sees a high velocity curtain at 250-400 km depth range beneath central North America. This feature is also seen by higher resolution P-wave tomography studies (e.g., *Li et al.*, 2007, *Ren et al.*, 2007; *Sigloch et al.*, 2008). Our updated radial anisotropy and azimuthal anisotropy images confirm the distinct upper mantle anisotropic domain beneath North America. This continent-wide multiple-layer upper mantle anisotropic domain has also been reported from many studies, e.g., in Rayleigh wave imaging (*Deschamps et al.*, 2008; *Chen et al.*, 2007; *Snyder and Bruneton*, 2007), in multiple-layer anisotropy modeling (*Snyder et al.*, 2003; *Currie et al.*, 2004; *Fox and Sheehan*, 2005; *Frederiksen et al.*, 2007; *Yuan et al.*, 2008), and in receiver functions (*Levin and Park*, 1999). *Deschamps et al.* (2008) speculates that the north trending lithospheric LPO was frozen into the lithosphere during northward drift of the North American plate during Mesozoic times. Some new but minor features appear in the shallow upper mantle in our anisotropic models, correlating well with the surface expression of some past and ongoing NA tectonic events.

16.3 Ongoing research

Currently we are working on improving our 3-D velocity model from the following aspects. First, we are collecting all the EarthScope data and broadband data from the Canadian National Data Center, which will greatly improve our data coverage and hence tomographic resolution, especially beneath the western US. To account for the irregular ray density brought in by the new datasets, we will densify our model spacing in the relevant regions (e.g., beneath western U.S.), which means that higher horizontal resolution (100 km) will be reached in those regions. Second, we are introducing a new 1-D reference model in our inversion. Our previous 1-D reference model, the Preliminary Reference Earth Model (PREM), has a 220-km velocity jump, which is, however, not a ubiquitous feature of the Earth (e.g., *Nettles and*

Dziewonski, 2008; *Kustowski et al.*, 2008). We are switching from the PREM model to a new 1-D reference model developed at UC, Berkeley (*Lekic and Cammarano*, pers. Comm.) that does not preserve the 220-km discontinuity. Lastly, we are incorporating into our tomographic model the upper mantle discontinuities. These upper mantle discontinuities, serving as either boundaries separating distinct upper mantle anisotropy domains (e.g., the LAB) or isotropic velocity gradients, are better constrained by other techniques, such as teleseismic receiver functions. We are currently exchanging data with research groups at Brown and Rice Universities: the LAB from those groups will be incorporated into our tomographic inversion as a priori constraints; in return, our new 3-D tomographic results will provide a better velocity model for the receiver function depth migration.

16.4 Acknowledgements

We thank the IRIS DMC and Canadian National Data Center for providing the waveform data. Figures are prepared using GMT (Wessel and Smith, 1998). This project is supported by NSF EAR-0643060.

16.5 References

Chen, C. W., S. Rondenay, D. S. Weeraratne, and D. B. Snyder, New constraints on the upper mantle structure of the Slave craton from Rayleigh wave inversion, *Geophys. Res. Lett., 34*, L10301, doi:10.1029/2007GL029535, 2007.

Currie, C., J. F. Cassidy, R. D. Hyndman, and M. G. Bostock, Shear wave anisotropy beneath the Cascadia subduction zone and western North American craton, *Geophys. J. Int., 157*, 341-353, 2004.

Deschamps, F., S. Lebedev, T. Meier, and J. Trampert, Azimuthal anisotropy of Rayleigh-wave phase velocities in the east-central United States, *Geophys. J. Int., 173*, 3, 827-843, 2008.

Fox, O., and A. F. Sheehan, Shear wave splitting beneath the CDROM transects, in The Rocky Mountain region–an evolving lithosphere: tectonics, geochemistry, and geophysics, edited by G. Randy and K. E. Karlstrom, American Geophysical Union, Washington DC, 2005.

Frederiksen, A. W. et al., Mantle fabric at multiple scales across an Archean-Proterozoic boundary, Grenville Front, Canada, *Phys. Earth and Plan. Int., 158*, 2-4, 240-263, 2006.

Kustowski, B., G. Ekstrom, and A. M. Dziewonski, Anisotropic shear-wave velocity structure of the Earth's mantle: A global model, *J. Geophys. Res, 113, B06306*, doi:10.1029/2007JB005169, 2008.

Li, C., R. D. van der Hilst, E. R. Engdahl, and S. Burdick, A new global model for P wave speed variations in Earth's mantle *Geochem. Geophys. Geosyst., 9*, doi:10.1029/2007GC001806, 2008.

Li, X., and B. Romanowicz, Comparison of global waveform inversions with and without considering cross branch coupling, *Geophys. J. Int., 121*, 695-709, 1995

Marone, F., Y. Gung, and B. Romanowicz, 3D radial anisotropic structure of the North American upper mantle from inversion of surface waveform data, *Geophys. J. Int.*, doi: 10.1111/j.1365-246X.2007.03456, 2007.

Marone, F., and B. Romanowicz, The depth distribution of azimuthal anisotropy in the continental upper mantle, *Nature, 447*, 7141, 198-201, 2007.

Nettles, M., and A. M. Dziewonski, Radially anisotropic shear-velocity structure of the upper mantle globally and beneath North America, *J. Geophys. Res, 113*, B02303, doi:10.1029/2006JB004819, 2008.

Ren, Y., E. Stutzmann, R. van der Hilst, D., and J. Besse, Understanding seismic heterogeneities in the lower mantle beneath the Americas from seismic tomography and plate tectonic history, *J. Geophys. Res, 112*, B01302, doi:10.1029/2005JB004154, 2007.

Sigloch, K., N. McQuarrie, and G. Nolet, Two-stage subduction history under North America inferred from multiple-frequency tomography, *Nature , 1*, 7, 458-462, 2008.

Snyder, D. B., M. G. Bostock, and G. D. Lockhart, Two anisotropic layers in the Slave craton, *Lithos, 71*, 529-539, 2003.

Snyder, D. B., and M. Bruneton, Seismic anisotropy of the Slave craton, NW Canada, from joint interpretation of SKS and Rayleigh waves, *Geophys. J. Int., 169*, 170-188, 2007.

Wessel, P., and W. H. F. Smith, New, improved version of the Generic Mapping Tools released, *Eos Trans. AGU, 79*, 49, 579, 1998.

Yuan, H. Y., K. Dueker, and D. L. Schutt, Testing five of the simplest upper mantle anisotropic velocity parameterizations using teleseismic S and SKS data from the Billings, Montana PASSCAL array, *J. Geophys. Res., 113*, B03304, doi:10.1029/2007JB0050922008.

17. Towards Regional tomography using the Spectral Element Method

Barbara Romanowicz, Aimin Cao, Federica Marone, Mark Panning, Paul Cupillard

17.1 Introduction

We are developing an approach which relies on a cascade of increasingly accurate theoretical approximations for the computation of the seismic wavefield, with the goal to develop a model of regional structure for a subregion of Southeast Asia (longitude 75 to 150 degrees and latitude 0 to 45 degrees). The selected area is highly heterogeneous, but is well surrounded by earthquake sources and includes high quality broadband digital stations. In previous years, we developed preliminary models based on time domain inversion of long period seismograms, in the framework of normal mode theory: 1) a 3D model based on the Nonlinear Asymptotic Coupling Theory (NACT, *Li and Romanowicz*, 1995), which includes the consideration of 2D kernels in the vertical plane containing source and receiver. This model was developed for a larger region (longitude 30-150 degrees and latitude -10 to 60 degrees), starting from a global 3D model (*Panning and Romanowicz*, 2006); 2) a 3D model based on the NBorn approximation (*Panning et al.*, 2008). This approach combines the 3D Born approximation with the path average approximation (PAVA) and allows us to accurately account for large accumulated phase delays on paths that sample large scale smooth anomalies. The resulting model has a horizontal resolution of about 200 km.

In parallel, a regional version of the Spectral Element Method (SEM) code, in spherical geometry, RegSEM, was completed (*Cupillard*, 2008). This code accepts a non-conformal grid, uses PML (Perfectly-Matched Layers) at the borders of the region, and includes general 3D anisotropy, Moho and surface topography, ocean bathymetry, attenuation, and ellipticity. Because each SEM run (i.e. for one event) is time consuming, we proposed to implement an approach in which the wavefields for several events are computed simultaneously. This approach was introduced by *Capdeville et al.* (2005) and tested on synthetic data at the global scale, but never applied to real data or at a regional scale.

17.2 Towards regional tomography using summed waveforms

In the past year, in collaboration with researchers at the Institut de Physique du Globe in Paris, we completed the codes and procedures that allow us to invert a collection of summed seismograms over the sub-region of Eurasia already considered for the NBORN inversion.

The computation of the forward wavefield using SEM is very accurate, but heavy computationally. It takes 2 hours to compute the wavefield of a single seismic event down to 60 sec (i.e., at long periods) on a modest computer cluster (32 cpu's). To speed up computations and develop the capability of performing many iterations and reaching higher frequencies, we have implemented the approach of *Capdeville et al.* (2005), in which the wavefield corresponding to many events is computed simultaneously. To do so, all the seismic sources considered are shifted in time to a common origin time, and the wavefield generated by this composite source is calculated once. The observed waveforms, at each station, thus consist of the summed observed seismograms for all events, each of them appropriately shifted in time, and are compared to the predicted synthetic wavefield. While these "summed" waveforms do not have a physical meaning, i.e. there are no identifiable seismic phases, they retain sufficient information to allow retrieval of 3D structure, even in the presence of realistic background noise, at least at long wavelengths. This approach can reduce computation time by one to several orders of magnitude, depending on the implementation. *Capdeville et al.* (2005) tested this approach in the framework of global tomography and a synthetic dataset. They showed that, even with realistic noise added to the synthetics, they can retrieve 3D upper mantle structure accurately from a single forward computation involving 50 events observed simultaneously at 150 stations worldwide.

In the adaptation of this method to our regional case, we have proceeded with the RegSEM code (rather than C-SEM) and have relaxed the restriction of all events observed by all stations, replacing the single summation over all events by a series of runs, each of which considers the sum of all events observed at a given station. The number of RegSEM runs is then equal to the number of stations considered in the region, which, in general, is significantly smaller than the number of events. Contrary to the NACT and NBorn cases, for which we collected teleseismic data, RegSEM, as currently implemented, requires sources and receivers to be included in the region of study. We thus collected an entirely new dataset, consisting of 96 events with $6.0< M_w <7.0$ observed simultaneously at 6 broadband GSN stations during the time period 1995 to 2007, with an epicentral distance between 5^o and 45^o.

Figure 2.37 shows the region of study and the ray coverage for our initial summed event experiment. Here, we have relaxed the restriction of teleseismic observations. The epicentral distances range from 5 to 40^o. In this case, we cannot perform any comparisons with the NACT or N-Born inversions, for which the theory breaks down at short distances; however, we can still perform comparisons with inversions obtained using the simpler Path Average (PAVA) approximation.

Figure 2.38 shows an example of comparison between "observed" versus RegSEM computed summed waveforms at station XAN, showing that, at these long periods, the starting model predicts the observed waveforms already quite well.

In order to reduce the computational time in the inverse step of the procedure, we also have opted, at least at this early stage, to compute partial derivatives approximately, using PAVA, in the inversion step of our procedure. We are assuming that, if our starting 3D model (the model derived using N-Born) is sufficiently accurate, these approximate partial derivatives will point us in the right direction and we will at the worst, need to compute a few more iterations to converge to the final model. Eventually, we can implement accurate numerical partial derivatives, whose calculation will also be faster, compared to conventional inversions, due to summation over events.

In order to test the summed event approach, we have first compared the results of an inversion obtained using, on the one hand side, the "summed event" seismograms at the 6 stations considered, and on the other, a "standard" approach, in which we have separately calculated the wavefield using RegSEM for all the events considered, and inverted the corresponding perturbations to the time domain waveforms, as we would do conventionally, using any of our previous inversion methods (PAVA, NACT, N-Born). The only difference in the latter is that now, the forward part of the modelling is computed using RegSEM, rather than mode perturbation theory. The synthetics have been computed down to 60s period, and the observed seismograms have been filtered accordingly. Figure 2.39 shows a comparison of the isotropic models obtained using the conventional approach (single event-station paths) versus the summed approach. The two RegSEM models are very similar indicating that the summed event approach holds promise. A striking feature of the RegSEM models is the fast velocity anomaly south of Korea shallow depth (30 km), which is not present in any of the models developed with asymptotic mode perturbation theory, which shows low velocities throughout the ocean basins at this depth. The fast velocity seen in the RegSEM models is likely an artifact, due to the inaccurate crustal model, which does not incorporate the thick sediments present in that region. Since RegSEM models the crust much more accurately than our usual inversions based on mode perturbation theory, these kind of details start to matter, even at periods as long as this test case.

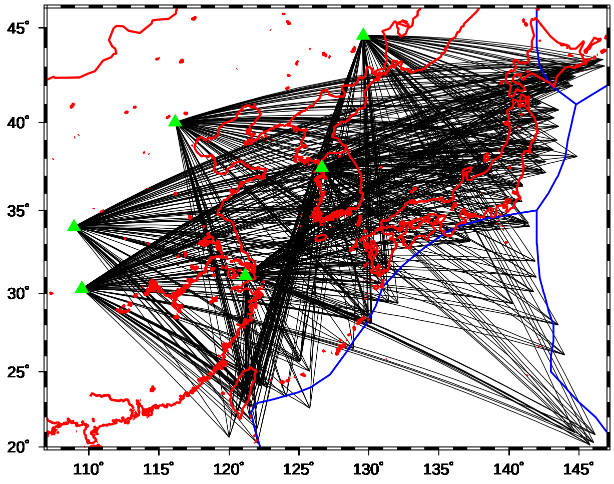

Figure 2.37: Raypath coverage achieved in the "summed seismogram" experiment. The stations are indicated by triangles.

17.3 Acknowledgements

This research was supported by NNSA contract No. DE-FC52-04NA25543 (BAA).

17.4 References

Capdeville, Y., E. Chaljub, J. P. Vilotte, and J. P. Montagner, Coupling the spectral element method with a modal solution for elastic wave propagation in global earth models, *Geophys. J. Int.*, *152*, 34-66, 2002.

Capdeville, Y., B. Romanowicz, and Y. Gung, Towards global earth tomography using the spectral element method: a technique based on source stacking, *Geophys. J. Int.*, *162*, 541-544, 2005.

Cupillard, P. , Simulation par la méthode des éléments spectraux des formes d'onde obtenues par corrélation de bruit sismique, These de Doctorat, Institut de Physique du Globe de Paris, 2008.

Li, X. D. and B. Romanowicz , Comparison of global waveform inversions with and without considering cross branch coupling, *Geophys. J. Int.*, *121*, 695-709, 1995.

Panning, M. and B. Romanowicz , A three dimensional radially anisotropic model of shear velocity in the whole mantle, *Geophys. J. Int.*, *167*, 361-379, 2006.

Panning, M., Y. Capdeville and B. Romanowicz , Do first order 3D Born finite-frequency kernels improve modeling of surface waveforms?, *Geophys. J. Int.*, in press, 2008.

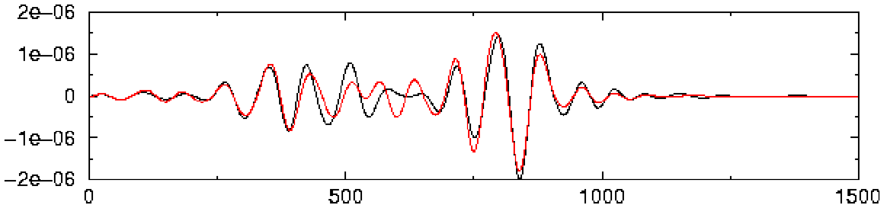

Figure 2.38: Summed seismogram on the vertical component at station XAN. Black: observed trace, red: synthetic trace computed using RegSEM for the starting 3D model (NBORN) shown in Figure 2.37. Both observed and synthetic traces have been filtered with a cut-off period of 60 s.

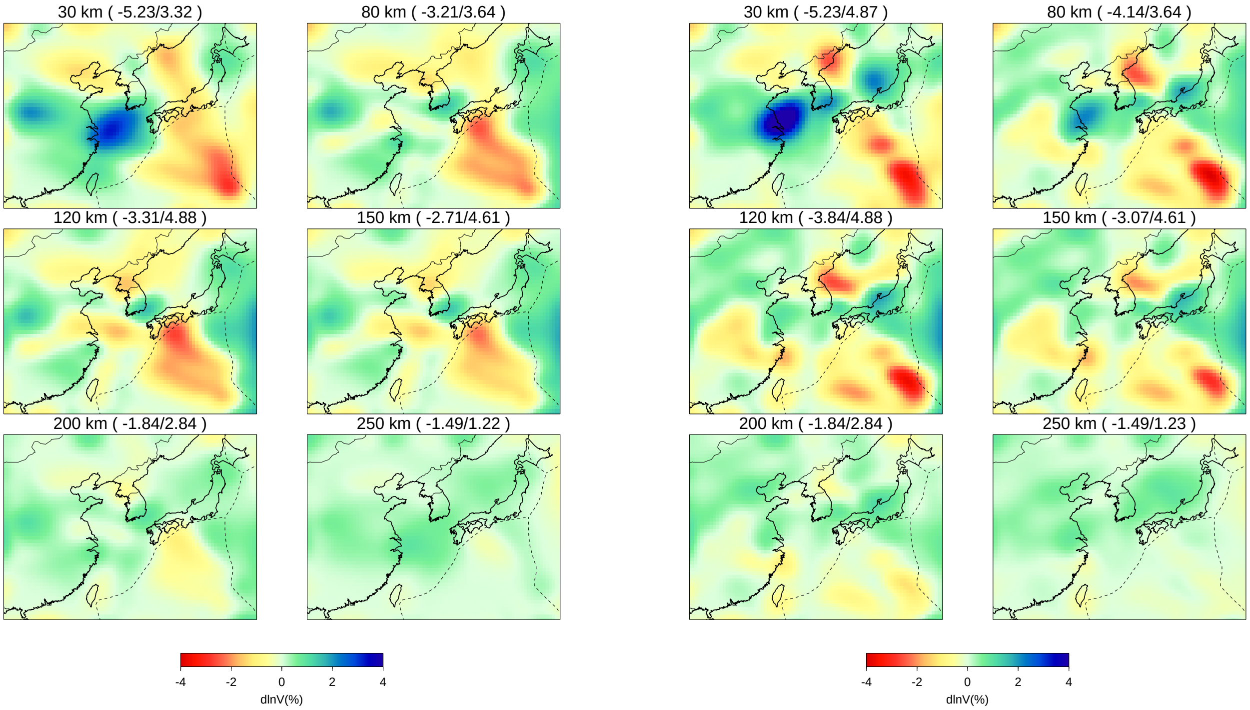

Figure 2.39: Comparison of upper mantle models obtained after one iteration from the starting NBORN model, using waveform data on the path collection shown in Figure 2.38, RegSEM for the forward part of the computation, and PAVA for the calculation of partial derivatives. Left: conventional computation using individual source-station paths. Right: summed-event computation. The models differ in some details, which is not surprising given that only 6 stations have been used.

18. A Brief Review of Observation of the Slichter Mode

Shan Dou, Robert Uhrhammer, Barbara Romanowicz

18.1 Introduction

Slichter mode ${}_1S_1$, which is caused by the translational oscillations of the solid inner core about its equilibrium position at the center of the Earth, was named after the seismologist Louis Slichter when he first claimed the detection of this mode from the data of the Chile Earthquake in 1960. The preliminary estimation of its period made by Louis Slichter proved to be too short (around 86 min). Up to now, the generally-accepted interpretation was that the frequency of the Slichter mode is principally controlled by the density jump between the inner and outer core, and the Archimedean force produced by the fluid outer core. According to theoretical calculations based on perturbation theory, its period is thought to be in the range of 4∼8 hours, and it splits into 3 singlets because of the Earth's rotation. As this translational mode can offer important information about the density jump at the ICB (Inner Core Boundary), much effort has been made to detect it. However, there are large uncertainties on its attenuation.

18.2 Review on the Detection of the Slichter Mode

Although the Slichter mode is crucial in determining the density difference across ICB, its detection is very challenging. The difficulties mainly come from the following aspects: (1)The largest displacement of the Slichter mode occurs at great depth (at ICB, see Figure 2.40), and its displacement is strongly attenuated as it goes through the liquid outer core. When the motion finally propagates to the surface of the Earth, it is too weak to be easily observed. For example, for an event as big as the 1960 Chile Earthquake(M_w 9.5), the theoretical estimation of its amplitude on the Earth's surface is only on the order of a nanogal; (2) As the period of the Slichter mode is very long (4∼8 hours), it sits in the "subseismic band" (i.e. frequency lower than 0.03mHz) that has very strong background noise; (3)The period of the Slichter mode is also very similar to that of Earth tides, which means that a precise tide model is needed to do the tidal correction. However, as tidal phenomena are quite complicated, it is very difficult to perform this correction with adequate confidence; (4) Q estimates vary by up to several order of magnitude.

Although the exact excitation mechanism of the Slichter mode is still unclear, many detection efforts were undertaken with the assumption that the Slichter mode is continuously excited. Therefore, very long time series can be used to analyze this ultra low frequency signal, but a flat instrumental response (in the frequency domain) is then required to avoid amplifying low frequency noise. Superconducting Gravimeters (SGs) can therefore facilitate the observation, as their response in subseismic bands is very flat and stable. Over 20 SGs are installed around the world, which make it possible to extract of global signals by stacking.

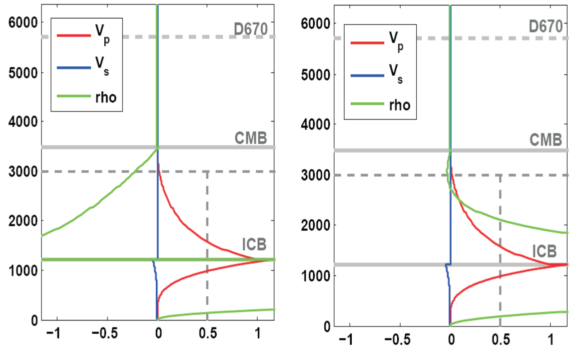

Figure 2.40: normalized theoretical sensitivity kernel of the displacement of ${}_1S_1$.Left: c00; right: c20(c00 and c20 are splitting coefficients). We use PREM model here.

The first claim of the detection of the Slichter mode after L. Slichter was made by *Smylie et al* (1992, Science). They used 4 long records from SGs in Europe: Brussels (1982∼1986), Brussels (1987∼1989), Bad Homburg (1986∼1988), Strasbourg (1987∼1991). They found out three singlets with periods of 3.5820 ± 0.0008, 3.7677 ± 0.0006, and 4.015 ± 0.001 hours, as well as Q values of 116,141 and 115, respectively. These frequency values are very close to the theoretical calculation based on 2nd order perturbation theory (*Dahlen and Sailor*, 1979). However, this promising observation was put into doubt when *Hinderer et al.* (1995) failed to reproduce *Smylie's* (1992) results. They used 2 simultaneous records at SG stations in Canada and France, and analyzed both the product spectra and cross-spectra. The whole process was optimal, as the phase information could be kept in this way, but the results were disappointing, as they could not detect the triplet in their spectra. They argued that cross-spectra should enhance coherent signals and interpreted the null observation as indicating that the triplet of *Smylie* was not the Slichter mode. Later, *Ochi et al.* (2000) designed a method to utilize the spatial dependency of the 3 singlets to obtain a better spectral estimate for each of them. They used 6 records from different observatories but covering the same time period. They then confirmed the presence of the triplet using an analysis based on product spectra. The mode showed up in the data from both Europe and outside of Europe, but with slightly different periods for both groups of stations. Again, *Rosat et al.* (2006) failed to reproduce *Ochi's* result. *Rosat et al.* developed a detection method based on predictions from theoretical models, which were similar to those used by *Ochi et al.* (2000), and applied it to one-year datasets of SG gravity using product spectra, but they were unable to observe the triplet. Many other attempts to observe the Slichter mode through SG data are not listed above, but they all have negative answers. Detection of this special mode is still a challenge.

18.3 Motivation and Future Work

SG data has played a key role in the study of the Slichter mode, but the disadvantages of these instruments are also apparent: (1) Since SGs are very expensive and have strict site condition requirements, they are still sparsely distributed globally; (2) Only a small part of SG data are directly shared on-line, and these data always have a delay of 6 months; (3) the SG data format is not used by seismologists, and the transfer function is not always known. Compared with SGs, STS-1 seismometers also have good performance at ultra low frequency (Figure 2.40), and the wide distribution of the STS-1 makes it an optimal instrument for global stacking. Also, the transfer functions are well known. For these reasons, we are trying to develop a standard procedure to search for the Slichter mode using STS-1 data.

18.4 Acknowldgements

We thank David Dolenc, David Crossley, and Ichiro Kawasaki for their help on tidal corrections.

18.5 References

Dahlen, F.A. and Sailor, R.V., Rotational and elliptical splitting of the free oscillations of the Earth, *Geophys. J. R. Astron. Soc. 58*, 609-623, 1979.

Hinderer, J., Crossley, D., and Jensen, O., A search for the Slichter triplet in superconducting gravimeter data, *Phys. Earth Plan. Int., 90*, 183-195, 1995.

Ochi Y., K. Fujita, I. Niki, H. Nishimura, N. Izumi, A. Sunahara, S. Naruo, T. Kawamura, M. Fukao, H. Shiraga, H. Takabe, K. Mima, S. Nakai, I. Uschmann, R. Butzbach, E. Forster, N. Courtier, B. Ducarme J. Goodkind, J. Hinderer, Y. Imanishi, N. Seama, H. Sun, J. Merriam, B. Bengert, D.E. Smylie D.E, Global superconducting gravimeter observations and the search for the translational modes of the inner core, *Phys. Earth and Plan. Int., 117,* 3-20, 2000.

Rosat, S., Y. Rogister, D. Crossley, J. Hinderer, A search for the Slichter triplet with superconducting gravimeters: impact of the density jump at the inner core boundary, *J. Geodynam., 41*, 296-306, 2006.

Slichter, L.B., The fundamental free mode of the Earth's inner core, *Science, 47,* 186-190, 1961.

Smylie, D.E., The inner core translational triplet and the density near Earth's center, *Science, 255,* 1678-1682, 1992.

Smylie, D.E., J. Hinderer, B. Richter and B. Ducarme, The product spectra of gravity and barometric pressure in Europe, *Phys. Earth and Plan. Int., 80,* 135-157, 1993.

19. What Does a Waveform Obtained by Correlation of a Diffuse Anisotropic Wavefield Contain?

Paul Cupillard and Yann Capdeville (IPG Paris)

19.1 Introduction

Recent developments have shown that the Green's function between two distant seismometers can emerge from the cross-correlation of several days of seismic noise recorded at the seismometers (*Shapiro and Campillo*, 2004). This provides new data that are greatly interesting for seismologists because they enable us to get information about the Earth structure in aseismic regions. Group-speeds on inter-station paths are now widely measured, and numerous high-resolution tomographic images appeared in the last three years.

Many theoretical developments tried to explain the phenomenon. All the theories only take into account the case of uniformly distributed noise sources. Now, an anisotropic flux as well as the absence of equipartition has to be considered to fully understand the limitations of the method. Indeed, noise consistently observed in seismic records mainly comes from the oceans (*Longuet-Higgins*, 1950), so that its distribution at the surface of the Earth clearly is nonhomogeneous. Here we study the effect of such a distribution by computing correlations of numerically generated seismic noise in an attenuating sphere.

19.2 Uniform Noise Sources Distribution

First, we compute synthetic noise to mimick the continuous oscillations that are consistently observed in seismic records. To create that noise, we randomly position three hundred sources on the Earth's surface. For each spatial component of each source, we generate a 24-hour time signal with random phase and flat spectrum filtered between 2 and 13 mHz. Using normal-modes summation in the Preliminary Reference Earth Model (*Dziewonski and Anderson*, 1981), the effect of all the sources is computed at three stations A, B and C located on the equator at longitude 0°, 20° and 70° respectively (Figure 2.41). Correlations between vertical components of displacement received at the stations are then calculated. That is the result of what we call a "realization". We perform 12,640 realizations (the total number of sources is then 3,792,000) and we stack all of them. Three different cases are studied, corresponding to different processes applied to the noise records : we distinguish raw noise (nothing is done), 1-bit noise (meaning that we completly disregard the amplitude) and whitened noise (meaning that the spectral amplitudes of each record are set to 1 in the chosen frequency band).

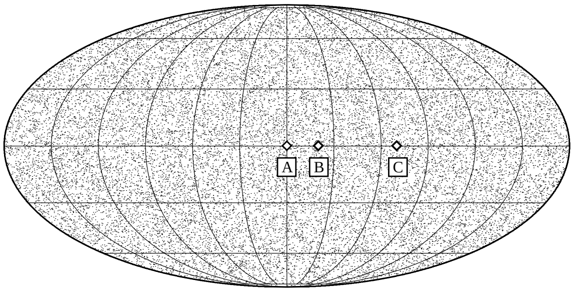

Figure 2.41: Location of receivers A, B and C (top). Station B (resp. C) is 20° (resp. 70°) away from A. Tiny dot pixels indicate location of 24,000 noise sources coming from 80 realizations of our numerical experiment.

With the normal-modes summation method, the Green's tensors between A and B and between A and C can be easily calculated. Figure 2.42 shows the comparison between Green's functions and the derivatives of our synthetic correlations with and without power spectral density correction. We note that the waveform and relative amplitudes between the signal from A and B and the signal from A and C are conserved for each kind of noise processing. This means that information about geometrical as well as intrinsic attenuation is contained in correlations whatever the technique we use to process the noise recordings. Travel times have been preferentially considered so far on seismic noise correlations, but the use of amplitude is now more and more questioned, and the result we present here is essential in this perspective. Nevertheless, it is in disagreement with the experimental result from *Larose et al* (2007) who recover the geometrical spreading with raw data but lose it with 1-bit or whitened noise. We don't have an explanation for this difference yet.

19.3 Non-Uniform Noise Sources Distribution

Here we perform the same experiment, except that noise sources are now confined in a 50°-radius disk at the surface of the sphere. We study cross-correlations from different azimuths by using records from 24 stations located in two circles around a central station A (Figure 2.43).

As in the previous section, we compare Green's functions and the derivatives of our correlations. Two azimuths are studied : 90° (i.e. stations 12 and 24, see Figure 2.44) and 30° (i.e. stations 2 and 14, see Figure 2.45). For the first azimuth, results are very similar to

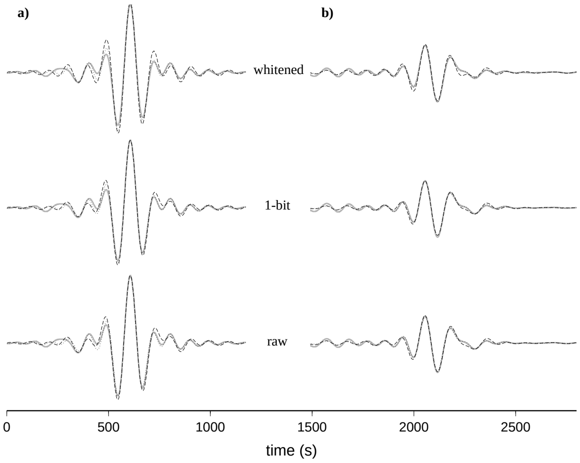

Figure 2.42: **a)** Comparison, for each kind of process applied to the noise records (raw, 1-bit normalization and whitening), between the A-B Green's function (gray lines) and the derivatives of our synthetic cross-correlations with (dotted lines) and without (dashed lines) power spectral density (PSD) correction. **b)** Same as a) for stations A and C. The PSD correction improves the waveform fits.

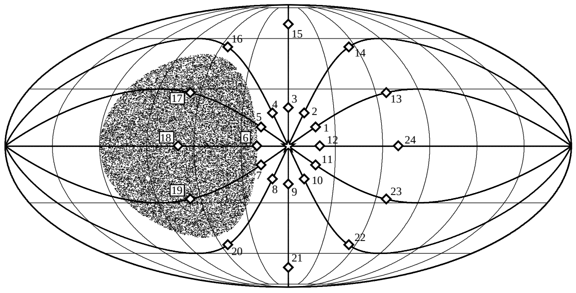

Figure 2.43: Location of the central station A (star) and the other receivers (numbered from 1 to 24). Stations 1 to 12 (resp. 13 to 24) are 20° (resp. 70°) far from A and spaced by an angle of 30°, defining twelve azimuths. Great circles that link the stations to the centre A are plotted to highlight the different azimuths. In addition, tiny dots indicate location of 24,000 noise sources coming from 80 realizations of our numerical experiment.

those observed in the uniformly distributed noise sources case: the power spectral density correction improves the waveforms' fit, overtones are not well excited, and attenuation is retrieved for the three different noise-processing procedures. Results from azimuth 30° are very different. An important phase shift between the Green's functions and the correlations is observed, both for station 2 and station 14. This is because the emergence of the signal is only due to sources far from the vicinity of the great circle, and contribution of such sources provides incorrect travel times.

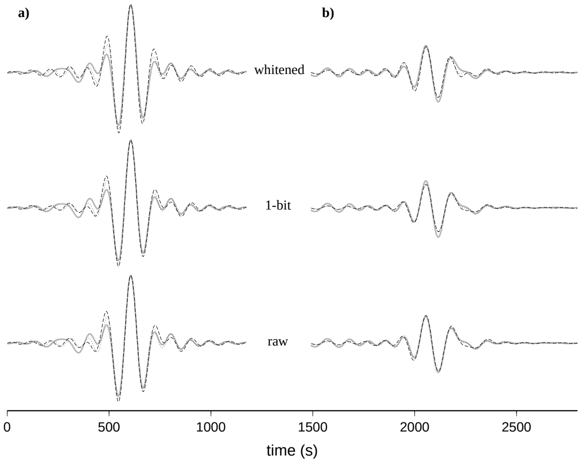

Figure 2.44: **a)** Comparison between the derivative of the correlation of station 12 by A and the corresponding Green's function. Gray lines correspond to the Green's function, whereas dotted and dashed lines are correlations respectively with and without power spectral density correction. **b)** Same as a) for station 24.

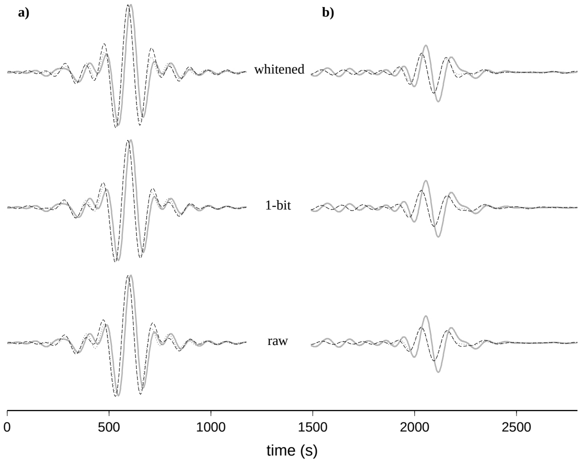

Figure 2.45: Same as Figure 2.44 for stations 2 and 14.

19.4 References

Dziewonski, A.M. and D.L. Anderson, Preliminary Reference Earth model, *Phys. Earth Planet. Inter., 25*, 297-356, 1981.

Longuet-Higgins, M.S., A theory on the origin of microseisms, *Philo Trans. R. Soc. Lond. A., 243*, 1-35, 1950.

Shapiro, N.M. and M. Campillo, Emergence of broaband Rayleigh waves from correlation of the ambient seismic noise, *Geophys. Res. Lett., 31*, L07614, 2004.

20. Measurement and implications of frequency dependence of attenuation

Vedran Lekic, Jan Matas, Mark Panning (Princeton University), and Barbara Romanowicz

20.1 Introduction

As they propagate through the Earth, seismic waves experience energy loss, which is summarized by $q = -\Delta E / 2\pi E_{max}$, where ΔE is the internal energy lost by a seismic wave in one cycle. Attenuation is high and nearly constant within a certain frequency band and rapidly falls off with frequency away from this band. The frequency dependence of q can be described using a power law, $q \propto \omega^{\alpha}$, with a model-dependent α that is usually thought to be smaller than 0.5 within the absorption band.

Though seismological efforts at constraining globally-averaged α within the absorption band have benefited from numerous measurements of surface wave or normal mode attenuation (see `http://mahi.ucsd.edu/Gabi/rem.html`), the determination of α has been confounded by the fact that oscillations at different frequencies can have very different depth sensitivities to elastic and anelastic properties of the earth. As a result of this trade-off between frequency and depth effects, radial variations of attenuation can obscure the α signal. The only studies attempting to obtain α within the absorption band have found α ranging from 0.1 to 0.3 while emphasizing the lack of resolution on the deduced values. More recent studies have relied upon analysis of body waves to argue for values of α in the 0.1-0.4 range (see *Romanowicz and Mitchell*, 2007). However, these studies were restricted to frequencies higher than 40mHz and were of regional extent, leaving unanswered the question of the average mantle α.

In light of these difficulties, seismic studies routinely assume that, within the seismic band, α cannot be resolved and thus implicitly rely on the frequency-independent attenuation model of *Kanamori and Anderson* (1977). We re-examine the model's applicability to the mantle using a new method based on the standard analysis of *Backus and Gilbert* (1970) that allows us to separate the effects of the radial q profile from those due to frequency dependence of q as described by α.

20.2 Method

We can relate a mode attenuation measurement q to material properties within the Earth via sensitivity (Fréchet) kernels K_μ and K_κ:

$$q = \frac{2}{\omega} \int_0^R dr \; \kappa_0 q_\kappa K_\kappa + \mu_0 q_\mu K_\mu, \qquad (2.11)$$

where R is the radius of the Earth, κ_0 and μ_0 are the reference radial profiles of bulk and shear moduli, and q_κ and q_μ are values of radial bulk and shear attenuation.

The sensitivity kernels of fundamental modes with similar frequencies are very similar, implying that the q datasets are highly redundant. We seek to exploit this redundancy and divide modes into a low and high frequency bin, denoted by superscript l and h, respectively. Each linear combination of Fréchet kernels of modes in each bin defines a new "hyperkernel":

$$\mathbf{H}^{\text{low}}_{\mu,\kappa} = \sum_{l=1}^{N_l} \gamma^l \mathbf{K}_{\mu,\kappa}{}^l \quad \text{and} \quad \mathbf{H}^{\text{high}}_{\mu,\kappa} = \sum_{h=1}^{N_h} \gamma^h \mathbf{K}_{\mu,\kappa}{}^h, \qquad (2.12)$$

where N_l and N_h are the number of modes in each bin, and the subscripts μ, κ denote that the kernels refer to either shear or bulk attenuation.

Each particular choice of γ^l and γ^h will yield hyperkernels with different depth sensitivities. Therefore, by requiring that γ^l and γ^h yield hyperkernels with identical sensitivities to the radial attenuation profile, it is possible to remove the trade-off between depth and frequency dependence of attenuation measurements. Since we focus on the effective α in the mantle, we require the hyperkernels to be zero outside the mantle while providing maximally uniform sensitivity in the mantle. In order to eliminate the contribution from poorly-constrained mantle bulk attenuation, we seek hyperkernels that are insensitive to q_κ.

To each hyperkernel corresponds a q value, which is a weighted average of the q measurements of its constituent normal modes:

$$q^{\text{low}} = \sum_{l=1}^{N_l} \gamma^l q^l \quad \text{and} \quad q^{\text{high}} = \sum_{l=1}^{N_h} \gamma^h q^h. \qquad (2.13)$$

Since the two hyperkernels have identical sensitivity to radial attenuation structure but differing frequency content, differences in q^{low} and q^{high} can be attributed to frequency dependence of attenuation. These effects of frequency dependence can be accounted for by projecting the individual mode q's to a reference value q_0 using:

$$q_{0_i} = q_i \left(\frac{\omega_i}{\omega_0} \right)^{\alpha}. \qquad (2.14)$$

In the absence of systematic measurement error, q^{low} and q^{high} will be reconciled at the reference frequency for the value of α that corresponds to the effective α of the mantle.

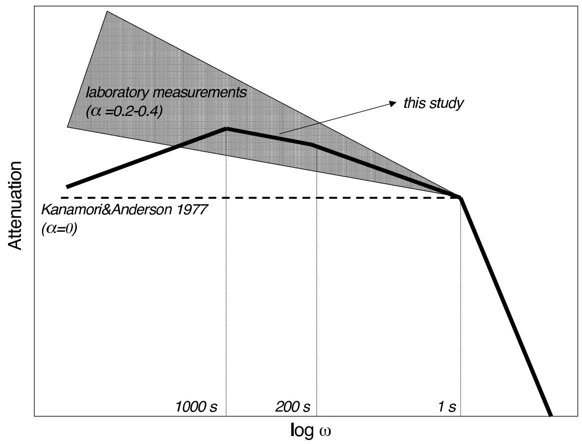

Figure 2.46: Preferred model of frequency dependence of attenuation within the absorption band. α is approximately 0.3 at periods shorter than 200 s, decreasing to 0.1 in the period range 300-800s, and becoming negative (-0.4) at periods longer than 1000s.

20.3 Results

After validating our method on a synthetic dataset, we apply it to existing attenuation measurements of free oscillations and surface waves spanning the period range 3200s-50s. We observe that effective α is likely to be frequency dependent. Specifically, α is negative at periods longer than 1000s and positive and increasing at shorter periods (see Figure 2.46). This conclusion runs against both the assumption of frequency-independent attenuation often used in seismology, and the constant, positive α model suggested by laboratory studies (*Jackson et al.*, 2005). A frequency-dependent effective α is nevertheless physically plausible. This is because the effective α that one would obtain by analyzing the normal-mode and surface-wave attenuation measurements is the result of an interplay of the *actual* α associated with the material at a given depth and the position of the absorption band. This interplay can give rise to a negative effective α as long as the actual α is negative at long periods at some depths. Furthermore, our preferred model of frequency dependence of attenuation is consistent with earlier studies that have relied upon body waves and have focused on higher frequencies (see Figure 2.46).

A non-zero value of α carries important implications for the construction of radial profiles of attenuation. Efforts at determining the radial profile of attenuation in the Earth have routinely assumed that attenuation is frequency independent. The resulting models have, therefore, mapped the signal of frequency-dependence of q into its depth profile.

Relating lateral variations of attenuation in terms of temperature requires knowing α, since when when α is zero, $\delta q/\delta T$ is a constant, whereas when α is positive, $\delta q/\delta T$ is exponentially dependent on temperature (*Minster and Anderson*, 1981). Recent studies of lateral attenuation variations rely on data with periods shorter than $\sim$ 300s (e.g. *Gung and Romanowicz*, 2004), at which periods our preferred model suggests that $\alpha \sim 0.3$. This value implies an exponential temperature dependence of attenuation, and justifies the interpretation of lateral attenuation variations in terms of temperature variations.

Intrinsic attenuation causes dispersion of seismic velocities, which must be corrected when datasets with different frequency content are used to simultaneously constrain Earth structure. Both the values of α and of q significantly affect the magnitude of the dispersion correction. For an α value of 0.3, the assumption of frequency-independent attenuation will result in 25% error for a frequency ratio of 10 and a 50% error for a frequency ratio of 100.

Finally, the precise knowledge of seismic velocity, its dispersion and associated attenuation is important for meaningful comparisons with other geophysical observables, such as the geoid. Future work should thus be aimed at improving the precision of q measurements and the development of radial q profiles that properly account for the frequency dependence of q.

20.4 Acknowledgements

This project was supported by NSF grants EAR-0336951 and EAR-0738284, NSF fellowship held by VL, and by the French CNRS-SEDIT program.

20.5 References

Backus, G.E. and J.F. Gilbert, Uniqueness in the inversion of inaccurate gross earth data, *Phil. Trans. R. Soc. London, 266*, 123-192, 1970.

Gung, Y. and B. Romanowicz, Q tomography of the upper mantle using three-component waveforms, *Geophys. J. Int.,157*, 813-830, 2004.

Jackson, I., S. Webb, L. Weston, and D. Boness, Frequency dependence of elastic wave speeds at high temperature: a direct experimental demonstration, *Phys. Earth Planet. Inter., 148*, 85-96, 2005.

Kanamori, H. and D.L. Anderson, Importance of physical dispersion in surface wave and free oscillation problems: Review, *Rev. Geophys. Space Phys., 15*, 105-112, 1977.

Minster, B. and D.L. Anderson, A model of dislocation-controlled rheology for the mantle, *Phil. Trans. R. Soc. Lond., 299*, 319-356, 1981.

Romanowicz, B. and B. Mitchell, Deep Earth structure: Q of the Earth from crust to core. In: Schubert, G. (Ed.), *Treatise on Geophysics, 1*, Elsevier, 731-774, 2007.

21. Nonvolcanic tremor activity modified by the 2003 M6.5 San Simeon and 2004 M6.5 Parkfield, California earthquakes

Aurélie Guilhem and Robert M. Nadeau

21.1 Introduction

The discovery of nonvolcanic tremors in the region of Parkfield-Cholame, California, along the major San Andreas Fault in 2005 (*Nadeau and Dolenc*, 2005) has given a new perspective on these deep long-duration, high-frequency (1 to 15 Hz) events, which previously were only observed along subduction zones. The California tremors show many of the characteristics of the subduction zone events in terms of depth, frequency range, waveform, and the absence of apparent P- and S- waves. However they are shorter in duration, up to tens of minutes versus hours to days. The presence in the area of five seismic networks, including the High Resolution Seismic Network (HRSN), gives the opportunity to detect and locate the tremor activity over a large region, even for distances approaching 200 km between stations. We performed a multi-year tremor analysis between August 2001 and 2008 and we studied the influence of the 2003 M6.5 San Simeon and 2004 M6.0 Parkfield earthquakes, the largest events to occur in the study region and time period, on the Parkfield-Cholame tremor activity.

21.2 Tremor activity history

Using a similar cross-correlation detection method described by *Obara* (2002), we searched nearly 7 years of tremor activity starting in August 2001 and found more than 1,700 nonvolcanic tremors with a cumulative duration of more than 9,700 minutes (Figure 2.47). The locations of the tremors based on envelope cross-correlation and station pair time delay indicate that the events are mainly distributed across the San Andreas Fault over a 10-15 km wide area offset to the west of the fault, beneath Cholame, California (Figure 2.48).

The tremor catalog was compared to the catalog of M0+ earthquakes of the same 40-by-40 km region centered on the town of Cholame, California. Analysis of the spatio-temporal evolution of the tremors during the seven years of the study (Figure 2.47) revealed a strong correlation between tremor rates and occurrences of the two largest earthquakes of the region: the 2003 M6.5 San Simeon and 2004 M6.0 Parkfield earthquakes. Following the two mainshocks, the tremor activity increased in a step-like pattern, which was persistent over several months. We noticed a step change of a factor of ∼ 3 in the cumulative duration of tremor activity over 3 months before and after the San Simeon earthquake. Similar observations followed the Parkfield earthquake, when the cumulative duration of the events increased by a factor of ∼ 5 between 3 months before and 3 months after the mainshock. The tremor rate changes were not the consequence of the emergence of longer tremors but of a larger tremor frequency. On the other hand, no increase in the number of small earthquakes was observed above the tremors after San Simeon (70 km away from tremor zone). However, we noticed a very strong increase (34 times the background level) in the seismicity rate after Parkfield. The close proximity of the Parkfield earthquake rupture to the tremor region explains the large number of aftershocks following it (Figure 2.48).

Also, following the two events, an aftershock-like decay of the tremor activity was observed. Aftershock sequences are evidence of re-adjustements of the stress field in the seismogenic zone after a mainshock. The similar pattern in the tremor activity at Parkfield suggests that tremor activity is also related to stress change.

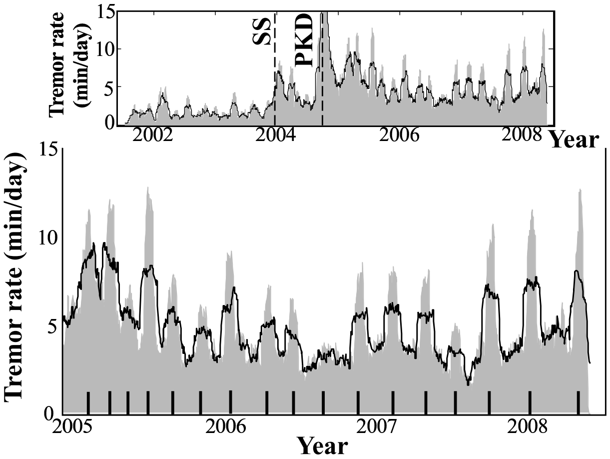

Figure 2.47: Tremor activity between August 2001 and May 2008. The gray filled areas show the tremor catalog smoothed over 20 days, and the black line shows the catalog smoothed over 40 days. The dashed lines (upper) indicate the time of the San Simeon (SS) and Parkfield (PKD) earthquakes. The tick marks (lower) show the episodes of tremors observed after Parkfield.

21.3 Tremors sensitive to small stress changes

We performed Coulomb stress changes maps (Figure 2.48) of the two strong earthquakes using the finite-source models computed by *Rolandone et al.* (2005) and *Kim and Dreger* (2008), respectively, to define the rupture zone. The Coulomb failure stress changes were calculated for vertical planes parallel to the San Andreas Fault (140° strike, 90° dip and 180° rake) at the median depth of the tremors (i.e. 20 km) and at seismogenic depth (i.e. 8 km) in two 10-by-10 km boxes centered on the tremor and earthquake locations. Following the 2003 San Simeon earthquake, the static Coulomb stress increased up to 12.5 kPa (0.125 bars) at 20 km depth and to 14.4 kPa (0.144 bars) at the earthquake depth. Typical stress changes inducing triggered earthquakes are on the order of 1 to 10 bars (*Stein*, 2004). The small stress changes observed following San Simeon at 8 km depth explained the absence of earthquake activation. However, changes in the tremor rate for less than 12.5 kPa stress increase suggest that tremors can be stimulated by significant low static stress changes. Following Parkfield, up to a 5-bar increase was transmitted into the earthquake zone, in agreement with the change recorded in the seismicity. At 20 km depth, the static stress changes were also higher after Parkfield than after San Simeon, with a maximum of 22.9 kPa (0.229 bars). Evidences of correlation between higher tremor rate and higher stress changes suggest that tremors are sensitive to stress variations at depth and that the degree of tremor activation is related to the level of stress change experienced.

21.4 Episodes of tremors

Since the Parkfield earthquake (from 2005 to present), the tremor activity has remained elevated relative to before the San Simeon earthquake (Figure 2.47). We have also noticed the emergence of quasi-periodic bursts of tremor activity starting after the end of the Parkfield aftertremor sequence in 2005. The episodes of tremors were not observed before the San Simeon earthquake or before the Parkfield earthquake. They consist of periods of higher frequency of the number of tremors and not of an increase in the duration (or amplitude) of individual tremors. The analysis of the episodes shows that the recurrence time between episodes is lengthening from ∼ 50 days in 2005 to ∼ 110 days in 2008, following a linear trend. The episodes of tremors may suggest very small stress variations in the deeper part of the crust generated after the Parkfield earthquake and possibly related to postseismic transients in depth.

21.5 Conclusions

The origin of the nonvolcanic tremors has yet to be determined; however several hypotheses have been proposed: fluid migration from subduction processes, shear coupling at depth, hydraulic fracturing, tidal stress variations, and small dynamic stress changes (less than 43 kPa) during the passage of teleseism surface waves. Our results suggest that tremors react to even smaller static stress change (less than 23 kPa) transmitted in their generating region. The degree of tremor activation also reflects the level of stress change at depth, and elevated activity persits well beyond the aftershock decay period following Parkfield.

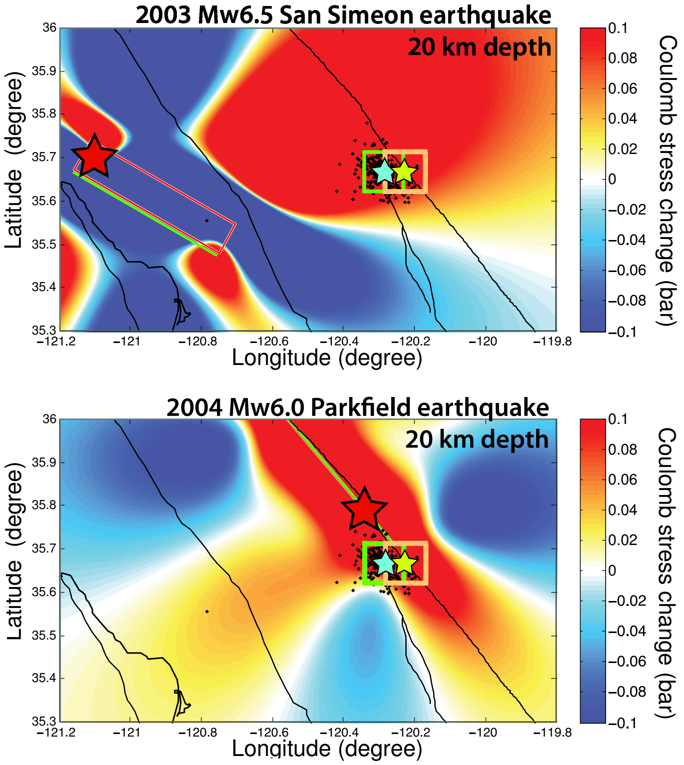

Figure 2.48: Coulomb stress maps for the San Simeon and Parkfield earthquakes at 20 km depth. The red star shows the mainshock location. The blue and yellow stars indicate the centroid of tremor and earthquake locations, respectively in their corresponding 10 km by 10 km boxes. The black dots show the tremor locations for 2006-2007.

21.6 References

Kim, A., and D. S. Dreger (2008), Rupture Process of the 2004 Parkfield Earthquake from Near-Fault Seismic Waveform and Geodetic Records, *J. Geophys. Res., 113*, B07308, doi:10.1029/2007JB005115.

Nadeau, R. M., and D. Dolenc (2005), Nonvolcanic Tremors Beneath the San Andreas Fault, *Science, 307*, 389.

Obara, K. (2002), Nonvolcanic Deep Tremor Associated with Subduction in Southwest Japan, *Science, 296*, 1,679-1,681.

Rolandone, F., D. Dreger, M. Murray, and R. Burgmann (2006),Coseismic Slip Distribution of the 2003 Mw6.6 San Simeon Earthquake, California, Determined from GPS Measurements and Seismic Waveform Data, *Geophys. Res. Lett., 33*, L16315.

Stein, R. S. (2004), Tidal Triggering Caught in the Act, *Science, 305*, 1,248-1,249.

22. Mapping the Rupture of the M_w 5.4 Alum Rock Earthquake

Margaret Hellweg, Angela Chung, Douglas Dreger, Ahyi Kim and Jack Boatwright (USGS Menlo Park)

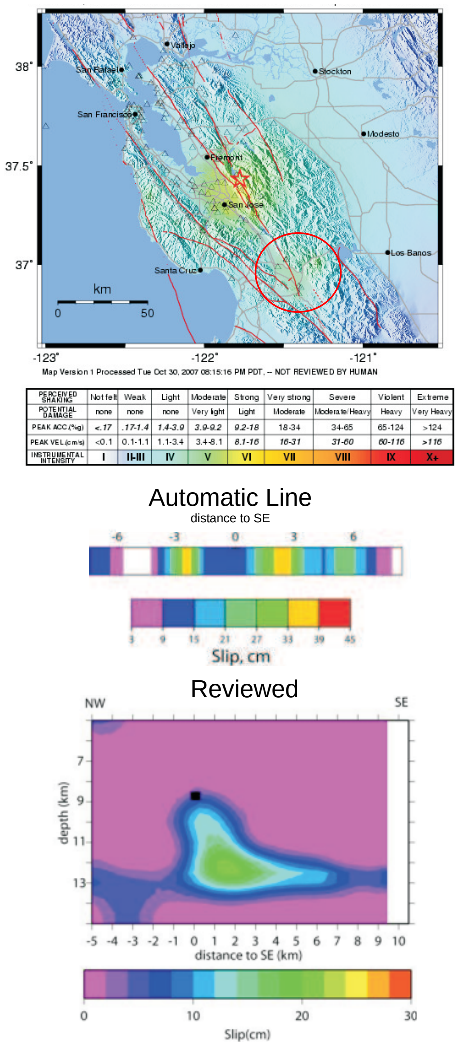

PERCEIVED SHAKING	Not felt	Weak	Light	Moderate	Strong	Very strong	Severe	Violent	Extreme
POTENTIAL DAMAGE	none	none	none	Very light	Light	Moderate	Moderate/Heavy	Heavy	Very Heavy
PEAK ACC.(%g)	<.17	.17-1.4	1.4-3.9	3.9-9.2	9.2-18	18-34	34-65	65-124	>124
PEAK VEL.(cm/s)	<0.1	0.1-1.1	1.1-3.4	3.4-8.1	8.1-16	16-31	31-60	60-116	>116
INSTRUMENTAL INTENSITY	I	II-III	IV	V	VI	VII	VIII	IX	X+

Figure 2.49: The Alum Rock earthquake occurred along the Calaveras Fault near San Jose. The ShakeMap (top) shows the epicenter and the levels of shaking experienced. Note the strong shaking (intensity VI) to the southeast of the epicenter (red circle). Both the finite fault line source and plane show rupture to the southeast from the epicenter (bottom).

22.1 Introduction

The largest earthquake since Loma Prieta shook the San Francisco Bay Area at 08:04 pm PDT on October 30, 2007 (03:04 UTC on October 31, 2007, Figure 2.49 (top)). It had M_w 5.4. Since the Loma Prieta earthquake, instrumentation in the region has improved, with many more digital stations, including short period, strong motion and broadband sensors. The Shakemap in Figure 2.49 (top) shows the epicenter (star), the level of shaking (colors) and the locations of stations which recorded the event (triangles). The automated finite-source solution (Figure 2.49 (upper part of bottom image)), based on the automated moment tensor, was available 9 minutes after the event. We present here finite fault results from the Alum Rock earthquake.

22.2 Moment Tensor Solution

The reviewed moment tensor solution (Figure 2.50) for the Alum Rock earthquake is 98 percent double couple, with strike, dip and rake of 323° , 87° and -180° . This motion is consistent with slip along the Calaveras Fault.

22.3 Finite Fault Solution

The automated finite-source line solution (Figure 2.49 (upper part of bottom image)) shows that slip was largely located southeast of the epicenter. Although the magnitude of this event is at the lower threshold for finite-source analysis given broadband waveforms and the simplified models used to compute Greens functions, the preliminary line-source as well as felt reports and peak ground motion maps indicate that the rupture had strong southeast directivity. One hour after the event, refined results in the plane source indicated that the fault ruptured southeast from the hypocenter.

Two line-source rupture models were produced by the automatic processing. For this event with small M_w 5.4, it was not possible to distinguish between the two conjugate line-source models. However, for the line-source parallel with the Calaveras fault (model shown in Figure 2.49 (upper part of bottom image)), most of the slip lies to the southeast of the epicenter.

We have prepared a finite-source inversion of the Alum Rock earthquake using the method of Dreger and Kaverina (2000). The model has a single fault plane and constant rake, rupture velocity, and rise time. The data and synthetics were bandpass filtered between 0.01 and 0.3 Hz. The lowpass filtering reduces the importance of high frequency arrivals and was performed because of concerns of the adequacy of the velocity model and Greens functions. Despite this restrictive filtering, southeast rupture is a dominant feature of the slip model (Figure 2.49, lower part of bottom image). Initially, the event ruptures downward and extends about 5 km to the southeast of the eipicenter. This extent of rupture is echoed in the locations of the aftershocks, which occurred exclusively to the southeast of the epicenter, and within 5 km. The

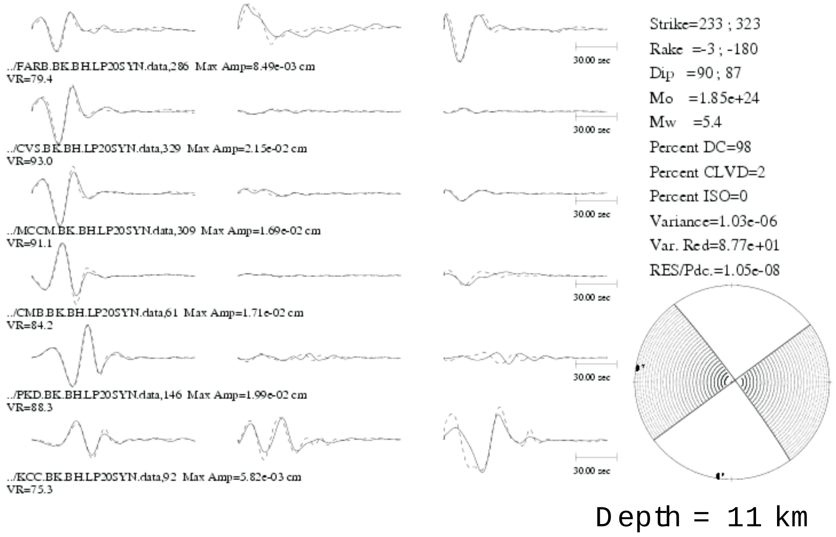

Figure 2.50: Moment tensor solution for the Alum Rock earthquake. The automatic solution used stations at short epicentral distances that were clipped or nonlinear. For this reviewed solution, the fits of the synthetics to the data are extremely good.

overall variance reduction is only 48 percent, and the vertical components, theoretically expected to be small given the focal mechanism, are not fit at all.

The details of the slip and the depth of the slip patch are not very well constrained, but are consistent with qualitative waveform analyses and with observed shaking (Figure 2.49 (top)). This model also argues for unilateral southeast rupture.

22.4 Perspectives

Future work is needed to more fully document the sensitivity of the finite-source model parameters. The peak slip in the model, assuming a rise time 0.3 seconds and rupture velocity of 80% of the shear wave velocity, is 17 cm. Like the moment tensor analysis, the finite source model produced an M_w 5.4.

22.5 Acknowledgements

Earthquake monitoring and reporting activities at the BSL are supported by the CISN funding of the California Governor's Office of Emergency Services under contract 6023-5 and the United States Geological Survey project 07HQAG0013.

22.6 References

Dreger, D. and A. Kaverina, Seismic remote sensing for the earthquake source process and near-source strong shaking: A case study of the October 16, 1999 Hector Mine earthquake, *Geophys. Res. Lett.*, *27*, 1941-1944, 2000.

23. Moment Tensors for Very Long Period Signals at Etna Volcano, Italy

Margaret Hellweg, Andrea Cannata (Universita Catania), Stefano Gresta (Universita Catania), Sean Ford, Guiseppi Di Grazia (INGV Sezione di Catania)

23.1 Introduction

Very long period signals (VLP, 10 s - 30 s) associated with long period events (0.5 Hz - 5 Hz) were observed at Etna Volcano, Italy, during June-November 2005 (Figure 2.51). They are only recorded at the broadband stations nearest to Etna's craters, ECPN, EBEL, EPDN and EPLC. These stations are part of the permanent seismic network run by the Catania Section of the Istituto Nazionale di Geofisica e Vulcanologia (INGV). Although the signal-to-noise (S/N) ratio for these VLPs is in general only poor to fair, they seem to recur, and can be classified into two families. We attempt to improve the S/N by stacking and to determine moment tensors for the VLP events.

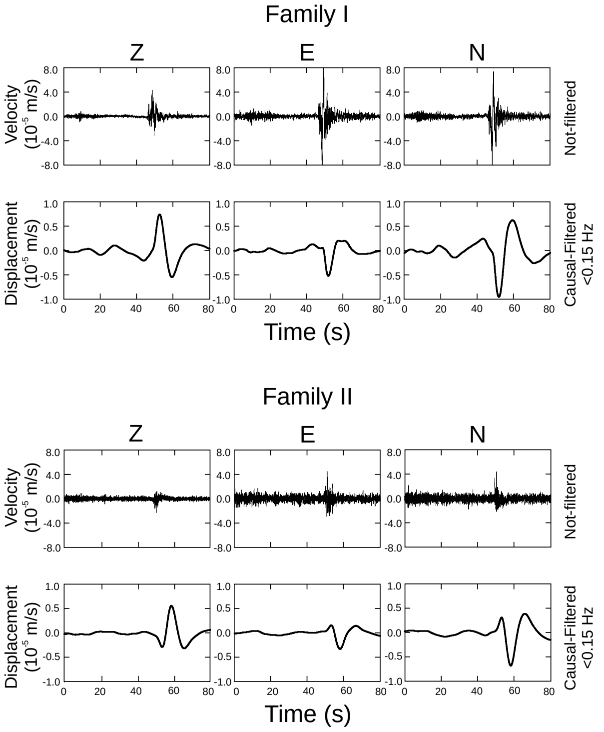

Figure 2.51: Example of long period (LP) associated very long period (VLP) events of Families I (top) and II (bottom). In each case, the upper rows show the broadband seismogram of the LP, while in the lower rows, the VLP signals are extracted by causal filtering.

23.2 Clustering and Stacking

The VLP events were clustered following *Green and Neuberg* (2006). For all events, (i) the vertical component of ECPN station (highest S/N) was lowpass filtered at 0.15 Hz to exclude the ocean microseisms; (ii) the correlation matrix was calculated for all events using 30 s of data; (iii) the cross correlation threshold was chosen to be 0.95 so that fairly dissimilar events would be classified as a single family, while members of one family would not be grouped with another; (iv) a master event was selected (the event with the most correlation values above the threshold); (v) the average family waveform was created as the stack of all events correlated with the master event; (vi) the stack waveform was then cross-correlated with the original seismic records, and all events with greater correlation than the threshold were grouped into a waveform family; (vii) the steps iv-vi were repeated until all events were classified into distinct groups; (viii) finally, a new correlation matrix was constructed with events sorted into families. In this procedure, no overlap was allowed between clusters; in fact, once an event was assigned to a group, it was removed from further correlation. We found that 85% of the events could be grouped into two main families of VLP events. Families I and II had 194 and 87 members, respectively.

For further analysis, we used stacked seismograms for the two VLP families from the four summit station. The stacks were created using signals filtered with a 4-pole, causal Butterworth bandpass filter (0.033 Hz - 0.167 Hz). Using waveforms from all stations from two members of the family (12 waveforms for each event), we tried different time lags between the two sets of signals. For each time lag value, we evaluated the similarity between the events by averaging the cross correlation coefficients calculated for each pair of corresponding waveforms (for example "ECPNz of event 1" and "ECPNz of event 2"). The time lag was chosen which gave the maximum average cross correlation coefficient and the signals for each component at each station were stacked. New events were compared with and then added to the stack event. Thus, all the events contributed to the stacked signals representing the two families (Figure 2.52). Although the stacking was performed on the Z, N and E components, we show the traces for Z, R and T with the optimum rotation determined using polarization analysis (*Plesinger et al.*, 1986). The S/N is clearly improved in the stacks, where several important characteristics are apparent. (1) For Family I , the first motion on the Z component is positive at all stations. (2) For Family II, the first motion on the Z component is negative at all stations. (3) For both families, the amplitudes on all components are considerably larger at ECPN and EPDN, the stations to the SW and NE of the active craters, than at EBEL and EPLC, which lie to the SE and NW.

23.3 Waveform Polarization

Note that there is little energy on the T-component at any of the stations (Figures 2.52 and 2.84). In addition, the vertical and radial components are "in phase", with both Z and R being negative or positive at the same time. This is generally an indication for P-waves. The directions of particle motion of Family I and Family II stacks are very similar, differing at each station by only a few degrees.

In the horizontal plane, the motion at ECPN and EPDN is polarized more or less toward the active craters. The motion at EPLC and EBEL is comparatively small and has both an element pointing toward the crater and a later segment of the motion oriented transversely. However, the S/N ratio at these two stations is poor.

In the vertical plane, both ECPN and EPDN (SW and NE of the craters, respectively) both point slightly downward toward the crater. On the plots of vertical motion, the particle motion diagrams are shown at the altitudes of the stations. Again, the motion for EBEL and EPLC are small, with a hint of "downward toward the crater".

23.4 Perspectives

The particle motion for these VLP signals is highly suggestive of either an initially opening (Family I) or initially closing (Family II) crack of fairly limited extent (little to no signal at EBEL and EPLC). There is a hint that the source is finite, as the directions of the horizontal particle motion change at ECPN and EPDN.

We have calculated Greens functions for full moment tensors using a simple half space velocity model. Initial inversions using *Minson and Dreger* (2008) indicate that a volume change explains a large portion of the waveforms. We will perform further analysis using a grid of sources to determine both the best source mechanism and its location.

23.5 References

Green, D., and J. Neuberg, Waveform classification of volcanic low-frequency earthquake swarms and its implication at Soufrire Hills Volcano, Monserrat, *J. Volcanol. Geotherm. Res.*, *153*, 51-63, 2006.

Minson, S. and D. Dreger, Stable Inversions for Complete Moment Tensors, In press *Geophys. Journ. Int.*, 2008.

Plesinger, A., M. Hellweg and D. Seidl, Interactive high-resolution polarization analysis of broad-band seismograms. *J. Geophysics*, *59*, 129-139, 1986.

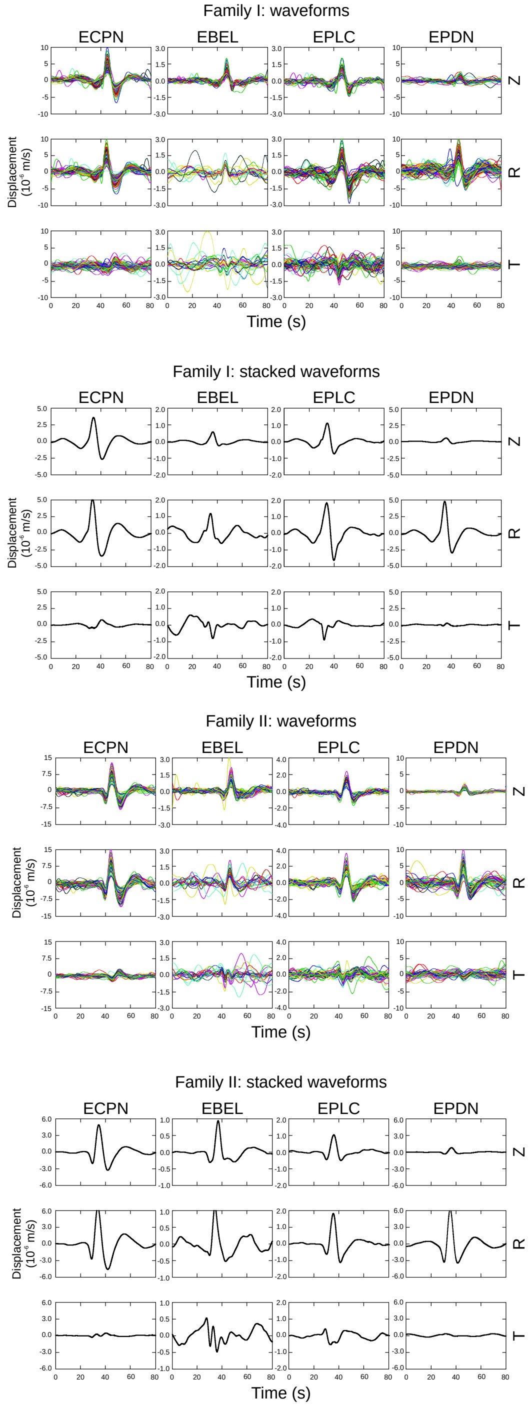

Figure 2.52: Stacked very long period (VLP) events of Family I (top) and Family II (bottom). The upper three traces show superimposed Z, R and T seismograms for all members at the 4 stations. Best azimuths were determined using polarization analysis. The lower traces show the stack seismograms.

24. Source Analysis of the February 24, 2008 M6 Wells, Nevada Earthquake

Douglas Dreger and Sean Ford

24.1 Introduction

On February 21, 2008 at 14:16:02 UTC, a M_w 6.0 earthquake occurred at 41.153 N, 114.867W, 10 km ENE of Wells, Nevada. This event caused significant damage in the historical section of the town. Unfortunately, there are no near-source strong motion recordings; however, at the time of the earthquake the EarthScope transportable array (TA) stations provided excellent records of the mainshock and aftershocks.

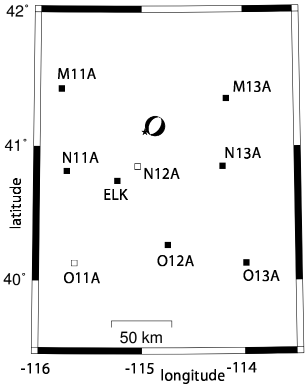

Figure 2.53: Locations of the transportable array and ANSS (ELK) stations. Solid symbols identify stations used in the finite-source inversion. Station N12A was omitted since it experienced a non-linear response, and O11A was omitted since ELK provided information from the same azimuth.

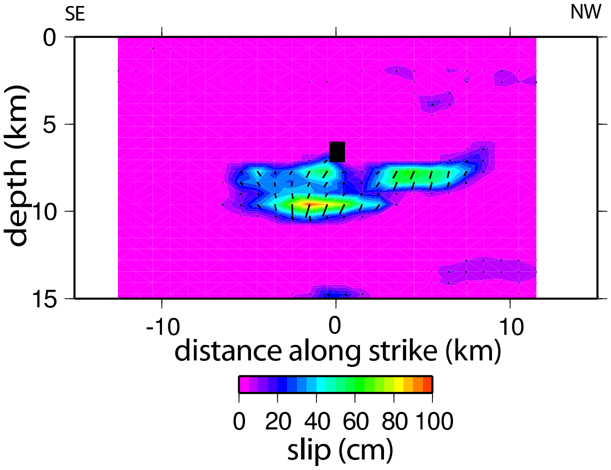

Figure 2.54: Slip model for SE-dipping fault plane. The color scale shows slip and the bars show the slip direction.

24.2 Seismic Moment Tensor

We determined a moment tensor solution using three-component, low frequency (0.02 to 0.05 Hz) displacement waves recorded by 47 stations of the NSF TA, and ANSS broadband seismic stations. Using the BSL seismic moment tensor code and the *Song et al.* (1996) velocity model, we obtained a normal faulting mechanism with the focal parameters strike=205, 35; rake=-96, -82; dip=40, 50. The source depth was constrained at 7 km as determined by the University of Nevada Reno Seismological Laboratory. The scalar seismic moment was determined to be $7.82x10^{24}$ dyne cm, corresponding to a M_w 5.9. The normal mechanism is consistent with the trend of basin and range faulting in the region; however, there is some question about whether west-dipping or east-dipping faults are active in the region.

24.3 Finite-Source Model

To determine the finite-source parameters we have inverted the three-component, broadband (f $>$ 0.02 Hz) displacement waveform data recorded at the 7 closest, on-scale, US and TA network stations (Figure 2.53) using the method of *Kaverina et al* (2002). We tested both nodal planes of the moment tensor double-couple solution over a range of rupture velocities, and found that the east-dipping nodal plane consistently provided the best fit to the data. Although the maximum in the goodness of fit parameter (variance reduction) is relatively broad, the best rupture velocity was found to be 2.8 km/s, or 78% of the shear wave velocity at the hypocenter depth. These initial inversions considered a constant rake (slip angle) obtained from the double-couple solution. We also performed an inversion allowing the rake to vary over the rupture plane, which resulted in a slightly more compact slip distribution. As Figure 2.54 shows the rupture is bilateral and slightly down-dip, but the largest slip is located to the southwest of the hypocenter in the direction of the town of Wells, Nevada. The slip in the variable rake model shows some variation but is predominantly normal, with the east-block down relative to the west-block. The peak slip in this model is 85 cm, with an average of 13 cm. The scalar seismic moment obtained by integrating the fault slip is $1.09x10^{25}$ dyne cm, corresponding to M_w 6.0. A rise time of 0.3 seconds was assumed. As Figure 2.55 shows, the fit to the regional data is very good.

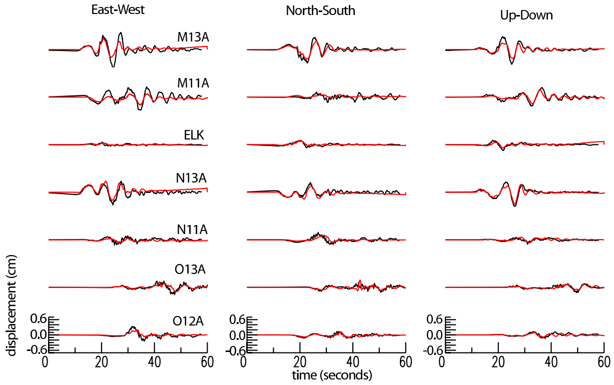

Figure 2.55: Observed three-component displacement records (black) are compared to synthetics (red). The data and synthetics are broadband with no filtering other than the polezero instrument response removal for the data.

24.4 ShakeMap

There are no strong motion stations located within 200 km of the Wells, NV earthquake, and, therefore, the ShakeMap (*Wald et al.*, 1999a) is based solely on empirical ground motion relations and scaling from reported Community Internet Intensity Map values (*Wald et al.*, 1999b). Using the slip distribution in Figure 2.54, and assuming a NEHRP class C site (555 m/s), we have simulated the near-fault strong shaking to produce a ShakeMap using the method proposed by *Dreger and Kaverin* (2000), and as discussed in *Dreger et al.*(2005) and *Rolandone et al.* (2006). Figure 2.56 compares the simulated peak ground velocity (shaded map) with the USGS ShakeMap (contours) and PGV at the regional TA stations. The simulated values are consistent with the observations, whereas the USGS ShakeMap over predicts values by more than a factor of 10. In Wells, NV we simulate a PGV of 10 cm/s, which is large enough to account for the considerable damage to the historic, unmaintained, unreinforced masonry buildings. The simulated sense of motion in Wells is down and to the east, which is consistent with reported westward chimney toppling, and sliding of heavy objects. This event occurred in a poorly instrumented region and demonstrates the difficulty in obtaining a ShakeMap under such conditions. This analysis shows, as in *Dreger and Kaverina* (2000), that in such poorly instrumented regions a regional data derived finite-source model from regional waveform modeling can be used to accurately simulate near-fault strong ground motions when no such recordings exist.

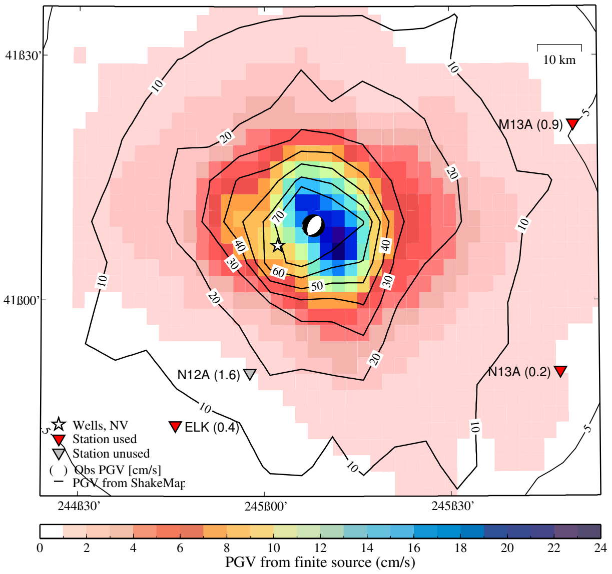

Figure 2.56: Simulated PGV (color shading) is compared to the USGS ShakeMap (contours) and PGV from TA stations (numbers in parenthases). There is good correlation between the finite-source simulated PGV and observations; however, the USGS ShakeMap shows values an order of magnitude larger. There were no near-fault strong motion data available for use in the USGS ShakeMap.

24.5 References

Dreger, D., and A. Kaverina, Seismic remote sensing for the earthquake source process and near-source strong shaking: A case study of the October 16, 1999 Hector Mine earthquake, *Geophys. Res. Lett., 27*, 1941-1944, 2000.

Dreger, D. S., L. Gee, P. Lombard, M. H. Murray, and B. Romanowicz, Rapid finite-source analysis and near-fault strong ground motions: Application to the 2003 M_w 6.5 San Simeon and 2004 M_w 6.0 Parkfield earthquakes, *Seism. Res. Lett., 76(1)*, 40-48, 2005.

Kaverina, A., D. Dreger, and E. Price, The combined inversion of seismic and geodetic data for the source process of the 16 October 1999 M_w 7.1 Hector Mine, California, Earthquake, *Bull. Seism. Soc. Am., 92(4)*, 1266-1280, 2002.

Rolandone, F., D. Dreger, M. Murray, and R. Bürgmann, Coseismic slip distribution of the 2003 M_w 6.6 San Simeon earthquake, California, determined from GPS measurements and seismic waveform data, *Geophys. Res. Lett., 33, L16315*, doi:10.1029/2006GL027079, 2006.

Song, X. J., D. V. Helmberger and L. Zhao, Broadband modelling of regional seismograms; the basin and range crustal structure, *Geophys. J. Int., 125(1)*, 15-29, 1996

Wald, D. J., V. Quitoriano, T. H. Heaton, H. Kanamori, C. W. Scrivner, and C. B. Worden, TriNet ShakeMaps: Rapid Generation of Instrumental Ground Motion and Intensity Maps for Earthquakes in Southern California, *Earthquake Spectra, 15*, 537-556, 1999a.

Wald, D. J. V. Quitoriano, L. A. Dengler, and J. W. Dewey, Utilization of the Internet for Rapid Community Intensity Maps, *Seismological Research Letters, 70(6)*, 680-697, 1999b.

25. Triggering effect of M>4 earthquakes on the observed occurrence of repeating events at Parkfield

Kate Huihsuan Chen, Roland Bürgmann, and Robert M. Nadeau

25.1 Introduction

A characteristic repeating earthquake sequence (RES) is defined as a group of events with nearly identical waveforms, locations, and magnitudes and thus represents a repeated rupture of the same patch of fault. The recurrence intervals of repeating earthquake ruptures are found to be highly variable, where the irregular recurrence of observed repeating events may reflect a response to nearby earthquakes, change in the strain rate, time-dependent or spatial variation in the frictional strength of the fault, or other effects such as fluid pressure variations (e.g., *Lay and Kanamori*, 1980; *Sleep and Blanpied*, 1994; *Vidale et al.*, 1994; *Nadeau et al.*, 1994; *Ellsworth*, 1995). The questions of interest regarding the recurrence properties of natural earthquake sequences are: How do the RESs respond to stress perturbation associated with larger earthquakes and to what range (both in space and time) are the triggering effects effective? To answer these questions, we need a statistically sufficient observational documentation of recurrence properties in natural earthquake populations.

25.2 Data and results

The detailed record of micro-earthquake data from the borehole High Resolution Seismic Network (HRSN) sites at Parkfield provides a unique opportunity to examine how larger events act on the observed occurrence of the repeating events. With the high level of detection of micro-earthquakes, the HRSN has revealed a larger number of repeating earthquakes ranging in magnitude from -0.4 to +1.7 (*Nadeau et al.*, 1995; *Nadeau and McEvilly*, 1997). During the period 1987-1998, 187 repeating sequences were identified, with a total of 1123 events. Using these data, we seek to illustrate how the larger earthquakes influence RESs' timing. We are interested in any potential variation of recurrence interval associated with the time of major events. The analysis has the following recurrence elements (Figure 2.57a): (1) "dt+": the time difference between a major earthquake and the recurrence of a repeating event subsequent to the major event; (2) "dt-": the time difference between a major earthquake and the repeating event prior to the major event; (3) "Tr-post": the duration of the first full recurrence interval following the major event; and (4) "Tr-cos": the recurrence interval spanning the major event, that is, the sum of dt- and dt+. These elements are later divided by the average recurrence interval of a given RES ($\tilde{\mathrm{Tr}}$). The percentage of normalized interval estimates at a distance of less and greater than 5 km from the major events are shown in Figure 2.57b. Extremely short times between the main event and subsequent RES events ($\mathrm{dt+}/\tilde{\mathrm{Tr}} < 0.1$) reflect triggering by the major events. In Figure 2.57b, the peak at $\mathrm{dt+}/\tilde{\mathrm{Tr}} < 0.1$) only appears in the near-field (e.g., in the plot for distances less than 5 km from the major event). This may suggest triggering by static stress as a cause of the short recurrence intervals immediately after the larger event.

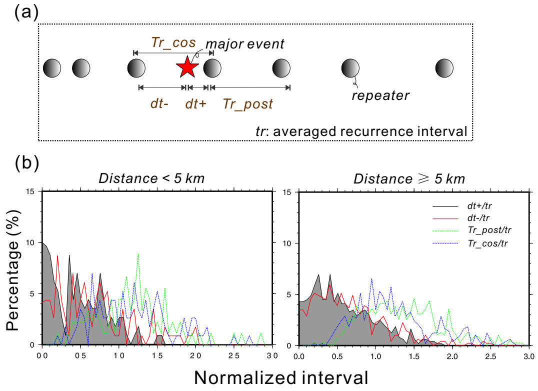

Figure 2.57: (a) Illustration of the four recurrence elements in time window. Star is the time of major event. Circles are the repeating events in a RES. (b) Percentage of normalized interval measurements (recurrence element divided by average recurrence interval) at a distance of less (left panel) and greater (right panel) than 5 km from M 4 hypocenters.

To further explore the region (both in space and time) where interaction between RESs and larger events is most evident, we have selected the 1993 M 4.5 earthquake, with a large number of RESs in the vicinity, for the following analysis. In Figure 2.58a the event chronologies of the RESs adjacent to the 1993 event reveal coherently reduced recurrence times over years (1993 to 1998) following the M>4 event. To quantify the enduring acceleration of recurrence, we determine the ratio of averaged post-1993 to pre-1993 recurrence intervals as a function of distance from the 1993 M 4.5 hypocenter in Figure 2.58b. Within a distance of 5 km from the M 4.5 event, most of the RESs (84%) have shorter post-1993 recurrence intervals compared to the pre-1993 intervals. We find that the enduring recurrence acceleration, defined by 'post-1993-Tr/pre-1993-Tr' of less than 1 in Figure 2.58b, can be documented 5 km from the major event.

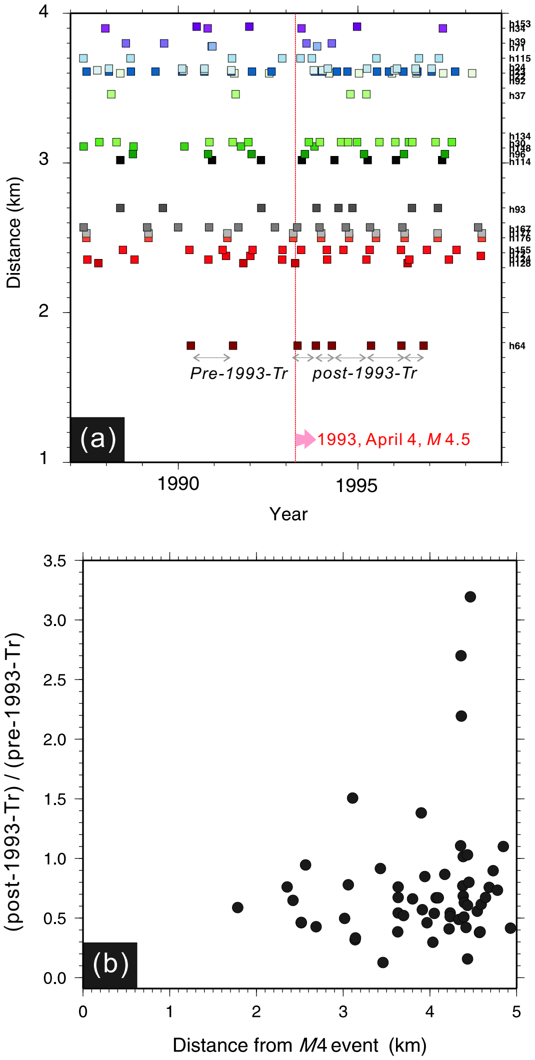

Figure 2.58: (a) Event chronologies of RESs as a function of distance from the 1993 M 4.5 hypocenter. Note that the distance is confined to be less than 4 km due to abundant RESs beyond 4 km. Red and blue arrows indicate the post-1993 and pre-1993 recurrence interval, respectively. (b) Ratio of the averaged post-1993 recurrence intervals and the average values of the pre-1993 recurrence intervals as a function of distance from 1993 M 4.5 event.

25.3 Discussion

The triggering effect of moderate events (M 4∼5) is observable in the temporal variation of recurrences from repeating earthquake data as shown by the unusually short dt+/tr in Figure 2.57b. The immediate acceleration of recurrence following the M 4∼5 events is only found to occur in the near field, which is possibly explained by static stress triggering. Different from the decaying recurrence rate that reflects afterslip following a large event, many of the Parkfield RESs exhibit a steady, accelerated recurrence since 1993. We argue that the long-lasting, reduced recurrence interval is not likely explained by the afterslip process. This acceleration may be part of a more broadly distributed increase in creep rates along this fault segment that is associated with a remarkable aseismic transient following several M > 4 events during the early 1990s (*Nadeau and McEvilly*, 1999; *Niu et al.*, 2003; *Murray and Segall*, 2005).

25.4 References

Ellsworth, W. L. (1995), Characteristic earthquakes and long-term earthquake forecasts; implications of central California seismicity, in Urban Disaster Mitigation: the Role of Science and Technology, Eds. Cheng, F.Y., and M.S. Sheu, *Elsevier Science Ltd.* 1-14.

Lay, T. and Kanamori, H. (1980), Earthquake doublets in the Solomon Islands, *Phys. Earth and Planet. Inter.*, 21, 283-304.

Murray, J., and P. Segall (2005), Spatiotemporal evolution of a transient slip event on the San Andreas fault near Parkfield, California, *J. Geophys. Res.*, 110, doi:10.1029/2005JB003651.

Sleep, N. H., and M. L. Blanpied (1994), Ductile creep and compaction: a mechanism for transiently increasing fluid pressure in mostly sealed fault zones. *Pure App. Geophys.*, v. 143, pp. 9-40.

Vidale, J. E., W. L. Ellsworth, A. Cole, and C. Marone (1994), Variations in rupture process with recurrence interval in a repeated small earthquake, *Nature*, 368, 624-626.

Nadeau, R., M. Antolik, P. A. Johnson, W. Foxall, and T. V. McEvilly (1994), Seismological studies at Parkfield III: Microearthquake clusters in the study of fault-zone dynamics, *Bull. Seismol. Soc. Am.*, 84, 247-263.

Nadeau, R. M., W. Foxall, and T. V. McEvilly (1995), Clustering and periodic recurrence of microeartqhuakes on the San Andreas fault at Parkfield, California, *Science*, 267, 503-507.

Nadeau, R. M. and T. V. McEvilly (1997), Seismological studies at Parkfield V: Characteristic microearthquake sequences as fault-zone drilling targets, *Bull. Seism. Soc. Am.*, 87, 1463-1472.

Nadeau, R. M. and T. V. McEvilly (1999), Fault slip rates at depth from recurrence intervals of repeating microearthquakes, *Science*, 285, 718-721.

Niu, F., P. G. Silver, R .M. Nadeau, T. V. McEvilly (2003), Stress-induced migration of seismic scatterers associated with the 1993 Parkfield aseismic transient event, *Nature*, 426, 544-548.

26. Realtime Test of the ElarmS Earthquake Early Warning Methodology

Richard M Allen, Holly Brown, Margaret Hellweg, Alexei Kireev, Douglas Neuhauser

26.1 Introduction

Modern seismic networks and telemetry systems make it possible to rapidly detect the beginnings of earthquakes. Combining these technical capabilities with recently developed methodologies to estimate earthquake magnitude using just a few seconds of P-wave data (e.g. *Allen and Kanamori,* 2003) makes it possible to provide a few seconds warning prior to damaging ground shaking. ElarmS is the methodology under development and testing at the Berkeley Seismological Laboratory. It is designed to provide earthquake early warnings by compiling data from multiple seismic stations, and updating those warnings every second as additional data becomes available (*Wurman et al.*, 2007).

26.2 Realtime state-wide testing

The Berkeley Seismological Laboratory is a partner in the state-wide effort to test algorithms for the purpose of earthquake early warning. This is an effort by CISN partners (UC Berkeley, Caltech, USC/SCEC, USGS and ETH Zurich) and funded by the USGS. The goal of the project is to implement early warning algorithms within the realtime processing system of the CISN to evaluate algorithm performance in terms of warning accuracy and timeliness.

The ElarmS algorithms have now been ported to continuous realtime processing in California. The system, referred to as ElarmS-RT, provides automated detection, location, magnitude estimation, and ground shaking prediction. As with the previous non-realtime implementations of ElarmS, the output can be displayed as an "AlertMap" which maps the predicted peak ground motion starting one second after the first seismic station to trigger and updates every second. In addition to these early warning products, ElarmS-RT also provides very rapid post-event information. One such product is the ElarmS-ShakeMap. It is available immediately after peak ground shaking has been observed within 100 km of the epicenter (the usual frame size of a ShakeMap) and is the same as the CISN ShakeMap except that the ElarmS magnitude estimate is used and the map is therefore available more rapidly.

26.3 Earthquake detections

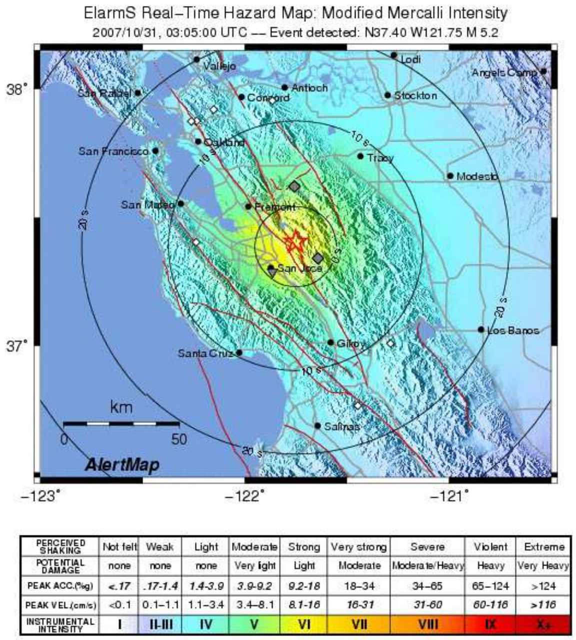

PERCEIVED SHAKING	Not felt	Weak	Light	Moderate	Strong	Very strong	Severe	Violent	Extreme
POTENTIAL DAMAGE	none	none	none	Very light	Light	Moderate	Moderate/Heavy	Heavy	Very Heavy
PEAK ACC.(%g)	<.17	.17-1.4	1.4-3.9	3.9-9.2	9.2-18	18–34	34–65	65–124	>124
PEAK VEL.(cm/s)	<0.1	0.1–1.1	1.1–3.4	3.4–8.1	8.1-16	16-31	31-60	60-116	>116
INSTRUMENTAL INTENSITY	I	II-III	IV	V	VI	VII	VIII	IX	X+

Figure 2.59: AlertMap: Ground motion prediction generated by ElarmS-RT using the data available 1 sec after the Alum Rock earthquake was detected.

ElarmS-RT was operational at the time of the October 30th, 2007, M_w 5.4 Alum Rock earthquake near San Jose, the largest earthquake to strike the San Francisco Bay Area since the 1989 Loma Prieta earthquake. The system first detected the earthquake when two seismic stations triggered simultaneously in the epicentral region. One second later, the first magnitude estimate of 5.2 was available and the first AlertMap (Figure 2.59) was calculated. The error in the MMI predictions at this time was 0.1 ± 0.6 (in MMI units). These are small errors, as can be seen by comparing Figure 2.59 with Figure 2.60 which shows the ElarmS-ShakeMap for the event. As time proceeded, additional data was incorporated and the errors in the ground motion prediction decreased further.

ElarmS-RT currently processes data 15 sec behind realtime. The current telemetry system in Northern California provides most data with 5 to 10 sec delay. By waiting 15 sec ∼90% of seismic stations have reported before a particular time increment is processed. Even with this 15 sec delay, ElarmS-RT computers had assessed the hazard posed by the Alum Rock earthquake before ground shaking was felt in San Francisco.

The ElarmS-ShakeMap is generated using the data

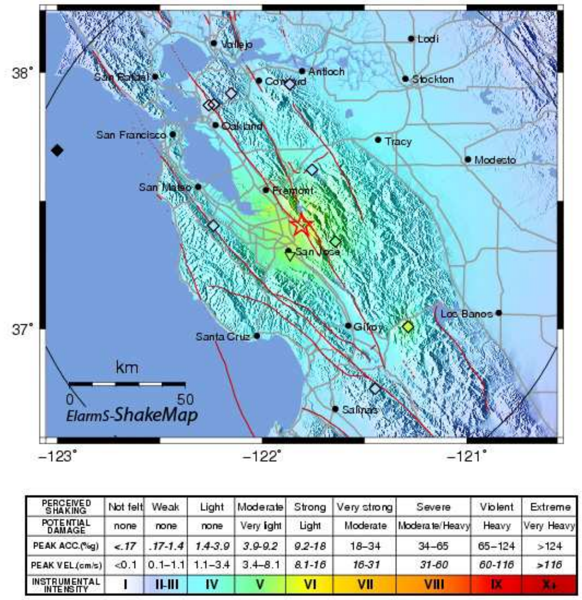

PERCEIVED SHAKING	Not felt	Weak	Light	Moderate	Strong	Very strong	Severe	Violent	Extreme
POTENTIAL DAMAGE	none	none	none	Very light	Light	Moderate	Moderate/Heavy	Heavy	Very Heavy
PEAK ACC.(%g)	<.17	.17-1.4	1.4-3.9	3.9-9.2	9.2-18	18–34	34–65	65–124	>124
PEAK VEL.(cm/s)	<0.1	0.1–1.1	1.1–3.4	3.4–8.1	8.1-16	16-31	31-60	60-116	>116
INSTRUMENTAL INTENSITY	I	II-III	IV	V	VI	VII	VIII	IX	X+

Figure 2.60: ElarmS-ShakeMap using observations of peak ground motion and ElarmS magnitude for the Alum Rock earthquake and typically available within 1.5 minutes. This is nearly identical to the CISN-ShakeMap.

available 30 sec after the origin time of all detected earthquakes. This time interval allows peak ground shaking to be observed within ∼100 km of the event. The ElarmS-ShakeMaps are usually available within 1.5 minutes of the origin time. The ElarmS-ShakeMap for the Alum Rock earthquake is shown in Figure 2.60 and is nearly identical to the CISN ShakeMap. CISN ShakeMaps are typically available in 7 to 10 minutes.

26.4 Conclusions

The Alum Rock earthquake was a successful illustration of ElarmS-RT performance. While the realtime testing of early warning in California has only just begun, some of the requirements for a fully implemented system are becoming clear. ElarmS performs well for all events M > 3 in the greater Bay Area where instrumentation is dense and typical station spacing is ∼20 km. To the north and south of the Bay Area along the San Andreas Fault System, instrument density drops and typical stations spacing is ∼100 km. In these regions, the system works, but is slower, as it takes longer for the radiating seismic waves to be sampled. East of the Mendocino Triple Junction, in the Sierras, and in the Central Valley of Northern California, current instrumentation is not sufficient for ElarmS operation.

26.5 Acknowledgements

Support for this project is provided by the USGS NEHRP program (06HQAG0147).

26.6 References

Allen, R. M., and H. Kanamori, The potential for earthquake early warning in southern California, *Science, 300,* 786-789, 2003.

Wurman, G., R. M. Allen, and P. Lombard, Toward earthquake early warning in northern California, *J. Geophys. Res., 112* (B08311), 2007.

27. Testing the ElarmS Methodology on Japanese Earthquakes

Holly Brown and Richard Allen

27.1 Introduction

Earthquake early warning systems are algorithms designed to detect the initial P-waves from an earthquake, rapidly estimate the magnitude of the event, and predict subsequent ground shaking in the surrounding regions. Earthquake Alarm Systems, or ElarmS, is one early warning algorithm that uses a network of seismic stations to hone in on the size and location of the earthquake. Averaging the magnitude estimates from multiple stations improves the accuracy of the estimate. ElarmS has been tested on multiple Northern and Southern California datasets, and now automatically processes streaming seismic data across California. In order to improve the robustness of the methodology, we test it on a dataset of large-magnitude events from Japan's Kyoshin Net (K-NET) strong-motion seismic network.

27.2 Dataset

K-NET consists of 1,000 digital strong-motion seismometers spaced at approximately 25km intervals throughout Japan. Each station is capable of recording acceleration up to 2000 cm/s^2. Our K-NET dataset contains 84 earthquakes occurring within 100km of K-Net stations between September 1996 and June 2008 (Figure 2.61). The local magnitudes range from 4.0 to 8.0, the largest being the 26 September 2003 Tokachi-Oki event. Forty-three of the events are of magnitude 6.0 or greater.

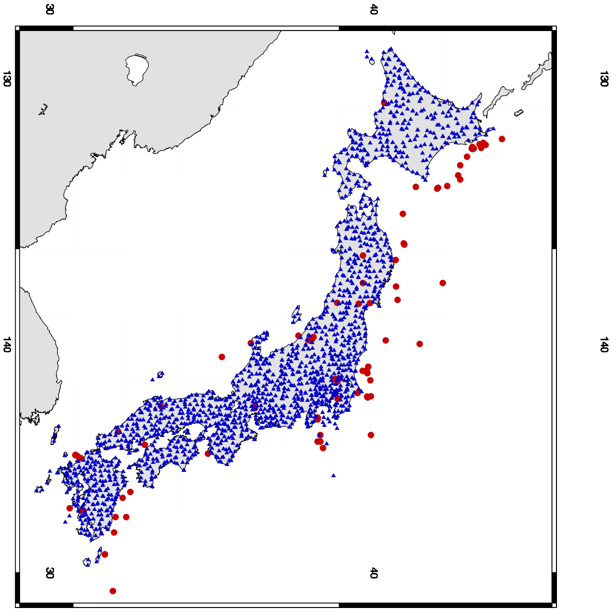

Figure 2.61: Map of events and K-NET stations: Large circles are events used in this study. Small triangles are K-NET stations.

27.3 Method

ElarmS estimates magnitude from the frequency content and peak displacement of the first several seconds of the P-wave arrival at each station. *Allen and Kanamori* (2003) and *Olson and Allen* (2005) documented an empirical relationship between the magnitude and the maximum frequency parameter τ_p^{max} of the P-wave. *Wurman et al* (2007) further showed a relationship between magnitude and peak displacement, P_d, in the initial seconds of the P-wave arrival. ElarmS utilizes both relationships to calculate two magnitude estimates, which it then averages together to improve accuracy in the final event estimate. As more stations report P-wave arrivals, ElarmS incorporates their τ_p^{max} and P_d measurements into the average for an overall estimate of event magnitude.

ElarmS in California assumes a fixed depth of 8km and estimates the epicentral distance with a two-dimensional grid search. In the Japanese subduction zone this is inappropriate. For the Japanese dataset we create a three-dimensional grid and calculate the IASP91 P-S travel time for seismic waves originating at each point of the grid. We then compare the calculated travel times to the observed P-S travel times at each station to find the best estimate of hypocentral location. Data is used only from stations within 100km of the hypocenter.

27.4 Results

We use a least-squares fit to calculate a local relationship between magnitude and τ_p^{max} of log10(τ_p^{max}) = -1.22 + 0.21*M, compared to log10(τ_p^{max}) = -0.78 + 0.15*M for Northern California (*Wurman et al*, 2007) (Figure 2.62*a*). The observed τ_p^{max} values from Japan are similar to those of Northern California, with a slightly steeper slope for Japan.

We also use a least squares fit to calculate a local relationship between magnitude and peak displacement of log10(P_d) = -4.02 + 0.66*M, corrected for epicentral distance, compared to log10(P_d) = -3.77 + 0.73*M for California (*Wurman et al*, 2007) (Figure 2.62*b*). The P_d relations have comparable slopes for Japan and Northern California, but Japan displays lower observed P_d values, implying greater attenuation in the region.

We further consider the effect of different quantities of data by limiting the number of stations used for magni-

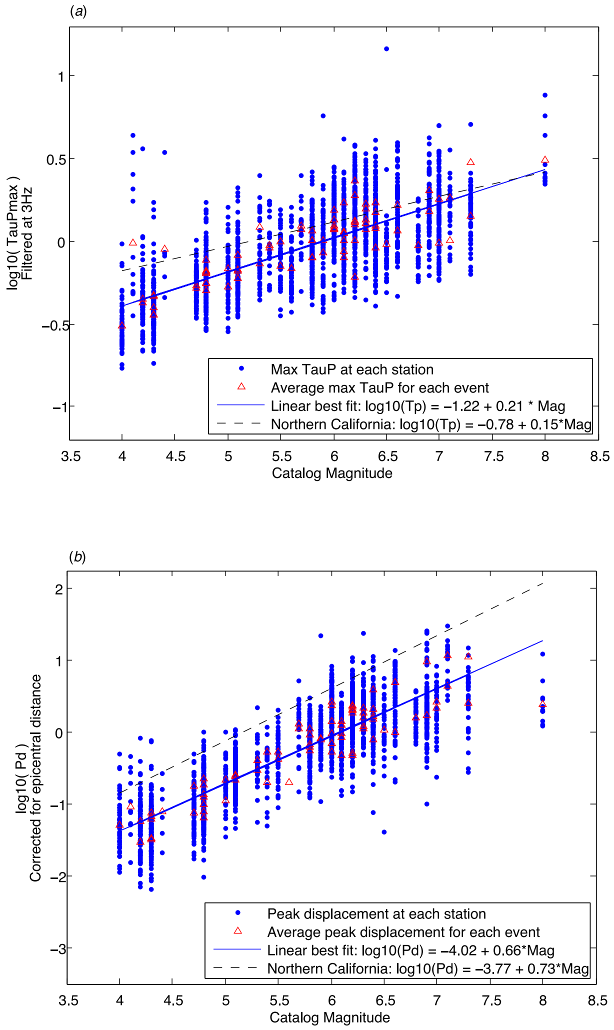

Figure 2.62: Observations from first 4 seconds of P-wave arrival at each station. (*a*)Observed $\log(\tau_p^{max})$ versus Catalog Magnitude. τ_p^{max} is peak frequency filtered at 3Hz. (*b*)Observed $\log(P_d)$ versus Catalog Magnitude. P_d is peak displacement corrected for epicentral distance.

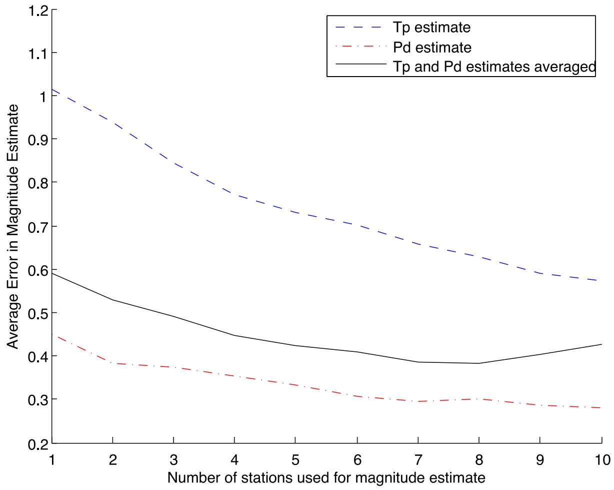

Figure 2.63: Magnitude error by number of stations

tude estimates. Figure 2.63 shows the average error in the ElarmS estimated magnitude using only the single closest station to the epicenter, the two closest stations, three closest, etc. The dashed lines show the error in the magnitude estimate using only τ_p^{max} or P_d. The solid line is the error using both τ_p^{max} and P_d.

The combined τ_p^{max} and P_d estimate has an average error of less than 0.6 magnitude units using only one station for each event, and that error drops lower with the addition of more stations. P_d by itself produces an average error of less than 0.5 magnitude units for all numbers of stations. τ_p^{max} by itself produces an error that is higher than that of P_d, but still less than one magnitude unit when using more than one station. Previous studies have shown that the ElarmS magnitude estimates are more robust for large events when τ_p^{max} and P_d estimates are combined (*Wurman et al*, 2007), although we have not yet verified this for the Japanese dataset.

27.5 Conclusion

The scaling relations between τ_p^{max} and magnitude and between P_d and magnitude are clearly evident for this Japanese dataset. This is a particularly valuable result given the large number of large (M>6) earthquakes, implying that the ElarmS methodology remains robust and useful for large magnitude events. The hypocentral depth algorithm we added for this study extends ElarmS' range of geologic settings to subduction zones, in addition to the strike-slip faults of California.

27.6 Acknowledgements

Support for this project is provided by the USGS NEHRP program (06HQAG0147).

27.7 References

Allen, R.M., and H. Kanamori, The potential for earthquake early warning in southern California, *Science, 300*, 786-789, 2003.

Olson, E.L., and R.M. Allen, The deterministic nature of earthquake rupture, *Nature, 438*, 212-215, 2005.

Wurman, G., R.M. Allen and P. Lombard, Toward earthquake early warning in northern California, *J. Geophys. Res., 112* (B08311), 2007.

28. Detection of Low-Frequency Earthquakes in the non-volcanic tremor beneath the San Andreas Fault: a prospective tool for investigating deep fault dynamics?

Andrea Cannata (University of Catania), Margaret Hellweg, Robert M. Nadeau, Stefano Gresta (University of Catania)

28.1 Introduction

Non-volcanic tremor (NVT) has been observed in Cascadia, in southwest Japan and along the San Andreas Fault (*Schwartz and Rokosky*, 2007). In southwest Japan, the NVT is accompanied by relatively energetic and isolated pulses that have been identified as low-frequency earthquakes (LFEs; *Shelly et al.*, 2006). Compared with nearby ordinary earthquakes with similar amplitudes, LFEs are enriched in low frequencies (1-5 Hz). These events occur almost exclusively as part of an extended tremor signal (*Shelly et al.*, 2006). The analysis of such events allows the source of tremor to be tracked with good resolution in time and space, providing the capability of monitoring slow slip with good precision as it migrates along the subduction zone (*Shelly et al.*, 2007). Episodes of NVT along the San Andreas Fault (*Nadeau and Dolenc*, 2005) occur less often, are shorter and release less energy than those in the subduction zones. The aim of this work is to develop a detection procedure for LFEs in the NVT recorded along the San Andreas Fault in 2006-2007. In fact, the study of these events could contribute to significantly improving our knowledge of the deep dynamics of the San Andreas fault.

28.2 Data and Detection Methods

In this work the seismic signals recorded by the High-Resolution Seismic Network (HRSN; Figure 2.64a; see Chapter 3, Section 4.) were used. The analysis was applied to seismic signals from 48 NVT tremor episodes. Data windows start about 10 minutes before the beginning of the NVT and stop about 10 minutes after they end, giving a total of approximately about 30 hours.

To verify that the channels work and to highlight the frequency band characterised by the highest energy during the NVT episodes, the seismic signal was analysed using a Fast Fourier Transform (FFT). The tremor time series was divided into windows about 16 s long. The spectrum was calculated for each window (overlapping by 8 s) with a frequency resolution of 0.06 Hz. Then, the time development of the spectrum and its average were calculated for each tremor episode. Amplitudes were highest in the frequency band from 2 to 8 Hz, if signals below 2 Hz are excluded, where the signal to noise ratio is low and the sensor response drops off. Based on this result we decided to analyse this frequency band.

The detection method is divided into two steps, trigger detection and trigger selection.

Trigger detection

Trigger detection was based on three STA/LTA algorithms (short time average over long time average), each of which evaluates the ratio between short- and long-term energy density (squared data to facilitate combining multi-channel data in a Pythagorean sense) to find amplitude transients (*Withers et al.*, 1998). The first, the standard STA/LTA, was applied to three narrow frequency bands 2-4, 4-6 and 6-8 Hz, producing three lists of triggers. Because the optimal lengths of the windows depend on the frequency content of the seismic signal, the lengths of the short and long windows were chosen to be 3 and 27 times the center period of the frequency band analysed, respectively. Moreover, in this first method the data window is rectangular. In the second algorithm, the adaptive standard STA/LTA, the entire 2-8 Hz band was analysed. As an estimator of the dominant peak frequency, needed to adaptively calculate the length of the short and long windows, the moving average of the instantaneous frequency over 1.5 s was used, and the data window was also rectangular. Finally, in the third algorithm, the adaptive recursive STA/LTA, the data were windowed using a decaying exponential. The frequency band analysed was 2-8 Hz and the window lengths were calculated adaptively, as in the second algorithm.

Using these three algorithms we obtained 5 lists of triggers for each station. Then, by sliding 10-second-long moving windows over the lists for all stations, groups of triggers common at more than two stations were formed. Thus, we obtained 5 lists of common triggers from 5 lists of triggers for each station.

Trigger Selection

Because the signals that we are looking for have small amplitudes, the STA/LTA thresholds were set to low values. Obviously, the lower this threshold is, the less “reliable” are the triggers obtained. Therefore, two selection criteria were used to retain only “reliable” triggers. The first was based on the number of stations: only the triggers common at least at “N” stations were taken into account. The second consisted of evaluating the consistency of the time distribution of the common triggers with the locations of the stations: we plotted longitude and latitude of the stations and trigger time in the x, y and z axes, respectively; then, we determined the best fit plane, the one minimizing the perpendicular distances

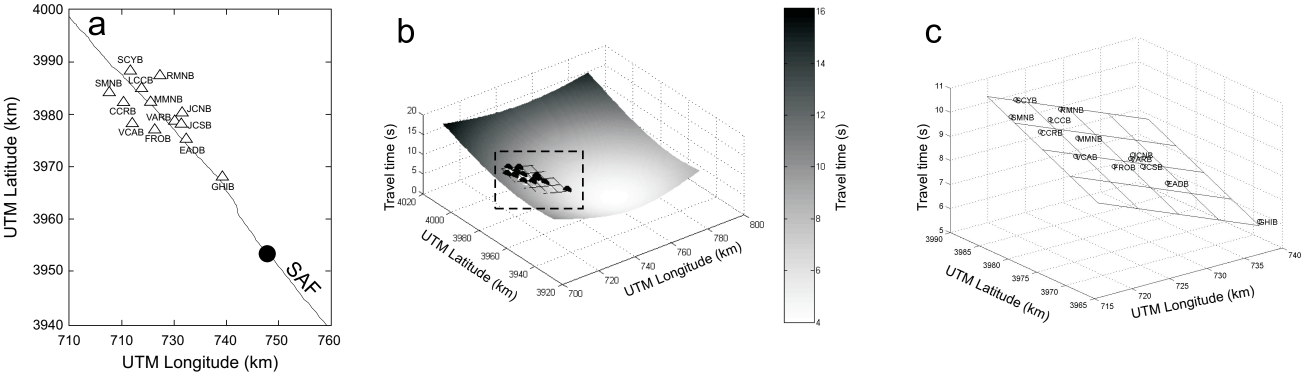

Figure 2.64: (a) Map showing the locations of the 13 stations belonging to the HRSN (triangles), a portion of the San Andreas Fault (SAF) and the epicentre of the theoretical source (black dot). (b) Distribution of the theoretical travel times (surface) and the fitting plane (grid plane) obtained taking into account only the 13 points corresponding to the stations (black dots); the dashed rectangle shows the portion of the plot highlighted in (c). (c) Theoretical travel times at the considered stations (black circles) and fitting plane (grid plane). See text for details.

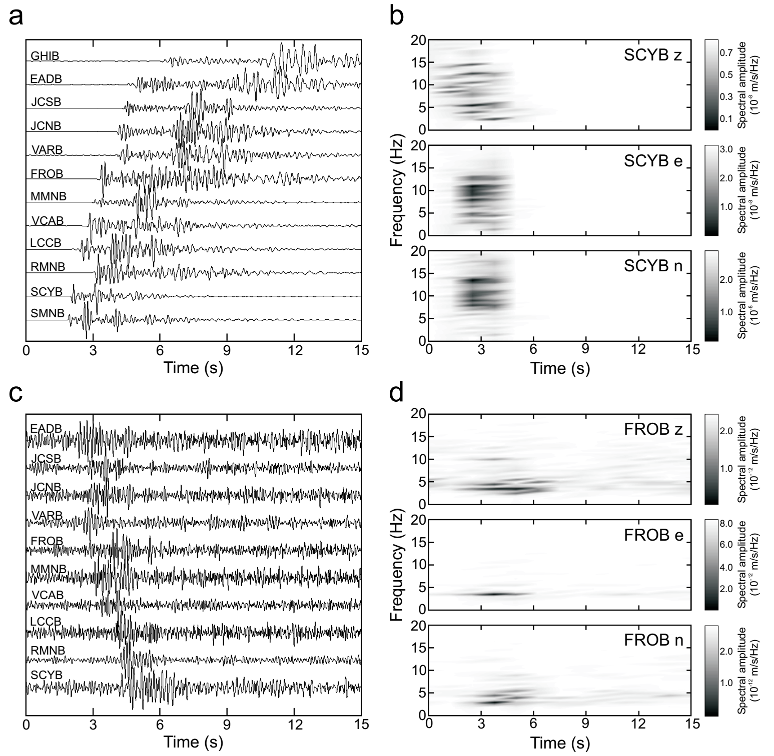

Figure 2.65: (a) Vertical component velocity recorded on January 30, 2006 (filter: 2-8 Hz) and (b) velocity spectrograms of the three components at SCYB. (c) Velocity signal of one of the horizontal component recorded on April 30, 2006 (filter: 2-8 Hz) and (d) velocity spectrograms of the three components at FROB.

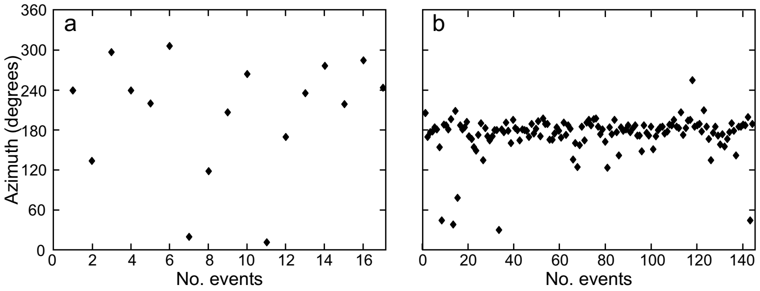

Figure 2.66: Azimuth values of the events of (a) group 1 and (b) group 2, obtained by using the plunge of the fitting plane.

from the stations, and calculated the residuals. Therefore, the triggers common at least at "N" stations were considered "reliable" if the sum of the rectified residuals was lower than a certain threshold, called "E". Obviously, this method is valid only if the source is far away from the station network; the tremor source location reported in *Nadeau and Dolenc* (2005) supports this assumption. By this fitting plane we were also able to roughly calculate an azimuth value for each group of common triggers, corresponding to the plunge direction of the plane. Figure 2.64a shows the epicentre of a theoretical source, located at depth of 20 km, roughly corresponding to the epicentre and the depth of the tremor source reported in *Nadeau and Dolenc* (2005); the distribution of the theoretical travel times, calculated using this theoretical source, are shown as the surface in Figure 2.64b and black circles in Figure 2.64c. In these figures, the best fit plane obtained taking into account only the 13 points corresponding to the stations is shown as a grid.

The values for "N" and "E" were chosen to be 7 and 10, respectively, as representing a good trade-off between consistency of the time distribution of the common triggers with the distribution of the stations, and high number of remaining groups of common triggers.

28.3 Detection Results

By applying the detection procedure on the 5 lists of common triggers, we found 161 "events" that can be divided into two groups. The first consists of 17 events with impulsive onsets, clear P- and S-waves arrivals and a broad spectrum (5-15 Hz) (Figure 2.65a,b). Based on these features we consider them to be earthquakes (most of them are reported in the Northern California Earthquake catalog). The second group has 144 events. They have emergent onsets, low overall amplitudes, generally higher amplitudes on the horizontal components than on the vertical, and a narrow spectrum enriched in low frequencies (below 8 Hz; Figure 2.65c,d).

While the azimuths, from the plunges of the best fit planes, for the first group are scattered, those of the second group are nearly constant (Figure 2.66a,b). Their direction is roughly consistent with the location of the tremor source reported in *Nadeau and Dolenc* (2005).

28.4 Conclusion

By developing an effective detection procedure, we were able to find two different groups of events in the seismic signal recorded during 48 episodes of NVT. The first family are earthquakes, most of which are reported in the NCSN catalog. The second was composed of tremor pulses, characterised by spectral content similar to the NVT and constant at all the stations, and by steady azimuth of seismic wave propagation, consistent with the location of the NVT source.

28.5 References

Nadeau, R.M., and D. Dolenc, Nonvolcanic tremors deep beneath the San Andreas fault, *Science*, *307*, doi:10.1126/science.1107142, 2005.

Obara, K., Nonvolcanic deep tremor associated with subduction in southwest Japan, *Science*, *296*, 1679-1681, 2002.

Shelly, D.R., Beroza, G.C., Ide, S., and S. Nakamula, Low-frequency earthquakes in Shikoku, Japan, and their relationship to episodic tremor and slip, *Nature*, *442*, 188-191, 2006.

Shelly, D.R., Beroza, G.C., and S. Ide, Non-volcanic tremor and low-frequency earthquake swarms, *Nature*, *446*, 305, 2007.

Schwartz, S.Y., and J.M. Rokosky, Slow slip events and seismic tremor at circum-Pacific subduction zones, *Rev. Geophys.*, *45*, RG3004, doi:10.1029/2006RG000208, 2007.

Withers, M., Aster, R., Young, C., Beiriger, J., Harris, M., Moore, S., and J. Trujillo, A comparison of select trigger algorithms for automated global seismic phase and event detection. *Bull. Seism. Soc. Am.*, *88*, 95-10, 1998.

29. Apparent Stress and Corner Frequency Variations in the 1999 Taiwan (Chi-Chi) Sequence

Kevin Mayeda and Luca Malagnini

29.1 Introduction

Apparent stress drop and corner frequency are measured for the Chi-Chi, Taiwan sequence beginning with the mainshock (M_w7.6) on 20 September 1999. Using the recent coda source ratio methodology introduced by *Mayeda et al.* [2007], we have obtained stable source ratio estimates using broadband local and regional stations on Taiwan. We find the following: (1) For the mainshock and 7 of the larger aftershocks ($>M_w$ 5.5), apparent stress is tightly clustered around 6 bars (± 2 bars); (2) In contrast, events below moment magnitude $\sim M_w$ 5.0 exhibit lower average apparent stress as well as larger scatter, ranging between ∼1.0 and 7.0 bars and are spatially variable; 3) For this dataset, the *Brune* [1970] omega-square source model fits the spectral shape for events $4.5<M_w<7.6$; however, a clear, step-wise break in self-similarity exists at around M_w 5.0. We hypothesize that the larger events are subject to the average state-of-stress over a broader region, whereas the smaller aftershocks are more sensitive to the local state-of-stress resulting from stress-field redistribution following the mainshock.

29.2 Earthquake Source Scaling

Aside from long-period regional and teleseismic waveform modeling estimates for M_w, broadband studies that extrapolate back to the source have always been hampered by inadequate knowledge of scale-dependent path and site effects. Radiated energy and corner frequency estimation over a broad range of event sizes requires significant frequency-dependent corrections, resulting in significant error that makes interpretation of the results highly questionable. There are, however, a number of local and regional methods that circumvent the problem of path and site corrections, namely the empirical Greens function deconvolution method [e.g., *Hough*, 1997] and amplitude ratio techniques [e.g., *Izutani*, 2005]. These approaches have gained popularity because adjacent or colocated events recorded at common stations have shared path and site effects, which therefore cancel. In this study we use a variant of the direct wave amplitude ratio, the coda ratio methodology of *Mayeda et al.* [2007], which has been shown to be roughly 3 times more stable than direct wave ratios and can be used with event pairs that are separated by several tens of kilometers, with little ill effects on data scatter. More recently, the method has been extended to datasets in Italy such as the San Giuliano di Puglia sequence in October 2001 [*Malagnini and Mayeda*, 2008] and the Colfiorito sequence of 1997 and 1998 [*Malagnini et al.*, 2008]. Over the past decade, a number of studies have suggested that earthquake scaling is either constant with high scatter or increases with increasing magnitude. Due to large errors and regional variations, it has been difficult to definitively tell which of these two ideas is correct. Knowledge of scaling, whether self-similar or not, is fundamental to earthquake rupture simulations and seismic hazard prediction, especially if there exist region-dependent variations in apparent stress.

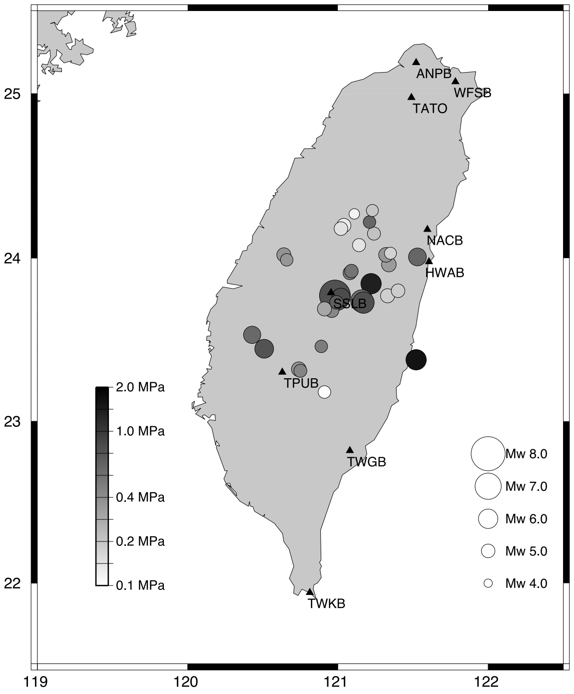

Figure 2.67: Map showing epicenters of events used in this study (circles) and broadband stations (triangles). Shading of events corresponds to the average apparent stress that was computed from the coda envelope ratios for each event.

29.3 Application to Chi-Chi, Taiwan Sequence

For this study, we selected 43 events ranging between M_w 4.4 and 7.6 recorded by 9 stations of the Broadband Array in Taiwan (BATS) (Figure 2.67). Stable M_ws for all the events were obtained from a previous coda calibration. The coda ratio methodology is outlined in *Mayeda* *et al.* [2007], so we only give a brief processing description here. First, narrowband time-domain envelopes ranging between 0.03 and 8.0-Hz were made using the two horizontal components and log-averaged for additional stability and smoothed. Coda synthetic envelopes were then fit to the data for each station so that relative amplitudes could be measured using an L-1 fitting routine for each narrowband envelope. Then ratios were formed for all possible event pairs by subtracting the log10 amplitudes for each station that recorded the event pair. Observed ratios were then fit by theoretical ratios derived from a modified *Brune* source spectra outlined in *Walter and Taylor*, [2001]. Figure 2.68 shows corner frequency estimates along with ± 1 standard deviation, and their corresponding apparent stress drops are shown in Figure 2.67. As found in other studies, the coda-derived source ratios exhibited little scatter, and thus source parameters, such as corner frequency, are well constrained when we fit the observed data with theoretical source models. The averaging nature of coda waves has been shown to provide significantly lower amplitude variance than any traditional direct phase method. We have obtained stable source ratio estimates using broadband local and regional stations on Taiwan. We find the following: (1) For the mainshock and 7 of the larger aftershocks ($> M_w$ 5.5), apparent stress is tightly clustered around 6 bars (± 2 bars); (2) In contrast, events below moment magnitude $\sim M_w$ 5.0 exhibit lower average apparent stress as well as larger scatter, ranging between ∼1.0 and 7.0 bars, and are spatially variable; 3) For this dataset, the *Brune* [1970] omega-square source model fits the spectral shape for events $4.5 < M_w < 7.6$; however, a clear, stepwise break in self-similarity exists at around M_w5.0. We hypothesize that the larger events are subject to the average state-of-stress over a broader region, whereas the smaller aftershocks are more sensitive to the local state-of-stress resulting from stress-field redistribution following the mainshock.

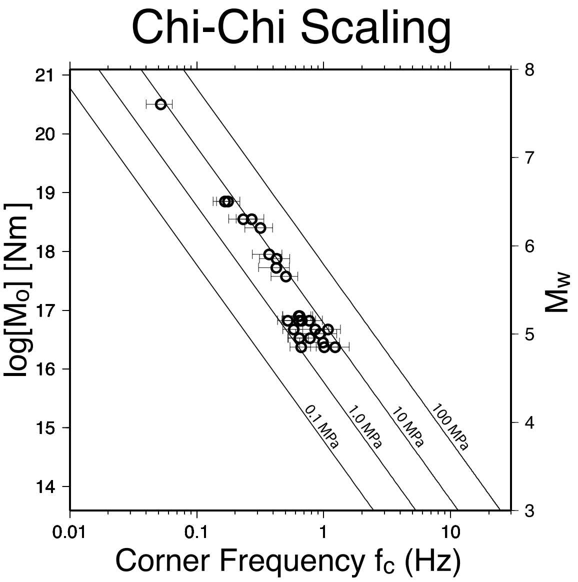

Figure 2.68: Moment versus corner frequency is plotted for the Chi-Chi sequence with lines of constant apparent stress. In general, the mainshock and larger aftershocks above M_w 5.5 have roughly the same scaling and apparent stress values, whereas for smaller events there is a clear shift and more scatter.

29.4 Acknowledgements

K. Mayeda was supported under Weston Geophysical subcontract No. GC19762NGD and AFRL contract No. FA8718-06-C-0024. Work by L. Malagnini was performed under the auspices of the Dipartimento della Protezione Civile, under contract S4, ProCiv-INGV (2004-06), project: "Stima dello scuotimento in tempo reale e quasi-reale per terremoti significativi in territorio nazionale".

29.5 References

Brune, J. N., Tectonic stress and spectra of seismic shear waves from earthquakes, *J. Geophys. Res.* 75, 4997-5009, 1970.

Hough, S.E., Empirical Greens function analysis: Taking the next step, *J. Geophys. Res.* 102, 5369-5384, 1997.

Izutani, Y., Radiated energy from the mid Nigata, Japan, earthquake of October 23, 2004 and its aftershocks, *Geophys. Res. Lett.* 32, L21313, doi:10.1029/2005GL024116, 2005.

Malagnini, L. and K. Mayeda, High-stress strike-slip faults in the Apennines: An example from the 2002 San Giuliano earthquakes (Southern Italy), *Geophys. Res. Lett.*, doi:10.1029/2008GL034024, 2008.

Malagnini, L., L. Scognamiglio, A. Mercuri, A. Akinci, K. Mayeda, Source scaling for ground motion prediction in central Italy: Evidence for strong non-self-similar behavior, accepted *Geophys. Res. Lett.*, 2008.

Mayeda, K., L. Malagnini, W.R. Walter, A new spectral ratio method using narrow band coda envelopes: Evidence for non-self-similarity in the Hector Mine sequence, *Geophys. Res. Lett.*, doi:10.1029/2007GL030041, 2007.

Walter, W. R. and S. R. Taylor (2001). A revised magnitude and distance amplitude correction (MDAC2) procedure for regional seismic discriminants: theory and testing at NTS, Lawrence Livermore National Laboratory Report, UCRL-ID-146882, `http://www.llnl.gov/tid/lof/documents/pdf/240563.pdf`

30. Source Analysis of the Crandall Canyon, Utah, Mine Collapse

Sean R. Ford, Douglas S. Dreger, William R. Walter (Lawrence Livermore National Laboratory)

30.1 Introduction

On 6 August 2007 a magnitude 3.9 seismic event was associated with the tragic collapse of a Utah coal mine, which ultimately killed six miners and three rescue workers. The event was recorded on the local network of the University of Utah Seismic Stations (UUSS) and the Advanced National Seismic System (ANSS) operated by the USGS. In addition, the NSF Earthscope USAarray stations had recently been installed in the region (www.earthscope.org). These stations provided good coverage (Figure 2.69a) enabling seismic source analysis of the recorded signals, which revealed an unusually shallow depth and anomalous radiation pattern, both contrary to the expectation for a tectonic earthquake.

30.2 Results

First motion polarities from vertical-component records of the seismic event are down, or dilatational, indicative of an implosional source (*Pechmann et al.*, 2008). Consistent with this observation, the moment tensor inversion of complete, three-component, low-frequency (0.02 to 0.10 Hz) ground displacement recovered a mechanism that also satisfies the observed first motions, and is most consistent with the gravity driven vertical collapse of a horizontally oriented underground cavity at a shallow depth consistent with the mine workings (Figure 2.69b). The total seismic moment of this mechanism was 1.91×10^{15} N-m ($M_W 4.2$). However, a closing horizontal crack theoretically has no Love wave excitation and in order to explain the large amplitude Love waves observed on the tangential component (Figure 2.69c) the mechanism must contain a secondary non-crack component that is 24% of the dominant vertical collapse moment (1.71×10^{15} N-m). The secondary source excitation of the moment tensor can be represented in multiple ways, as the moment tensor decomposition is non-unique (*Jost et al.*, 1989). Plausible interpretations of the secondary source include additional vertical dip-slip faulting, horizontal shear, non-uniform crack closure, and elastic relaxation in response to the mine collapse.

The source-type diagram (*Hudson et al.*, 1989) in Figure 2.69b illustrates the deviation from a pure earthquake double-couple (DC) source at the center in terms of a volumetric component (explosion or implosion) on the ordinate, and deviatoric component in terms of a volume compensated linear vector dipole (CLVD) on the abscissa. The moment tensor solution for the 6 August 2007 event plots in the region of a negative or closing crack. The diagram shows that despite the secondary source component the seismic waveforms are best fit by a model that is primarily comprised of a closing horizontal crack, or underground collapse, and is similar to solutions obtained for other mine and Nevada Test Site (NTS) cavity collapses (*Ford et al.*, 2008). In contrast, NTS nuclear explosions modeled with the same method (*Ford et al.*, 2008) plot squarely in the explosion region of the diagram. Both the explosions and collapses are significantly separated from the population of earthquakes, which locate in the center of the diagram. Deviation from pure DC mechanisms in the earthquake population can be a result of several factors including complex faulting, noise, and the effect of approximate Earth structure models on the basis Greens functions for the inversion. Despite the scatter within the three source populations, there is clear separation between each, indicating that regional distance seismic moment tensor methods are capable of source-type discrimination.

30.3 Conclusions

Our findings show that the seismic waveforms associated with the mine collapse primarily reflect the collapse; however, the seismic source process was more complex than observed in other collapse events (*Pechmann et al.*, 1995) with a large secondary source generating strong Love waves. This application of seismic moment tensor analysis demonstrates the feasibility of continuous monitoring of regional distance seismic wavefields for source-type identification including nuclear explosion monitoring and given rapid access to the seismic waveform data, for emergency response applications.

30.4 Acknowledgements

Sponsored by National Nuclear Security Administration, Office of Nonproliferation Research and Development, Office of Defense, Nuclear Nonproliferation. Contract No. DE FC52-06NA27324. We thank Bruce Julian for the code to make the source-type plots.

30.5 References

Ford, S., D. Dreger and W. Walter (2008). Identifying isotropic events using a regional moment tensor inversion, accepted by *J. Geophys. Res.*

Jost, M. L. and R. B. Herrmann (1989). A student's guide to and review of moment tensors, *Seismol. Res. Lett., 60* 2, 37-57.

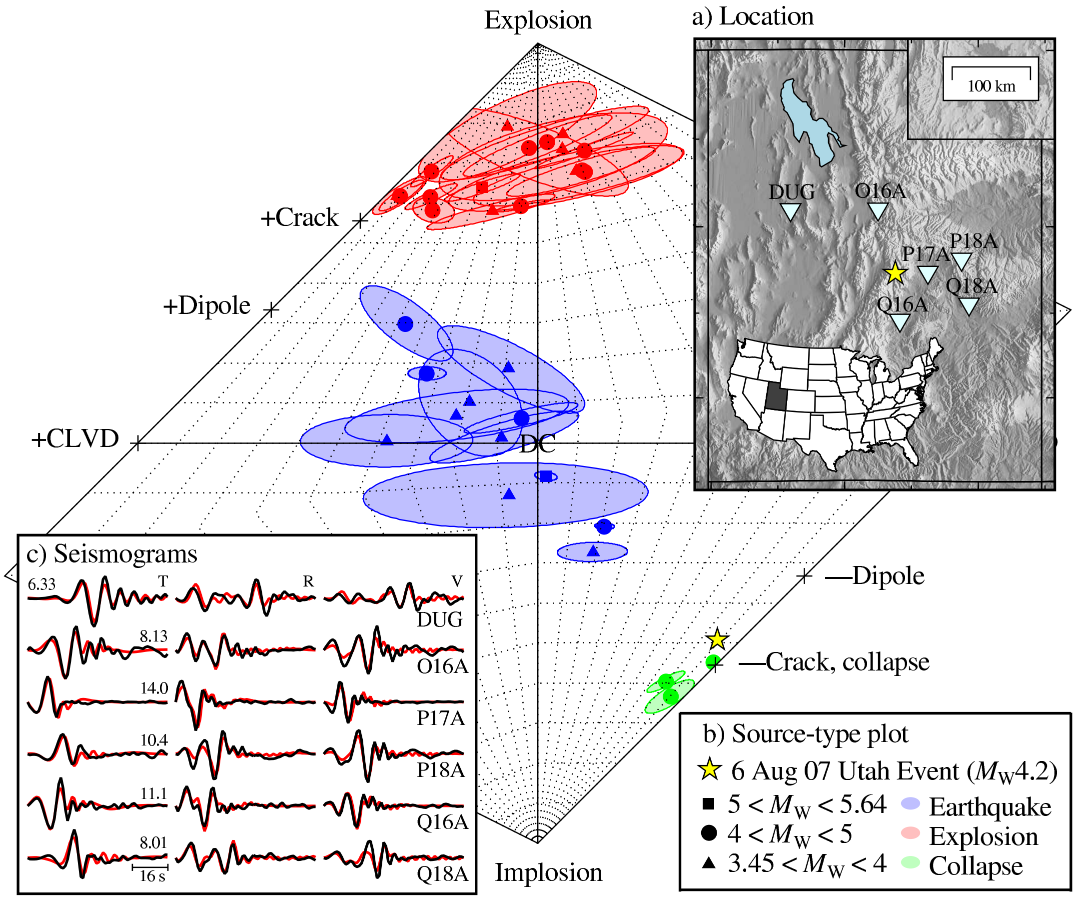

Figure 2.69: a) Locations of the August 6, 2007 event and 6 of the closest USArray and ANSS stations. b) Source type plot from the method of *Hudson et al* (1989) shows clear separation of populations of earthquakes, explosions and collapses. The yellow star shows the solution for the August 6, 2007 seismic event. c) Observed seismograms (black) are compared to synthetics (red) for the non-double-couple solution, which is dominated by a horizontal closing crack (b). The maximum displacement (10^{-7} m) of each set of tangential (T), radial (R), and vertical (V) observations is given. (See color version of this figure at the front of the research chapter.)

Hudson, J. A., R. G. Pearce, R. G., and R. M. Rogers (1989). Source type plot for inversion of the moment tensor, *J. Geophys. Res., 9* (B1), 765-774.

Pechmann, J. C., W. J. Arabasz, K. L. Pankow, R. Burlacu, and M. K. McCarter (2008), Seismological report on the 6 Aug 2007 Crandall Canyon Mine collapse in Utah, *Seism Res. Lett., 79* 5, 10-12.

Pechmann, J. C., W. R. Walter, S. J. Nava, and W. J. Arabasz (1995). The February 3, 1995, ML 5.1 seismic event in the trona mining district of southwestern Wyoming, *Seism. Res. Lett., 66* 3, 25-34.

31. Interactions Between Early Earthquake Slip History and Final Magnitude

Gilead Wurman, Richard M. Allen and David D. Oglesby (University of California, Riverside)

31.1 Introduction

One commonly accepted model for the behavior of fault ruptures is the cascading rupture model [*Bak and Tang*, 1989; *Steacy and McCloskey*, 1998; *Ide and Aochi*, 2005; *Otsuki and Dilov*, 2005; *Sato and Mori*, 2006], which describes a cascading failure of successive fault patches as a result of loading by the rupture of preceding patches. Because the rupture of a given patch is unaffected by those patches ahead of the rupture front, this model predicts that earthquakes should be non-deterministic for the duration of their rupture. That is, there should be no discernible information about the extent of the final rupture until it has completely finished propagating.

Recent observations of the spectral character of P-waves [*Olson and Allen*, 2005; *Lockman and Allen*, 2005, 2007; *Wurman et al.*, 2007; *Lewis and Ben-Zion*, 2007] suggest that there is some information in the early seismic arrivals that may be correlated to the final magnitude of the event, and that in many cases this information is available before the rupture has completed. These data suggest that there may be an additional effect which is not accounted for by the cascading rupture model, which lends the rupture at least a degree of determinism.

Olson and Allen [2005] hypothesized that this determinism is provided by the intensity of the early rupture history of the earthquake. A higher stress concentration at the focus of the earthquake generates a stronger early rupture phase, which imparts sufficient energy to the rupture to overcome barriers on the fault surface and produce a large earthquake. Conversely, an area of lower stress around the focus generates a comparatively weak early rupture, and the rupture may not gain enough energy to overcome the same barriers, and stops before becoming a large earthquake. Henceforth we use the term "nucleation" to describe the early dynamic (radiative) rupture history of the event, rather than a long-term (quasistatic) aseismic nucleation.

31.2 Model setup

We test this concept by modeling the dynamics of a planar fault with stochastic initial stress conditions, with systematically varying stress in the nucleation region. We use the Support Operators Rupture Dynamics (SORD) dynamic fault code [*Ely et al.*, 2008]. The initial shear stress field is generated randomly using the method of *Ripperger et al.* [2007]. One realization of an initial stress field is shown in Figure 2.70a.

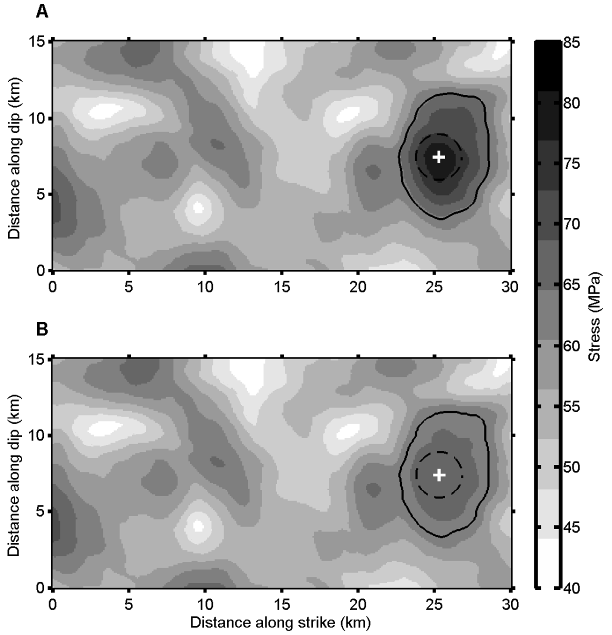

Figure 2.70: Initial distribution of shear stress on the fault plane, with high nucleation stress (a) and reduced nucleation stress (b). Dashed black circle represents region of forced nucleation, with black + marking nucleation point. Black solid contour shows region of nucleation stress scaling, and white dashed contours show regions where initial shear stress is less than dynamic yield stress.

We select an appropriate nucleation point by examining the asperities in our stress realization and selecting the highest-stress asperity on the fault that is broad enough to accommodate the 3 km diameter of the nucleation zone. To simulate varying nucleation stresses, we take a contour around the nucleation point at 64 MPa, approximately halfway between static and dynamic yield stress. Within that contour, we scale the stresses up or down such that the maximum stress is between 64 MPa and 80 MPa as desired. This process provides strong differences in the strength of nucleation, while largely preserving the spatial characteristics of the stress field. Outside the 64 MPa contour, the stress field remains identical between model runs. Figure 2.70b shows the stress field for the same realization as in Figure 2.70a, but with a weak nucleation.

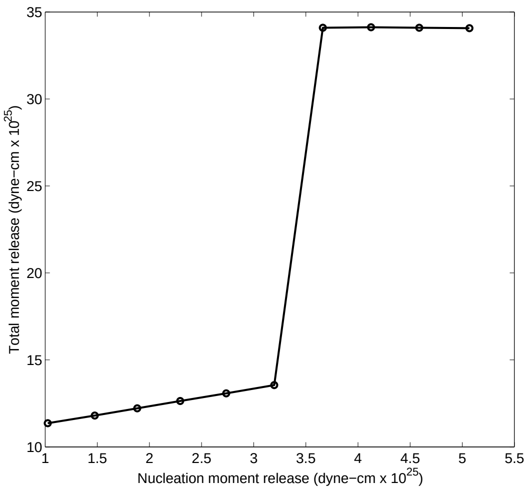

Figure 2.71: Total moment release vs. moment released in the first 2 seconds of rupture.

31.3 Results

We vary the peak nucleation stress between 64 and 80 MPa in increments of 1.6 MPa and allow the rupture to propagate to completion. We consider the moment release of the nucleation phase to be all moment released within the first 2 seconds of the rupture. This allows time for the effects of artificial nucleation to end, as well as for the rupture to propagate across the region of scaled nucleation stress. Figure 2.71 shows the total moment release in each run as a function of the nucleation moment release. Seismic moment is calculated at each element as $M_0 = \mu SD$, where D is the slip in cm at the element, S is the area of each element, $10^8 cm^2$, and $\mu = 3x10^{11} dynes/cm^2$. The total moment release is the sum of the moment at all nodes on the fault plane.

Figure 2.72 shows the final stress distribution and final slip on the fault for a high-stress nucleation case (80 MPa peak stress, 2.72a and 2.72c) and a low-stress case (65.6 MPa peak stress, 2.72b and 2.72d). A comparison of these figures to Figures 2.70a and b and the plot in Figure 2.71 shows that there is a point at which the initial nucleation is strong enough to overcome the low-stress barrier in the middle of the fault, and the rupture propagates through to the asperity on the other side. The behavior exhibited in this example is highly sensitive to the parameterization of the initial stress distribution. A distribution with slightly higher minimum shear stress will rupture through the entire fault for all initial conditions, while a distribution with lower minimum shear stress will never proceed past the nucleation asperity. This entire range is observed over a variation of less than 0.5 MPa in minimum initial shear stress.

31.4 Discussion and Conclusions

Because the moment release after 2 seconds of rupture can be correlated to the moment release at the end of the rupture, this model supports the concept of determinism in the rupture resulting from the strength of the nucleation phase. However, the rupture area in this realization has only two asperities and one barrier, which does not demonstrate that this behavior can extend to more heterogeneous faults. Because barriers require additional crack energy to propagate through, they reduce the available energy for the continuation of the rupture on the other side of the barrier.

The behavior presented here is only stable for a narrow range of stress parameters. It is particularly sensitive to the degree to which stresses on the fault plane are allowed to be less than the dynamic yield stress. Thus, only finely-tuned stress parameters create faults whose modeled behavior explains the observations of determinism in real earthquakes. If we regard the observations of earthquake scaling as reliable, and the mechanism shown in this study is responsible for the observed scaling behavior, our results may serve to constrain the possible state of in situ stress in real faults. However, this result is dependent on the methodology we use with regard to how we vary the intensity of nucleation. A different choice in terms of frictional parameterization, such as rate-and-state weakening, or spatially varying friction coefficients, may also have an effect on the range of possible initial shear stresses. Even within the bounds of the method used in this study, other realizations of initial stress conditions will also produce slightly varying results. Indeed, given the dearth of observations of stress on real faults, it is difficult to know what a reasonable state of initial shear stress is to begin with. A suite of models and stress patterns will provide a greater understanding of the state of stress on real faults.

31.5 Acknowledgements

The authors thank Luis Dalguer and Geoff Ely for assistance with dynamic rupture codes. This work was partially supported by USGS NEHRP Grant 06HQAG0147.

31.6 References

Bak, P. and C. Tang, Earthquakes as a Self-Organized Critical Phenomenon, *J. Geophys. Res. B, 94,* 15635-15637, 1989.

Ely, G.P., S.M. Day, and J.B. Minster, A support-operator method for viscoelastic wave modeling in 3-D heterogeneous media, *Geophys. J. Int. 172,* 331-344, 2008.

Ide, S. and H. Aochi, Earthquakes as multiscale dynamic ruptures with heterogeneous fracture surface energy, *J. Geophys. Res. B, 110,* B11303, doi:10.1029/2004JB003591, 2005.

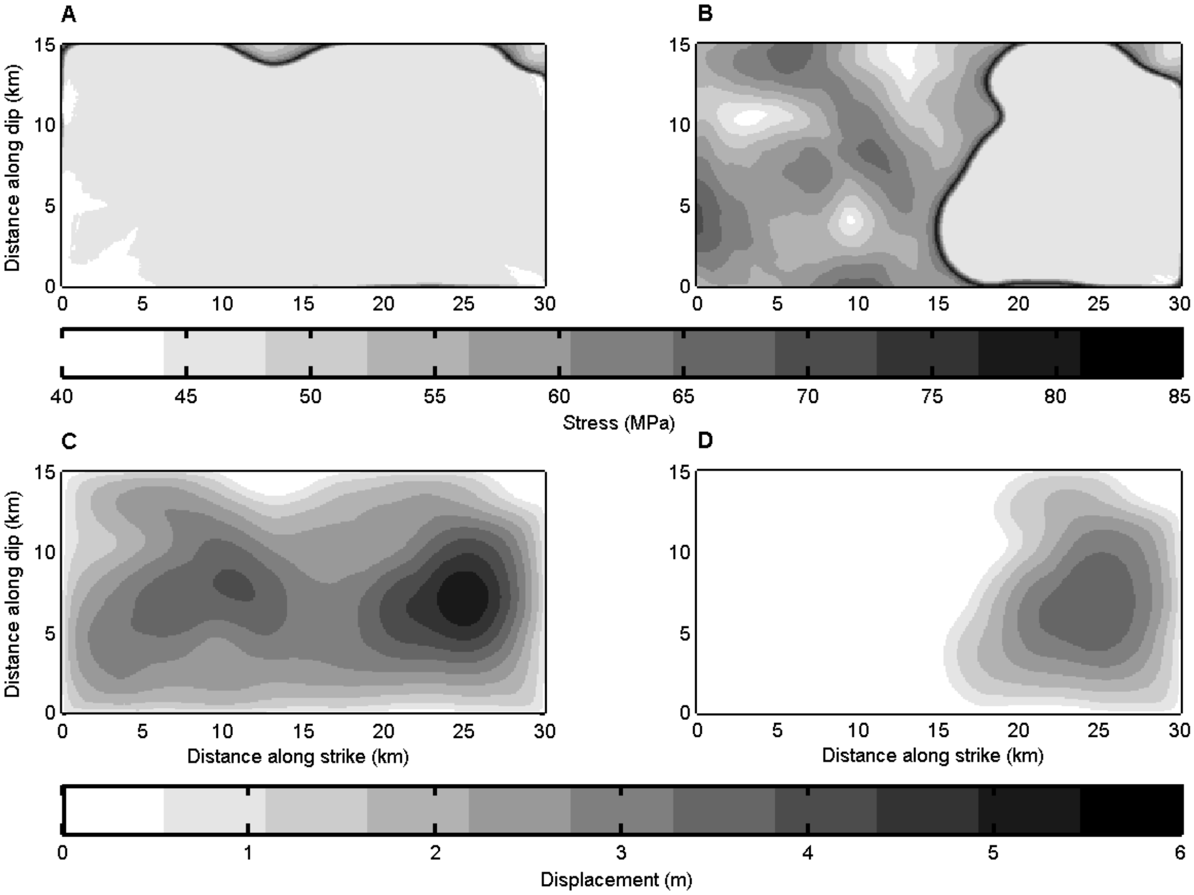

Figure 2.72: Final shear stress and final slip for the low-stress nucleation case (a,c) and the high-stress nucleation case (b,d). In the high-stress case, the rupture propagated through the barrier in the middle of the model, and in the low-stress case it was arrested at that barrier.

Lewis, M.A. and Y. Ben-Zion, Examination of scaling between proposed early signals in P waveforms and earthquake magnitudes, *Geophys. J. Int., 171,* 1258-1268, 2007.

Lockman, A.B. and R.M. Allen, Single-station earthquake characterization for early warning, *Bull. Seism. Soc. Am., 95,* 2029-2039, 2005.

Lockman, A.B. and R.M. Allen, Magnitude-period scaling relations for Japan and the Pacific Northwest: Implications for earthquake early warning, *Bull. Seism. Soc. Am., 97,* 140-150, 2007.

Olson, E.L. and R.M. Allen, The deterministic nature of earthquake rupture, *Nature, 438,* 212-215, doi:10.1038/nature04214, 2005.

Otsuki, K and T. Dilov, Evolution of hierarchical self-similar geometry of experimental fault zones: Implications for seismic nucleation and earthquake size, *J. Geophys. Res. B., 110,* B03303, doi:10.1029/2004JB003359, 2005.

Ripperger, J, J.-P. Ampuero, P.M. Mai, and D. Giardini, Earthquake Source Characteristics from Dynamic Rupture with Constrained Stochastic Fault Stress, *J. Geophys. Res. B, 112,* B04311, doi:10.1029/2006JB004515, 2007.

Sato, K. and J. Mori, Scaling relationship of initiations for moderate to large earthquakes, *J. Geophys. Res. B, 111,* B05306, doi:10.1029/2005JB003613, 2006.

Steacy, S.J. and J. McCloskey, What controls an earthquake's size? Results from a heterogeneous cellular automaton, *Geophys. J. Int., 133,* F11-F14, 1998.

Wurman, G., R.M. Allen, and P. Lombard, Toward Earthquake Early Warning in Northern California, *J. Geophys. Res. B, 112,* B08311, doi:10.1029/2006JB004830, 2007.

32. Correlated Changes in Nonvolcanic Tremor, Seismic Velocity and Fault Displacement Associated with the 2003 San Simeon and 2004 Parkfield Earthquakes.

R.M. Nadeau, F. Brenguier [1,2] M. Campillo [2] C. Hadziioannou [2] N.M. Shapiro, [1] E. Larose [2]
[1] **(Sismologie, Institut de Physique du Globe de Paris & CNRS, Paris, France)**
[2] **(Laboratoire de Geophysique Interne et Tectonophysique & CNRS, Grenoble, France)**

32.1 Introduction

Since their discovery in 2002 (*Obara*, 2002), deep (~ 15-40 km) nonvolcanic tremors (long-duration seismic signals with no clear P or S waves) have generally been found in transition zones between freely slipping and locked fault (*Rogers and Dragert*, 2003; *Nadeau and Dolenc*, 2005; *Brudzinski and Allen*, 2007; *Payero et al.*; 2008). In most cases, the tremors occur in subduction zones; hence, fluids from dehydration processes are believed to play an important role in tremor generation. Changes in the rate of tremor activity also often correlate with transient fault deformation (slow-slip events) and with dynamic stress changes from tides and surface waves of teleseismic (distant) earthquakes (*Gomberg et al.*, 2007, *Rubinstein et al.*, 2008).

These associations suggest that a better understanding of the mechanisms responsible for tremors may provide important clues to the rheology of deep fault zones and processes responsible for generating large earthquakes. Reported here is a recently discovered correlation between changes in nonvolcanic tremor activity and changes in seismic velocity and fault deformation along the central San Andreas fault occurring conjunctively with the 22 December 2003, M6.5 San Simeon and 28 September 2004, M6.0 Parkfield earthquakes (*Brenguier et al.*, 2008b).

32.2 Continuous Borehole Seismic Data

To monitor variations in seismic velocities and nonvolcanic tremor, we analyzed more than 5 years (January, 2002 to October, 2007) of continuous seismic data from the 13 borehole seismic stations of the Berkeley High Resolution Seismic Network (HRSN). The analyses also spanned the two strongest earthquakes occurring within 100 km of Parkfield, CA: the Mw = 6.5 San Simeon Earthquake of 22 December 2003, whose epicenter was located 60 km west of Parkfield, and the Mw = 6.0 Parkfield Earthquake of 28 September 2004. Sensor depths of the HRSN stations range between 60 and 300 m, thus reducing locally generated noise and effects of temperature variations and precipitation.

32.3 Data Sets

Seismic Velocity Change

For every possible pair combination of stations we computed the daily cross-correlation of seismic noise using the procedure of (*Brenguier et al.*, 2007), yielding 91 x 2140 days = 194,740 cross-correlation and autocorrelation time functions. A Reference Green Function (RGF) was computed for each station pair by stacking the daily cross-correlations for the entire 2140 day period (*Brenguier et al., 2008b*). The velocity changes were then determined by measuring time delays between the RGF and 30 day stacks of cross- correlation functions in the frequency range 0.1 to 0.9 Hz (Brenguier et al., 2008a, 2008b). By measuring the slope of the travel time shifts, dt, as function of time, t, we then estimated the relative time perturbation (dt/t), which is the opposite value of the medium's relative velocity change (dv/v). Finally, following *Brenguier et al.* (2008a), we averaged the relative time delays over all station pairs to increase the measurement accuracy.

Tremor Activity

During the study period, 1577 tremor events ranging in duration from 3 to 21 minutes were detected using 3 to 8 Hz filtered continuous records from the HRSN and root-mean-square envelope techniques (*Obara*, 2002; *Brenguier et al.*, 2008b). In total, 8962 minutes of tremor activity was detected. These tremors are estimated to have occurred between 20 and 40 km depth, indicating that they are related to deep processes along the fault zone (*Nadeau and Dolenc*, 2005). A 30 day averaged rate history of tremor activity was then generated from these data for comparison to the seismic velocity and deformation data (Figure 2.73).

Surface Deformation

Surface deformation measurements used in this study (primarily GPS) were obtained over the internet from the USGS web site and selected and processed as described in *Brenguier et al.* (2008b). More detail concerning the USGS deformation and GPS networks and related surface deformation measurements can be found at, `http://earthquake.usgs.gov/research/parkfield/deform.php` and `http://quake.usgs.gov/research/deformation/twocolor/pkf_continuous_gps.html`.

32.4 Results

The correlated evolution of the nonvolcanic tremors, seismic velocities, and fault zone deformation suggests

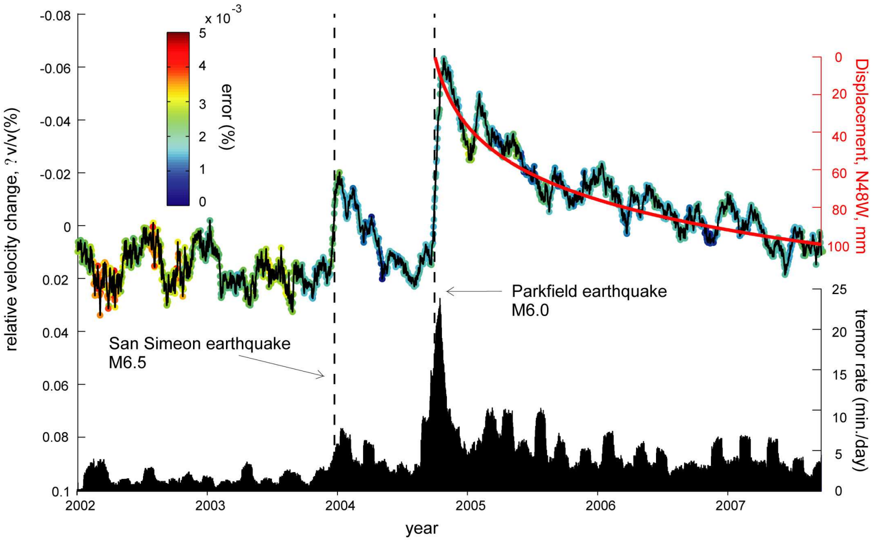

Figure 2.73: Seismic velocity changes (upper time history), surface displacements from GPS (upper, curve following Parkfield event) and tremor activity (lower time history) near Parkfield. The displacement curve represents the postseismic fault parallel displacements along the San Andreas fault as measured by GPS at station POMM. The tremor rates are averaged over a centered 30 day moving time window.

the presence of two physical mechanisms generating changes in crustal and fault zone properties: 1) shallow damage within the fault zone and near surface layers from strong ground shaking by the mainshocks and 2) coseismic stress change and postseismic relaxation extending down to nonvolcanic tremor depths (~ 30 km). The results also demonstrate that measurements of velocity change from seismic noise analysis can be useful for studying the continuous time evolution of stress in the vicinity of seismogenic faults and tremor zones.

32.5 Acknowledgements

The HRSN is funded by USGS grant 07HQAG0014. Research support was from ANR (France) under 05CATT01001, PRECORSIS, ANR06-CEXC005, and COHERSIS, from NSF under EAR0537641 and EAR0544730 and from USGS grant 06HQGR0167.

This collaboration arose from discussions at the 2nd joint BSL/IPGP workshop on Seismology and Seismotectonics: BSL and IPGP research perspectives, held at Berkeley Seismological Laboratory (BSL) on December 16-17, 2007 and co-sponsored by BSL and the Project International de Cooperation Scientifique (PICS) awarded to the 'Departement de Sismologie' at the 'Institut de Physique du Globe de Paris' (IPGP).

32.6 References

Brenguier F., N.M. Shapiro, M. Campillo, A. Nercessian, V. Ferrazzini, 3-D surface wave tomography of the Piton de la Fournaise volcano using seismic noise correlations, *Geophys. Res. Lett., 34,* L02305, doi:10.1029/2006GL028586, 2007.

Brenguier F., N.M. Shapiro, M. Campillo, V. Ferrazzini, Z. Duputel, O. Coutant, A. Nercessian, Towards forecasting volcanic eruptions using seismic noise, *Nature Geoscience, 1,* 126-130, 2008a.

Brenguier F., M. Campillo, C. Hadziioannou, N.M. Shapiro, R.M. Nadeau and E. Larose, Postseismic Relaxation Along the San Andreas Fault at Parkfield from Continuous Seismological Observations, *Science, in press,* 2008b.

Brudzinski, M. and R.M. Allen, Segmentation in Episodic Tremor and Slip All Along Cascadia, *Geology, 35,* 907-910, 2007.

Gomberg, J., J.L. Rubinstein, Z. Peng, K.C. Creager and J.E. Vidale, P. Bodin, Widespread Triggering of Non-Volcanic Tremor in California, *Science, 319,* 173, 2008.

Nadeau, R.M. and D. Dolenc, Nonvolcanic Tremors Deep Beneath the San Andreas Fault, *Science, 307,* 389, 2005.

Obara, K., Nonvolcanic Deep Tremor Associated with Subduction in Southwest Japan, *Science, 296,* 1679-1681, 2002.

Payero, J. S., V. Kostoglodov, N. Shapiro, T. Mikumo, A. Iglesias, X. Peres-Campos and R. W. Clayton (2008), Nonvolcanic Tremor Observed in the Mexican Subduction Zone, *Geophys. Res. Lett., 35,* L07305, doi:10.1029/2007GRL32877, 2008.

Rogers, G. and H. Dragert, Episodic Tremor and Slip on the Cascadia Subduction Zone: The Chatter of Silent Slip, *Science, 300,* 1942-1943, 2003.

Rubinstein, J. L., M. La Rocca, J.E. Vidale, K.C. Creager and A.G. Wech (2007), Tidal Modulation of Non-Volcanic Tremor, *Science, 319,* 186-189, 2008.

33. Moderate earthquake ground motion validation in the San Francisco Bay Area

Ahyi Kim, Douglas Dreger, and Shawn Larsen

33.1 Introduction

We performed 3D ground motion simulations for 10 recent moderate earthquakes in the San Francisco Bay Area to evaluate the two versions of the USGS 3D velocity models. Comparisions were made in terms of modeling phase arrival timing, peak ground motion amplitudes, and general seismic waveforms. One model, version 5.1.0 was released in 2005 (*Brocher et al.*, 2005; *Jachens et al.*, 2006) and it was used by *Rodgers at al.* (2007)to simulate waveforms of moderate earthquakes in the San Francisco Bay Area in the low frequency band (f < 0.25Hz). Rodgers found that version 5.1.0 predicted the peak amplitude well but that energy arrived earlier than observed. The other model, version 8.3.0, was released in May 2008 (*Brocher* 2008), was used to simulate the ground motions for the 1906 San Francisco earthquake (*Aagaard et al.*, 2008b), and was validated by modeling the 1989 Loma Prieta earthquake strong ground motions (*Aagaard et al.*, 2008a). This model reduced both P- and S-wave velocities in granite, Franciscan, gabbro, lower crust, and upper mantle to correct the earlier phase arrival timing mismatch reported by *Rodgers et al.* (2007). We directly compared the two models in each 200m grid layer and found that the mean velocity of each layer was reduced by approximately 5% in the depth range from 5 to 30km in model 8.3.0.

33.2 Computational set up and 3D model used in the simulations

For the 3D waveform modeling, we used the elastic finite-difference code, E3D developed by *Larsen and Schultz* (1995). With the BSL cluster we can simulate ground motions throughout the greater San Francisco Bay Region to a maximum frequency of 0.5 Hz for models with a minimum wave speed of 500m/s. We have performed simulations of 9 Mw4.1-5.0 events using source parameters obtained from the BSL Moment Tensor Catalog (Table 2.1). Broadband seismic data was obtained from the Berkeley Digital Seismic Network (BDSN), and strong motion data was obtained from the USGS strong Motion Instrumentation Program (SMIP) and the California Geologic Survey (CGS) California Strong Motion Instrumentation Program (CSMIP). The data was corrected to absolute ground velocity (cm/s). We compare synthetic and observed ground velocity in three passbands, namely 0.03-0.15Hz, 0.1-0.25Hz, and 0.1-0.5Hz.

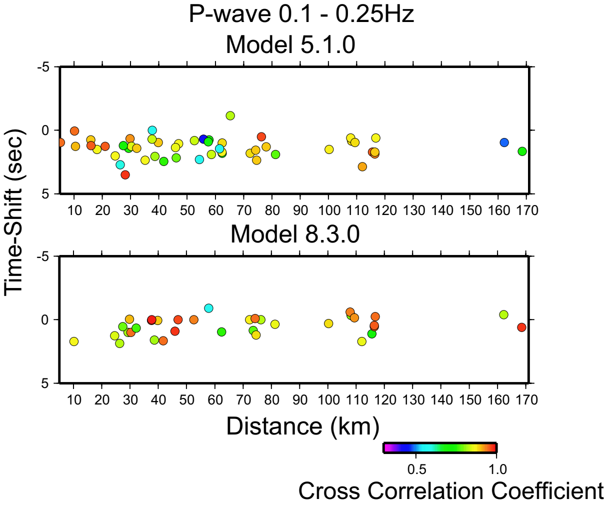

Figure 2.74: Top shows the relative time shift between synthetic and observed P-waves for model 5.1.0. Positive time shift means the synthetics is early and the model is fast. The color scale shows the level of cross-correlation of the synthetic and observed P waveforms. The bottom shows the same for model 8.3.0.

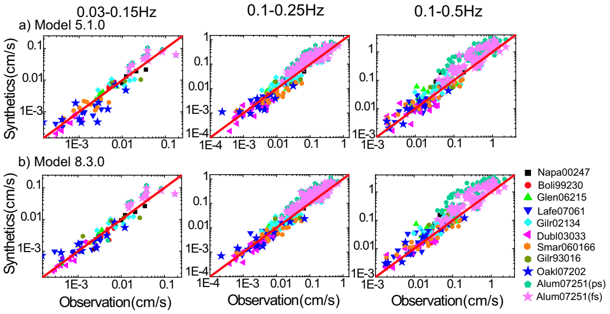

Figure 2.75: Top row shows the comparison between observed and synthetic PGV in three passbands, 0.03-0.15, 0.1-0.25, and 0.1-0.5 Hz for model 5.1.0. The bottom row shows the same for model 8.3.0. The symbols are for different simulated events. The corresponding legends are to the right.

33.3 Modeling results

We performed an analysis of P-wave arrival times by using cross-correlation to determine arrival time differences. For this analysis we low pass filtered the velocity records using an acausal Butterworth filter with corners of 0.1 and 0.5Hz, and then used waveform cross-

ID	Date	lon	lat	Strike	Dip	Rake	Depth	Moment	Mw
gilr93016	01/16/1993	-121.46	37.03	331	83	166	7	2.40E+23	4.9
boli99230	08/18/1999	-122.69	37.91	115	49	69	8	7.25E+22	4.5
napa00247	09/03/2000	-122.41	38.38	60	75	18	11	3.74E+23	5
gilr02134	05/14/2002	-121.6	36.97	212	87	-6	8	2.86E+23	4.9
dubl03033	02/02/2003	-121.94	37.74	67	88	-19	14	1.36E+22	4.1
smar06166	06/15/2006	-121.49	37.1	360	78	-152	5	4.18E+22	4.4
glen06215	08/03/2006	-122.59	38.36	256	86	19	5	5.64E+22	4.4
lafe07061	03/02/2007	-122.1	37.9	82	89	-1	14	2.77E+22	4.2
oakl07202	07/20/2007	-122.18	37.8	321	89	168	5	2.52E+22	4.2
alum07251	10/31/2007	-121.78	37.43	323	87	180	11	1.85E+24	5.4

Table 2.1: Earthquakes simulated in this study. Event ID and the source parameters are obtained from BSL Moment Tensor Catalog.

correlation to find the relative arrival times. We limited the synthetic to shift in time by plus or minus two seconds (for f $<$ 0.5Hz) to avoid possible cycle skipping. As Figure 2.74 shows, consistent with *Rodgers et al.* (2007) for S-e arrival times, the P-wave arrival times for model 5.1.0 are systematically early. The arrival time difference increase with distance suggests it is a systematic error in the seismic wave speed, where P-wave velocity is too high. A recalculation using model 8.3.0 shows that the simulated arrivals are still a little early, but that most of the disagreement with the observations has been accounted for.

The comparison of Peak Ground Velocity (PGV) for both models 5.1.0 and 8.3.0 reveals that both 3D models predict the observed PGV well (Figure 2.75). The comparison shown is for over 4 orders of magnitude values exceeding 1 cm/s where damage begins to manifest in weak unreinforced structures. In the low frequency band (0.03 - 0.15Hz), all of the small events are essentially point-sources, and we see that there is very good one-to-one correspondence between observed and simulated PGV. Both models perform well, but model 8.3.0 seems to reduce the dispersion slightly. This is also true of the intermediate passband (0.1-0.25 Hz). At higher frequencies, the correlation remains good; however, unaccounted for source effects for the larger events, and 3D wave propagation and site conditions become more important, leading to higher dispersion in the predicted amplitudes. Since PGV seems to scale approximately linearly in large events (e.g. *Boore and Atkinson*, 2008; *Campbell and Bozorgnia*, 2008), and PGV in large events is carried by waves of 1 to several seconds period, well within the ranges of the passband of our simulations, the comparison strongly suggests that both 3D velocity models, and particularly model 8.3.0, are suitable for simulating strong ground motion scenarios for the region's high risk faults. It is noted however that the comparison in Figure 2.75 is log-scale, and that the dispersion represents a factor of 2 to 4 in simulated motions. This fact should be considered in the interpretation of predictive maps of scenario earthquake simulations (e.g. *Aagaard et al.*, 2008b). Finally, for the largest event that we considered, the 2007 Mw 5.4 Alum Rock earthquake, there can be significant differences in simulated PGV depending upon the assumed duration of the source. For this event, at most stations synthetic PGV is overestimated, which is due to the strong southwestward rupture directivity and the fact that most stations are located to the northwest of the epicenter. For this event, we also simulated the ground motions by including a uniform slip finite-source model with southeastward rupture. Using this simple finite-source model reduced the amplitude at stations located to the northwest of the epicenter and improved the overall PGV fit (Figure 2.75).

Although the PGV is relatively well explained, and in many cases the three component waveforms match that data well, there remain paths that could benefit from model refinement. In Figure 2.76a three component waveforms for the Bolinas earthquake are compared, and in all cases, except the paths to BDM and POTR, the fit is good. The paths to BDM and POTR are in the same general eastward direction, yet while the fit to the BDM record is much improved with the model 8.3.0, there remains significant misfit at POTR indicating unmodeled structure north of delta, and possibly in the San Pablo Bay. In Figure 2.76b for the 2002 Gilroy earthquake, the two closest stations have good agreement with the primary S waveform amplitudes, but the model fails to explain the large secondary surface wave train at station 1404 due to sediments in the Hollister and Salinas valleys. While the synthetics explain PGV at sites 1404 and 1854 within a factor of less than two (190% and 130%, respectively), they significantly under predict the duration of strong shaking.

33.4 References

Aagaard, B. T., T. M. Brocher, D. Dolenc, D. Dreger, R. W. Graves, S. Harmsen, S. Hartzell, S. Larsen, and M.L. Zoback, Ground-Motion Modeling of the 1906 San Francisco Earthquake, Part I: Validation Using the 1989

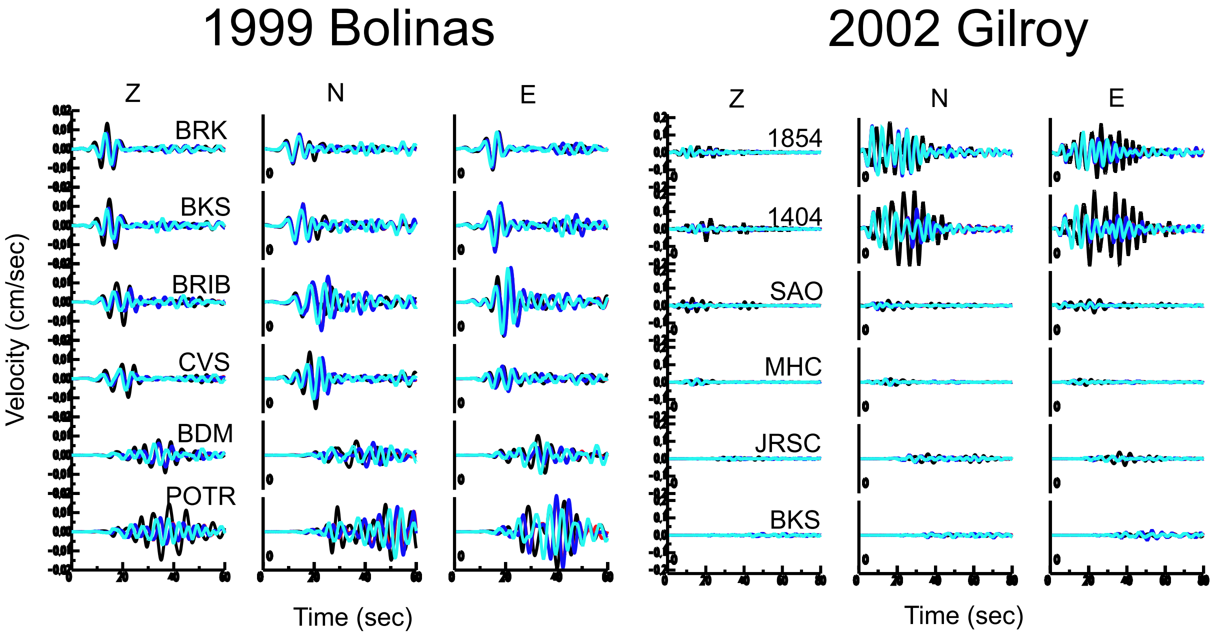

Figure 2.76: Three-component velocity waveforms (black) for 1999 Bolinas earthquake (a) and 2002 Gilroy earthquake (b) are compared to synthetics for models 5.1.0 (cyan) and 8.3.0 (blue). The data and synthetics have been bandpass filtered between 0.10 to 0.25Hz.

Loma Prieta Earthquake, *Bull. Seism. Soc. Am.*, 98, 989-1011, doi: 10.1785/0120060409,2008a.

Aagaard, B. T. M. Brocher, D. Dolenc, D. Dreger, R. W. Graves, S. Harmsen, S. Hartzell, S. Larsen, K. McCandless, S. Nilsson, N. A. Petersson, A. Rodgers, B. Sjogreen, and M. L. Zoback, Ground-Motion Modeling of the 1906 San Francisco Earthquake, Part II: Ground-Motion Estimates for the 1906 Earthquake and Scenario Events, *Bull. Seism. Soc. Am.*, 98, 1012-1046, doi: 10.1785/0120060410,2008b.

Boore, D. M. and G. M. Atkinson, Ground-motion prediction equations for the average horizontal component of PGA, PGV, and 5%-damped PSA at spectral periods between 0.01 s and 10.0 s, *Earthquake Spectra* 24, 99-138,2008.

Brocher, T. M., Emprical relations between elastic wave speeds and density in the Earth's crust, *Bull. Seism. Soc. Am.*, 95 No. 6, 2081-2092,2005.

Dreger D. and B. Romanowicz, Source Characteristics of Events in the San Francisco Bay Region, USGS open-file report, 94-176, 301-309, 1994.

Brocher, T., Compressional and Shear-wave velocity versus depth relations for common rock types in Northern California, *Bull. Seism. Soc. Am.*, 98 No. 2, 950 - 968, 2008.

Campbell, K. and Y. Bozorgnia, NGA Ground Motion Model for the Geometric Mean Horizontal Component of PGA, PGV, PGD and 5% Damped Linear Elastic Response Spectra for Periods Ranging from 0.01 to 10 s, *Earthquake Spectra* 24, 139-171,2008.

Jachens, R., R. Simpson, R. Graymer, C. Wentworth, T. Brocher, Three-dimensional geologic map of northern and central California: A basic model for supporting ground motion simulation and other predictive modeling, 2006 SSA meeting abstract, *Seism. Res. Lett.*, 77, No.2, p 270, 2006.

Larsen, S. and C. A. Shultz, ELAS3D: 2D/3D elastic finite-difference wave propagation code, Technical Report No. UCRL-MA-121792, 1995.

Rodgers A., N., A. Petersson, S. Nilsson, B. Sjogreen, and K. McCandless, Broadband waveform modeling of moderate earthquakes in the San Francisco Bay Area and preliminary assessment of the USGS 3D Seismic velocity model, *Bull. Seism. Soc. Am.*, 98 no. 2, 969-988, 2008.

34. Recalibrating M_L for CISN

Robert Uhrhammer, Margaret Hellweg, Pete Lombard, Kate Hutton (Caltech), Egill Hauksson (Caltech), Allan Walter (USGS Pasadena), Dave Oppenheimer (USGS Menlo Park)

34.1 Research Objectives

Richter (1935) and *Gutenberg and Richter* (1942) developed the local magnitude scale using Wood-Anderson seismographs. *Richter* (1935) defined "local" magnitude measured at a certain station as: $M_L = \log A$ - $\log A_o(\Delta)$ + dM_L. Here M_L is the local magnitude estimate; $\log A$ is the logarithm of the maximum trace amplitude A (in mm) recorded by a standard Wood-Anderson torsion seismograph; $\log A_o(\Delta)$ is the logarithm of a standard event of magnitude zero at the same epicentral distance Δ in km; and dM_L is the adjustment for that station. The M_L estimate for an event is then the arithmetic average of the individual estimates from the Wood-Anderson seismographs that recorded the event.

In the past thirty years, the instrumentation with which we measure earthquakes has changed, and we can now process the data digitally. Nonetheless, we would like to continue to assign events with local magnitudes which are consistent with those that have been calculated in Northern and Southern California in the past.

In 2006-2007, we reported the development of a new $\log A_o(\Delta)$, valid in all of California for hypocentral distances from 1 km to 500 km. In this year, agreement was reached on a set of station corrections, and the CISN M_L parameters were validated by comparing M_L values determined using the "new" and "old" systems.

34.2 Data Set

A set of approximately 100,000 waveforms from 255 candidate earthquakes recorded by 1160 horizontal channels (Station-Network-Channel-Location, or SNCL labels are used to describe each) from the AZ, BK, CI and NC networks was selected. The candidate events were selected from the CISN 2000-2006 seismicity by gridding the state into 50 km square bins. Two events were selected for each bin: the largest M_L 3+ event, and the largest M_L 3+ event in 2006 (or second largest if the largest 2000-2006 event in the bin occurred in 2006) to obtain adequate data USArray stations. The SNCL channels included both broadband and strong motion instruments. The data set was culled to remove events and SNCLs with fewer than 7 data each and to also remove data with event-SNCL distances greater than 500 km. Local magnitude (M_L) was calculated from each channel's trace by deconvolving the instrument response and convolving the response of a Wood-Anderson seismograph (*Uhrhammer et al*, 1996). For each event, differences for all SNCL pairs were calculated, giving a dataset with more than 10 million differential observations. The differential data were inverted, via constrained linear least-squares with two constraints: (1) $\log A_o(100km)$ = -3; and (2) the sum of the dM_Ls for selected SNCLs with historical dM_L values = the sum of their historical dM_L values. This approach was taken to ensure consistency with past magnitudes determined in Northern and Southern California.

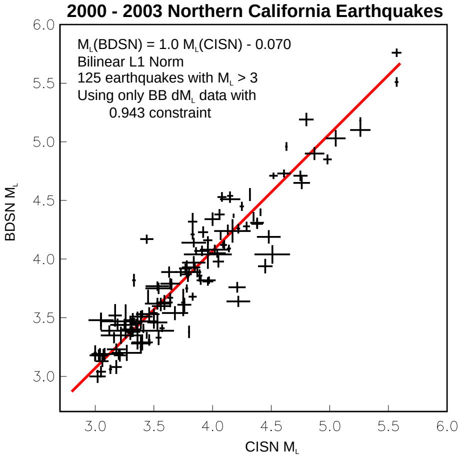

Figure 2.77: Comparison of M_L for Northern California (NC) earthquakes recorded in 2000-2003 determined using the new CISN function and with parameters currently used in NC. Uncertainties exist for both measurements and depend mainly on the number of SNCLs used in the calculation. The slope is close to 1 and the intercept close to 0, indicating good agreement.

34.3 $\log A_o$ and SNCL dM_Ls

The constrained linear least-squares perturbations to the $\log A_o$ function were found to be very stable and well represented by a sixth order Chebyshev polynomial at hypocentral distances from 8 km to 500 km hypocentral distance. At shorter distances, it is approximated by a line with a slope close to 2. This $\log A_o$ form was adopted and an algorithm was developed and used in the subsequent inversions for the dM_L SNCL adjustments. The dM_Ls for the broadband SNCLs were then determined and found to be acceptable for the colocated strong motion sensors as well.

To assess the consistency of the CISN M_L with existing M_Ls, we performed three comparisons. In Figure 2.77, M_L values taken from the Northern California database are compared against CISN M_L determined for

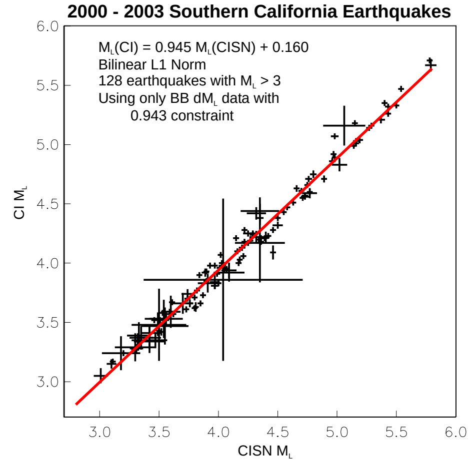

Figure 2.78: Comparison of M_L for Southern California (SC) earthquakes recorded in 2000-2003 determined using the new CISN function and with parameters currently used in SC. Uncertainties exist for both measurements and depend mainly on the number of SNCLs used in the calculation. The slope is close to 1 and the intercept close to 0, indicating good agreement.

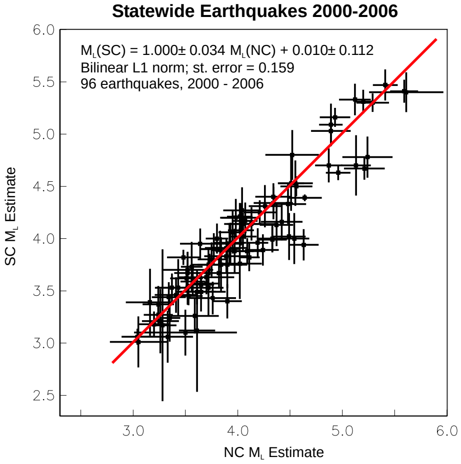

Figure 2.79: CISN M_L for events from 2000-2006 recorded in both Northern and Southern California. The horizontal axis gives M_L for an event calculated using only Northern California SNCLs while the vertical axis gives the M_L from Southern California SNCLs. The greater uncertainty for Northern California M_L results from the lower density of seismic stations.

the same events using the same Wood-Anderson amplitudes. In the figure, the uncertainties for both magnitudes are shown; they depend primarily on the number of SNCLs contributing to the determination. As both M_L values have uncertainties, the best fit line is calculated using a bilinear L1 norm. Reassuringly, the slope of the line is close to one and the intercept close to zero, indicating agreement between the two M_L systems. Figure 2.78 makes a similar comparison for Southern California earthquakes. Here again, the slope is one, to within the uncertainty, and the intercept is zero.

In a final validation step, we selected a set of 96 earthquakes recorded by both Northern and Southern California stations during the interval 2000-2006 (Figure 2.79. CISN M_L values determined only using Northern (horizontal axis) or Southern (vertical axis) SNCLs also agree well (slope=1, intercept=0).

Significance of Findings

The new state-wide $\log A_o$ and station corrections for determining magnitudes will improve reporting for earthquakes in all of California on several counts. First, M_L was being calculated using only a subset of the currently existing broadband stations in both Northern and Southern California, as only they had been calibrated. In the past 10 years, many broadband stations and strong motion stations have been added to the networks. With the additional stations, M_L determination should become much more reliable. Second, until now Northern (*Uhrhammer et al*, 1996) and Southern California (*Kanamori et al*, 1999) have been using different $\log A_o$ functions, with their attendant dM_L values for each SNCL. Thus different magnitudes were often determined by Northern or Southern California for an earthquake if it was near the boundary of the reporting regions, or for very large earthquakes in the other region. Figure 2.79 shows that this will no longer be the case. The CISN M_L system is being used in Southern California since February 2008. It will be implemented in Northern California with the transition to the new event processing software.

34.4 Acknowledgements

Work on this project has been supported by the CISN funding of the California Governor's Office of Emergency Services under contract 6023-5 and the United States Geological Survey project 07HQAG0013.

34.5 References

Richter, C.F., An instrumental earthquake magnitude scale, *Bull. Seismol. Soc. Am.*, *25*, 1-32, 1935.

Gutenberg, B. and Richter, C. F, Earthquake magnitude, intensity, energy and acceleration, *Bull. Seismol. Soc. Am.*, *32*, 163-192, 1942.

Uhrhammer, R., Loper. S. J., Romanowicz, B., Determination of local magnitude using BDSN broadband records *Bull. Seismol. Soc. Am.*, *86*, 1314-1330, 1996.

Kanamori, H., Maechling, P., Hauksson, E., Continuous Monitoring of Ground-Motion Parameters *Bull. Seismol. Soc. Am.*, *89*, 311-316, 1999.

35. Seismic Deployments across the Pacific Northwest

Rob Porritt, Richard Allen, Devin Boyarko (Miami University, Ohio), Mike Brudzinski (Miami University, Ohio), Hector Hinojosa (Miami University, Ohio), Gene Humphreys (University of Oregon), Alan Levander (Rice University), Leland O'Driscal (University of Oregon), Yungo Zhal (Rice University)

35.1 Introduction

The Flexible Array (FA) component of the USArray densifies the station coverage already provided by the Transportable Array (TA) and permanent networks. FA experiments are PI driven, supported by the PASSCAL instrument center at New Mexico Tech, and usually last 1-3 years. UC Berkeley is currently involved in two such experiments. The Flexible Array Mendocino Experiment (FAME) with the University of Oregon and Rice University is a dense 79 station network in Northern California and the FlexArray along Cascadia Experiment for Segmentation (FACES) is a 23 station array throughout Oregon and Washington in collaboration with Miami University of Ohio. Both experiments employ Guralp CMG-3T broadband seismometers continuously sampling at 40 samples per second with a flat response to approximately 120 seconds period. The figure displays the station coverage along the US West Coast from just north of San Francisco to Seattle.

35.2 Flexible Array Mendocino Experiment (FAME)

The Mendocino Experiment is designed to image the crust and upper mantle in Northern California around the Mendocino Triple Junction (MTJ). The 79 stations with a 25km average spacing constitute one fifth of all broadband instruments available from the PASSCAL instrument center. This array consists of three main parts: a dense line along the coast from Cape Mendocino to Healdsburg, CA, an evenly spaced distribution throughout inland Northern California, and 14 stations inherited from the Sierra Nevada Earthscope Project (SNEP) in the southeast region of the array. The instruments were primarily installed in two surges: the first in July 2007 and the second in October 2007. The experiment will run through the fall of 2009.

The primary goal of FAME is to investigate and further understand the complex proccesses and structures involved at the intersection of the North America, Gorda, and Pacific plates where a subduction zone and two transform boundaries meet. This triple junction is migrating to the north relative to a fixed North America plate and thus provides a rare opportunity to study an unstable triple junction. FAME will improve the understanding of how and why the tectonics change from a transform fault to a subduction zone along the west coast.

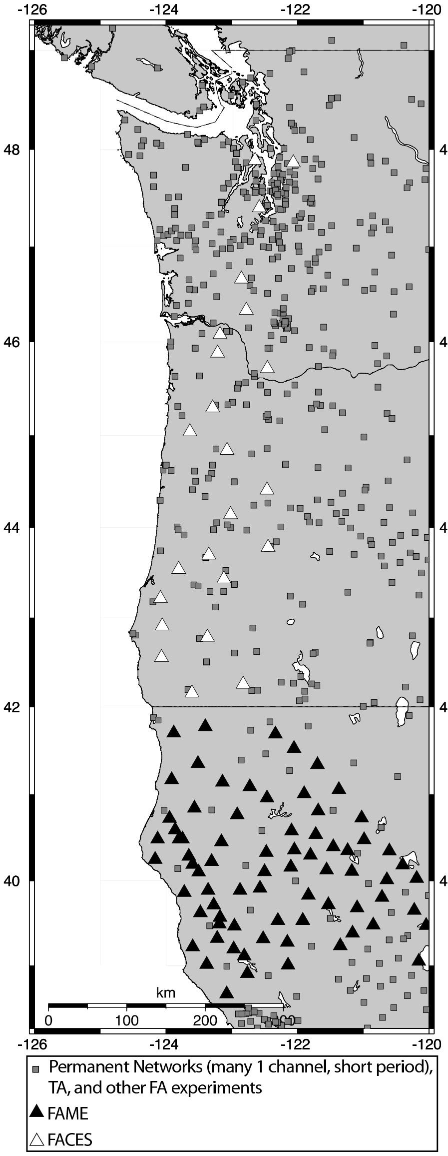

Figure 2.80: Map of current stations available through the IRIS DMC.

Gorda crust and overlying sediment subduct and become incorporated in accretionary terranes from the Cascadia subduction zone. This mass flows into the emerging transform margin and becomes structured into the San Andreas strike-slip system. Simultaneously, slab gap opening south of the Gorda slab causes asthenospheric ascent and decompression melting, which magmatically underplates North America near the San Andreas fault. The reprocessed and inflated lithosphere thickens to create a small Cape Mendocino orogenic plateau. Meanwhile, erosion moves large fractions of the upper crust back to the subduction zone along tectonically controlled north-trending rivers. Nearby, Gorda-Juan de Fuca subduction results in the Cascade volcanoes, which also contribute to continental crust growth, segregation and recycling. The 3-D seismic velocity models of the crust and upper mantle, which will be developed as part of this project, will be included in event and strong ground motion characterization for Northern California and southern Oregon, a site of potentially devastating great earthquakes.

35.3 FlexArray along Cascadia Experiment for Segmentation (FACES)

FACES is a long array from the California/Oregon border to Seattle deployed at an average spacing of 40km. The majority of stations are in Oregon due to its relatively sparse coverage from permanent networks. The stations were installed in early November 2007. The availability of cellular phone coverage throughout the region allows deployment of modems on most of the stations for real time telemetry. This is the first FA experiment to employ this technology allowing constant monitoring of the state of the network from anywhere with Internet access.

The recurrence of Episodic Tremor and Slip (ETS) is widely observed, but poorly understood. Recent findings show segmentation in recurrance interval of ETS along the Cascadia Subduction Zone (*Brudzinski and Allen*, 2007). The region appears to be split into three primary zones of distinct recurrence intervals. The best preliminary correlation appears to be with the geologic terrain of the continental plate. The increased station density due to FACES throughout this region will better illuminate this phenomenon.

35.4 Innovations in station deployment

A common installation difficulty results from an uneven base upon which the seismometer is set. In these deployments, when possible, self-leveling grout was employed and left to set overnight. This allowed for minimal effort being exerted to level the sensors.

Heat fluctuations can damage both the sensor and the controlling electronics package and temperature changes can become a significant source of noise. To combat these dangers, the sensors are placed in a plastic bag and surrounded with insulating sand. The electronics package is protected by a standard plastic case with reflective material reducing the effect of direct sunlight.

The most exciting development in the current deployments is the utilization of telemetry through cellular phone service. A small cellular modem is installed with the electronics package of the sensor and sends station health information and realtime data back to the BSL through cell phone towers. FACES is currently the largest deployment using this technology.

35.5 Acknowledgements

The authors would like to thank the following for their hard work installing and servicing various stations: Derry Webb, Marcos Alvarez, Lloyd Carothers, Eliana Arias Dotson, Pat Ryan, Lisa Linville, Pallavi Chethan, Kevin Jensen, Chris McMillan, Stefany Sit, Andrew Tran, Summer Ohlendorf, Dan'L Martinez, Valerie Zimmer, Will Levandowski, Amanda Thomas, Heidi Reeg, Nickles Badger, Tom Owens, Eileen Evans, Holly Brown, Joanne Emerson, Ajay Limaye, Rick Lellinger.

This work has been made possible with the resources available through the PASSCAL instrument center at New Mexico Tech.

Funding has come from NSF grants EAR0643392 and EAR0745934 for FAME and EAR0643007 for FACES.

35.6 References

Brudzinski, M. and R.M. Allen, Segmentation in Episodic Tremor and Slip All Along Cascadia, *Geology*, 907-910, 2007.

36. TMTS, the interactive moment tensor review interface, and the Berkeley Moment Tensor Catalog

Jennifer Taggart, Angela Chung, Rick McKenzie, Peggy Hellweg, and Doug Dreger

36.1 Research Objectives

Since 1992, the BSL has been calculating moment tensor solutions for selected events in Northern California (*Romanowicz et al, 1993*). At present, moment tensor solutions are calculated in real time for most events with M_w 3.5 and above in Northern California (*Pasyanos et al, 1996*). The newest version of the program used for reviewing them is a Web-based interface, TMTS. The implementation at UCB is based on a package developed at Caltech (*Clinton et al*, 2007) and uses the waveform moment tensor inversion code developed by Dreger (*Minson and Dreger*, 2008). This interface allows analysts to calculate solutions from any computer with Web access and a browser. The interface relies on recent waveforms in the DART and archived data at the NCEDC (see Chapter 3, Section 6.). In addition, TMTS allows the calculation of deviatoric moment tensor solutions and optionally the full moment tensor. In the past, solutions have been stored in the Berkeley Moment Tensor Catalog, a text file with the strike, rake, and dip of the fault plane solution as well as moment, M_w, and a listing of the stations used. The new moment tensor review interface connects to a database where all the information needed to recreate the moment tensor solution is saved (see Figure 2.81). Thus, porting the catalog to the new database required us to recalculate each moment tensor using TMTS.

36.2 Data Set

We selected earthquakes in the Berkeley Moment Tensor Catalog from within the reporting region for recalculation with the new interface and inclusion in the database. Geysers events and events outside the region were set aside. Events from the years 2004 and 2005 were assigned to the USGS for training purposes.

36.3 Approach

When recalculating the moment tensors with the new program, we made an effort to match the original solution as closely as possible. Provided three or more stations were used, the same stations were used for the recalculation. For earthquakes with M_w between 3.5 and 4.0 and with an original solution of high quality, we tried to match the strike, rake, and dip of the original solution to within 10 degrees and the M_w to within .1. For earthquakes with M_w above 4.0, the strike, rake, and dip were to match within 5 degrees and the M_w to within .05. We also attempted to match the value for M_0.

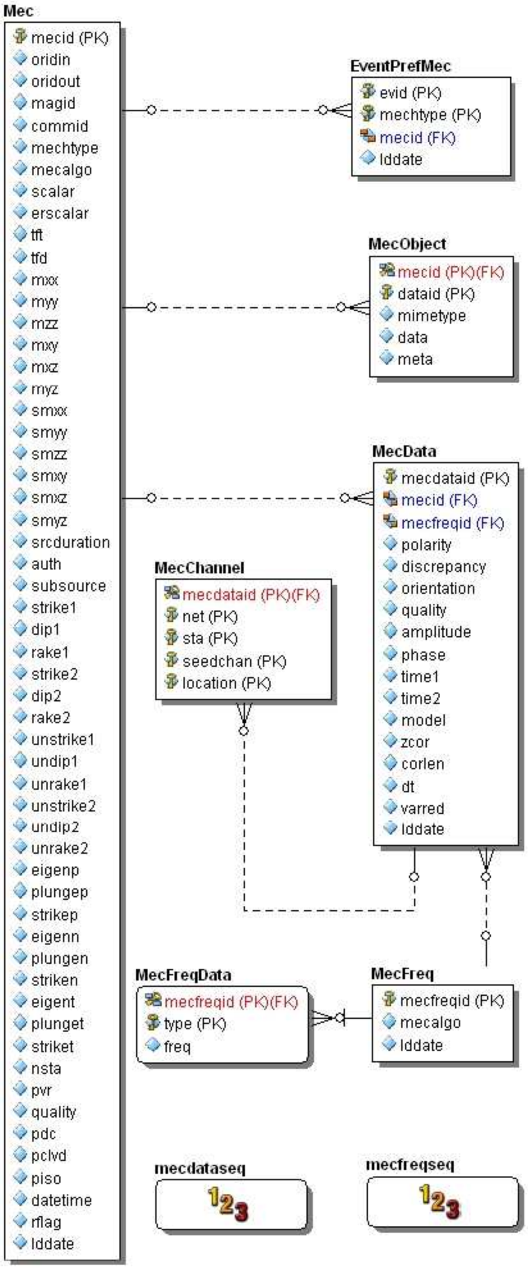

Figure 2.81: Tables and relationships in the database where the moment tensor information is stored.

TMTS has a number of features that make calculation of moment tensors faster. When an event loads, the program automatically selects a set of stations based on distance and azimuth. Stations can be changed using the buttons on the Station Normal page, accessible by a tab in the program. The Station Advanced tab takes the user to a page where other parameters can be changed. Users can choose between three filters, and, for each station, the correlation length between the seismogram and the synthetics can be changed to any value, facilitating analysis of different-sized earthquakes at different distances. Three sets of synthetic Greens functions are available to account for the velocity structure of different areas of California. The Zcorr, a value that determines how far to advance the synthetic seismogram and depends on station-event distance, can be set to any value for each station to allow fine-tuning and correcting misfits. The depth can be fixed once it is known, allowing quicker recalculations when refining the solution. On the left hand side, next to the tabs, a plot of the variance reduction, a measure of fit, is shown at different depths. This plot can also be shown in another window or tab of the Web browser. A plot of variance reduction over percent double couple and plots of each full solution at the program's 12 chosen depths can be shown in this way as well. In contrast to the previous arrangement, where parameters had to be changed in text files and multiple programs had to be run at the command line, TMTS makes each option available as a button or box.

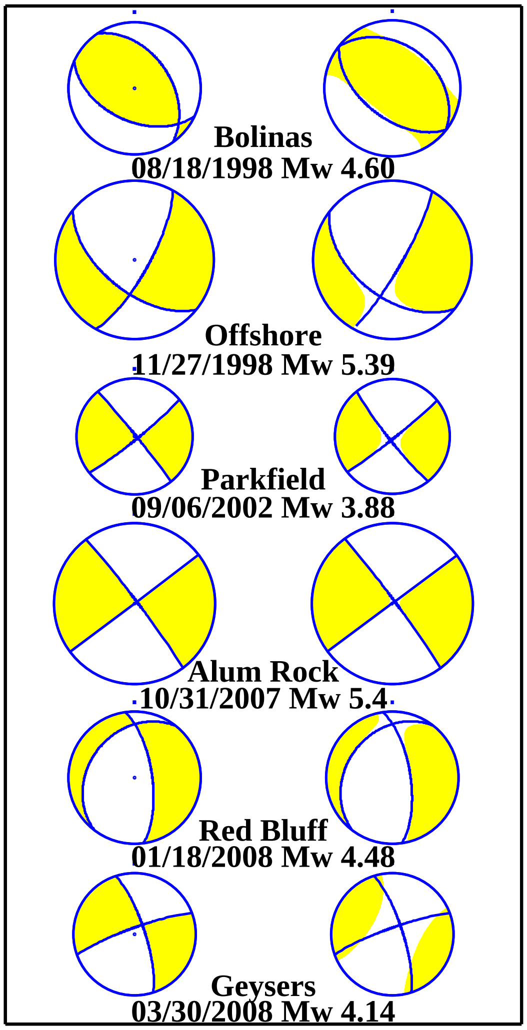

Figure 2.82: Comparison between selected moment tensors in the UCB catalog and deviatoric moment tensors calculated with the new program (right).

36.4 Significance of Findings

In Figure 2.82, selected mechanisms from the UCB catalog are compared with the deviatoric moment tensors calculated with the new program. At the top is the August 18, 1998 Bolinas event, an earthquake with an unusual moment tensor for that area. Next is an example of a shallow offshore event. An event from the Parkfield area and the October 31, 2007 Alum Rock event both show a high degree of double couple. In contrast, the Geysers earthquake at the bottom is an event where the compensated linear vector dipole component of the deviatoric solution is important. Also shown is the smaller of the two January 2008 Red Bluff events. Non double couple elements in the solution may be real (*Dreger et al, 2000, Dreger et al, 2008, Ford et al, 2008*), as is likely to be the case for the Geysers event. For small events, they may indicate a relatively poor signal-to-noise ratio.

Approximately 350 moment tensors for earthquakes in Northern California are now in the database with their complete waveforms and all of the parameters involved in their calculation. Table 2.2 shows the year by year breakdown of recomputed events. In Figure 2.83, a comparison of M_w from the old and new moment tensor catalog shows no systematic bias toward higher or lower values with the new program. Plans are in place to make the new Berkeley moment tensor database searchable so that researchers can call up full solutions of events that meet their criteria.

36.5 Acknowledgements

Implementation at UCB would not have been possible without the programming support provided by Alexei Kireev, Pete Lombard, and Doug Neuhauser.

Work on this project was supported by the CISN funding of the California Governor's Office of Emergency Services under contract 6023-5 and the United States Geological Survey project 07HQAG0013.

Year	Old Catalog	New Catalog
1995	68	50
1996	51	34
1997	68	54
1998	46	39
1999	42	38
2000	29	22
2001	28	24
2002	23	19
2003	41	34
2004	59	USGS
2005	20	USGS
2006	27	23
2007	34	22

Table 2.2: Table of events in old and new catalogs.

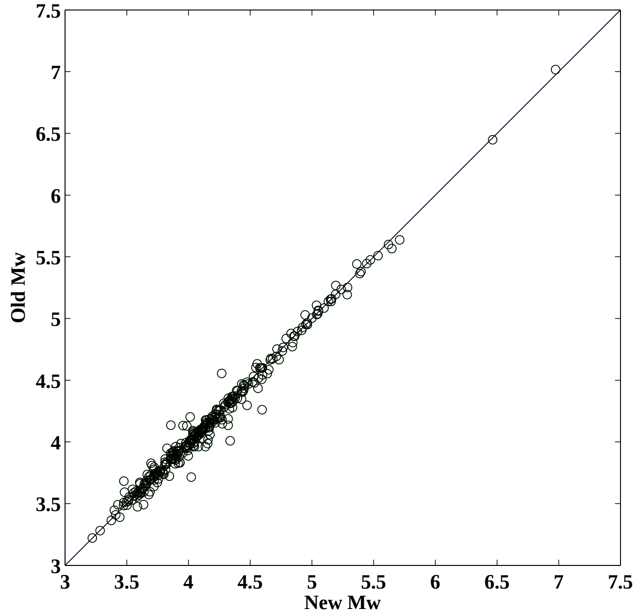

Figure 2.83: Comparison of values of M_w for moment tensors calculated with both programs.

36.6 References

Clinton, J.F., E. Hauksson, and K. Solanki, An Evaluation of the SCSN Moment Tensor Solutions: Robustness of the M_w Magnitude Scale, Style of Faulting, and Automation of the Method, *Bull. Seism. Soc. Am.*, **96**, 1689 - 1705, 2006.

Dreger, D. S., H. Tkalcic, and M. Johnston, Dilational processes accompanying earthquakes in the Long Valley Caldera, *Science*, **288**, 122-25, 2000.

Dreger, D., S.R. Ford, and W.R. Walter (2008), Source analysis of the Crandall Canyon, Utah mine collapse, *Science*, **321**, 217, 2008.

Ford, S. R., D. S. Dreger and W. R. Walter, Source Characterization of the August 6, 2007 Crandall Canyon Mine Seismic Event in Central Utah, submitted to *Seism. Res. Lett.*, 2008.

Minson, S. and D. Dreger, Stable Inversions for Complete Moment Tensors, *Geophys. Journ. Int.*, in press.

Pasyanos, M.E., D.S. Dreger, and B. Romanowicz, Toward Real-Time Estimation of Regional Moment Tensors, *Bull. Seism. Soc. Am.*, **86**, 1255-1269, 1996.

Romanowicz, B. D. Dreger, M . Pasyanos, and R. Uhrhammer (1993). Monitoring of Strain Release in Central and Northern California Using Broadband Data, *Geophys. Res. Lett.*, **20**, 1643-1646, 1993.

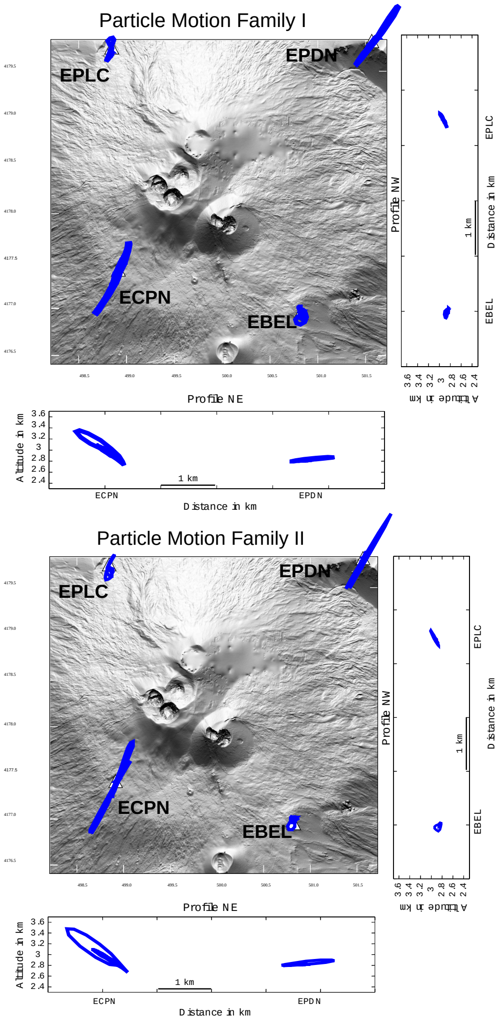

Figure 2.84: From Chapter 2, Section 23: Particle motion for very long period (VLP) events of Family I (top) and Family II (bottom). The map view shows particle motion in the horizontal plane; the two cross sections (to the right of and below the maps) show particle motion across the crater from ECPN to EDPN and from EPLC to EBEL.

Chapter 3

BSL Operations

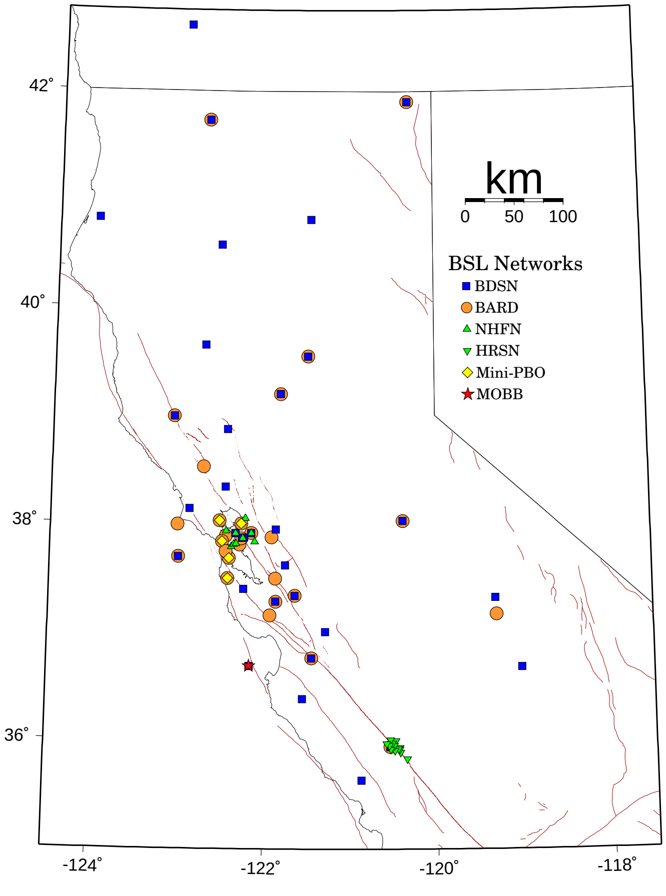

Figure 3.1: Map illustrating the distribution of BSL networks in Northern and Central California.

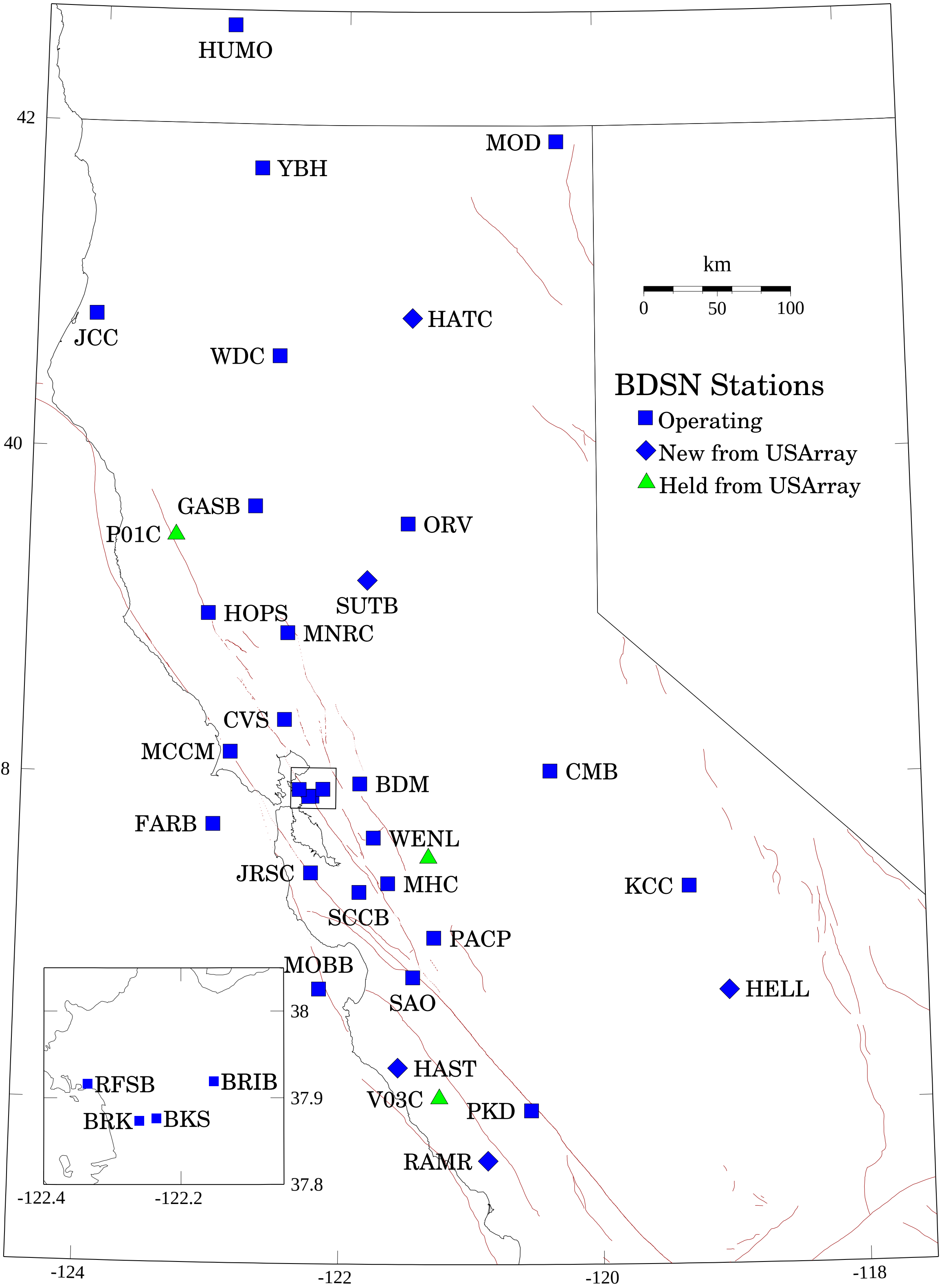

Figure 3.2: Map illustrating the distribution of BDSN stations in Northern and Central California.

1. Berkeley Digital Seismic Network

1.1 Introduction

The Berkeley Digital Seismic Network (BDSN) is a regional network of very broadband and strong motion seismic stations spanning Northern California and linked to UC Berkeley through continuous telemetry (Figure 3.2 and Table 3.1). The network is designed to monitor regional seismic activity at the magnitude 3+ level as well as to provide high quality data for research in regional and global broadband seismology.

Since 1991, the BDSN has grown from the original 3 broadband stations installed in 1986-87 (BKS, SAO, MHC) to 32 stations, including an autonomous ocean-bottom seismometer in Monterey Bay (MOBB). We take particular pride in high quality installations, which often involve lengthy searches for appropriate sites away from sources of low-frequency noise as well as continuous improvements in installation procedures and careful monitoring of noise conditions and problems. While maintenance and repair were an important focus of this year's efforts, we were also able to add five new stations as the USArray deployment left California. Considerable engineering and research activities were also involved in several projects to develop and test new instrumentation (see Section 7., Section 9., and Chapter 1, Section 34.). The project involving new electronics for the STS-1 seismometers, the E300, was completed, and we have deployed the beta version of the electronics for testing at several stations. It is currently at KCC. We also made progress in testing a new, low-cost sensor for pressure and temperature to be installed at seismic and GPS sites. Finally, the BSL is part of a team to develop and test a new version of the STS-1 seismometer.

As always, the expansion of our network to increase the density of state-of-the-art strong motion/broadband seismic stations and improve the joint earthquake notification system in this seismically hazardous region, one of BSL's long term goals, must be coordinated with other institutions and is contingent on the availability of funding.

Equally important to network growth, data quality and the integrity of the established network must be preserved. The first generation of broadband seismometers installed by BSL have been operating for almost 25 years. At the same time, the first generation of broadband data loggers are entering their 17th year of service. This requires continued vigilance and the commitment of time and resources to both repairs and upgrades.

1.2 BDSN Overview

Twenty-nine of the BDSN sites are equipped with three component broadband seismometers and strong-motion accelerometers, and a 24-bit digital data acquisition system or data logger. Two additional sites (RFSB and SCCB) consist of a strong-motion accelerometer and a 24-bit digital data logger. The ocean-bottom station MOBB is equipped with a three component broadband seismometer. Data from all BDSN stations, except MOBB, are transmitted to UC Berkeley using continuous telemetry. In order to avoid data loss during utility disruptions, each site has a three-day supply of battery power; many are accessible via a dialup phone line. The combination of high-dynamic range sensors and digital data loggers ensures that the BDSN has the capability to record the full range of earthquake motion required for source and structure studies. Table 3.2 lists the instrumentation at each site.

Most BDSN stations have Streckeisen STS-1 or STS-2 three-component broadband sensors (*Wielandt and Streckeisen*, 1982; *Wielandt and Steim*, 1986). A Guralp CMG-3T downhole broadband sensor contributed by LLNL is deployed in a post-hole installation at BRIB. A Guralp CMG1-T is deployed at MOBB. The strong-motion instruments are Kinemetrics FBA-23, FBA-ES-T or MetroZet accelerometers with ± 2 g dynamic range. The recording systems at all sites are either Q330, Q680, Q730, or Q4120 Quanterra data loggers, with 3, 6, 8, or 9 channel systems. The Quanterra data loggers employ FIR filters to extract data streams at a variety of sampling rates. In general, the BDSN stations record continuous data at .01, 0.1, 1.0, 20.0 or 40.0, and 80 or 100 samples per second. However, at some sites, data at the highest sampling rate are sent in triggered mode using the Murdock, Hutt, and Halbert event detection algorithm (*Murdock and Hutt*, 1983) (Table 3.3). In addition to the 6 channels of seismic data, signals from thermometers and barometers are recorded at many locations (Figure 3.3).

As the broadband network was upgraded during the 1990s, a grant from the CalREN Foundation (California Research and Education Network) in 1994 enabled the BSL to convert data telemetry from analog leased lines to digital frame-relay. The frame-relay network uses digital phone circuits which support 56 Kbit/s to 1.5 Mbit/s throughput. Since frame-relay is a packet-switched network, a site may use a single physical circuit to communicate with multiple remote sites through the use of "permanent virtual circuits". Frame Relay Access Devices (FRADs), which replace modems in a frame-relay network, can simultaneously support a variety of interfaces such as RS-232 async ports, synchronous V.35 ports, and ethernet connections. In practical terms, frame relay communication provides faster data telemetry between

Code	Net	Latitude	Longitude	Elev (m)	Over (m)	Date	Location
BDM	BK	37.9540	-121.8655	219.8	34.7	1998/11 -	Black Diamond Mines, Antioch
BKS	BK	37.8762	-122.2356	243.9	25.6	1988/01 -	Byerly Vault, Berkeley
BRIB	BK	37.9189	-122.1518	219.7	2.5	1995/06 -	Briones Reservation, Orinda
BRK	BK	37.8735	-122.2610	49.4	2.7	1994/03 -	Haviland Hall, Berkeley
CMB	BK	38.0346	-120.3865	697.0	2	1986/10 -	Columbia College, Columbia
CVS	BK	38.3453	-122.4584	295.1	23.2	1997/10 -	Carmenet Vineyard, Sonoma
FARB	BK	37.6978	-123.0011	-18.5	0	1997/03 -	Farallon Island
GASB	BK	39.6547	-122.716	1354.8	2	2005/09 -	Alder Springs
HAST	BK	36.3887	-121.5514	542.0	3	2006/02 -	Carmel Valley
HATC	BK	40.8161	-121.4612	1009.3	3	2005/05 -	Hat Creek
HELL	BK	36.6801	-119.0228	1140.0	3	2005/04 -	Miramonte
HOPS	BK	38.9935	-123.0723	299.1	3	1994/10 -	Hopland Field Stat., Hopland
HUMO	BK	42.6071	-122.9567	554.9	50	2002/06 -	Hull Mountain, Oregon
JCC	BK	40.8175	-124.0296	27.2	0	2001/04 -	Jacoby Creek
JRSC	BK	37.4037	-122.2387	70.5	0	1994/07 -	Jasper Ridge, Stanford
KCC	BK	37.3236	-119.3187	888.1	87.3	1995/11 -	Kaiser Creek
MCCM	BK	38.1448	-122.8802	-7.7	2	2006/02 -	Marconi Conference Center, Marshall
MHC	BK	37.3416	-121.6426	1250.4	0	1987/10 -	Lick Obs., Mt. Hamilton
MNRC	BK	38.8787	-122.4428	704.8	3	2003/06 -	McLaughlin Mine, Lower Lake
MOBB	BK	36.6907	-122.1660	-1036.5	1	2002/04 -	Monterey Bay
MOD	BK	41.9025	-120.3029	1554.5	5	1999/10 -	Modoc Plateau
ORV	BK	39.5545	-121.5004	334.7	0	1992/07 -	Oroville
PACP	BK	37.0080	-121.2870	844	0	2003/06 -	Pacheco Peak
PKD	BK	35.9452	-120.5416	583.0	3	1996/08 -	Bear Valley Ranch, Parkfield
RAMR	BK	37.9161	-122.3361	416.8	3	2004/11 -	Ramage Ranch
RFSB	BK	37.9161	-122.3361	-26.7	0	2001/02 -	RFS, Richmond
SAO	BK	36.7640	-121.4472	317.2	3	1988/01 -	San Andreas Obs., Hollister
SCCB	BK	37.2874	-121.8642	98	0	2000/04 -	SCC Comm., Santa Clara
SUTB	BK	39.2291	-121.7861	252.0	3	2005/10 -	Sutter Buttes
WDC	BK	40.5799	-122.5411	268.3	75	1992/07 -	Whiskeytown
WENL	BK	37.6221	-121.7570	138.9	30.3	1997/06 -	Wente Vineyards, Livermore
YBH	BK	41.7320	-122.7104	1059.7	60.4	1993/07 -	Yreka Blue Horn Mine, Yreka

Table 3.1: Stations of the Berkeley Digital Seismic Network currently operating. Each BDSN station is listed with its station code, network id, location, operational dates, and site description. The latitude and longitude (in degrees) are given in the WGS84 reference frame, and the elevation (in meters) is relative to the WGS84 reference ellipsoid. The elevation is either the elevation of the pier (for stations sited on the surface or in mining drifts) or the elevation of the well head (for stations sited in boreholes). The overburden is given in meters. The date indicates either the upgrade or installation time.

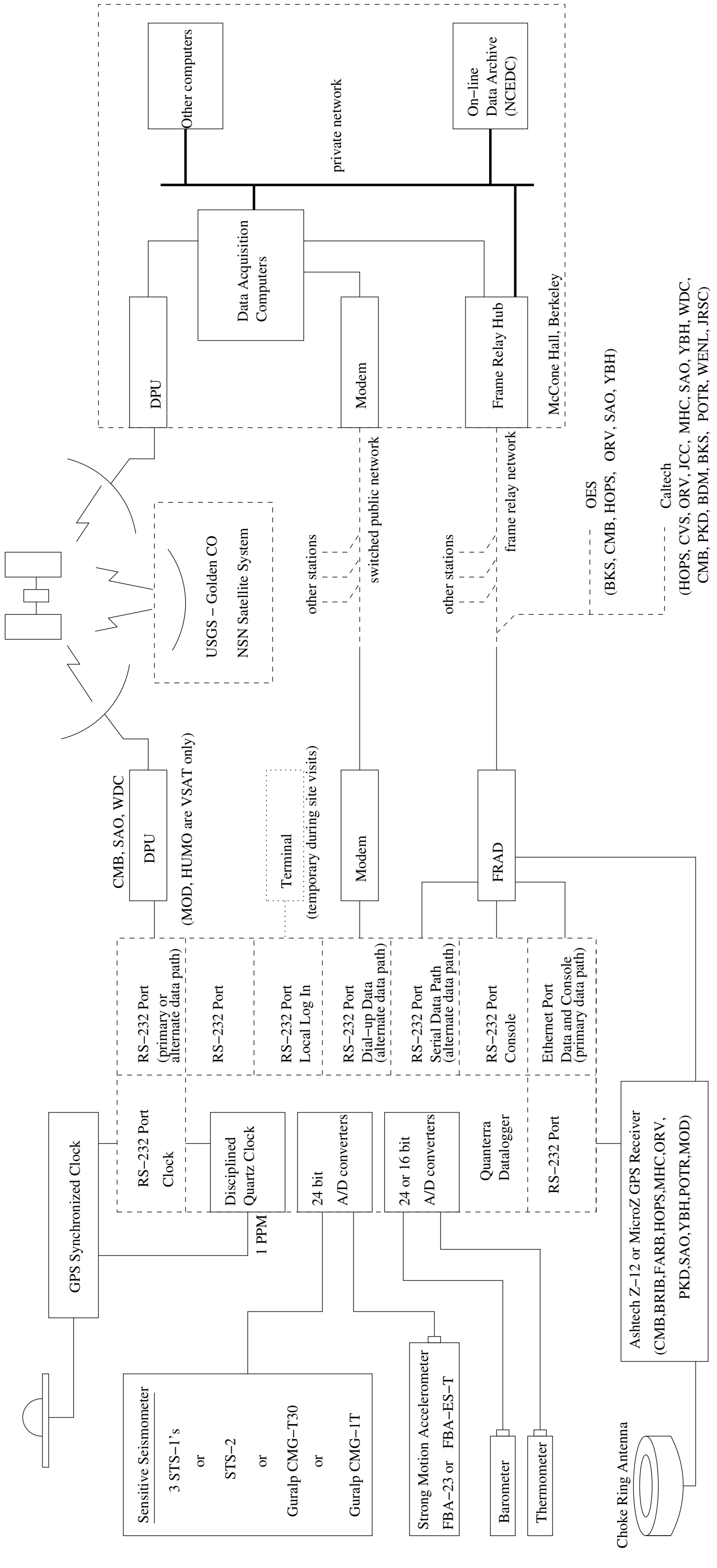

Figure 3.3: Schematic diagram showing the flow of data from the sensors through the data loggers to the central acquisition facilities of the BSL.

Code	Broadband	Strong-motion	data logger	T/B	GPS	Other	Telemetry	Dial-up
BDM	STS-2	FBA-23	Q4120	X			FR	
BKS	STS-1	FBA-23	Q980	X		Baseplates	FR	X
BRIB	CMG-3T	FBA-23	Q980		X	Vol. Strain	FR	X
BRK	STS-2	FBA-23	Q680				LAN	
CMB	STS-1	FBA-23	Q980	X	X	Baseplates	FR	X
CVS	STS-2	FBA-23	Q4120	X			FR	
FARB	CMG-3T	FBA-23	Q4120	X	X		R-FR/R	
GASB	STS-2	FBA-ES-T	Q4120	X			R-FR	
HAST	STS-2	FBA-ES-T	Q330				R-Sat	
HATC	STS-2	FBA-ES-T	Q330				T-1	
HELL	STS-2	FBA-ES-T	Q330				R-Sat	
HOPS	STS-1	FBA-23	Q980	X	X	Baseplates	FR	X
HUMO	STS-2	FBA-ES-T	Q4120	X			VSAT	X
JCC	STS-2	FBA-23	Q980	X			FR	X
JRSC	STS-2	FBA-23	Q680				FR	X
KCC	STS-1	FBA-23	Q980	X		Baseplates	R-Mi-FR	X
MCCM	STS-2	FBA-ES-T	Q4120				VSAT	
MHC	STS-1	FBA-23	Q980	X	X		FR	X
MNRC	STS-2	FBA-ES-T	Q4120	X			None	X
MOBB	CMG-1T		GEOSense			Current meter, DPG	None	
MOD	STS-1*	FBA-ES-T	Q980	X	X	Baseplates	VSAT	X
ORV	STS-1	FBA-23	Q980	X	X	Baseplates	FR	X
PACP	STS-2	FBA-ES-T	Q4120	X			Mi/FR	
PKD	STS-2	FBA-23	Q980	X	X	EM	R-FR	X
RAMR	STS-2	FBA-ES-T	Q330				R-FR	X
RFSB		FBA-ES-T	Q730				FR	
SAO	STS-1	FBA-23	Q980	X	X	Baseplates, EM	FR	X
SCCB		MetroZet	Q730		X		FR	
SUTB	STS-2	FBA-EW-T	Q330				R-FR	
WDC	STS-2	FBA-23	Q980	X			FR	X
WENL	STS-2	FBA-23	Q4120	X			FR	
YBH	STS-1 & STS-2	FBA-23	Q980	X	X	Baseplates	FR	X

Table 3.2: Instrumentation of the BDSN as of 06/30/2007. Except for PKD1, RFSB, SCCB and MOBB, each BDSN station consists of collocated broadband and strong-motion sensors, with a 24-bit Quanterra data logger and GPS timing. The stations RFSB and SCCB are strong-motion only, while MOBB has only a broadband sensor. Additional columns indicate the installation of a thermometer/barometer package (T/B), collocated GPS receiver as part of the BARD network (GPS), and additional equipment (Other), such as warpless baseplates or electromagnetic sensors (EM). The obs station MOBB also has a current meter and differential pressure gauge (DPG). The main and alternate telemetry paths are summarized for each station. FR - frame relay circuit, LAN - ethernet, Mi - microwave, POTS - plain old telephone line, R - radio, Sat - Commercial Satellite, VSAT - USGS ANSS satellite link, None - no telemetry at this time. An entry like R-Mi-FR indicates telemetry over several links, in this case, radio to microwave to frame relay. (*) During 2007-2008 the STS-1 at this station was replaced by an STS-2.

the remote sites and the BSL, remote console control of the data loggers, services such as FTP and telnet to the data loggers, data transmission to multiple sites, and the capability of transmitting data from several instruments at a single site, such as GPS receivers and/or multiple data loggers. Today, 25 of the BDSN sites use frame-relay telemetry for all or part of their communications system.

As described in Section 7., data from the BDSN are acquired centrally at the BSL. These data are used for rapid earthquake reporting as well as for routine earthquake analysis (Section 2. and 8.). As part of routine quality control (Section 7.), power spectral density (PSD) analyses are performed continuously and are available on the internet.

The occurrence of a significant teleseism also provides the opportunity to review station health and calibration. Figure 3.4 displays BDSN waveforms for a M_w 7.7 deep focus earthquake in the Sea of Okhotsk region on July 5, 2008.

BDSN data are archived at the Northern California Earthquake Data Center. This is described in detail in Section 6.

Sensor	Channel	Rate (sps)	Mode	FIR
Broadband	UH?	0.01	C	Ac
Broadband	VH?	0.1	C	Ac
Broadband	LH?	1	C	Ac
Broadband	BH?	20/40	C	Ac
Broadband	HH?	80/100	C	Ac/Ca
SM	LL?	1	C	Ac
SM	BL?	20/40	C	Ac
SM	HL?	80/100	C	Ac/Ca
Thermometer	LKS	1	C	Ac
Barometer	LDS	1	C	Ac

Table 3.3: Typical data streams acquired at BDSN stations, with channel name, sampling rate, sampling mode, and the FIR filter type. SM indicates strong-motion; C continuous; T triggered; Ac acausal; Ca causal. The LL and BL strong-motion channels are not transmitted over the continuous telemetry but are available on the Quanterra disk system if needed. The HH channels are recorded at two different rates, depending on the data logger. Q4120s and Q330s provide 100 sps and causal filtering; Q680/980s provide 80 sps and acausal filtering.

Electromagnetic Observatories

In 1995, in collaboration with Dr. Frank Morrison, the BSL installed two well-characterized electric and magnetic field measuring systems at two sites along the San Andreas Fault which are part of the Berkeley Digital Seismic Network. Since then, magnetotelluric (MT) data have been continuously recorded at 40 Hz and 1 Hz and archived at the NCEDC (Table 3.4). At least one set of orthogonal electric dipoles measures the vector horizontal electric field, E, and three orthogonal magnetic sensors measure the vector magnetic field, B. These reference sites, now referred to as electromagnetic (EM) observatories, are collocated with seismometer sites so that the field data share the same time base, data acquisition, telemetry, and archiving system as the seismometer outputs.

Sensor	Channel	Rate (sps)	Mode	FIR
Magnetic	VT?	0.1	C	Ac
Magnetic	LT?	1	C	Ac
Magnetic	BT?	40	C	Ac
Electric	VQ?	0.1	C	Ac
Electric	LQ?	1	C	Ac
Electric	BQ?	40	C	Ac

Table 3.4: Typical MT data streams acquired at SAO, PKD, BRIB and JRSC with channel name, sampling rate, sampling mode, and FIR filter type. C indicates continuous; T triggered; Ac acausal.

The MT observatories are located at Parkfield (PKD1, PKD) 300 km south of the San Francisco Bay Area, and Hollister (SAO), halfway between San Francisco and Parkfield (Figure 3.2). In 1995, initial sites were established at PKD1 and SAO, separated by a distance of 150 km, and equipped with three induction coils and two 100 m electric dipoles. PKD1 was established as a temporary seismic site, and when a permanent site (PKD) was found, a third MT observatory was installed in 1999 with three induction coils, two 100 m electric dipoles, and two 200 m electric dipoles. PKD and PKD1 ran in parallel for one month in 1999, and then the MT observatory at PKD1 was closed.

Data at the MT sites are fed to Quanterra data loggers, shared with the collocated BDSN stations, synchronized in time by GPS and sent to the BSL via dedicated communication links.

Since 2004, new electromagnetic instrumentation has been installed at various Bay Area stations in conjunction with Simon Klemperer at Stanford University. Sensors are installed at JRSC, MHDL and BRIB.

1.3 2007-2008 Activities

USArray

When the USArray deployment began in Northern California, the BSL contracted with IRIS to contribute data from 19 BDSN stations. The stations were CMB, CVS, FARB, GASB, HOPS, HUMO, JCC, JRSC, KCC, MCCM, MNRC, MOD, ORV, PACP, PKD, POTR, WDC, WENL, and YBH. In the fall of 2007, the USArray pulled out equipment from its temporary sites. No data from the BDSN was sent to USArray after November 2007. For the USArray, the BSL modified the data loggers to change the BH sampling rate from 20 Hz to 40 Hz, a sampling rate which we continue to use.

During the station installation phase in Northern and Central California, the BSL collaborated with USArray to identify and permit sites that might be suitable as BDSN stations. Several were located at UC reserves and field stations. Data from these sites (Figure 3.2) were sent directly to the BSL as well as to the Array Network Facility and used in routine analysis to assess their performance. As the USArray left, we retained eight of the temporary sites (HAST, HATC, HELL, P01C, RAMR, S04C, SUTB and V03C). BSL engineers contacted the landowners prior to IRIS's departure. They received permission and made arrangements to continue operating stations at these sites. Because the overall objectives of the USArray deployment differ from the BSL's, their

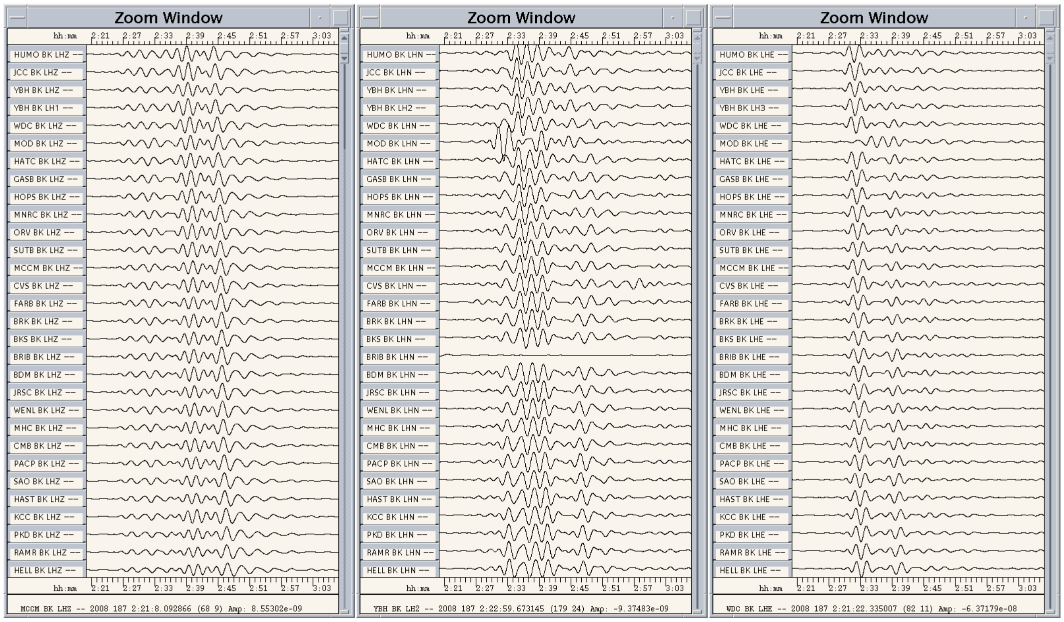

```
MCCM BK LHZ -- 2008 187 2:21:8.092866 (68 9) Amp: 8.55302e-09
YBH BK LH2 -- 2008 187 2:22:59.673145 (179 24) Amp: -9.37483e-09
WDC BK LHE -- 2008 187 2:21:22.335007 (82 11) Amp: -6.37179e-08
```

Figure 3.4: Long period waveforms recorded across BDSN from the deep M_w 7.7 teleseism which occurred on July 5, 2008, in the Sea of Okhotsk at 53.888° N, 152.869° E. The traces are deconvolved to ground velocity, scaled absolutely, and ordered from top to bottom by distance from the epicenter. The highly similar waveforms recorded across the BDSN provide evidence that the broadband sensors other than the N component at BRIB are operating within their nominal specifications. The sensor at MOD is currently an STS-2, which is rotated by 90° , so the N and E components are exchanged.

sites' construction and infrustructure are also different. As each station was reinstrumented, BSL engineers made a special effort to minimize or eliminate water that accumulated in the vaults/pits from condensation. Five of the sites have now been reinstrumented (see below). All of these sites operate using solar power, and are equipped with Q330 data loggers and STS-2 seismometers. The strong motion sensor is either a Kinemetrics EPISensor or Metrozet TSA 100 accelerometer. Continuous data telemetry to Berkeley has been achieved from all sites using a variety of methods.

Station Installation, Upgrades, Maintenance and Repairs

Given the remoteness of the off-campus stations, BDSN data acquisition equipment and systems are designed, configured, and installed so that they are both cost effective and reliable. As a result, the need for regular station visits has been reduced. Nonetheless, the broadband seismometers installed by BSL are of the first generation and are now approaching 25 years in age. Concurrently, the first generation of broadband data loggers are now 17 years old. Computer systems are retired long before this age, yet the electronics that form these data acquisition systems are expected to perform without interruption.

In 2007-2008 one focus of BSL's technical efforts went toward maintaining and repairing existing instrumentation, stations and infrastructure. In addition, equipment was installed at five former USArray stations. While expanding the data acquisition network continues to be a long term goal of BSL, it is equally important to assure integrity of the established network and preserve data quality.

RAMR: Ramage Ranch, San Luis Obispo County, CA This former USArray site is on private property at the Ramage Ranch west of Paso Robles, California. Seismic equipment was reinstalled in September, 2007. The site required a number of visits, however, to develop engineering solutions to improve the USArray vaults. At RAMR the vault is a 1.5 meter corregated plastic culvert with a plastic lid set vertically into the native limestone. The lid is covered with soil and must be shoveled free each time entry is desired. Both the STS-2 and the strong motion sensor sit on the bottom of the vault along with a pump to remove accumulating water. The data logger, telemetry radio, batteries, and solar charge controller sit on a shelf of foam insulation above the seismometers. The telemetry antenna, external clock antenna and solar panel are mounted on a mast 10 meters from the vault. The cables pass through a buried conduit.

As it is built, condensation forming in the conduit and filling it eventually drains into the vault and settles at the bottom. Within the vault, moisture also condensed and dripped from the underside of the lid. This water vapor was present year round - even during the rain free summer months. The USArray seismometers were continuously wet and often standing in about 50 mm of water. The sump pump could not remove water below this level.

Fearing long-term damage from corrosion, BSL engineers did not reinstall seismometers until the accumulated water vapor had been removed from the vault and provisions made to prevent condensation from forming. In the original construction, the sole connection of the vault to the outside air was the cable conduit containing cables. BSL engineers emptied more than twenty liters of water from the conduits and pulled a 4 mm tube from inside the vault to the top of the mast. Next a "tee" section was added to the mast and the cables routed out one leg of the tee together with the newly installed tube. The area around the cables and tube was carefully plugged with expanding foam. A solar vent was added to the remaining section of the tee.

In the newly configured "tube within a conduit", a restricted and controlled amount of outside air is continuously pulled through the tubing into the vault by the suction created by the solar vent. The air is exhausted during daylight hours by the solar vent. Water vapor does not condense on the underside of the lid. The air exchange is at a rate beyond the nominal bandwidth of the seismometers.

BSL engineers returned to the site several times after the instruments were installed in order to optimize the solar panel, trim newly grown brush from the solar panel and telemetry antenna, and monitor the success of the vent system. Engineers also replaced the power system for the receiving radio at the frame relay drop.

SUTB: Sutter Buttes, Butte County, CA BSL engineers reinstalled instrumentation at the former USArray site at SUTB in April and May 2008. The site is located on private land north of the BARD-GPS site at Sutter Buttes. Continuous telemetry is achieved via digital radio telemetry relay to the GPS site atop Sutter Buttes, and onward to the frame relay circuit at station ORV.

As described at RAMR, BSL engineers installed a solar powered ventilation system to eliminate condensation within the vault. Engineers also relocated the mast supporting the solar panel and radio antennas from beneath the canopy of an oak tree. The radio link remains problematic with remote troubleshooting required regularly.

HATC: Hat Creek Observatory, Lassen County, CA Instrumentation was reinstalled at the former USArray site at Hat Creek in April of 2008. The site is located on property owned by the University of California within the boundaries of the radio telescope array. Data are telemetered continuously from the site via the Observatory's T-1 line back to Berkeley. The support and cooperation of the UCB Astronomy department merits special mention.

HAST: Hastings Reserve, Monterey County, CA BSL engineers reinstalled instrumentation in the USArray vault at the Hastings Reserve in March of 2008. The site is located on property owned by the University of California system and operated as a biological field station (`http://www.hastingsreserve.org`). As at RAMR, BSL engineers installed solar ventilation at HAST to eliminate condensation within the vault. Telemetry from the site is accomplished via digital radio link to the University operated satellite link.

HELL: Hellweg Property, Fresno County, CA BSL reinstalled instrumentation in the USArray vault on property owned by Peggy Hellweg of the BSL in March of 2008. Telemetry from the site is accomplished via digital radio link and leased commercial satellite internet.

As at RAMR, BSL engineers installed solar ventilation at HELL to eliminate condensation within the vault.

V03C: Fort Hunter-Liggett, Monterey County, CA The USArray site V03C of interest to the BSL is located on federal property at Fort Hunter-Liggett in Monterey County. This military base is administered by the US Army Corp of Engineers. USArray initially paid a substantial permitting fee to receive permission to occupy the site.

BSL has indicated to the Corp of Engineers that we would be taking over operation of the site, and as a member of the IRIS consortium, have already paid the necessary permit fee. Our proposal appears to have been well received, and the permit transfer is currently being processed. We expect that the site will be reinstrumented with the 2008 calender year.

WENL: The BSL station WENL began operating in 1997. The equipment is installed in a high humidity adit used for storing and aging wine. BSL engineers replaced cables and the STS-2 seismometer this year after a reduction in the instrument's sensitivity (signal levels) was observed. Since WENL was installed, growth and development at the winery caused increases in the background noise levels over the past several years. A search for a suitable replacement site has begun.

HOPS: The BDSN station at Hopland, California, has been operating since October, 1994. The station is located approximately 100 miles northwest of Berkeley. In the summer of 2007, BSL engineers temporarily removed the control electronics for the STS-1 seismometers at HOPS. The external connectors on the electronics were found to have corroded sufficiently that currents leaked from pin-to-pin. Under magnification, the electronics were also found to have white "fuzz" growing on individual components. The resultant electrical leakage can reduce the seismometer's response to ground movement or even completely stop it. The electronics were thoroughly cleaned in an alchohol solution, and all connectors were replaced.

When the cleaned electronics were replaced at HOPS, a calibration pulse was initiated using the factory electronics. The data were used to calculate the responses of the instruments. Then, the newly developed E300 electronics were substituted. The seismometers were run with the E300 control electronics for six weeks, after which the original electronics were reinstalled.

The development and testing of MetroZet E300 electronics are described more fully in Section 9.

KCC: At station KCC (Kaiser Creek California) BSL engineers removed the STS-1 seismometers during 2006-2007 and installed an STS-2, an instrument consistent with the specifications of the TA. This provided the opportunity to use the three STS-1 components at Berkeley's Byerly Vault in the STS-1 electronics upgrade program. In November 2007, the STS-1 seismometers were reinstalled at KCC.

When the STS-1 seismometers were reinstalled at KCC, normal leveling and orientation procedures were followed. The prototype E300 electronics were also installed and the calibration features of the new electronics were exercised while the BSL engineers were on site. The calibration features could not be remotely activated once the engineers returned to Berkeley. Some grounding issue affecting the network connection is thought to be the reason. The network connection to the seismometer control E300 prototype has not been resolved at this time. It is, however, convenient to have the E300 electronics for the STS-1 seismometers installed at this site, as it allows remotely operated recentering.

MCCM: Continuous data telemetry from the station MCCM is achieved using VSAT equipment supplied by ANSS. During 2007, engineers from BSL installed additional hardware so that the VSAT system could be rebooted remotely if it should hang up or some other failure should occur.

BSL also received permission from the California State Park system and the California Department of Forestry and Fire (CDF) to install two digital radio repeaters so that data from MCCM can be relayed to Berkeley by means other than the VSAT. We are currently awaiting specific siting instructions from the CDF on the radio tower at St Helena.

JRSC: The equipment at station JRSC is operated and maintained by BSL on behalf of Stanford University. In April of 2008, the strong motion FBA-23 was replaced with a MetroZet model TSA-100S sensor. The replacement sensor is plug compatible with the other strong motion sensors within the BDSN network. Additionally, the removed sensor did not provide the differential output that the Quanterra data logger expects. This incompatibility manifests itself in the form of ground loops and high instrument noise. The replacement TSA-100A sensor was purchased and provided by Stanford.

MHC: In late 2007, the strong motion Episensor at station MHC began to exhibit an offset on the east component. This is usually consistent with a sensor problem. Although the engineers from BSL installed a replacement sensor, the same symptoms continued during the next month. A second trip to the site revealed that the cable between the data logger and the sensor had become so stressed that an individual wire had disconnected at the back of the connector shell. The connector was repaired onsite.

Additionally, BSL engineers proactively replaced the BARD GPS receiver which had been operating continuously since 1996. These recievers have been known to lose their software when their internal battery dies. Repair and upgrade of these receivers is described elsewhere in this publication.

MHDL and OXMT: The BSL equipment at MHDL and OXMT is co-located with USGS instruments as part of the miniPBO network. BSL engineers developed a scheme to isolate power to all instruments. The scheme involves separate AC-DC power supplies for each of the six instrument sets at the site. BSL engineers replaced several of the power supplies at each of the sites during 2007-2008 that had been damaged by mice infestation.

OHLN: The BSL equipment at OHLN is co-located with USGS instruments as part of the miniPBO array. Power to the site is provided by the local school district. Several times during the year, maintenance workers at the school inadvertently cut power to the seismic site. Power was always restored after BSL personnel contacted the school authority.

FARB: BSL has operated instrumentation on SE Farallon Island continuously since 1994. Beginning initially with a GPS receiver, broadband seismic instruments were added in 1996. Because of the highly corrosive marine environment, the radio telemetry antennas have been replaced every two years.

Continuous seismic and GPS telemetry from the island is achieved using redundant 900 mHz and 2.4 gHz digital radio transceivers. The 900 mHz link operates from the island, through the Golden Gate, to the hills above the Berkeley campus. The 2.4 gHz link operates from the island to the University of California Medical Science building in San Francisco. From San Francisco, a frame relay circuit completes the data link to Berkeley.

In the fall of 2007, BSL engineers made several trips to the island to replace and realign the antennas. During the same trips, the BSL engineers enabled digital radios for the use and benefit of the USFWS and the biologist stationed there. This link provides both data and VOIP services to the inhabitants of the island. BSL engineers also replaced all of the receiving antennas on the San Francisco end of links.

The Monterey Bay Ocean Bottom Seismic Observatory (MOBB)

The Monterey Ocean Bottom Broadband observatory (MOBB) is a collaborative project between the Monterey Bay Aquarium Research Institute (MBARI) and the BSL. Supported by funds from the Packard Foundation to MBARI, NSF/OCE funds and UC Berkeley funds to BSL, its goal has been to install and operate a long-term seafloor broadband station as a first step towards extending the on-shore broadband seismic network in Northern California to the seaside of the North-America/Pacific plate boundary, providing better azimuthal coverage for regional earthquake and structure studies. It also serves the important goal of evaluating background noise in near-shore buried ocean floor seismic systems, such as may be installed as part of temporary deployments of "leap-frogging" arrays (e.g. Ocean Mantle Dynamics Workshop, September 2002).

BSL staff put significant effort in the development of procedures to minimize instrumental noise caused by air circulation inside the seismometer package casing (see 2001-2002 and 2002-2003 BSL Annual Reports). These procedures were later applied to the preparation of 3 similar packages destined for installation on the Juan de Fuca plate in the framework of University of Washington's Keck project.

This project follows the 1997 MOISE experiment, in which a three component broadband system was deployed for a period of 3 months, 40 km offshore in Monterey Bay, with the help of MBARI's "Point Lobos" ship and ROV "Ventana" (Figure 3.5). MOISE was a cooperative program sponsored by MBARI, UC Berkeley, and the INSU, Paris, France (*Stakes et al.*, 1998; *Romanowicz et al.*, 1999; *Stutzmann et al.*, 2001). During the MOISE experiment, valuable experience was gained on the technological aspects of such deployments, which contributed to the success of the present MOBB installation.

The successful MOBB deployment took place April 9-11, 2002, and the station has been recording data autonomously ever since (e.g. *Romanowicz et al.*, 2003). It comprises a three component very broadband CMG-1T seismometer system, a diffential pressure gauge, (DPG, *Cox et al.*, 1984) and a current meter. Data from the DPG are acquired with a sampling rate of 1 sps and are crucial for the development and implementation of a posteriori noise deconvolution procedures to help counteract the large contribution of infragravity wave noise in the period range 20-200 sec. Procedures for removal of ingravity wave noise as well as signal generated noise have been developed.

Twenty-three "dives" involving the MBARI ship "Point Lobos" and ROV "Ventana" have so far taken place to exchange data loggers and battery packages during the time period 04/10/02 to 06/30/08. In February 2004, the N/S component seismometer failed. It was temporarily replaced, from 05/19/04 to 07/09/04, by one of the Keck seismometer packages which was conveniently available at that time. The original seismometer was sent back to Guralp Systems Ltd. for repair and successfully reinstalled on 07/09/04.

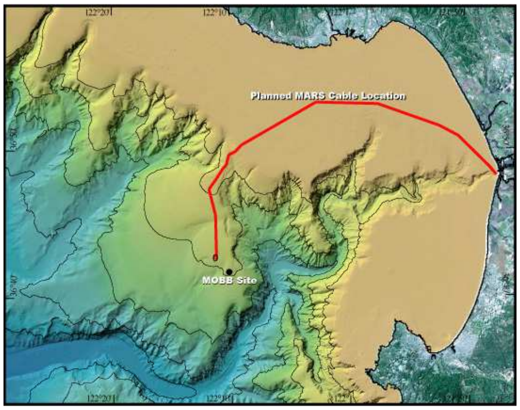

Figure 3.5: Location of the MOBB station in Monterey Bay, California, against seafloor and land topography. The path of the MARS cable is indicated by the solid line.

The data collection from the broadband seismic system is fairly complete. However, there have been recurring DPG sensor as well as DPG data storage problems in the first two years of the MOBB operation. Well recorded DPG data are available since 03/18/2004.

The MOBB station is located close to the path of the MARS cable (Figure 3.5) which was deployed in the spring of 2007. The connection of MOBB to the MARS cable will allow continuous, real-time data acquisition from this site. Developing the interface for the connection to MARS is the object of a recently funded NSF project. Work on this project commenced in the summer of 2007. Installation is planned in spring 2009.

1.4 Acknowledgements

Under Barbara Romanowicz's general supervision, Peggy Hellweg and Doug Neuhauser oversee the BDSN data acquisition operations, and Bill Karavas heads the engineering team. John Friday, Jarrett Gardner, Rick Lellinger and Bob Uhrhammer contribute to the operation of the BDSN. Karl Kappler has been responsible for the operation of the EM observatories. Bill Karavas, Bob Uhrhammer, and Peggy Hellweg contributed to the preparation of this section.

The California Governor's Office of Emergency Services and the Federal Emergency Management Agency provided funds for the istrumenation installed at the new stations HAST, HATC, HELL, RAMR and SUTB.

MOBB is a collaboration between the BSL and MBARI, involving Barbara Romanowicz, Bob Uhrham-

mer and Doug Neuhauser from the BSL, and Paul McGill from MBARI. The MBARI team also has included Steve Etchemendy (Director of Marine Operations), Jon Erickson, John Ferreira, Tony Ramirez and Craig Dawe. The MOBB effort at the BSL is supported by UC Berkeley funds. MBARI supports the dives and data recovery. The MOBB seismometer package was funded by NSF/OCE grant #9911392. The development of the interface for connection to the MARS cable is funded by NSF/OCE grant #0648302.

1.5 References

Cox, C., T. Deaton and S. Webb, A deep-sea differential pressure gauge, *J. Atm. Ocean. Tech., 1*, 237-245, 1984.

Crawford W. C., and S. C. Webb, Identifying and removing tilt noise from low- frequency (<0.1 Hz) seafloor vertical seismic data, *Bull. Seis. Soc. Am., 90*, 952-963, 2000.

Murdock, J., and C. Hutt, A new event detector designed for the Seismic Research Observatories, *USGS Open-File-Report 83-0785,* 39 pp., 1983.

Romanowicz, B., D. Stakes, J. P. Montagner, P. Tarits, R. Uhrhammer, M. Begnaud, E. Stutzmann, M. Pasyanos, J.F. Karczewski, and S. Etchemendy, MOISE: A pilot experiment towards long term sea-floor geophysical observatories, *Earth Planets Space, 50,* 927-937, 1999.

Romanowicz, B., D. Stakes, R. Uhrhammer, P. McGill, D. Neuhauser, T. Ramirez, and D. Dolenc, The MOBB experiment: a prototype permanent off-shore ocean bottom broadband station, *EOS Trans. AGU*, Aug 28 issue, 2003.

Stakes, D., B. Romanowicz, J.P. Montagner, P. Tarits, J.F. Karczewski, S. Etchemendy, D. Neuhauser, P. McGill, J-C. Koenig, J.Savary, M. Begnaud, and M. Pasyanos, MOISE: Monterey Bay Ocean Bottom International Seismic Experiment, *EOS Trans. AGU, 79*, 301-309, 1998.

Stutzmann, E., J.P. Montagner et al., MOISE: a prototype multiparameter ocean-bottom station, *Bull. Seism. Soc. Am., 81*, 885-902, 2001.

Wielandt, E., and J. Steim, A digital very broadband seismograph, *Ann. Geophys., 4*, 227-232, 1986.

Wielandt, E., and G. Streckeisen, The leaf spring seismometer: design and performance, *Bull. Seis. Soc. Am., 72*, 2349-2367, 1982.

Zürn, W., and R. Widmer, On noise reduction in vertical seismic records below 2 mHz using local barometric pressure, *Geophys. Res. Lett., 22*, 3537-3540, 1995.

2. California Integrated Seismic Network

2.1 Introduction

Advances in technology have made it possible to integrate separate earthquake monitoring networks into a single seismic system as well as to unify earthquake monitoring instrumentation. In California, this effort began in the south with the TriNet Project. There Caltech, the California Geological Survey (CGS), and the USGS combined efforts to create a unified seismic system for southern California. With major funding provided by the Federal Emergency Management Agency (FEMA), the California Governor's Office of Emergency Services (OES), and the USGS, the TriNet project provided the opportunity to upgrade and expand the monitoring infrastructure, combining resources in a federal, state and university partnership. In 2000, the integration effort expanded to the entire State with the formation of the California Integrated Seismic Network (CISN, see 2000-2001 Annual Report). To this end, UC Berkeley and the USGS Menlo Park and Pasadena offices joined forces with Caltech and the CGS. The CISN is now in the eighth year of collaboration and its seventh year of funding from the OES.

2.2 CISN Background

Organization

The organizational goals, products, management, and responsibilities of the CISN member organizations are described in the founding MOU and in the strategic and implementation plans. To facilitate activities among institutions, the CISN has formed three management centers:

- Southern California Earthquake Management Center: Caltech/USGS Pasadena
- Northern California Earthquake Management Center: UC Berkeley/USGS Menlo Park
- Engineering Strong Motion Data Center: California Geological Survey/USGS National Strong Motion Program

The Northern and Southern California Earthquake Management Centers are operating as twin statewide earthquake processing centers serving information on current earthquake activities, while the Engineering Strong Motion Data Center has the responsibility for producing engineering data products and distributing them to the engineering community.

The Steering Committee, made up of two representatives from each core institution and a representative from OES, oversees CISN projects. The position of chair rotates among the institutions; Rob Clayton took over as chair of the Steering Committee in June 2008 from Jeroen Tromp to complete Caltech's tenure.

An external Advisory Committee represents the interests of structural engineers, seismologists, emergency managers, industry, government, and utilities, and provides review and oversight. The Advisory Committee is chaired by Stu Nishenko of Pacific Gas and Electric Company. It last met in October 2007. Agendas from the meetings and the resulting reports may be accessed through the CISN Web site (`http://www.cisn.org/advisory`).

The Steering Committee has formed other committees, including a Program Management Group to address planning and coordination and a Standards Committee to resolve technical design and implementation issues.

In addition to the core members, other organizations contribute data that enhances the capabilities of the CISN. Contributing members include: University of California, Santa Barbara; University of California, San Diego; University of Nevada, Reno; University of Washington; California Department of Water Resources; Lawrence Livermore National Lab; and Pacific Gas and Electric.

CISN and ANSS

The USGS Advanced National Seismic System (ANSS) is being developed along a regionalized model. Eight regions have been organized, with the CISN representing California. David Oppenheimer of the USGS represents the CISN on the ANSS National Implementation Committee (NIC).

Over the past 9 years, ANSS funding in California has been directed primarily to the USGS Menlo Park to expand the strong-motion instrumentation in the San Francisco Bay Area. As a result, more than 100 sites have been installed or upgraded, significantly improving the data available for ShakeMaps.

As the ANSS moves forward, committees and working groups are being established to address issues of interest. BSL faculty and staff have been involved in several working groups of the Technical Integration Committee, including Doug Dreger, Pete Lombard, Doug Neuhauser, Bob Uhrhammer, and Stephane Zuzlewski.

CISN and OES

The California Governor's Office of Emergency Services has had a long-term interest in coordinated earthquake monitoring. The historical separation between

Northern and Southern California and between strong-motion and weak-motion networks resulted in a complicated situation for earthquake response. Thus, OES has been an advocate of increased coordination and collaboration in California earthquake monitoring and encouraged the development of the CISN. In FY01-02, Governor Gray Davis requested support for the CISN, to be administered through OES. Funding for California Geological Survey, Caltech and UC Berkeley was made available in spring 2002, officially launching the statewide coordination efforts. Following the first year of funding, OES support led to the establishment of 3-year contracts to the UC Berkeley, Caltech, and the California Geological Survey for CISN activities. The first multi-year award covered activities in 2002-2005. The three-year contract for 2006-2008 has just been completed. Past CISN-related activities are described in previous annual reports.

2.3 2007-2008 Activities

The CISN funding from OES has supported a number of activities at the BSL during the past year.

Adopting USArray Stations

In late 2003, the CISN concluded a memorandum of agreement with the Incorporated Research Institutions in Seismology (IRIS) covering the duration of the USArray project in California. As a result, data from 19 stations operated by the BSL and 41 stations operated by Caltech were contributed to USArray's travelling array (TA) during its California deployment. The BSL also provided accelerometers for use at TA sites which might be of interest as future BDSN stations. We monitored the data from these stations in real time and included the data in ShakeMaps and moment tensors. In addition, data from these TA stations were included in our development of new parameters that are valid statewide for determining M_L (see Research Study 34.). The TA moved out of California during the fall of 2007, and the BSL adopted eight of the sites. Instrumentation has been installed at RAMR, HAST, HATC, HELL, and SUTB (see Section 1.). Support for the equipment has come from FEMA Hazard Grant Mitigation Program Funds and from CISN funding. Vaults have been left open at P01C, S04C, and V03C, which the BSL will instrument when funding becomes available.

Northern California Earthquake Management Center

As part of their effort within the CISN, the BSL and the USGS Menlo Park are implementing the new generation of the Northern California joint notification system. Section 8. describes the operations of the existing Management Center and reports on the design and implementation progress.

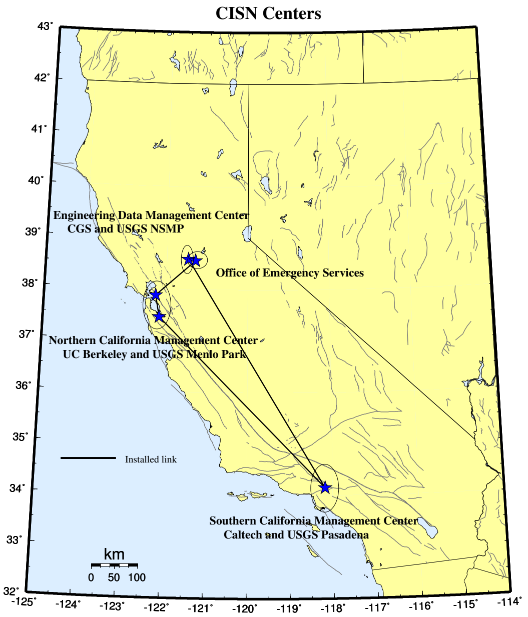

Figure 3.6: Map showing the geographical distribution of the CISN partners and centers. The communications "ring" is shown schematically with installed links (solid lines).

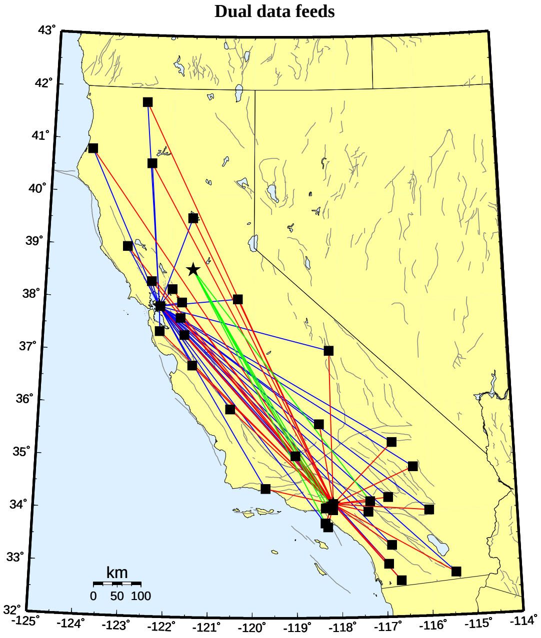

Figure 3.7: Map showing the 30 stations selected to send data directly to the Northern and Southern California processing centers, and the 5 stations that send data directly to the Engineering Data Center and the Southern California processing center.

In order to move ahead with plans for restructuring the Northern California earthquake monitoring system, the USGS Menlo Park and BSL have been improving their communications infrastructure. At present, the BSL and the USGS Menlo Park are connected by two dedicated T1 circuits. One circuit is a component of the CISN ring, while the second circuit was installed in 2004-2005 (Figure 3.8) to support dedicated traffic between Berkeley and Menlo Park above and beyond that associated with the CISN.

The installation of the second dedicated T1 between Berkeley and Menlo Park freed up a frame-relay connection deployed by the BSL as part of the CalREN project in mid-1990s. The BSL has reconfigured this frame-relay circuit to serve as a second data acquisition link. BDSN data acquisition is now distributed between two frame-relay T1 circuits, eliminating what had been a single point of failure. An additional Permanent Virtual Circuit (PVC) has also been implemented at each BDSN site so that each station has connections to both T1s. This has improved the robustness of data acquisition at the BSL by providing redundancy in the incoming circuit.

In the long term, the BSL and USGS Menlo Park hope to be connected by high-bandwidth microwave or satellite service. Unfortunately, we have not yet been able to obtain funding for such an additional communication link.

2.4 Statewide Integration

BSL staff are involved in many elements of the statewide integration effort. The Standards Committee, chaired by Doug Neuhauser, continues to define and prioritize projects important to the development and implementation of the statewide earthquake processing system and to establish working groups to address them (see minutes from meetings and conference calls at `http://www.cisn.org/standards/meetings.html`).

Dual Station Feeds: Early in the existence of CISN, "dual station feeds" were established for 30 stations (15 in Northern California and 15 in Southern California) (Figure 3.7). The Northern California Earthquake Management Center (NCEMC) is using data from the Southern California stations to estimate magnitudes on a routine basis. A subset of these stations are being used for the moment tensor inversions, a computation that is sensitive to the background noise level.

Data Exchange: Pick exchange was initiated between the NCEMC and its Southern California counterpart in 2001-2002. The software CISN has developed to produce and exchange the reduced amplitude timeseries has also been completed. Currently, these timeseries are being exchanged at the NCEMC, but not yet statewide. Using a common format, the CISN partners continue to exchange observations of peak ground motion with one another following an event or a trigger. This step increases the robustness of generating products such as ShakeMap, since all CISN partners now exchange data directly with one another. This also improves the quality of ShakeMaps for events on the boundary between Northern and Southern California, such as the San Simeon earthquake, by allowing all data to be combined in a single map. Finally, this is a necessary step toward the goal of generating statewide ShakeMaps.

The Software Calibration & Standardization: CISN partners are working to standardize the software used for automatic earthquake processing and earthquake review, as well as to calibrate it. Currently, the software implemented at the NCEMC and at the Southern California Earthquake Management Center is very different. During the past year in the NCEMC, we have worked on preparing a version of the Southern California TriNet software for implementation as CISN software in the NCEMC.

- Magnitude: Calibrating magnitude estimates has proven to be more difficult than originally anticipated. As described in 2003-2004, evidence indicates that there is a bias between the Northern and Southern California estimates of local magnitude M_L. Efforts to understand this issue have been hampered by the lack of a good statewide dataset. Bob Uhrhammer has selected data from 180 earthquakes distributed throughout the state and comprising recordings from 976 horizontal components from the AZ, BK, CI and NC networks (see Research Study 34.). In January 2007, we agreed on a $logA_o$ function suitable for statewide use. Station-specific corrections for M_L have now been defined for most broadband/strong motion stations. We are working to develop station-specific corrections for strong motion only stations, and to tie the new system in with historical stations. A final component of the magnitude efforts is the determination of a magnitude reporting hierarchy. For the near future, each region will continue to use its own preferences for magnitude reporting.

- ShakeMap: At present, ShakeMaps are generated on 5 systems within the CISN. Two systems in Pasadena generate "SoCal" Shakemaps; 2 systems in the Bay area generate "NoCal" Shakemaps; and 1 system in Sacramento generates ShakeMaps for all of California. The Sacramento system uses QDDS to provide the authoritative event information for Northern and Southern California.

  The dearth of stations in the near source region of the 2003 San Simeon earthquake raised the issues of how to measure the quality of a ShakeMap and how to quantify the uncertainty. A subset of the Working Group worked on this issue, based on the work of *Hok and Wald* (2003). *Lin et al* (2006) pre-

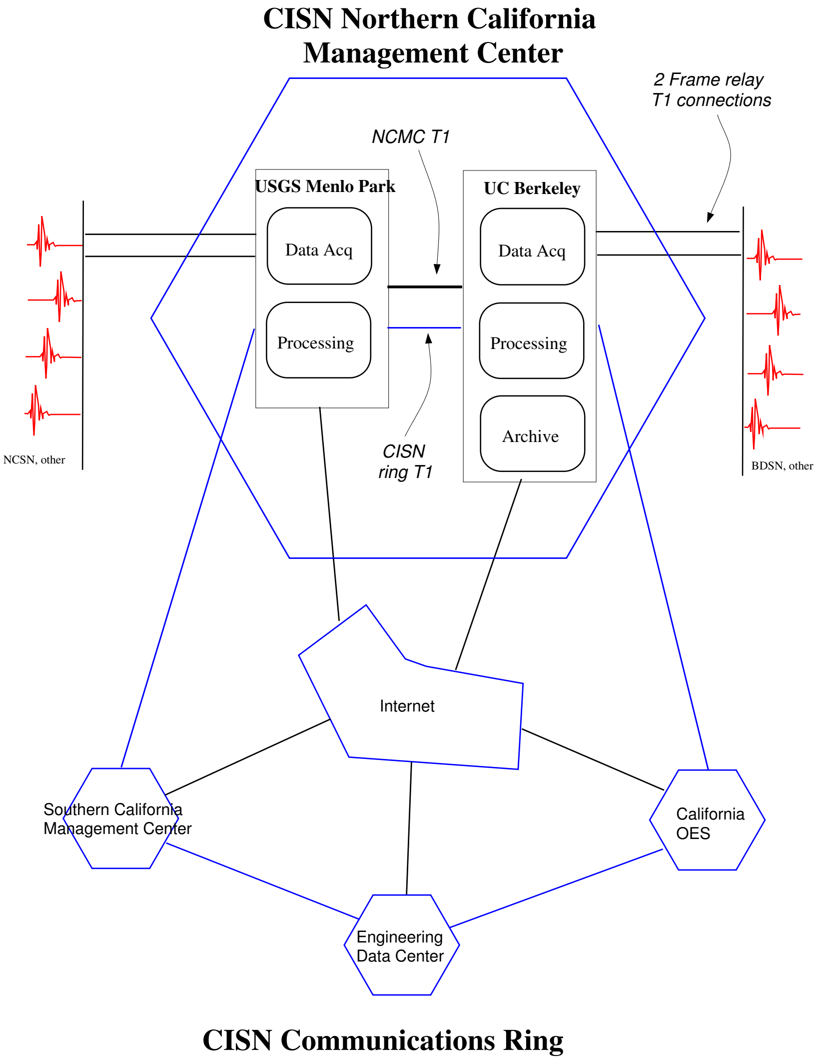

Figure 3.8: Schematic diagram illustrating the connectivity between the real-time processing systems at the USGS Menlo Park and UC Berkeley, forming the Northern California Management Center, and with other elements of the CISN.

sented progress toward quantifying ShakeMap uncertainty, and ShakeMaps are now published with a grade.

A second goal of this effort was to improve the robustness of ShakeMap generation and delivery by taking advantage of the fact that ShakeMaps are generated in the Bay Area, Pasadena, and Sacramento. Ongoing efforts in this direction will likely be based on the new USGS ShakeMap webpages at the National Earthquake Information Center.

- Location Codes: The CISN adopted a standard for the use of "location" codes (part of the Standard for the Exchange of Earthquake Data (SEED) nomenclature to describe a timeseries based on network-station-channel-location) in the late fall of 2003. USGS and UC Berkeley developers modified the Earthworm software to support their use. After the transition at USGS Menlo Park away from the CUSP analysis system to `Jiggle` in late November, 2006, all networks in the CISN implemented location codes in their systems.

- Metadata Exchange: Correct metadata are vital to CISN activities, as they are necessary to ensure valid interpretation of data. CISN is working on issues related to their reliable and timely exchange. The CISN Metadata Working Group compiled a list of metadata necessary for data processing and developed a model for their exchange. In this model, each CISN member is responsible for the metadata for its stations and for other stations that enter into CISN processing through it. For example, Menlo Park is responsible for the NSMP, Tremor, and PG&E stations, while Caltech is responsible for the Anza data. At the present time, dataless SEED volumes are used to exchange metadata between the NCEMC and the SCEMC. The Metadata Working Group is developing a Station XML format for metadata exchange. This vehicle is expandable, and will probably allow exchange of a more comprehensive set of metadata than dataless SEED volumes, some of which may be necessary for other systems, for example in V0 formatted data.

- Leap second compatibility: Northern and Southern California databases handled leap seconds differently. A major software programming effort in the past year has been directed toward taking this into account. The data processing and analysis software now treats leap seconds consistently. All packages can be configured to pass the time information to the database in nominal or true time, as necessary.

- Standardization: The CISN's focus on standardization of software continues. For example, the BSL and the USGS Menlo Park are adapting the software running at the SCEMC for use at the NCEMC and are currently testing its various elements. The adoption of `Jiggle` in northern California in late November 2007 was the first step in the implementation of the new software. Current efforts are directed toward the implementation and testing of the complete system (see Section 8.). This software will be offered to other regional neworks of the ANSS in the near future.

CISN Display

CISN Display is an integrated Web-enabled earthquake notification system designed to provide earthquake information for emergency response at 24/7 operations centers. First responders, organizations with critical lifelines and infrastructure, and emergency responders are invited to register for an account at `http://www.cisn.org/software/cisndisplay.htm`.

The application provides users with maps of real-time seismicity and automatically provides access to Web-related earthquake products such as ShakeMaps. CISN Display also offers an open source GIS mapping tool that allows users to plot freely available layers of public highways, roads and bridges, as well as private layers of organizational-specific infrastructure and facilities information. The current version of CISN Display is 1.4. Its primary enhancement over the previous version is the development of a kiosk-mode for public display purposes.

Earthquake Information Distribution

The USGS hosted a workshop in October 2004 to develop plans for the installation and use of the EIDS software. Doug Neuhauser and Pete Lombard participated in this workshop, which resulted in a document outlining the steps necessary for the installation and migration of the earthquake notification system from the current Quake Data Distribution Services (QDDS) to EIDS.

Outreach

Since FY05-06, the CISN Web site (`www.cisn.org`) has been supported by two servers located at Berkeley and Caltech. The Web servers are set up so that the load can be distributed between them, providing improved access during times of high demand. With the increased robustness provided by the new servers, the CISN provides access to certain earthquake products directly from `www.cisn.org`. For example, ShakeMaps are now served directly from the CISN Web site, in addition to being available from several USGS Web servers and the CGS. The design and content of `http://www.cisn.org` continues to evolve. The Web site is an important tool for CISN outreach as well as for communication and documentation among the CISN partners.

The CISN continues to support the dedicated Web site for emergency managers. Following a suggestion from the Advisory Committee, we have designed a Web site to provide personalized access to earthquake information. Known as "myCISN," the Web site is available at `eoc.cisn.org`. Access to the Web site is limited to registered users in order to provide highly reliable access. At present, "myCISN" is a single Web server located at UC Berkeley. However, modifications to the database are underway to allow for multiple servers in the future. A second computer, already purchased, will either be installed in Sacramento or in Southern California.

As part of the CISN, the BSL is contributing to efforts to raise awareness of earthquakes and preparedness as the 140 anniversary of the 1868 Hayward Fault earthquake approaches on October 21, 2008. In particular, we will be co-hosting the *Third Conference on Earthquake Hazards in the Eastern Bay Area* as well as organizing and participating in other related activities.

2.5 Acknowledgements

CISN activities at the BSL are supported by funding from the Governor's Office of Emergency Services.

Barbara Romanowicz and Peggy Hellweg are members of the CISN Steering Committee. Peggy Hellweg is a member of the CISN Program Management Group, and she leads the CISN project at the BSL with support from Doug Neuhauser. Doug Neuhauser is chair of the CISN Standards Committee, which includes Peggy Hellweg, Pete Lombard, and Stephane Zuzulevski as members.

Because of the breadth of the CISN project, many BSL staff members have been involved, including: John Friday, Jarrett Gardner, Peggy Hellweg, Bill Karavas, Alexei Kireev, Rick Lellinger Pete Lombard, Doug Neuhauser, Charley Paffenbarger, Bob Uhrhammer and Stephane Zuzlewski. Peggy Hellweg contributed to this section. Additional information about the CISN is available through reports from the Program Management Group.

2.6 References

Hok, S., and D. J. Wald, Spatial Variability of Peak Strong Ground Motions: Implications for ShakeMap Interpolations, *EOS. Trans. AGU, 84(46)*, F1121, 2003.

Lin, K-W., D. Wald, B. Worden and A.F. Shakal, Progress toward quantifying CISN ShakeMap uncertainty, *Eighth National Conference on Earthquake Engineering, San Francisco, California, April 18-21, 2006.*

3. Northern Hayward Fault Network

3.1 Introduction

Complementary to the regional broadband network, the Hayward Fault Network (HFN) (Figure 3.9 and Table 3.5) is a deployment of borehole-installed, wide-dynamic range seismographic stations along the Hayward Fault and throughout the San Francisco Bay toll bridges network. Development of the HFN initiated through a cooperative effort between the BSL and the USGS, with support from the USGS, Caltrans, EPRI, the University of California Campus/Laboratory Collaboration (CLC) program, LLNL, and LBNL. The project's objectives included an initial characterization period followed by longer-term monitoring effort using a backbone of stations from among the initial characterization set. Subsequent funding from Caltrans, however, has allowed for continued expansion of the backbone station set for additional coverage in critical locations.

The HFN consists of two components. The Northern Hayward Fault Network (NHFN), operated by the BSL, consists of 29 stations with various operational statuses. These include stations located on Bay Area bridges and now at borehole sites of the Mini-PBO (MPBO) project, which were installed with support from NSF and the member institutions of the MPBO project. The NHFN is considered part of the BDSN and uses the network code BK. The Southern Hayward Fault Network (SHFN) is operated by the USGS and currently consists of 5 stations. This network is considered part of the NCSN and uses the network code NC. The purpose of the HFN is threefold: 1) to increase substantially the sensitivity of seismic data to low amplitude seismic signals, 2) to increase the recorded bandwidth for seismic events along the Hayward fault, and 3) to obtain bedrock ground motion signals at the bridges from more frequent, smaller earthquakes.

Data with these attributes contribute significantly to a variety of scientific objectives including: a) investigating bridge responses to stronger ground motions from real earthquakes, b) obtaining a significantly lower detection threshold for microearthquakes and possible nonvolcanic tremor signals, c) increasing the resolution of the fault-zone seismic structure (e.g., in the vicinity of the Rodgers Creek/Hayward Fault step over), d) improving monitoring of spatial and temporal evolution of seismicity (to magnitudes approaching $M \sim> -1.0$) that may signal behavior indicative of the nucleation of large damaging earthquakes, e) the investigation of earthquake scaling, physics, and related fault processes, f) improving working models for the Hayward fault, and g) using these models to make source-specific response calculations for estimating strong ground shaking throughout the Bay Area.

This section is primarily focused on the NHFN and activities associated with the BSL operations.

3.2 NHFN Overview

The initial characterization period of HFN development ended in 1997. During that period, the NHFN sensors provided signals to on-site, stand-alone Quanterra Q730 and RefTek 72A-07 data loggers, and manual retrieval and download of data tapes was required. Also in that year, the long-term monitoring phase of the project began, involving the installation of 24-bit data acquisition and communication platforms and data telemetry to the BSL archives for a backbone of the initial NHFN stations.

Over the years, Caltrans has provided additional support for the upgrade of two non-backbone sites to backbone operational status and for the addition of several new sites to the monitoring backbone. These expansion efforts are ongoing. Also since the transition to the long-term monitoring phase, the 5 stations of the MPBO project have been folded into the NHFN.

Of the 29 stations considered part of the NHFN history, 13 of the stations are currently operational, with telemetered data streams flowing continuously into the BSL's BDSN processing stream with subsequent archival in the Northern California Earthquake Data Center (NCEDC) archive. These include the 5 MPBO sites. Nine of the 29 stations are non-backbone stations that have not been upgraded to continuous telemetry. Though collection of data from these sites has been discontinued, their borehole sensor packages are still in place (having been grouted in), and efforts to find funding for upgrade of these sites with Quanterra Q4120, Q730, or Q330 data loggers and continuous telemetry continue. One of the upgraded backbone sites (BBEB) now operates only as a telemetry repeater site because access to the borehole was cut off during seismic retrofit work on the eastern span of the Bay Bridge in August of 2007. One original backbone site (SMCB) was also upgraded from a post-hole to a deep borehole installation in 2007 and was renamed SM2B.

The remaining 5 sites are in the process of being added to the NHFN backbone. Four of the sites have been drilled and instrumented and are awaiting installation of their electronics and infrastructures. Equipment has been purchased for the 1 remaining site (PINB), which is awaiting final land-use agreement from the Regional Parks district and drilling by Caltrans. We have also begun negotiating a land-use agreement with Cal Maritime for permission to install a new borehole at that site,

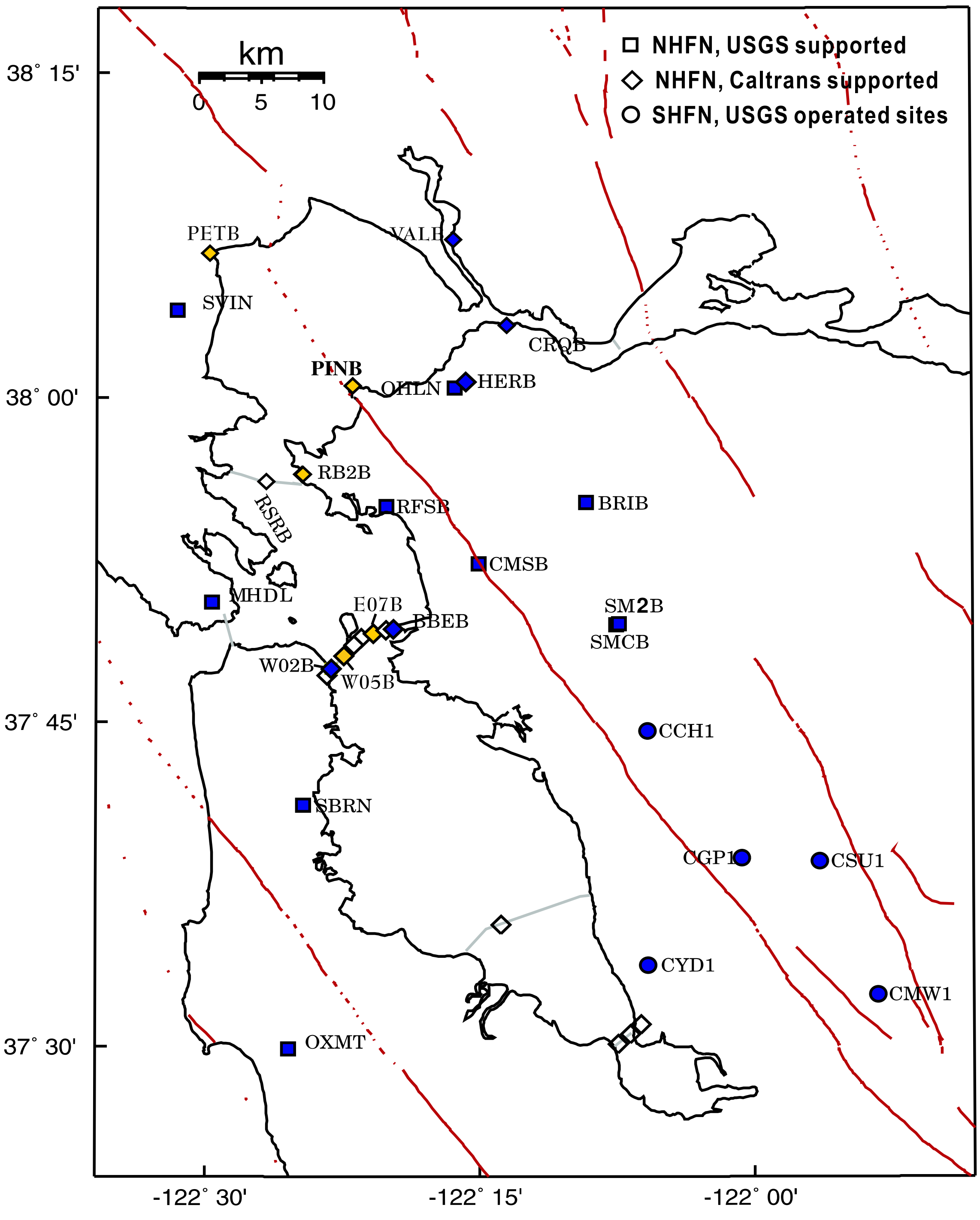

Figure 3.9: Map showing the locations of the HFN stations operated by the BSL (NHFN - squares and diamonds) and the USGS (SHFN - circles). Operational sites are filled blue/black, while sites in progress are yellow/grey. Other instrumented but currently non-operational boreholes are indicated as open symbols. Now, station BBEB operates only as a telemetry repeater site because access to the borehole was cut off during seismic retrofit work on the eastern span of the Bay Bridge.

Code	Net	Latitude	Longitude	Elev (m)	Over (m)	Date	Location
VALB	BK	38.1215	-122.2753	-24	155.8	2005/11 - current	Napa River Bridge
PETB	BK	38.1189	-122.5011	-30	113	in progress	Petaluma River Bridge
CRQB	BK	38.05578	-122.22487	-25	38.4	1996/07 - current	CB
HERB	BK	38.01250	-122.26222	-25	217.9	2000/05 - current	Hercules
PINB*	BK	38.0113	-122.3653	tbd	tbd	in progress	Point Pinole
BRIB	BK	37.91886	-122.15179	219.7	108.8	1995/06 - current	BR, Orinda
RFSB	BK	37.91608	-122.33610	-27.3	91.4	1996/01 - current	RFS, Richmond
CMSB	BK	37.87195	-122.25168	94.7	167.6	1994/12 - current	CMS, Berkeley
SMCB	BK	37.83881	-122.11159	180.9	3.4	1997/12 - 2007/06	SMC, Moraga
SM2B	BK	37.8387	-122.1102	200	150.9	2007/06 - current	SMC, Moraga
SVIN	BK	38.03325	-122.52638	-21	158.7	2003/08 - current	MPBO, St. Vincent's school
OHLN	BK	38.00742	-122.27371	-0	196.7	2001/07 - current	MPBO, Ohlone Park
MHDL	BK	37.84227	-122.49374	94	160.6	2006/05 - current	MPBO, Marin Headlands
SBRN	BK	37.68562	-122.41127	4	157.5	2001/08 - current	MPBO, San Bruno Mtn.
OXMT	BK	37.4994	-122.4243	209	194.2	2003/12 - current	MPBO, Ox Mtn.
BBEB	BK	37.82167	-122.32867	-31	150.0	2002/05 - 2007/08	BB, Pier E23
E17B	BK	37.82086	-122.33534		160.0	1995/08 - current *	BB, Pier E17
E07B	BK	37.81847	-122.34688	tbd	134.0	1996/02 - current *	BB, Pier E7
YBIB	BK	37.81420	-122.35923	-27.0	61.0	1997/12 - current *	BB, Pier E2
YBAB	BK	37.80940	-122.36450		3.0	1998/06 - current *	BB, YB Anchorage
W05B	BK	37.80100	-122.37370	tbd	36.3	1997/10 - current *	BB, Pier W5
W02B	BK	37.79120	-122.38525	-45	57.6	2003/06 - current	BB, Pier W2
SFAB	BK	37.78610	-122.3893		0.0	1998/06 - current *	BB, SF Anchorage
RSRB	BK	37.93575	-122.44648	-48.0	109.0	1997/06 - current *	RSRB, Pier 34
RB2B	BK	37.93	-122.41	tbd	133.8	2003/07 - current *	RSRB, Pier 58
SM1B	BK	37.59403	-122.23242		298.0	not recorded	SMB, Pier 343
DB3B	BK	37.51295	-122.10857		1.5	1994/09 - 1994/11	DB, Pier 44
					62.5	1994/09 - 1994/09	
					157.9	1994/07 - current *	
DB2B	BK	37.50687	-122.11566			1994/07 - current *	DB, Pier 27
					189.2	1992/07 - 1992/11	
DB1B	BK	37.49947	-122.12755		0.0	1994/07 - 1994/09	DB, Pier 1
					1.5	1994/09 - 1994/09	
					71.6	1994/09 - 1994/09	
					228.0	1993/08 - current *	
CCH1	NC	37.7432	-122.0967	226		1995/05 - current	Chabot
CGP1	NC	37.6454	-122.0114	340		1995/03 - current	Garin Park
CSU1	NC	37.6430	-121.9402	499		1995/10 - current	Sunol
CYD1	NC	37.5629	-122.0967	-23		2002/09 - current	Coyote
CMW1	NC	37.5403	-121.8876	343		1995/06 - current	Mill Creek

Table 3.5: Stations of the Hayward Fault Network. Each HFN station is listed with its station code, network id, location, operational dates, and site description. The latitude and longitude (in degrees) are given in the WGS84 reference frame. The elevation of the well head (in meters) is relative to the WGS84 reference ellipsoid. The overburden is given in meters. The start dates indicate either the upgrade or installation time. The abbreviations are: BB - Bay Bridge; BR - Briones Reserve; CMS - Cal Memorial Stadium; CB - Carquinez Bridge; DB - Dumbarton Bridge; MPBO - mini-Plate Boundary Observatory; RFS - Richmond Field Station; RSRB - Richmond-San Rafael Bridge; SF - San Francisco; SMB - San Mateo Bridge; SMC - St. Mary's College; and, YB - Yerba Buena. The * for station PINB indicates that this station name has been requested but has not yet been approved and may change. The * in the Date column indicates the stations that have recorded data from an earlier period of manually retrieved tapes, but that are currently off-line. Note that station BBEB now operates only as a telemetry relay station and no longer records seismic activity.

Site	Geophone	Accelerometer	Z	H1	h2	data logger	Notes	Telem.
VALB	Oyo HS-1	Wilcoxon 731A	TBD	TBD	TBD	Q330		FR
PETB	Oyo HS-1	Wilcoxon 731A	TBD	TBD	TBD	TBD		TBD
CRQB	Oyo HS-1	Wilcoxon 731A	-90	251	341	Q4120		FR
HERB	Oyo HS-1	Wilcoxon 731A	-90	TBD	TBD	Q4120		FR
PINB	Oyo HS-1	Wilcoxon 731A	TBD	TBD	TBD	TBD		TBD
BRIB	Oyo HS-1	Wilcoxon 731A	-90	79	349	Q4120	Acc. failed, Dilat.	FR
RFSB	Oyo HS-1	Wilcoxon 731A	-90	256	346	Q4120		FR
CMSB	Oyo HS-1	Wilcoxon 731A	-90	19	109	Q4120		FR
SMCB	Oyo HS-1	Wilcoxon 731A	-90	76	166	None at present	Posthole	FR
SM2B	Oyo HS-1	Wilcoxon 731A	TBD	TBD	TBD	Q4120		FR
SVIN	Mark L-22		-90	298	28	Q4120	Tensor.	FR/Rad.
OHLN	Mark L-22		-90	313	43	Q4120	Tensor.	FR
MHDL	Mark L-22		-90	TBD	TBD	Q4120	Tensor.	FR
SBRN	Mark L-22		-90	347	77	Q4120	Tensor.	FR
OXMT	Mark L-22		-90	163	253	Q4120	Tensor.	FR
BBEB	Oyo HS-1	Wilcoxon 731A	-90	TBD	TBD	None at present	Acc. failed	Radio
E17B	Oyo HS-1	Wilcoxon 731A	-90	TBD	TBD	None at present		
E07B	Oyo HS-1	Wilcoxon 731A	-90	TBD	TBD	None at present		
YBIB	Oyo HS-1	Wilcoxon 731A	-90	257	347	None at present	Z geop. failed	FR/Rad.
YBAB	Oyo HS-1	Wilcoxon 731A	-90	TBD	TBD	None at present		
W05B	Oyo HS-1	Wilcoxon 731A	-90	TBD	TBD	None at present		
W02B	Oyo HS-1	Wilcoxon 731A	-90	TBD	TBD	Q4120		Radio
SFAB	None	LLNL S-6000	TBD	TBD	TBD	None at present	Posthole	
RSRB	Oyo HS-1	Wilcoxon 731A	-90	50	140	None at present	2 acc. failed	FR
RB2B	Oyo HS-1	Wilcoxon 731A	-90	TBD	TBD	None at present	1 acc. failed	
SM1B	Oyo HS-1	Wilcoxon 731A	-90	TBD	TBD	None at present		
DB3B	Oyo HS-1	Wilcoxon 731A	-90	TBD	TBD	None at present	Acc. failed	
DB2B	Oyo HS-1	Wilcoxon 731A	-90	TBD	TBD	None at present		
DB1B	Oyo HS-1	Wilcoxon 731A	-90	TBD	TBD	None at present	Acc. failed	
CCH1	Oyo HS-1	Wilcoxon 731A	-90	TBD	TBD	Nanometrics HRD24	Dilat.	Radio
CGP1	Oyo HS-1	Wilcoxon 731A	-90	TBD	TBD	Nanometrics HRD24	Dilat.	Radio
CSU1	Oyo HS-1	Wilcoxon 731A	-90	TBD	TBD	Nanometrics HRD24	Dilat.	Radio
CYD1	Oyo HS-1	Wilcoxon 731A	-90	TBD	TBD	Nanometrics HRD24	Dilat.	Radio
CMW1	Oyo HS-1	Wilcoxon 731A	-90	TBD	TBD	Nanometrics HRD24	Dilat.	Radio

Table 3.6: Instrumentation of the HFN as of 06/30/2008. Every HFN downhole package consists of collocated 3-component geophones and accelerometers, with the exception of MPBO sites which have only 3-component geophones and are also collecting tensor strainmeter data. Six HFN sites (5 of the SHFN and 1 of the NHFN) also have dilatometers (Dilat.). Currently, 13 NHFN sites have Quanterra data loggers with continuous telemetry to the BSL. The remaining backbone sites are either still being developed with support from Caltrans or are being upgraded to Quanterra data loggers. The 5 SHFN sites have Nanometrics data loggers with radio telemetry to the USGS. The orientation of the sensors (vertical - Z, horizontals - H1 and H2) are indicated where known or identified as "to be determined" (TBD).

which is eventually to replace a particularly noisy backbone station at the south end of the Carquinez bridge (CRQB). With support for drilling and the purchase of a sensor package from Caltrans, the plan is to transfer the surface infrastructure and recording equipment at CRQB to the Cal Maritime site after Caltrans drill time becomes available and package installation is complete.

Installation/Instrumentation: The NHFN Sensor packages are generally installed at depths ranging between 100 and 200 m, the non-backbone non-operational Dumbarton bridge sites being exceptions with sensors at multiple depths (Table 3.5).

The five former MPBO sites that are now part of the NHFN have 3-component borehole geophone packages. Velocity measurements for the MPBO sites are provided by Mark Products L-22 2 Hz geophones (Ta-

Sensor	Channel	Rate (sps)	Mode	FIR
Accelerometer	CL?	500.0	T	Ca
Accelerometer	HL?	200.0	C	Ca
Accelerometer	BL?	20.0	C	Ac
Accelerometer	LL?	1.0	C	Ac
Geophone	DP?	500.0	T,C	Ca
Geophone	EP?	200.0	C	Ca
Geophone	EP?	100.0	C	Ca
Geophone	BP?	20.0	C	Ac
Geophone	LP?	1.0	C	Ac

Table 3.7: Typical data streams acquired at NHFN sites, with channel name, sampling rate, sampling mode, and FIR filter type. C indicates continuous, T triggered, Ca causal, and Ac acausal. Typically, the DP1 continuous channel is archived and the remaining high sample rate data (i.e., CL and DP channels) are archived as triggered snippets. Prior to Sept. 2004, however, only triggered data was archived for all high sample rate channels. Currently operational stations CRQB, HERB, BRIB, RFSB, CMSB, SM2B, and W02B record at maximum sample rates of 500 Hz; VALB at maximum 200 Hz and MPBO sites (SVIN, OHLN, MHDL, SBRN, OXMT) at maximum 100 Hz.

ble 3.6). All the remaining backbone and non-backbone NHFN sites have six-component borehole sensor packages. The six-component packages were designed and fabricated at LBNL's Geophysical Measurement Facility and have three channels of acceleration, provided by Wilcoxon 731A piezoelectric accelerometers, and three channels of velocity, provided by Oyo HS-1 4.5 Hz geophones.

The 0.1-400 Hz Wilcoxon accelerometers have lower self-noise than the geophones above about 25-30 Hz, and remain on scale and linear to 0.5 g. In tests performed in the Byerly vault at UC Berkeley, the Wilcoxon is considerably quieter than the FBA-23 at all periods, and is almost as quiet as the STS-2 between 1 and 50 Hz.

All 13 operational NHFN backbone sites have Quanterra data loggers with continuous telemetry to the BSL. Signals from these stations are digitized at a variety of data rates up to 500 Hz at 24-bit resolution (Table 3.7). The data loggers employ causal FIR filters at high data rates and acausal FIR filters at lower data rates.

Data Rates and Channels: Because of limitations in telemetry bandwidth and disk storage, 8 of the 9 (excluding VALB) six-component NHFN stations transmit one channel of geophone data continuously (i.e., their vertical geophone channels) and an additional 3 channels of triggered data in 90 sec. snippets. A Murdock, Hutt, and Halbert (MHH) event detection algorithm (*Murdock and Hutt*, 1983) is operated independently at each station on 500 sps data for trigger determinations. Because the accelerometer data is generally quieter, the 3 triggered channels are taken from the Wilcoxon accelerometers when possible. However, there is a tendency for these powered sensors to fail, and, in such cases, geophone channels are substituted for the failed accelerometers. Station VALB also transmits data from only 4 channels; however, all channels are transmitted continuously. Continuous data for all channels at reduced rates (20 and 1 sps) are also transmitted to and archived at the BSL. The five MPBO originated sites transmit their 3-component continuous geophone data streams at 100, 20 and 1 sps, which are also archived at BSL.

Station Maintenance

Ongoing network maintenance involves regular inspection of the collected seismic waveform data and spectra of nearby seismic events, and also of noise samples. Other common problems include changes to background noise levels due to ground loops and failing preamps, as well as power and telemetry issues. Troubleshooting and remediation of problems often require a coordinated effort, with a technician at the BSL to examine seismic waveforms and spectra while the field technicians are still on site. BSL technicians and researchers regularly review data and assist in troubleshooting.

The NHFN station hardware has proven to be relatively reliable. Nonetheless, numerous maintenance and performance enhancement measures are still carried out. In particular, when a new station is added to the backbone, extensive testing and correction for sources of instrumental noise (e.g., grounding related issues) and telemetry through-put are carried out to optimize the sensitivity of the station. Examples of maintenance and enhancement measures that are typically performed include: 1) testing of radio links to ascertain reasons for unusually large numbers of dropped packets, 2) troubleshooting sporadic problems with numerous frame relay telemetry dropouts, 3) manual power recycle and testing of hung Quanterra data loggers, 4) replacement of blown fuses or other problems relating to dead channels identified through remote monitoring at the BSL, 5) repair of frame relay and power supply problems when they arise, and 6) correcting problems that arise due to various causes, such as weather or cultural activity.

Quality Control

- Power Spectral Density Analyses: One commonly used quality check on the performance of the borehole installed network includes assessment of the power spectral density (PSD) distributions of background noise. Shown in Figure 3.10 are power spectral density (PSD) plots of background noise for vertical component geophone channels of the 13 operating NHFN stations for a 30 minute period beginning

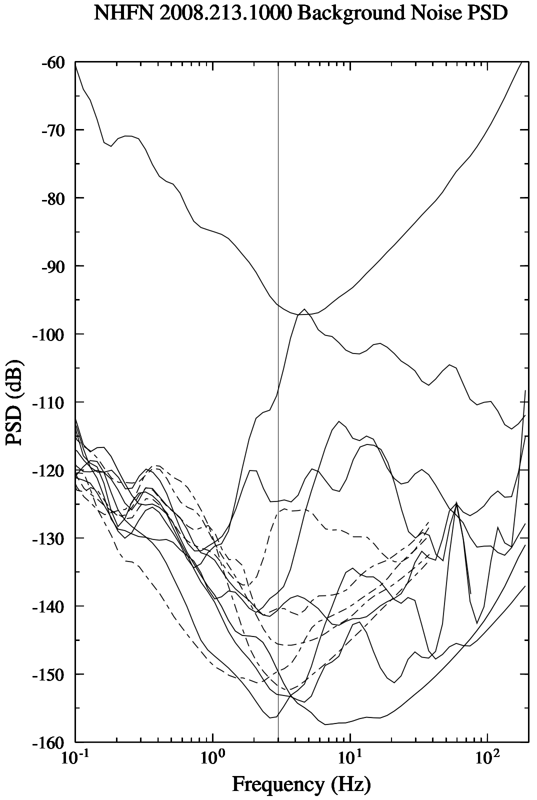

Figure 3.10: Plot showing typically observed background noise PSD for the NHFN borehole stations (including the MPBO in dashed lines) as a function of frequency. The data are from 2 am local time on a Sunday morning. Note that there is considerable variation in the general level and structure of the individual station background noise PSD estimates. The signals from three of the stations (RFSB, SM2B, and VALB) have 60 Hz noise (sometimes accompanied by 120 and 180 Hz harmonics), which is indicative of the presence of ground loops that need to be addressed. The PSD ranking of the stations of the stations at 3 Hz (near minimum PSD for most NHFN stations) is:

CMSB.BK.DP1	-156.28314
SM2B.BK.DP1	-152.98677
OXMT.BK.EP1	-151.68407
SVIN.BK.EP1	-149.62009
BRIB.BK.DP1	-149.20291
MHDL.BK.EP1	-145.56151
RFSB.BK.DP1	-140.75999
SBRN.BK.EP1	-140.37402
W02B.BK.DP1	-138.14912
OHLN.BK.EP1	-126.25831
VALB.BK.EP1	-124.60077
CRQB.BK.DP1	-109.07751
HERB.BK.DP1	-95.616780

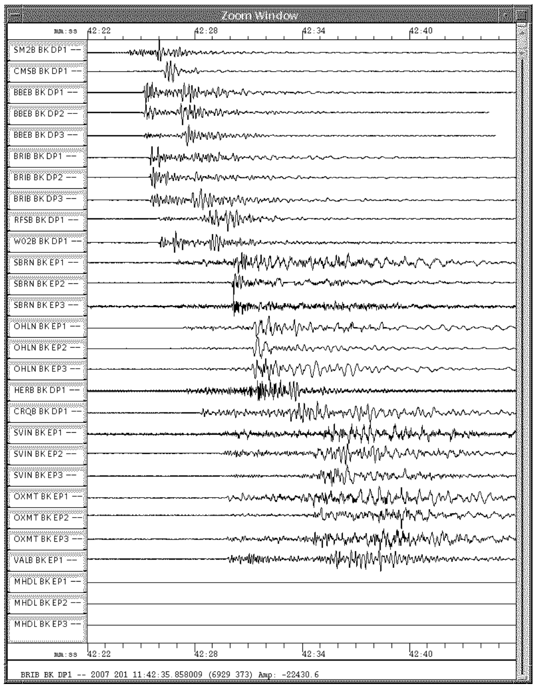

Figure 3.11: Plot of unfiltered P-wave seismograms, recorded on the geophones of the 14 NHFN borehole stations operational at the time of the event (i.e., before station BBEB was terminated due to Bay Bridge retrofit work), for a recent Bay Area earthquake (20 July 2007, M4.2 Piedmont, CA). The stations have been ordered by increasing distance from the event (top to bottom). It is immediately apparent from this simple display that station MHDL was dead and needed immediate attention.

at 2 AM local time on 7/31/2008 (Thursday morning). By periodically generating such plots, we can rapidly evaluate the network's recording of seismic signals across the wide high-frequency spectrum of the borehole NHFN sensors. Changes in the responses often indicate problems with the power, telemetry, or acquisition systems or with changing conditions in the vicinity of station installations that are adversely affecting the quality of the recorded seismograms. In general, background noise levels of the borehole NHFN stations are more variable and generally higher than those of the Parkfield HRSN borehole stations (see Parkfield Borehole Network section). This is due in large part to the significantly greater cultural noise in the Bay Area. For example the noisiest station (i.e., HERB) is located within a Caltrans maintenance yard which often has maintenance vehicle traffic during evening hours. The second noisiest station (CRQB) is located near the southern bridge abutment of the Carquinez Bridge for Freeway 80, which has heavy traffic most hours of the day.

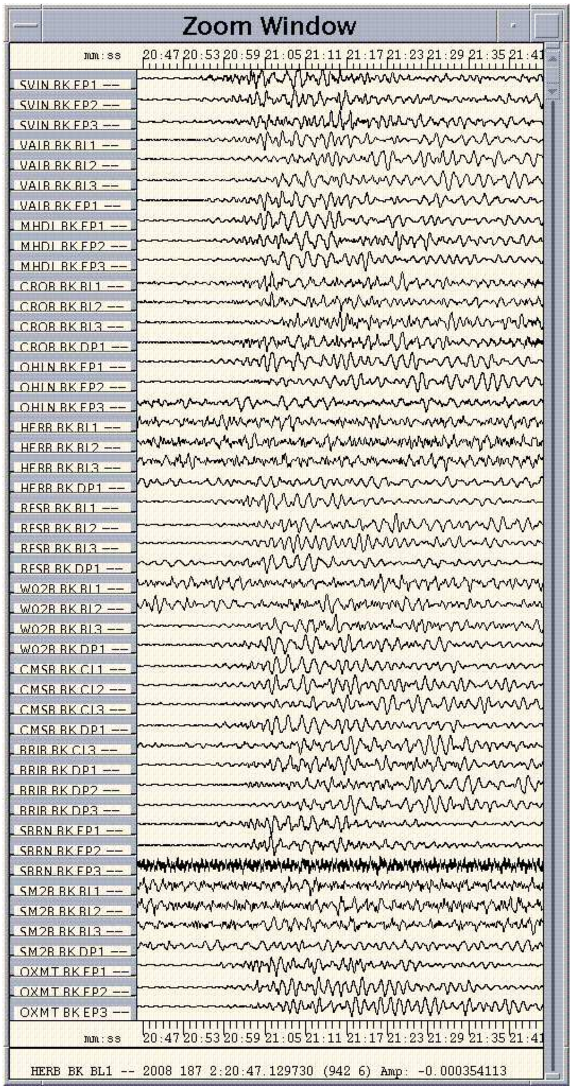

Figure 3.12: Plot of inferred relative ground velocity P-wave seismograms of the deep focus M_w 7.7 earthquake in the Sea of Okhotsk (Lat.: 53.8920; Lon.: 152.8840; 6688 km from Parkfield, CA; depth 636 km) occurring on July 5, 2008 at 02:12:04 (UTC) recorded by all channels of the borehole NHFN in operation at the time. All station waveforms in the plots are ordered by distance from the earthquake. Data has been 0.5-4 Hz bandpass filtered, and the highest available sampling rate for a given component is plotted.

On average the MPBO component of the NHFN sites is more consistent and somewhat quieter. This is due in large part to the greater average depth of the MPBO sensors, the locations of MPBO stations in regions with generally less industrial and other cultural noise sources, and possibly to the absence of powered sensors (i.e. accelerometers) in their borehole sensor packages.

One of the most pervasive problems at NHFN stations equipped with the Q4120 data loggers is power line noise (60 Hz and its harmonics at 120 and 180 Hz). This noise reduces the sensitivity of the MHH detectors and can corrupt research based on full waveform analyses. When NHFN stations are visited, the engineer at the site and a seismologist at the BSL frequently work together to identify and correct ground-loop problems, which often generate 60, 120, and 180 Hz contamination from inductively coupled power line signals.

- Real Event Displays: Another method for rapid assessment of network performance is to generate and evaluate the seismograms from moderate local and large teleseismic earthquakes recorded by the NHFN stations.

  Shown in Figure 3.11 is an example display of NHFN geophone channels for a local M4.2 event occurring on 20 July 2007 near Piedmont, CA. It is immediately apparent from this simple display that station MHDL was dead and needed immediate attention. It is also apparent from the 60 Hz buzz underlying the earthquake signal for stations SBRN and HERB that the grounding schemes for these channels may be in need of modification. At any given station, 60 Hz related noise sources can change over periods of weeks to months, requiring continued vigilance and adaptability of the grounding scheme in order to maintain the desired high sensitivity to low amplitude seismic signals.

  Figure 3.12 shows inferred relative ground velocity P-wave seismograms of the deep focus M_w 7.7 earthquake in the Sea of Okhotsk (Lat.: 53.8920; Lon.: 152.8840) occurring on July 5, 2008 at 02:12:04 (UTC) ($\sim$ 6000 km from the Bay Area, CA; depth 636 km) recorded on all operational channels (geophones and accelerometers) of the NHFN borehole stations. The seismic data from the quake was telemetered directly to the BSL and was available for analysis by the Northern California Seismic System (NCSS) real-time/automated processing stream within a few seconds of being recorded by the NHFN. Waveforms in the plots are ordered by distance from the epicenter.

  This is a good signal source for examining the relative responses of the BK borehole network station/components to seismic ground motion, and these indicate that the following stations were not responding normally to teleseismic ground motions at the time of this event:
  CRQB.BK.BL1, CRQB.BK.BL2, CRQB.BK.BL3, CRQB.BK.DP1 - high background noise level in all four components with a hint of the teleseismic signal visible

OHLN.BK.EP3 - digitizer bit noise, no seismic signal present
HERB.BK.BL1, HERB.BK.BL2, HERB.BK.BL3, HERB.BK.DP1 - digitizer bit noise on all four components
RFSB.BK.DP1 - asymmetric waveform and high frequency burst noise present which masks the teleseimsic signal
SBRN.BK.EP3 - coherent noise with a narrow 30+ dB peak at $\sim$1.4 Hz and a 40+ dB narrow peak at $\sim$3.4 Hz
SM2B.BK.BL1, SM2B.BK.BL2, SM2B.BK.BL3, SM2B.BK.DP1 - digitizer bit noise on all four components

By rapidly generating such plots following large teleseismic events, quick assessment of the HRSN seismometer responses to real events are easily done and corrective measures implemented with relatively little delay.

- Geophone Calibration Tests: Comparisons of the inferred ground accelerations generated by local earthquakes from co-sited NHFN geophone and accelerometer pairs show that the waveforms generally are quite coherent in frequency and phase response, but that their inferred ground accelerations differ significantly. At times, the amplitudes differ by up to a factor of 2 while the times of the peak amplitudes are identical. This implies that the free period, and damping of the geophones are well characterized. However, it also indicates that the generator constant is not accurate (assuming that the corresponding ground accelerations inferred from the accelerometers are accurate).

  Generally speaking, the accelerometers, being an active device, are more accurate and also more stable than the geophones, so it is reasonable to assume that the most likely reason for the difference is that the assumed generator constants for the geophones are inaccurate. *Rodgers et al.* (1995) describe a way to absolutely calibrate the geophones in situ and to determine their generator constant, free period and fraction of critical damping. The only external parameter that is required is the value of the geophone's inertial mass.

  We have built a calibration test box which allows us to routinely perform the testing described by *Rodgers et al.* whenever site visits are made. The box drives the signal coil with a known current step and rapidly switches the signal coil between the current source and the data logger input. From this information, expected and actual sensor response characteristics can be compared and corrections applied. Also, changes in the sensor response over time can be evaluated so that adjustments can be made, and pathologies arising in the sensors due to age can be identified. Once a geophone is absolutely calibrated, we also check the response of the corresponding accelerometer.

3.3 2007-2008 Activities

Over the past year, in addition to routine maintenance, operations, quality control, and data collection, NHFN project activities have included: a) integration of NHFN data into the Northern California Seismic System (NCSS) real-time/automated processing stream, online SeisNetWatch state-of-health monitoring tool, and online SeismiQuery metadata access, b) efforts to obtain additional funds for future upgrade and expansion of the network, c) leveraging NHFN activities through partnerships with various institutions outside of BSL, d) network adaptations to compensate for changing conditions associated with retrofit work on Bay Area bridges, and e) new station additions and network expansion efforts.

Integration into the NCSS, SeisNetWatch, and SeismiQuery

The NHFN is primarily a research network that complements regional surface networks by providing downhole recordings of very low amplitude seismic signals (e.g., from micro-earthquakes or non-volcanic tremor) at high gain and low noise. Nonetheless we have now also completed the integration of data flow from all operating NHFN stations into the Northern California Seismic System (NCSS) real-time/automated processing stream for response applications and collection of basic data for long-term hazards mitigation. The NCSS is a joint USGS (Menlo Park) and Berkeley Seismological Laboratory (BSL) entity with earthquake reporting responsibility for Northern California, and data from networks operated by both institutions are processed jointly to fulfill this responsibility.

Through this integration, the NHFN picks, waveforms, and NCSS event locations and magnitudes are automatically entered into a database where they are immediately available to the public through the NCEDC and its DART (Data Available in Real Time) buffer. The capability for monitoring state of health information for all NHFN stations using SeisNetWatch has also now been added, and up-to-date dataless SEED formatted metadata is now made available by the NCEDC with the SeismiQuery software tool.

Additional Funding

Operation of this Bay Area borehole network is funded by the ANSS and through a partnership with the California Department of Transportation (Caltrans). ANSS provides operations and maintenance (O&M) support for a fixed subset of 9 stations that were initiated as part of previous projects in which the USGS was a participant. Caltrans provides O&M support for an additional 10 stations that have been or are in the process of being added to the network with Caltrans partnership grants. Caltrans also continues to provide additional support for upgrade and expansion when possible.

This year, we also submitted a competitive proposal to Caltrans to expand the NHFN with 3 additional borehole installations and to upgrade several NHFN sites with strong-motion surface sensors to provide up-hole downhole data for fundamental research on amplification effects in the upper ~1-200 meters. Unfortunately, in spite of high hopes on the part of both Caltrans and ourselves, the proposal was not funded in this year's round. Nonetheless, we are continuing our discussions with our partners at Caltrans for a possible resubmittal of the proposal this coming year.

Partnerships

The NHFN is heavily leveraged through partnerships with various institutions, and we have continued to nurture and expand these relationships. Over the past year we have actively collaborated through partnerships with Caltrans and St. Mary's College. We have also been working with Cal Maritime Academy, the East Bay Parks District, UNAVCO, Lawrence Berkeley National Laboratory, and non-ANSS components of the USGS, to either resurrect previously funded partnership activities or to establish entirely new partnerships focused on continued NHFN expansion.

Network Adaptation

In August of 2007, recording of seismic signals from one of the NHFN backbone sites (BBEB) was necessarily terminated due to seismic retrofit work on the east span of the Bay Bridge. The borehole site containing the permanently emplaced seismic package is being effectively destroyed by the project, so reactivation of recording from the site will not be possible. The BBEB installation also served as a relay site for data telemetry from other borehole stations on the east and west spans of the bridge. Fortunately the portions of the BBEB installation critical for telemetry relay were recoverable, and we have now revitalized its role as the principal relay site for NHFN stations located along the Bay Bridge.

New Installations

We have now fully upgraded our only post-hole (3.4 meter deep) site (SMCB) with a deep borehole (150.9 meter) installation (SM2B) at St. Mary's College. An overlap period of ~60 days of coincident data from both stations was also collected and analyzed in July of 2007 for calibration purposes, and the new site is on-line and contributing real-time data to the NCSS. Over the past year, considerable field effort has been placed into hardening the site and knocking down spurious noise sources so that the data currently being recorded by SM2B is now on par with the quality of borehole data from other NHFN sites and of significantly better signal to noise than was available from the 3.4 meter post-hole installation.

Also through our partnership with Caltrans, significant progress on infrastructure installation has been made at 4 additional sites where deep boreholes have been drilled and instrumented (PETB, E07B, W05B, and RB2B). These sites are expected to come on-line in the next year as contributed efforts from our Caltrans partner are completed and as retrofit projects on the Bay Bridge are completed.

With Caltrans funding, we have also purchased sensors and instrumentation for 2 additional sites, and Caltrans will provide drilling for these sites as spare drilling crew time becomes available (i.e., holes of opportunity). Permit negotiations for these two sites (PINB, shown in Figure 3.9; and a site at Cal Maritime Academy, north of the Carquinez bridge) are in their final stages. Once permits have been granted, drilling and sensor installation at these two sites will take place as Caltrans drill crews become available.

3.4 Acknowledgments

Thomas V. McEvilly, who passed away in February 2002, was instrumental in developing the Hayward Fault Network, and, without his dedication and hard work, the creation and continued operation of the NHFN would not have been possible.

Under Bob Nadeau's and Doug Dreger's general supervision, Rich Clymer, Doug Neuhauser, Bob Uhrhammer, Bill Karavas, John Friday, and Rick Lellinger all contribute to the operation of the NHFN. Bob Nadeau prepared this section.

Support for the NHFN is provided by the USGS through the NEHRP grant program (grant no. 07HQAG0014) and by Caltrans through grant no. 59A0578. Pat Hipley of Caltrans has been instrumental in the effort to continue to upgrade and expand the network. Larry Hutchings and William Foxall of LLNL have also been important collaborators on the project in years past.

3.5 References

Rodgers, P.W., A.J. Martin, M.C. Robertson, M.M. Hsu, and D.B. Harris, Signal-Coil Calibration of Electromagnetic Seismometers, *Bull. Seism. Soc. Am., 85*(3), 845-850, 1995.

Murdock, J. and C. Hutt, A new event detector designed for the Seismic Research Observatories, *USGS Open-File-Report 83-0785,* 39 pp., 1983.

4. Parkfield Borehole Network (HRSN)

4.1 Introduction

The operation of the High Resolution Seismic Network (HRSN) at Parkfield, California began in 1987, as part of the United States Geological Survey (USGS) initiative known as the Parkfield Prediction Experiment (PPE) (*Bakun and Lindh*, 1985).

Figure 3.13 shows the location of the network, its relationship to the San Andreas fault, sites of significance from previous and ongoing research using the HRSN, double-difference relocated earthquake locations from 1987-1998, routine locations of seismicity from August 2002 to July 2003, nonvolcanic tremor locations from January 2006 through December 2007, and the epicenter of the 1966 and 2004 M6 earthquakes that motivated much of the research. The HRSN records exceptionally high-quality data, owing to its 13 closely-spaced three-component borehole sensors (generally emplaced in the extremely low attenuation and background noise environment at 200 to 300 m depth (Table 3.8), its high-frequency wide bandwidth recordings (0-100 Hz; 250 sps), and its sensitivity to very low amplitude seismic signals (e.g., recording signals of micro-earthquakes with magnitudes below magnitude 0.0 Ml).

Several aspects of the Parkfield region make it ideal for the study of small earthquakes and nonvolcanic tremors and their relationship to tectonic processes and large earthquakes. These include the fact that the network spans the SAFOD (San Andreas Fault Observatory at Depth) experimental zone, the nucleation region of earlier repeating magnitude 6 events and a significant portion of the transition from locked to creeping behavior on the San Andreas fault, the availability of three-dimensional P and S velocity models (*Michelini and McEvilly*, 1991), a long-term HRSN seismicity catalogue (complete to very low magnitudes and that includes at least half of the M6 seismic cycle), a well-defined and simple fault segment, the existence of deep nonvolcanic tremor (NVT) activity, and a relatively homogeneous mode of seismic energy release as indicated by the earthquake source mechanisms (over 90% right-lateral strike-slip).

In a series of journal articles and Ph.D. theses, the cumulative, often unexpected, results of UC Berkeley's HRSN research efforts (see: `http://www.seismo.berkeley.edu/seismo/faq/parkfield_bib.html`) trace the evolution of a new and exciting picture of the San Andreas fault zone responding to its plate-boundary loading, and they are forcing new thinking on the dynamic processes and conditions within the fault zone at the sites of recurring small earthquakes and deep nonvolcanic tremors (*Nadeau and Dolenc, 2005*).

The Parkfield area has also become an area of focus of the EarthScope Project (`http://www.earthscope.org`) through the SAFOD experiment (`http://www.icdp-online.de/sites/sanandreas/news/news1.html`), and the HRSN is playing a vital role in this endeavor. SAFOD is a comprehensive project to drill into the hypocentral zone of repeating M $\sim$ 2 earthquakes on the San Andreas Fault at a depth of about 3 km. The goals of SAFOD are to establish a multi-stage geophysical observatory in close proximity to these repeating earthquakes, to carry out a comprehensive suite of down-hole measurements in order to study the physical and chemical conditions under which earthquakes occur, and to monitor and exhume rock, fluid, and gas samples for extensive laboratory studies (*Hickman et al.*, 2004).

4.2 HRSN Overview

Installation of the HRSN deep (200-300m) borehole sensors initiated in late 1986, and recording of triggered 500 sps earthquake data began in 1987. The HRSN sensors are 3-component geophones in a mutually orthogonal gimbaled package. This ensures that the sensor corresponding to channel DP1 is aligned vertically and that the others are aligned horizontally. Originally a 10 station network, completed in 1988, the HRSN was expanded to 13 borehole stations in late July 2001, and the original recording systems (see previous Berkeley Seismological Laboratory (BSL) Annual Reports) were upgraded to 24 bit acquisition (Quanterra 730s) and 56K frame relay telemetry to UCB. Properties of the sensors are summarized in Table 3.9.

The 3 newest borehole stations were added, with NSF support, at the NW end of the network as part of the SAFOD project to improve resolution of the structure, kinematics, and monitoring capabilities in the SAFOD drill-path and target zones. Figure 3.13 illustrates the location of the drill site, the new borehole sites, and locations of earthquakes recorded by the initial and upgraded/expanded HRSN.

These 3 newest SAFOD stations have a similar configuration to the original upgraded 10 station network and include an additional channel for electrical signals. Station descriptions and instrument properties are summarized in Tables 3.8 and 3.9. All the HRSN data loggers employ FIR filters to extract data at 250 and 20 Hz (Table 3.10).

The remoteness of the drill site and new stations required an installation of an intermediate data collection point at Gastro Peak, with a microwave link to our facility on the California Department of Forestry's (CDF) property in Parkfield. The HRSN stations use SLIP to

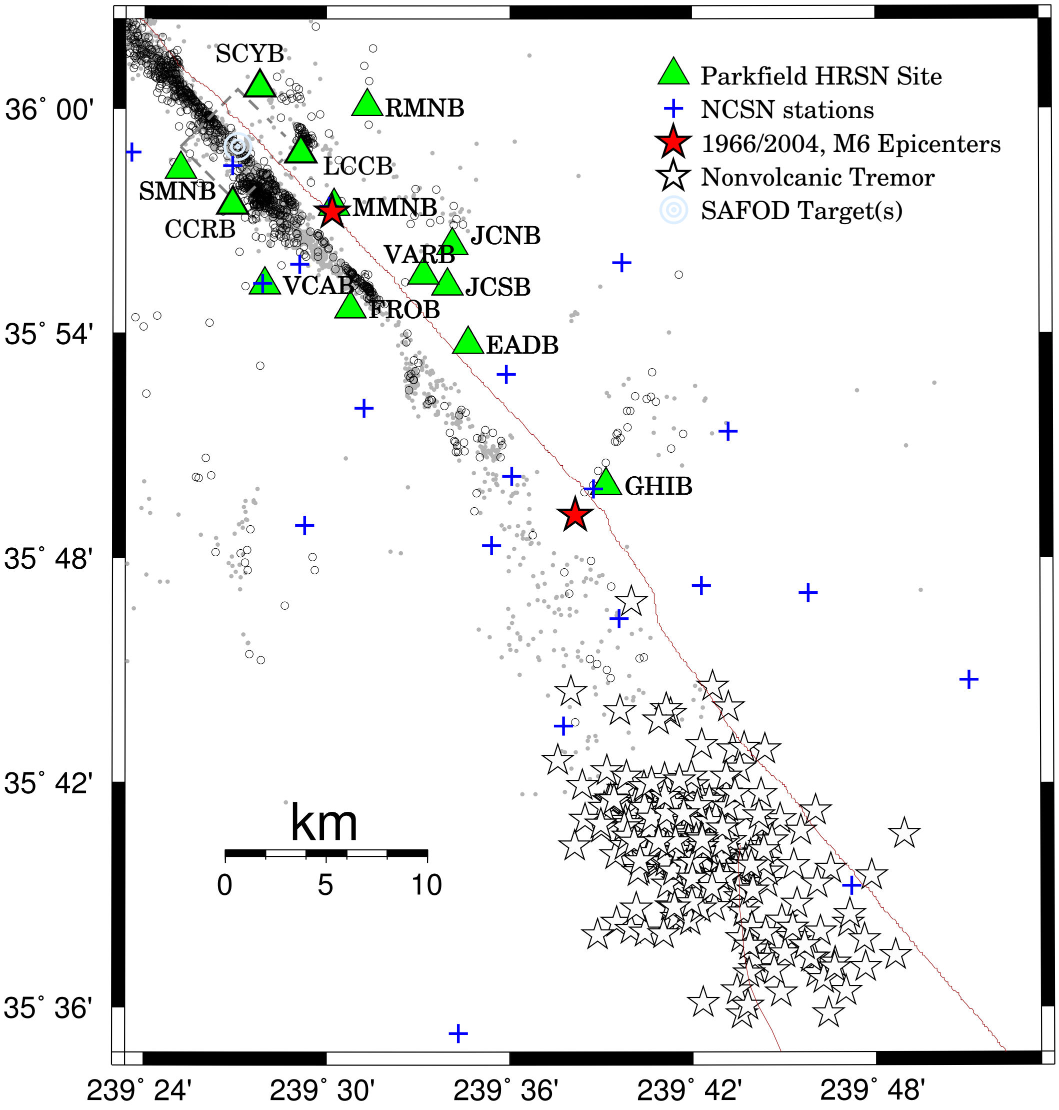

Figure 3.13: Map showing the San Andreas Fault trace and locations of the 13 Parkfield HRSN stations, the repeating M2 SAFOD targets (a 4 km by 4 km dashed box surrounds the SAFOD zone), and the epicenters of the 1966 and 2004 M6 Parkfield main shocks. Also shown are double-difference relocations of nonvolcanic tremors in the Cholame, CA area (January 2006 through December 2007), routine locations of earthquakes recorded by the expanded and upgraded 13 station HRSN (small open circles) and locations of events recorded by the earlier vintage 10 station HRSN relocated using an advanced 3-D double-differencing algorithm (gray points) applied to a cubic splines interpolated 3-D velocity model (*Michelini and McEvilly*, 1991).

Site	Net	Latitude	Longitude	Surf. (m)	Depth (m)	Date	Location
EADB	BP	35.89525	-120.42286	466	245	01/1988 -	Eade Ranch
FROB	BP	35.91078	-120.48722	509	284	01/1988 -	Froelich Ranch
GHIB	BP	35.83236	-120.34774	400	63	01/1988 -	Gold Hill
JCNB	BP	35.93911	-120.43083	527	224	01/1988 -	Joaquin Canyon North
JCSB	BP	35.92120	-120.43408	455	155	01/1988 -	Joaquin Canyon South
MMNB	BP	35.95654	-120.49586	698	221	01/1988 -	Middle Mountain
RMNB	BP	36.00086	-120.47772	1165	73	01/1988 -	Gastro Peak
SMNB	BP	35.97292	-120.58009	699	282	01/1988 -	Stockdale Mountain
VARB	BP	35.92614	-120.44707	478	572	01/1988 - 08/19/2003	Varian Well
VARB	BP	35.92614	-120.44707	478	298	08/25/2003 -	Varian Well
VCAB	BP	35.92177	-120.53424	758	200	01/1988 -	Vineyard Canyon
CCRB	BP	35.95718	-120.55158	595	251	05/2001 -	Cholame Creek
LCCB	BP	35.98005	-120.51424	640	252	08/2001 -	Little Cholame Creek
SCYB	BP	36.00938	-120.53660	945	252	08/2001 -	Stone Canyon

Table 3.8: Stations of the Parkfield HRSN. Each HRSN station is listed with its station code, network id, location, date of initial operation, and site description. The latitude and longitude (in degrees) are given in the WGS84 reference frame. The surface elevation (in meters) is relative to mean sea level, and the depth to the sensor (in meters) below the surface is also given. Coordinates and station names for the 3 new SAFOD sites are given at the bottom.

Site	Sensor	Z	H1	H2	RefTek 24	RefTek 72-06	Quanterra 730
EADB	Mark Products L22	-90	170	260	01/1988 - 12/1998	12/1998 - 07/1999	03/2001 -
FROB	Mark Products L22	-90	338	248	01/1988 - 12/1998	12/1998 - 07/1999	03/2001 -
GHIB	Mark Products L22	90	failed	unk	01/1988 - 12/1998	12/1998 - 07/1999	03/2001 -
JCNB	Mark Products L22	-90	0	270	01/1988 - 12/1998	12/1998 - 06/2001	03/2001 -
JCSB	Geospace HS1	90	300	210	01/1988 - 12/1998	12/1998 - 07/1999	03/2001 -
MMNB	Mark Products L22	-90	175	265	01/1988 - 12/1998	12/1998 - 06/2001	03/2001 -
RMNB	Mark Products L22	-90	310	40	01/1988 - 12/1998	12/1998 - 07/1999	03/2001 -
SMNB	Mark Products L22	-90	120	210	01/1988 - 12/1998	12/1998 - 06/2001	03/2001 -
VARB	Litton 1023	90	15	285	01/1988 - 12/1998	12/1998 - 07/1999	03/2001 -
VCAB	Mark Products L22	-90	200	290	01/1988 - 12/1998	12/1998 - 06/2001	03/2001 -
CCRB	Mark Products L22	-90	N45W	N45E	-	-	05/2001 -
LCCB	Mark Products L22	-90	N45W	N45E	-	-	08/2001 -
SCYB	Mark Products L22	-90	N45W	N45E	-	-	08/2001 -

Table 3.9: Instrumentation of the Parkfield HRSN. Most HRSN sites have L22 sensors and were originally digitized with a RefTek 24 system. After the failure of the WESCOMP recording system, PASSCAL RefTek recorders were installed. In July of 1999, 6 of the PASSCAL systems were returned to IRIS and 4 were left at critical sites. Since July 25, 2001, the upgraded network uses a Quanterra 730 4-channel system. For the three new stations (bottom) horizontal orientations are approximate (N45W and N45E) and will be determined more accurately as available field time permits.

Sensor	Channel	Rate (sps)	Mode	FIR
Geophone	DP?	250.0	T and C	Ca
Geophone	BP?	20.0	C	Ac

Table 3.10: Data streams currently being acquired at operational HRSN sites. Sensor type, channel name, sampling rate, sampling mode, and type of FIR filter are given. C indicates continuous; T triggered; Ac acausal; Ca causal. "?" indicates orthogonal, vertical, and 2 horizontal components.

transmit TCP and UDP data packets over bidirectional spread-spectrum radio links between the on-site data acquisition systems and the central recording system at the CDF. Prior to June, 2008, six of the sites transmitted directly to a router at the central recording site. The other seven sites transmitted to a router at Gastro Peak, where the data are aggregated and transmitted to the central site over a 4 MBit/second digital 5.4 GHz microwave link. All HRSN data are recorded to disk at the CDF site. Due to disproportionately increasing landowner fees for access to the Gastro Peak site, we have been in the process of reducing our dependence on that site, and, as of this report, data from three of the stations previously telemetering through Gastro Peak have been routed through an alternative site and Hogs Canyon (HOGS) (See "2007-2008 Activities," this section).

The upgraded and expanded system is compatible with the data flow and archiving common to all the elements of the BDSN/NHFN and the NCEDC (Northern California Earthquake Data Center), and is providing remote access and control of the system. It has also provided event triggers with better timing accuracy and is also now recording continuous 20 and 250 sps data for all channels of the HRSN, which flow seamlessly into both the USGS automated earthquake detection system and into Berkeley's NCEDC for archiving and online access to the community. The new system also helps minimize the problems of timing resolution, dynamic range, and missed detections, in addition to providing the added advantage of conventional data flow (the old system (1987-2001) recorded SEGY format).

Another feature of the new system that has been particularly useful both for routine maintenance and for pathology identification has been the Internet connectivity of the central site processing computer and the station data loggers with the computer network at BSL. Through this connection, select data channels and on-site warning messages from the central site processor are sent directly to BSL for evaluation by project personnel. If, upon these evaluations, more detailed information on the HRSN's performance is required, additional information can also be remotely accessed from the central site processing computer at Parkfield. Analysis of this remotely acquired information has been extremely useful for trouble shooting by allowing field personnel to schedule and plan the details of maintenance visits to Parkfield. The connectivity also allows certain data acquisition parameters to be modified remotely when needed, and commands can be sent to the central site computer and data loggers to modify or restart processes when necessary.

The network connectivity and seamless data flow to the NCEDC also provides near-real-time monitoring capabilities that are useful for rapid evaluation of significant events as well as the network's overall performance level. For example, shown in Figure 3.14 are P-wave seismograms of the deep focus M_w 7.7 earthquake in the Sea of Okhotsk (Lat.: 53.8920; Lon.: 152.8840) occurring on July 5, 2008 02:12:04 (UTC) (6688 km from Parkfield, CA; depth 636 km) recorded on the DP1 (vertical) channels of the 12 HRSN borehole stations in operation at the time. No casualties were reported from this event. The seismic data from the quake was telemetered to Berkeley and available for analysis by the Northern California Seismic System (NCSS) real-time/automated processing stream within a few seconds of being recorded by the HRSN. All station waveforms in the plots are ordered by distance.

This is a good signal source for examining the relative responses of the BP borehole network station/components to seismic ground motion, and these and corresponding waveform plots for the horizontal (DP2 and DP3 channels) indicate that the following stations were not responding normally to seismic ground motions at the time of this event:
JCSB.BP.DP2 - spiking - no seismic response
JCSB.BP.DP3 - digitizer bit noise - no seismic response
GHIB.BP.DP1 - digitizer bit noise - no seismic response
LCCB.BP.DP1 - poor response
LCCB.BP.DP1 - poor response
MMNB.BP.DP1 - low frequency drift - no response
MMNB.BP.DP2 - low frequency drift - no response
In addition, the ground velocities inferred from the two horizontal components at RMNB and the DP2 horizontal at VCAB are significantly higher than the corresponding ground velocities inferred from the other operating BP network horizontal components. By rapidly generating such plots following large teleseismic events, quick assessment of the HRSN seismometer responses to real events is easily done and corrective measures implemented with relatively little delay.

Data Flow

Initial Processing Scheme. Continuous data streams on all HRSN components are recorded at 20 and 250 sps on disk on the local HRSN computer at the CDF facility. These continuous data are transmitted in near-real-time to the Berkeley Seismological Laboratory (BSL) over a T1 link and then archived at the NCEDC. In addition, the near-real-time data are being transmitted over the T1 circuit to the USGS at Menlo Park, CA where they are integrated into the Northern California Seismic System (NCSS) real-time/automated processing stream. This integration has also significantly increased the sensitivity of the NCSN catalog at lower magnitudes, effectively doubling the number of small earthquake detections in the critical SAFOD zone.

Shortly after being recorded to disk on the central site HRSN computer, event triggers for the individual station data are also determined, and a multi-station trigger association routine then processes the station triggers and generates a list of potential earthquakes. For each potential earthquake that is detected, a unique event identification number (compatible with the NCEDC classification scheme) is also assigned. Prior to the San Simeon earthquake of December 22, 2003, 30 second waveform segments were then collected for all stations and components and saved to local disk as an event gather, and event gathers were then periodically telemetered to BSL and included directly into the NCEDC earthquake database (dbms) for analysis and processing.

Because of its mandate to detect and record very low magnitude events in the Parkfield area, the HRSN is extremely sensitive to changes in very low amplitude seismic signals. As a consequence, in addition to detecting very small local earthquakes at Parkfield, the HRSN also detects numerous regional events and relatively distant and small amplitude nonvolcanic tremor events. For example, spot checks of aftershocks following the M6.5 San Simeon earthquake of December 22, 2003 using continuous data and HRSN event detection listings have revealed that the overwhelming majority of HRSN detections following San Simeon resulted from seismic signals generated by San Simeon's aftershocks, despite the HRSN's ~50 km distance from the events. Data from the California Integrated Seismic Network (CISN) show that there were ~1,150 San Simeon aftershocks with magnitudes > 1.8 in the week following San Simeon, and during this same period, the number of HRSN event detections was ~10,500 (compared to an average weekly rate before San Simeon of 115 detections). This suggests that, despite the ~50 km distance, the HRSN is detecting San Simeon aftershocks well below magnitude 1.

Current Processing. Since the beginning of the network's data collection in 1987, and up until recently, the local and regional events were discriminated based on analyst assessment of S-P times, and only local events with S-P times less than ~2.5 sec at the first arriving station were picked and located as part of the HRSN routine catalog. However, because of the network's extreme sensitivity to the large swarm of aftershocks from the San Simeon and M6 Parkfield earthquakes of September 2004 (e.g., in the first 5 months following the San Simeon mainshock, over 70,000 event detections were made by the HRSN system, compared to an average 5 month detection rate of 2500 prior to San Simeon) and because of ever declining funding levels, this approach has had to be abandoned.

The dramatic increase in event detections vastly exceeded the HRSN's capacity to process both the continuous and triggered event waveform data. To prevent the loss of seismic waveform coverage, processing of the triggered waveform data has been suspended to allow the telemetry and archiving of the 20 and 250 sps continuous data to continue uninterrupted. Cataloging of the event detection times from the modified REDI real-time system algorithm is also continuing, and the continuous waveform data is currently being telemetered directly to the BSL and USGS over the T1 link for near-real-time processing and archiving at the NCEDC, for access to the research community.

Funding to generate catalogs of local events from the 10s of thousands of aftershock detections has not been forthcoming, and, as a consequence, major changes in our approach to cataloging events have been implemented. The HRSN data is now integrated into NCSN automated event detection, picking, and catalog processing (with no analyst review). In addition, a high resolution procedure is now being developed to automatically detect, pick, locate, double-difference relocate, and determine magnitudes for similar and repeating events down to very low magnitudes (i.e., below magnitude -1.0Ml). These new schemes are discussed in more detail in the activities section below.

4.3 2007-2008 Activities

In addition to the routine operations and maintenance of the HRSN (California's first and longest operating borehole seismic network), research into: a) how to process ongoing similar and repeating seismicity to very low magnitudes, b) ongoing non-volcanic tremors in the Parkfield-Cholame area, c) SAFOD related activities, and d) various approaches to lowering operational (primarily landowner fee) costs have been the primary driving forces behind most of the HRSN project's activities this year.

Operations and Maintenance

Routine maintenance tasks required this year to keep the HRSN in operation include cleaning and replacement of corroded electrical connections; grounding adjustments; cleaning of solar panels; re-seating, resoldering, and replacement of faulty pre-amp circuit cards; testing and replacement of failing batteries; and insulation and painting of battery and data logger housings to address problems with low power during cold weather. Remote monitoring of the network's health using the Berkeley Seismological Laboratory's SeisNetWatch software is also performed to identify both problems that can be

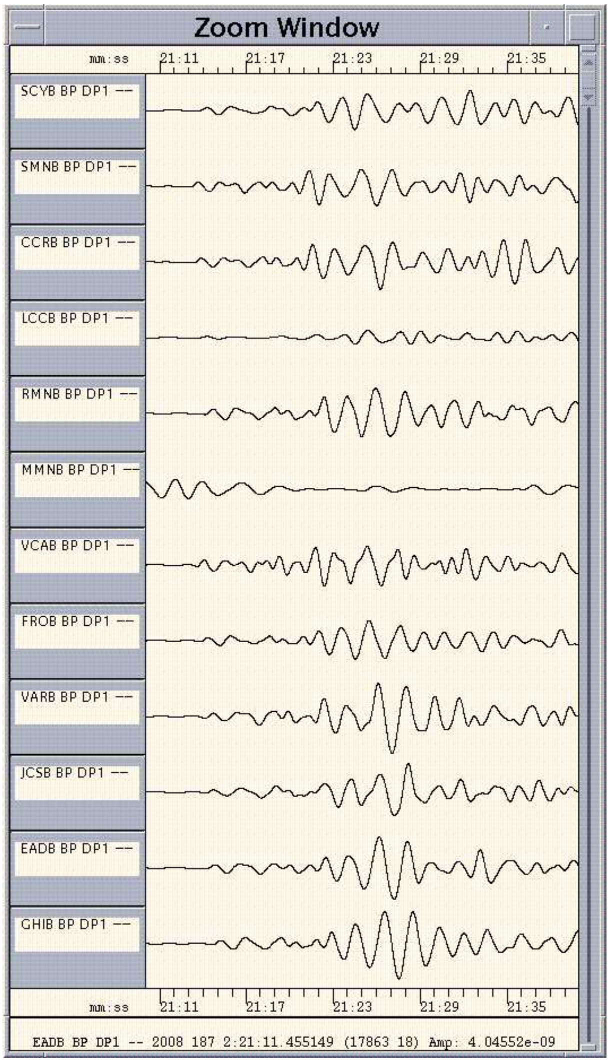

```
EADB BP DP1 -- 2008 187 2:21:11.455149 (17863 18) Amp: 4.04552e-09
```

Figure 3.14: Plot of P-wave seismograms of the deep focus M_w 7.7 earthquake in the Sea of Okhotsk (Lat.: 53.8920; Lon.: 152.8840; 6688 km from Parkfield, CA; depth 636 km) occurring on July 5, 2008 02:12:04 (UTC) recorded on the DP1 (vertical) channels of the 12 HRSN borehole stations in operation at the time. All station waveforms in the plots are ordered by distance from the earthquake. Here, vertical component geophone (velocity) data have been 0.1-0.5 Hz bandpass filtered.

resolved over the Internet (e.g. rebooting of data acquisition systems due to clock lockups) and more serious problems requiring field visits. Over the years, such efforts have paid off handsomely by providing exceptionally low noise recordings of very low amplitude seismic signals produced by microearthquakes (below magnitude 0.0Ml) and nonvolcanic tremors.

Also in the spring of this year, the central site processing computer at our CDF site failed. We had previously obtained funds to purchase a back-up computer at the site, and these funds were used to purchase a new computer which is now installed and operating properly. During the failure, data was telemetered directly over the T1 line, resulting in relatively little data loss. Now, with the computer processing reestablished, backup support in case of telemetry failures is once again in place.

In the Spring of 2008, signals from HRSN station JCNB began showing signs of deterioration. Shortly thereafter, data flow from this station stopped completely. Field investigation showed that the borehole sensor and cable had been grouted to within ~100 feet of the surface and that a rodent had found itself trapped in the upper 100 foot void space and chewed through the cable, thus severing the connection to the deep borehole package. At this time, costs for reestablishing connection to the cable at depth have been prohibitive, and it is also likely that the grouted-in sensor has been compromised by fluids running down the exposed cable. Hence, plans are being made to substitute either a surface seismometer or a borehole sensor package within the open 100 foot section of the borehole to provide continued seismic coverage at the JCNB site.

The network connectivity over the T1 circuit also allows remote monitoring of various measures of the state of health of the network in near-real-time, such as background noise levels. Shown in Figure 3.15 are power spectral density (PSD) plots of background noise for vertical components of the HRSN for a 30 minute period beginning at 2 AM local time on day 7/31/2008 (Thursday morning). By periodically generating such plots, we can rapidly evaluate the network's recording of seismic signals across the wide high-frequency spectrum of the borehole HRSN sensors. Changes in the responses often indicate problems with the power, telemetry, or acquisition systems, or with changing conditions in the vicinity of station installations that are adversely effecting the quality of the recorded seismograms.

Notable in Figure 3.15 are the relatively low PSD levels and overall consistency for most of the HRSN stations. One exception is the relatively high PSD for station LCCB's DP1 channel, which at the time of the PSD analysis was experiencing serious spiking and elevated noise levels across the entire spectrum. Also notable on the DP1 channels for stations GHIB and SCYB are 60 Hz noise peaks, which are indicative of ground loop problems. Noise peaks for station RMNB can also be seen at 15 Hz and 30 and 60 Hz harmonics. These spectral peaks are not always present but occur for about 4 hours at night every other day or so when the Southern California Gas company's generator kicks in to supplement the charging of batteries for their otherwise solar powered installation located about 30 m from the RMNB site.

Once state of health issues are identified with the PSD analyses, further remote tests can be made to more specifically determine possible causes for the problem, and corrective measures can then be planned in advance of field deployment within a relatively short period of time.

Reducing Operational costs

The increased scientific activity in the rural Parkfield area due to SAFOD has lead to an increased demand for site access and development on privately owned property and a corresponding increase in access fees charged by private land owners. As a result, land use fees paid by the HRSN project have increased dramatically from less than $1000 annually prior to the SAFOD effort to over $14,000. This represents over 15% of the entire HRSN budget with no corresponding increase in support from the project's funding agency. To compensate for the increased landowner costs, maintenance efforts have had to be cut back, and network performance has suffered.

To help alleviate the problem, this year we have begun implementing plans to minimize our dependence on access to private lands. This has primarily involved establishing alternative telemetry paths for HRSN sites with a minimum of additional effort and equipment. Central to this effort has been reaching cooperative agreements with other agencies involved in research in the area (i.e., the USGS and UNAVCO).

To date, telemetry paths for three HRSN sites (SCYB, CCRB, and SMNB) have been redirected from the Gastro Peak relay site to an alternative relay site at Hogs Canyon (HOGS) through an agreement with the USGS. Plans to redirect telemetry of an additional 4 sites from Gastro Peak (MMNB,VARB,LCCB, and GHIB) through Mine Mountain are now being field tested, and, if proven sound, negotiations with UNAVCO and the Mine Mountain landowner will be undertaken and infrastructure for the alternative paths will be installed.

Tremor Monitoring

The HRSN data played an essential role in the discovery of nonvolcanic tremors along the San Andreas Fault (SAF) below Cholame, CA (*Nadeau and Dolenc, 2005*). The Cholame tremors occupy a critical location between the smaller Parkfield (~M6) and much larger Ft. Tejon (~M8) rupture zones of the SAF (Figure 3.13). Because the time-varying nature of tremor activity is believed to reflect time-varying deep deformation and presumably episodes of accelerated stressing of faults, and because an anomalous increase in the rate of Cholame tremor activity preceded the 2004 Parkfield M6 by ~21 days, we are continuing to monitor the tremor activity observable by the HRSN to look for anomalous rate changes that may signal an increased likelihood for another large SAF event to the SE. Some recent results of the monitoring effort are described further in the "Research" section of this report.

Similar Event Catalog

The increased microseismicity rates resulting from the San Simeon M6.5 and Parkfield M6 events and the increased interest in even smaller events in the SAFOD target zone have required new thinking on how to detect and catalog microearthquakes recorded by the HRSN. One action taken to help address this problem has been to integrate HRSN data streams into the NCSN event detection and automated cataloging process. This approach has been successful at discriminating small events in the local Parkfield area from other types of event detections and for providing automated locations of a significantly increased number of small events in the local area (approximately double that of the NCSN network alone). However, the HRSN sensitized NCSN catalog is still only catching about 1/2 the number of local events previously cataloged by the HRSN, and waveforms for the small events are not typically made available. In addition, unlike the previous HRSN catalog, the additional events added by the NCSN-HRSN integration are not reviewed by an analyst, nor do they generally have magnitude determinations associated with them. In some cases, the selection rules used for the integrated catalog also result in exclusion of events that are otherwise included by the NCSN.

These limitations severely hamper ongoing efforts relying on similar and characteristically repeating microearthquakes. They also reduce the effectiveness of research relying on numerous very small magnitude events in the SAFOD zone (e.g. for monitoring seismicity in the SAFOD target region).

To help overcome these limitations, we are continuing our efforts to develop and implement our automated similar event cataloging scheme based on cross-correlation and pattern scanning of the continuous HRSN data now being archived. The method uses a small number of reference events whose waveforms, picks, locations, and magnitudes have been accurately determined, and it automatically detects, picks, locates, and determines magnitudes for events similar to the reference event to the level of accuracy and precision that only relative event analysis can bring.

The similar event detection is also remarkably insensitive to the magnitude of the reference event used, allowing similar events ranging over several magnitude units to be fully cataloged using a single reference event. It also does a remarkably good job even when seismic energy from multiple events is superposed. Once a cluster of similar events has been cataloged, it is a relatively straightforward process to identify characteristically repeating microearthquake sequences within the cluster (frequently a single similar event "cluster" will contain several sequences of repeating events).

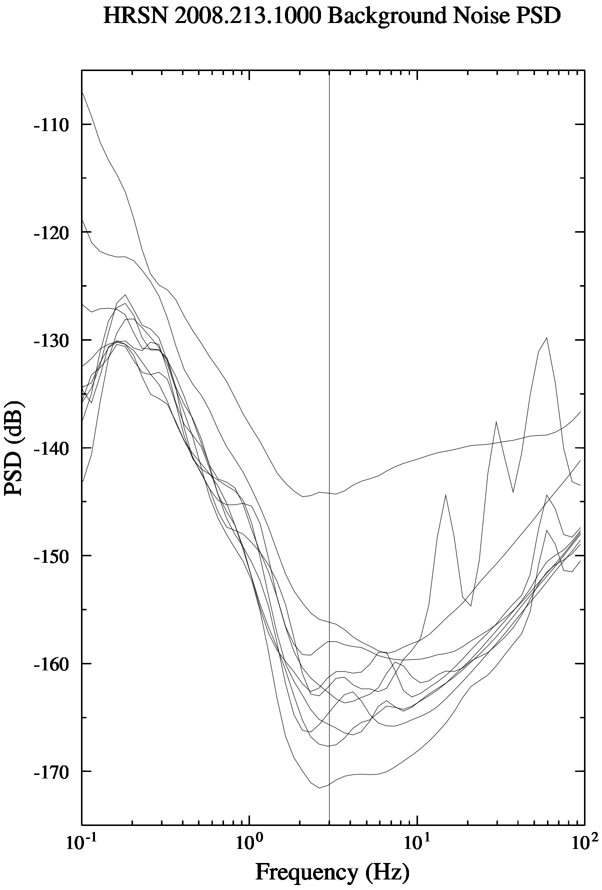

Figure 3.15: Background noise Power Spectral Density (PSD) levels for the 250 sps vertical component channels (DP1) of the HRSN borehole stations as a function of frequency. The data are from 2 AM Local time on 7/31/2008 (Thursday morning). The vertical (DP1) channels for stations CCRB and MMNB were out during this period. The 2 Hz minimum for the sensors occurs because of the 2 Hz sensors used at these sites. Below 2 Hz, noise levels rise rapidly and the peak at 5 to 3 sec (.2 to .3 Hz) is characteristic of teleseismic noise observed throughout California. The PSD (dB) ranking at 3 Hz (intersection with vertical line) for the vertical channels in operation at the time of the analysis was:
SCYB.BP.DP1 -171.30859
FROB.BP.DP1 -167.66554
SMNB.BP.DP1 -165.58936
EADB.BP.DP1 -164.69122
JCSB.BP.DP1 -162.62303
RMNB.BP.DP1 -162.25391
GHIB.BP.DP1 -161.32861
VCAB.BP.DP1 -157.98297
VARB.BP.DP1 -156.12631
LCCB.BP.DP1 -144.19135

This high level of precision and low magnitude completeness has already proven useful to SAFOD for helping to delineate and constrain the active fault structure in the target zone (see, "Efforts in Support of SAFOD", below). It has also proven vital this year for helping to resolve a long-standing debate in the seismologic community regarding the stress-drop scaling issues by providing pairs of nearly collocated events with similar waveforms but significantly differing magnitudes for use in kinematic slip inversions using an eGf approach (*Dreger et al.*, 2007).

This year, the automated cataloging procedure for similar events is continuing to be refined to capture even smaller events and events over a larger area, as well as for increased processing speed. Eventually, a composite catalog of similar event groups from throughout the HRSN coverage zone is planned.

Further development of the similar event processing approach also holds promise in other applications where automated and precise monitoring of bursts of seismic activity to very low magnitudes is desirable (e.g. in aftershock zones or in volcanic regions) or where automated updates of preexisting repeating sequences and their associated deep slip estimates are desired.

Efforts in Support of SAFOD

An intensive and ongoing effort by the EarthScope component called SAFOD (San Andreas Fault Observatory at Depth) is underway to drill through, sample, and monitor the active San Andreas Fault at seismogenic depths and in very close proximity (within a few 10s of km or less) of a repeating magnitude 2 earthquake site. The HRSN data plays a key role in these efforts by providing low noise and high sensitivity seismic waveforms from active and passive sources, and by providing a backbone of very small earthquake detections and continuous waveform data.

As of early September, 2007, SAFOD drilling had penetrated the fault near the HI repeating target sequence and collected core samples in the fault region that presumably creeps and surrounds the repeatedly rupturing HI patch. Unfortunately, due to complications during drilling, penetration and sampling of the fault patch involved in repeating rupture was not possible. Future efforts will be focused on long-term monitoring of the ongoing chemical, physical, seismological, and deformational properties in the zone (particularly any signals that might be associated with the next repeat of the SAFOD repeating sequences).

HRSN activities this year have contributed in three principal ways to these and longer-term SAFOD monitoring efforts:
1) Integration and processing of the HRSN data streams with those from the NCSN in the Parkfield area continues, effectively doubling the number of small events available for monitoring seismicity in the target zone and for constraining relative locations of the ongoing seismic activity.

2) Telemetry of all HRSN channels (both 20 and 250 sps data streams) continues to flow directly from Parkfield, through the USGS Parkfield T1 and the NCEMC T1, to the USGS and the BSL for near-real-time processing, catalog processing, and data archiving on the web-based NCEDC. This also provides near immediate access of the HRSN data to the SAFOD community without the week- or month-long delay associated with the previous procedure of having to transport DLT tapes to Berkeley to upload and quality check the data.

3) We have also continued to apply our prototype similar event automated catalog approach to the primary, secondary, and tertiary SAFOD target zones as a continued effort to monitor the SAFOD target zone activity at very high relative location precision.

During the final push to penetrate the repeating SAFOD target last Fall, our SAFOD similar event detections and catalogs were also used by the working group to extract data from the corresponding PASO array, Pilot Hole, NCSN, and mainhole data sets for integration with the HRSN data in order to provide the detailed information that was needed by drill crews for the final targeting of the HI target penetration and coring.

4.4 Acknowledgments

Thomas V. McEvilly, who passed away in February 2002, was the PI on the HRSN project for many years. Without his dedication, continued operation of the HRSN would not have been possible. Under Bob Nadeau's and Doug Dreger's general supervision, Rick Lellinger, Rich Clymer, Bob Uhrhammer, Doug Neuhauser, Peter Lombard, Bill Karavas, John Friday and Don Lippert all contribute to the operation of the HRSN. Bob Nadeau prepared this section. During this reporting period, operation, maintenance, and data processing for the HRSN project was supported by the USGS, through grant 07HQAG0014.

4.5 References

Bakun, W. H., and A. G. Lindh, The Parkfield, California, prediction experiment, *Earthq. Predict. Res., 3*, 285-304, 1985.

Dreger, D., R.M. Nadeau, and A. Morrish, Repeating Earthquake Finite-Source Models: Strong Asperities Revealed on the San Andreas Fault, *Geophys. Res. Lett.*, revised version submitted, 2007.

Hickman, S., M.D. Zoback and W. Ellsworth, Introduction to special section: Preparing for the San Andreas Fault Observatory at Depth, *Geophys. Res. Lett., 31*, L12S01, doi:10.1029/2004GL020688, 2004.

Michelini, A. and T.V. McEvilly, Seismological studies at Parkfield: I. Simultaneous inversion for velocity structure and hypocenters using B-splines parameterization, *Bull. Seismol. Soc. Am., 81*, 524-552, 1991.

Nadeau, R.M. and D. Dolenc, Nonvolcanic Tremors Deep Beneath the San Andreas Fault, *SCIENCE, 307*, 389, 2005.

5. Bay Area Regional Deformation Network

5.1 Introduction

This year was the second of the funded BARD project for the period 2007-2010. In consequence, this year, we have continued to push forward the efforts initiated in the previous year. One new site was installed (UCSF). According to our specifications, this site is collecting 1Hz data and buffering 5Hz data. The scientific efforts have focused on the processing of the high-rate GPS data in order to include the GPS solutions (static offsets and dynamic waveforms) in the existing monitoring system for the seismic activity in Northern California (magnitude determination, moment tensors, and the Elarms system). With Doug Dreger, we are about to release a slip distribution model for the 2004 seismic event based on high rate GPS waveforms only.

5.2 BARD overview

Description of the network

The BSL currently maintains and operates 30 BARD stations (twenty-six bi-frequency sites and four L1 sites). The sampling rate varies from 1 to 30 seconds, and the data are transmitted continuously over a serial connection. Most stations use frame relay technology, either alone or in combination with radio telemetry.

Of the 30 sites, ten (BRIB, CMBB, FARB, HOPB, MHCB, ORVB, PKDB, SAOB, SUTB, and YBHB) are collocated with broadband seismic stations of the BDSN with which they share continuous frame-relay telemetry to UC Berkeley. These sites use the Quanterra data loggers to store and retrieve the GPS data converted to MiniSEED format (*Perin et al.,* 1998). The MiniSEED approach provides more robust data recovery from onsite backup on the Quanterra disks following telemetry outages.

Another five stations (SVIN, MHDL, OHLN, OXMT, and SBRN) have been installed in the last 3 years in the SFBA and along the Hayward Fault as the Berkeley part of a multi-institutional effort funded by the NSF/MRI program to improve strain monitoring in the SFBA using an integrated approach, with significant participation of the USGS/MP (*Murray et al.*, 2002a). These stations include borehole tensor strainmeters, three-component borehole seismic velocity sensors, downhole pore pressure and tilt sensors, and GPS receivers. This project served as a prototype for the strainmeter installations planned for PBO, which faces many of the same station installation, configuration, and data retrieval issues we have addressed. Consequently, these 5 stations have received the nickname *mini-PBO.* From July 2001 to August 2002, five boreholes were drilled to about 200-m depth and equipped with tensor strainmeters recently developed by CIW and 3-component L22 (velocity) seismometers. For this project, we developed a self-centering GPS antenna mount for the top of the borehole casings, which are mechanically isolated from the upper few meters of the ground, to provide a stable, compact monument that allows access to the top of the borehole casing for downhole maintenance. The 5 GPS receivers were progressively installed and connected to Quanterra 4120 data loggers, which provide backup and telemetry capabilities. The completion of the last station (MHDL), located in the Marin Headlands, took longer because it required AC power, which PG&E installed in December 2005. The site is operational since September 1, 2006. In addition, 10-minute interval data, which are retrieved from all the sites by the USGS via a backup GOES satellite system, show that all the sites are successfully measuring strains due to tidal effects and to local and teleseismic earthquakes (*Murray et al.*, 2002b).

The remaining BSL/BARD stations only record C-GPS data.

Each BSL/BARD station uses a low-multipath chokering antenna, most of which (except the “mini-PBO” ones discussed above) are mounted to a reinforced concrete pillar approximately 0.5-1.0 meter above the ground level. The reinforcing steel bars of the pillar are drilled and cemented into a rock outcrop to improve long-term monument stability. A low-loss antenna cable is used to minimize signal degradation on the longer cable setups that normally would require signal amplification. Low-voltage cutoff devices are installed to improve receiver performance following power outages. Most stations are equipped with aging Z-12 receivers, which were originally programmed to record data once every 30 s and observe up to 12 satellites simultaneously at elevations down to the horizon. The antennas are equipped with SCIGN antenna adapters and hemispherical domes, designed to provide security and protection from weather and other natural phenomena and to minimize differential radio propagation delays. The BSL acquired 7 Ashtech MicroZ-CGRS (uZ) receivers with NSF funding for the Mini-PBO project. These have been installed at the “mini-PBO” stations, and two have been used to replace failing Z12s at other stations (CMBB and MODB). At these sites, the data are collected using only direct serial connections and are susceptible to data loss during telemetry outages.

There is growing interest in collecting higher rate data for a variety of applications. For example, GPS measurements can accurately track the propagation of earthquake dynamic motions both on the ground (*e.g., Lar-*

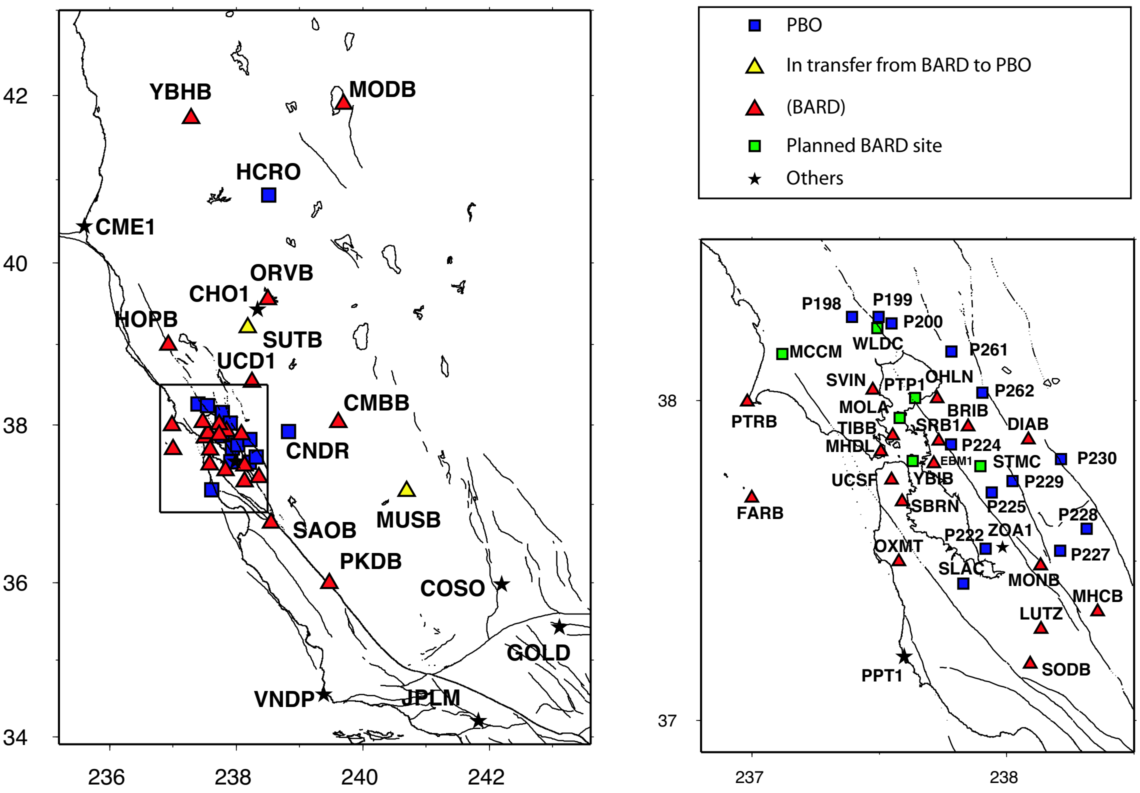

Figure 3.16: Operational BARD stations (red triangles) in northern California (left) and in the San Francisco Bay area (zoom on the right). PBO C-GPS sites are indicated by blue squares and planned BARD sites for period 2007-2010 are symbolized by green ones.

son et al., 2003) and in the atmosphere (*e.g., Artru et al.*, 2001, *Ducic et al.*, 2003), providing complementary information to seismic observations (calibration of integrated acceleration and velocity sensor data) and estimates of earth structure (direct observation of surface wave propagation over the oceans). We started collecting 1 Hz observations at 2 stations (DIAB and MONB) in 2003. In the last year, we have progressively upgraded the telemetry to continuous 1 Hz telemetry at 3 additional stations (BRIB, HOPB, and PTRB), where the bandwidth of the existing telemetry system allowed it. At stations collocated with broadband seismic sensors, the seismic data has priority for telemetry, because it is used in the Northern California real-time earthquake notification system (see `http://www.cisn.org/ncmc/`) making this upgrade more difficult and in general not feasible with the current Z12 receivers because of insufficient data compression. All data collected from BARD/BSL are publicly available at the Northern California Earthquake Data Center (NCEDC; `http://www.ncedc.org/bard/`).

Between 1993 and 2001, the BSL acquired 29 Ashtech Z-12 and Micro-Z receivers from a variety of funding sources, including from federal (NSF and USGS), state (CLC), and private (EPRI) agencies. The network enhances continuous strain measurements in the Bay Area and includes several profiles between the Farallon Islands and the Sierra Nevada in order to better characterize the larger scale deformation field in Northern California (Figure 3.16). During the last two years 10 NETRS have been purchased via the UNAVCO purchase program. Theses receivers will help to upgrade the network to full high-rate capabilities. Three receivers are operating today (BRIB, MHDL and DIAB).

The number of continuous GPS stations in Northern California is significantly increasing with over 250 new site installations planned by 2008 as part of the Plate Boundary Observatory (PBO) component of the NSF-funded Earthscope project. UNAVCO and researchers from BARD and the other regional networks, such as SCIGN, BARGEN, and PANGA, are funded by NSF to fold operation and maintenance of about 200 existing stations, which constitute the PBO Nucleus network, into the PBO array by 2008. Two BSL-maintained stations (SUTB and MUSB) are included in the PBO Nucleus network. The other BSL stations are either collocated with seismic instrumentation or are located near the San Andreas Fault where real-time processing of the GPS data for earthquake notification is a high priority. Another 23 Northern California stations, including most of the Parkfield network, will be included in the PBO Nucleus, and we are working with UNAVCO to facilitate their transition to UNAVCO control.

BARD Stations

The majority of the BSL BARD stations use a low-multipath choke-ring antenna, most of which are mounted to a reinforced concrete pillar approximately 0.5–1.0 meter above local ground level. The reinforcing steel bars of the pillar are drilled and cemented into a rock outcrop to improve long-term monument stability. A low-loss antenna cable is used to minimize signal degradation on the longer cable setups that normally would require signal amplification. Low-voltage cutoff devices are installed to improve receiver performance following power outages. Most use Ashtech Z-12 receivers that are programmed to record data once every 30 seconds and observe up to 12 satellites simultaneously at elevations down to the horizon. The antennas are equipped with SCIGN antenna adapters and hemispherical domes, designed to provide security and protection from weather and other natural phenomena, and to minimize differential radio propagation delays.

Data from most BSL-maintained stations are collected at 15 or 30-second intervals and transmitted continuously over serial connections (Table 5.2). Station TIBB uses a direct radio link to Berkeley, and MODB uses VSAT satellite telemetry. Most stations use frame relay technology, either alone or in combination with radio telemetry. Fourteen GPS stations are collocated with broadband seismometers and Quanterra data loggers (Table 3.2). With the support of IRIS, we developed software that converts continuous GPS data to MiniSEED opaque blockettes that are stored and retrieved from the Quanterra data loggers (*Perin et al.,* 1998), providing more robust data recovery from onsite disks following telemetry outages.

Data from BRIB, CMBB, DIAB, HOPB, MHCB, MHDL, MONB, OHLN, OXMT, PTRB, SBRN, SRB1, SVIN, TIBB, and UCD1 in the Bay Area, and 13 stations in the Parkfield region (all but PKDB), are now being collected at 1-second intervals. All high-rate observations collected by these stations are currently available from the NCEDC. Collecting at such high-frequency (for GPS) allows dynamic displacements due to large earthquakes to be better measured; however, this 30-fold increase in data can pose telemetry bandwidth limitations. We are planning to convert additional stations to 1-second sampling where possible during the next year. The acquisition of the 5 NETRS bundles will help to complete this project (see Subsection 5.3). In the Bay Area, we have converted stations that have sufficient bandwidth and are currently assessing bandwidth issues at other stations. Prior to the September 28, 2004 M6 Parkfield earthquake, data from the Parkfield stations were collected on an on-site computer, written to removable disk once per month, and sent to SOPAC for long-term archiving (decimated 30-sec data is acquired daily via the BSL frame relay circuit). In response to the earthquake, we modified the procedures

	Sites	Lat. (deg.)	Lon. (deg)	Receiver	Telem. .	Sampling rate	Collocated Network	Location
1	BRIB	37.91	237.84	**NETRS**	T1	**1Hz**	BDSN	Briones Reservation, Orinda
2	CMBB	38.03	239.61	A-UZ12	FR	1Hz	BDSN	Columbia College, Columbia
3	DIAB	37.87	238.08	A-Z12	FR	1Hz		Mt. Diablo
4	FARB	37.69	236.99	A-Z12	R-FR/R	15 s	BDSN	Farallon Island
5	EBMD	37.81	237.71	T-SSI	R	1Hz		East Bay Mud Headquarters
6	HOPB	38.99	236.92	**TR 4000**	FR	**1Hz**	BDSN	Hopland Field Stat., Hopland
7	LUTZ	37.28	238.13	A-Z12	FR	30 s		SCC Comm., Santa Clara
8	MHCB	37.34	238.35	A-Z12	FR	1Hz	BDSN	Lick Obs., Mt. Hamilton
9	MHDL	37.84	237.50	T-NETRS	FR	1Hz	mini-PBO	Marin Headlands
10	MODB	41.90	239.69	A-UZ12	NSN	15 s		Modoc Plateau
11	MONB	37.48	238.13	A-Z12	FR	1Hz		Monument Peak, Milpitas
12	MUSB	37.16	240.69	A-Z12	R-Mi-FR	30 s		Musick Mt.
13	OHLN	38.00	237.72	A-UZ12	FR	1Hz	mini-PBO	Ohlone Park, Hercules
14	ORVB	39.55	238.49	A-Z12	FR	15 s	BDSN	Oroville
15	OXMT	37.49	237.57	A-UZ12	FR	1Hz	mini-PBO	Ox Mountain
16	PKDB	35.94	239.45	A-Z12	FR	30 s	BDSN	Bear Valley Ranch, Parkfield
17	PTRB	37.99	236.98	A-Z12	R-FR	**1Hz**		Point Reyes Lighthouse
18	SAOB	36.76	238.55	A-Z12	FR	30 s	BDSN	San Andreas Obs., Hollister
19	SBRN	37.68	237.58	A-Z12	FR	1Hz	mini-PBO	San Bruno
20	SODB	37.16	238.07	A-Z12	R-FR	30 s		Soda Springs, Los Gatos
21	SRB1	37.87	237.73	T-SSE	FR	1Hz		SRB building, Berkeley
22	SUTB	39.20	238.17	A-Z12	R-FR	30 s	BDSN	Sutter Buttes
23	SVIN	38.03	237.47	A-UZ12	R-FR	1Hz	mini-PBO	St Vincents
24	TIBB	37.89	237.55	A-UZ12	R	1Hz		Tiburon
25	UCD1	38.53	238.24	**NETRS**	WEB	1Hz		UC - Davis
26	YBHB	41.73	237.28	A-Z12	FR	15 s	BDSN	Yreka Blue Horn Mine, Yreka
27	UCSF	37.75	237.55	NETRS	FR	1Hz		UC-San Francisco, San Francisco
28	BDM	37.95	238.13	NETRS			BDSN	Black Diamond Mines Park, Antioch
29	MCCM	38.14	237.12	NETRS			BDSN	Marconi Conference Center, Marshall
30	PTP1	38.00	237.64	NETRS			NHFN	Point Pinole Regional Park

Table 3.11: List of the BARD sites maintained by the BSL. Five models of receiver are operating now: Trimble 4000 SSE (T-SSE), Trimble 4000 SSI (T-SSI), Trimble NETRS, (T-NETRS), Ashtech Z12, and Ashtech Micro Z (A-UZ12). The replacement of the Ashtech Z12 by Trimble NETRS will make the receiver park more homogeneous. The telemetry types are listed in column 6. FR = Frame Relay, R = Radio, Mi= Microwave, WEB = DSL line. Some sites are transmiting data over several legs with different telemetry. Changes from the last year's network table are highlighted in bold typography. The sites 28 to 30 are in progress. For these 3 sites, the instrumentation is available, and permit request procedures have been started.

to download 1-second data converted to compact RINEX format at hourly intervals, which does not significantly impact the telemetry bandwidth.

Data archival

The Northern California Earthquake Data Center (NCEDC), operated jointly by the BSL and USGS, archives all permanent-site GPS data currently being collected in Northern California. In the past months, due to the transition to PBO, some sites are not present in the NCEDC archive (PPT1, for instance). All the sites available will be archived as in the past. We archive the Federal Aviation Administration (FAA) sites all over the west Pacific coast (the closest one is ZOA1). Data importation and quality assurance are automated, although some manual correction of unusual data problems is still required.

As part of the activities funded by the USGS through the BARD network, the NCEDC has established an archive of the 7000+ survey-mode occupations collected by the USGS since 1992. The NCEDC continues to archive non-continuous survey GPS data. The initial dataset archived is the survey GPS data collected by the USGS Menlo Park for northern California and other locations. The NCEDC is the principal archive for this dataset. Significant quality control efforts were implemented by the NCEDC (*Romanowicz et al.*, 1994) to ensure that the raw data, scanned site log sheets, and RINEX data are archived for each survey. All of the USGS MP GPS data has been transferred to the NCEDC, and virtually all of the data from 1992 to the present has been archived and is available for distribution. We are also archiving additional high-precision GPS data sets from Northern California (mainly Parkfield measurements). Together with graduate students in the department, who are now using the GAMIT software to process survey-mode data in the San Francisco Bay area, we are working to combine the survey-mode and C-GPS solutions into a self-consistent velocity field for Northern California. The campaign velocity field computed from campaign measurements by UCB and USGS groups has been published by *d'Alessio et al.*, (2005).

Data from five of our sites (HOPB, MHCB, CMBB, OHLN, and YBHB) are sent to the National Geodetic Survey (NGS) in the framework of the CORS (Continuous Operating Reference Stations) project (`http://www.ngs.noaa.gov/CORS/`). The data from these five sites are also distributed to the public through the CORS ftp site.

5.3 2007-2008 Activities

New stations and upgrades

Permit requests: The permit releases of the sites PTP1 and BDM have encountered administrative delays during the year. However, an agreement has been reached, and the permits are currently at UC Berkeley to be signed by the Real Estate office.The installation of these sites should be completed during the next year. A new site has been installed on the roof top of a UCSF building. This site, as well as the other NETRS site is transmitting real-time 1Hz data and is recording on-site 5Hz data available in case of emergency.

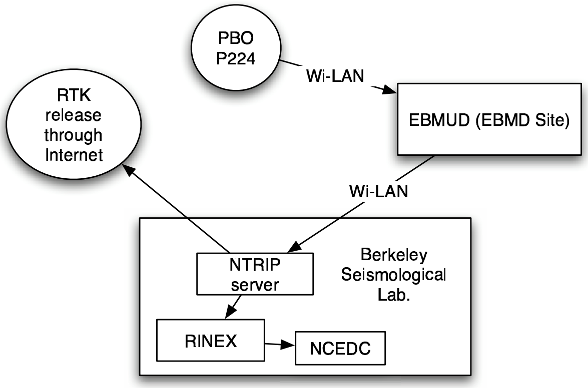

Figure 3.17: Present BSL operations at EBMUD site and planned operations between the PBO site P224 and BSL. Since its installation in 2003, the EBMD site was sending data to BSL using an internet DSL connection. The data collected (Trimble 5700 receiver) are now sent to BSL using a WI-LAN radio connection. The connection represents an upgrade of the quality of the radio link. The data collected here are thus more safely sent to BSL in case of a large seismic event.

Real-Time Kinematic (RTK) service: In the framework of the collaboration with EBPARK, BSL is distributing RTK corrections for some sites. This experimental project aims at developing collaborations with private users or local institutions in Northern California. We hope to densify the network and reduce monumentation and telemetry costs associated with the installation and operation of new sites. This year we have been encountering issues related to the Trimble user of our RTK network. After a series of tests, we requested assistance from the local reseller to complete a reliable connection between one of our NETRS and the Trimble remote device.

Meteorological Sensors and troposphere: In February 2008, we received funding to install three meteorological sensors at GPS sites, in collaboration with UC Riverside. Two of these sensors will be installed at the site SBRN.

SBRN move: The site SBRN has been damaged 3 times this year. The staff decided to move this site to a safer location near the existing one. For a period of time, two receivers will be operated simultaneously in order to check the stability of the current site. It is likely the new site will not keep the code SBRN.

Replacement of CHAB site: We are looking for a new site to replace the existing site CHAB. This 1992 installation is of foremost importance due to its proximity to the Hayward Fault; however, it might be difficult to restore if service is discontinued.

5.4 Data Analysis and Results

CALREF, a stable reference frame for Northern California

The BARD dataset has been processed in the ITRF2000 (*Altamimi et al.*, 2002). The solutions (*Houlié and Romanowicz*, in prep) are in good agreement with campaign solutions (BAVU and USGS) previously released (*d'Alessio et al.,* 2005). The new coordinates release for the BARD network includes currently operating sites and velocities for the sites transferred from BSL to PBO during the last two years.

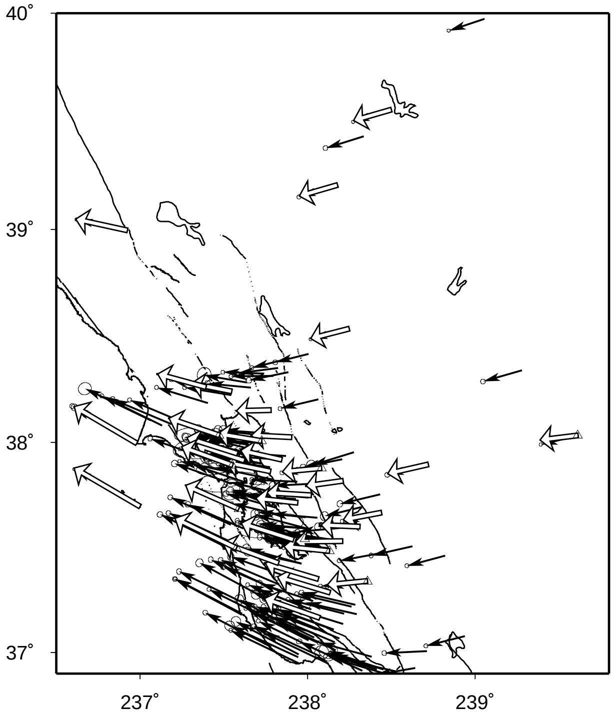

Figure 3.18: Comparison of the BARD solutions (white arrows) with the Bay Area Velocity Unification (BAVU) solutions (black arrows). All the data available at the BSL between 1994 and 2006 have been reprocessed (From *Houlié and Romanowicz,* in prep). BAVU website: `http://seismo.berkeley.edu/~burgmann/RESEARCH/BAVU/`

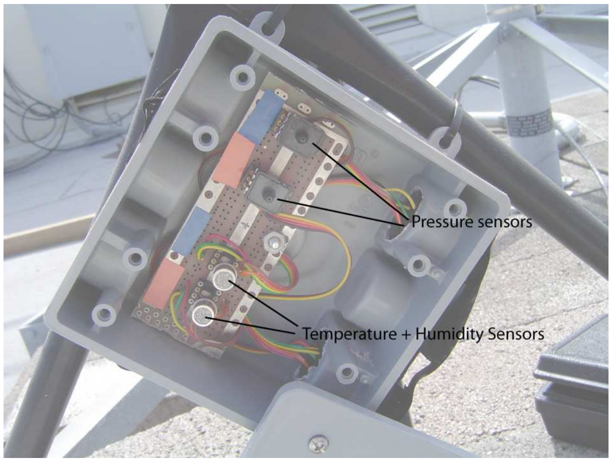

Figure 3.20: Meteorological pair of sensors designed by John Friday.

All the BARD sites have been processed jointly with IGS sites in California. No *a priori* constraints have been assumed during the processing. All the velocities included in the first release of California Reference Frame (CALREF) are given in Table 3.12. The CALREF will provide velocities and coordinates of sites located in the Bay Area at specific epochs. Each solution will be associated with error estimations (formal and real). Every surveyor will be able to control the reference site coordinates for a given survey.

The CALREF processing is being reprocessed to integrate the meteorological data collected at some sites during the last decade.

Quick processing of a selection of sites

In addition to the daily and long-term processing, we developed an additional channel of processing dedicated to the quick solutions. This processing focuses on locating 4 sites in order to provide quick solution offsets in less than 10 minutes. These offsets will thus be available for use in the local moment tensor inversions.

BARD products released on the web

A series of products are released on the new BARD website (`http:/www/ncedc.org/bard/`). The list of products released covers various domains (from time-series to daily troposphere maps) that can potentially benefit from GPS data and will encourage collaboration with BSL researchers and others. All products are updated daily.

Troposphere study in Southern California and in SFBA

Preliminary work completed during the previous year led to a project funded by the Southern California Earthquake Center (SCEC). We are processing years 2006, 2007, and 2008 of the GPS data for the San Gabriel Valley and extending this study to the east. This year,

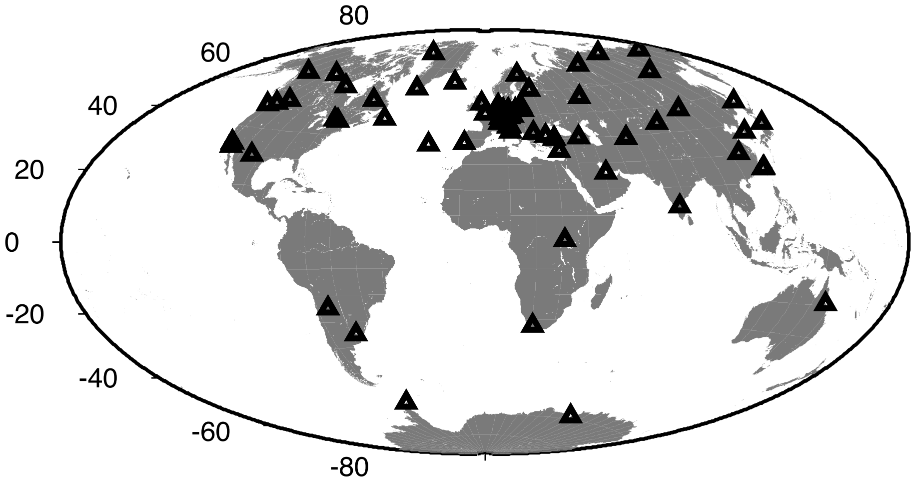

Figure 3.19: Map of the 74 GPS sites, available at SOPAC, collecting meteorological parameters. Only two of these sites are in California (JPLM and SIO3). The sensors we propose to install along BARD instruments will benefit the GPS community.

we will apply similar processing to the BARD network. Two meteorological packages will be operated at SBRN during August 2008 and likely at BRIB during the year 2008/2009. These sensors (Figure 3.20) were designed by John Friday. We hope to minimize the effect of the troposphere on BARD solutions and improve their repeatability.

2004 Parkfield slip distribution update

This year, we have focused our efforts on the high-rate data and their application to seismological products. We have produced high-rate GPS time-series. In collaboration with Doug Dreger, a slip distribution model based on GPS waveforms only has been computed. This slip model was presented at the AGU Fall Meeting 2007. We confirm that the GPS waveforms can be used to constrain fault slip model for large seismic events ($M_w > 6$).

5.5 Acknowledgements

Barbara Romanowicz oversees the BARD program. Nicolas Houlié, Rich Clymer, Bill Karavas, Rick Lellinger, John Friday, and Doug Neuhauser contributed to the operation of the BARD network. The operation of the BARD network is partially supported by funding from the USGS/NEHRP program (grant number 07HQAG0031) and funding from the NSF/UNAVCO *PBO nucleus* grant (number 0453975-09).

5.6 References

Altamimi, Z., P. Sillard, and C. Boucher , ITRF2000: A new release of the International Terrestrial Reference Frame for earth science applications, *J. Geophys. Res.,* 107(B10), 2214, doi:10.1029/2001JB000561, 2002

Artru, J., P., Lognonné and E., Blanc, Normal modes modeling of post-seismic ionospheric oscillations, *Geophys. Res. Lett.*, 28, 697-700, 2001

d'Alessio, M. A., I. A. Johanson, R. Bürgmann, D. A. Schmidt, and M. H. Murray, Slicing up the San Francisco Bay Area: Block kinematics from GPS-derived surface velocities, *J. Geophys. Res.*, 110, B06403, doi:10.1029/2004JB003496, 2005.

Ducic, V., J. Artru and P. Lognonné, Ionospheric remote sensing of the Denali Earthquake Rayleigh surface waves, *Geophys. Res. Lett.*, 30, 18, 2003

Houlié, N. and Romanowicz, B., CALREF, a stable reference frame for the Northern California, submitted.

Larson, Using 1-Hz GPS Data to Measure Deformations Caused by the Denali Fault Earthquake, *Science*, 300, 1421–1424, 2003

Murray, M., Neuhauser D., Gee, L., Dreger, D., Basset, A., and Romanowicz, B., Combining real-time seismic and geodetic data to improve rapid earthquake information , *EOS. Trans. AGU, 83(47),* G52A-0957, 2002.

Perin, B. J., C. M. Meertens, D. S. Neuhauser, D. R. Baxter, M. H. Murray, and R. Butler, Institutional collaborations for joint seismic and GPS measurements, *Seismol. Res. Lett., 69,* 159, 1998.

Romanowicz, B., B. Bogaert, D. Neuhauser, and D. Oppenheimer, Accessing northern California earthquake data via Internet, *EOS Trans. AGU, 75,* 257–260, 1994.

Site	Lon.	Lat	Ve (mm/y)	Vn (mm/y)	σ_e (mm/y)	σ_n (mm/y)	Start
BAY1*	197.29	55.19	-6.3	-25.5	0.0000	0.0000	1996.08
BAY2	197.29	55.19	-5.6	-25.2	0.0400	0.0300	1996.08
BRIB	237.85	37.92	-24.8	5.6	0.0100	0.0100	1993.58
CMBB	239.61	38.03	-22.9	-2.8	0.0100	0.0100	1993.92
CNDR	238.72	37.90	-24.4	-5.5	0.0200	0.0200	1999.27
DIAB	238.08	37.88	-23.7	-2.2	0.0100	0.0100	1998.33
FARB	237.00	37.70	-39.8	23.3	0.0100	0.0100	1994.00
GOLD*	243.11	35.43	-18.2	-5.4	0.0000	0.0000	1989.95
HCRO	238.53	40.82	-18.0	-8.7	0.1400	0.1500	2003.50
HOPB	236.93	39.00	-31.1	6.8	0.0100	0.0100	1995.58
JPLM*	241.83	34.21	-36.6	11.8	0.0000	0.0000	1989.44
LUTZ	238.14	37.29	-31.7	9.5	0.0100	0.0100	1996.33
MHCB	238.36	37.34	-24.2	-2.4	0.0100	0.0100	1996.33
MODB	239.70	41.90	-16.9	-9.1	0.0200	0.0200	1999.83
MOLA	237.58	37.95	-30.5	9.7	0.0100	0.0100	1993.75-2002.22
MONB	238.13	37.49	-27.5	2.7	0.0100	0.0100	1998.50
MUSB	240.69	37.17	-22.3	-4.0	0.0100	0.0100	1997.83
OHLN	237.73	38.01	-26.4	4.4	0.0200	0.0200	2001.83
ORVB	238.50	39.56	-22.7	-6.6	0.0100	0.0100	1996.83
OXMT	237.58	37.50	-36.9	18.0	0.0600	0.0600	2004.12
P181(PBO)	237.62	37.92	-29.0	9.6	0.3800	0.4000	2005.09
P198 (PBO)	237.39	38.26	-29.2	7.9	0.0900	0.1000	2004.77
P200 (PBO)	237.55	38.24	-24.3	4.7	0.2000	0.2200	2005.73
P222 (PBO)	237.92	37.54	-31.5	10.0	0.1100	0.1200	2005.26
P224 (PBO)	237.78	37.86	-26.9	5.5	0.1000	0.1100	2005.25
P225 (PBO)	237.94	37.71	-25.2	2.7	0.0900	0.1000	2005.14
P227 (PBO)	238.21	37.53	-28.6	-0.4	0.5800	0.6300	2006.20
P228 (PBO)	238.31	37.60	-23.5	1.0	0.4300	0.4700	2005.93
P229 (PBO)	238.02	37.75	-26.8	1.6	0.1100	0.1200	2005.29
P230 (PBO)	238.21	37.82	-22.5	-3.1	0.1100	0.1200	2005.15
P261 (PBO)	237.78	38.15	-21.0	-0.5	0.0900	0.1000	2004.50
P262 (PBO)	237.90	38.03	-24.2	1.2	0.1100	0.1200	2005.32
PKDB	239.46	35.95	-43.0	18.7	0.0100	0.0100	1996.67
PPT1*	237.61	37.19	-40.7	22.1	0.0000	0.0000	1996.14
PTRB	236.98	38.00	-37.7	22.2	0.0100	0.0100	1998.58
S300	238.44	37.67	-22.9	-4.4	0.0200	0.0200	1998.48
SAOB	238.55	36.77	-41.4	22.0	0.0100	0.0100	1997.58
SBRN	237.59	37.69	-32.0	14.2	0.0300	0.0300	2003.18
SODA	26.39	67.42	18.7	34.1	0.1400	0.1600	1994.70
SODB	238.07	37.17	-33.1	11.7	0.0100	0.0100	1996.33
SUAA	237.83	37.43	-33.7	12.4	0.0100	0.0100	1994.30
SUTB	238.18	39.21	-23.1	-6.7	0.0100	0.0100	1997.33
SVIN	237.47	38.03	-30.5	10.3	0.0400	0.0400	2003.89
THAL	238.07	37.35	-32.0	9.5	0.2000	0.2200	2003.00
TIBB	237.55	37.89	-30.8	11.2	0.0100	0.0100	1994.42
UCD1	238.25	38.54	-23.1	-6.0	0.0100	0.0100	1996.38
VNDP*	239.38	34.56	-42.2	20.9	0.0000	0.0000	1992.48
YBHB	237.29	41.73	-15.8	-6.7	0.0100	0.0100	1996.75

Table 3.12: CALREF 2006 official velocities. All velocities and estimated errors (σ)are indicated in mm per year. For each site, the relevant time-span and the network are specified. The sites with a star are the sites for which the velocities have been used during the combination of the daily solutions.

6. Northern California Earthquake Data Center

6.1 Introduction

The Northern California Earthquake Data Center, a joint project of the Berkeley Seismological Laboratory (BSL) and the U.S. Geological Survey at Menlo Park, serves as an online archive for various types of digital data relating to earthquakes in Central and Northern California. The NCEDC is located at the Berkeley Seismological Laboratory, and has been accessible to users via the Internet since mid-1992.

The primary goal of the NCEDC is to provide a stable and permanent archival and distribution center of digital geophysical data for networks in Northern and Central California. These data include seismic waveforms, electromagnetic data, GPS data, strain, creep, and earthquake parameters. The seismic data comes principally from the Berkeley Digital Seismic Network (BDSN) operated by the Seismological Laboratory, the Northern California Seismic Network (NCSN) operated by the USGS, the Berkeley High Resolution Seismic Network (HRSN) at Parkfield, the EarthScope USArray Transportable Array stations in Northern California, the various Geysers networks, and selected stations from adjacent networks such as the University of Reno, Nevada network and the Southern California Seismic Network (SCSN). GPS data are primarily from the Bay Area Regional Deformation (BARD) GPS network and the USGS/Menlo Park GPS surveys. The collection of NCSN digital waveforms dates from 1984 to the present, the BDSN digital waveforms date from 1987 to the present, and the BARD GPS data date from 1993 to the present. The BDSN includes stations that form the specialized Northern Hayward Fault Network (NHFN) and the MiniPBO (MPBO) borehole seismic and strain stations in the SF Bay Region. Additional seismic and strain data from the EarthScope Plate Boundary Observatory (PBO) and the San Andreas Fault Observatory at Depth (SAFOD) are also archived at the NCEDC.

The NCEDC also provides support for earthquake processing and archiving activities of the Northern California Earthquake Management Center (NCEMC), a component of the California Integrated Seismic Network (CISN). The CISN is the California regional organization of the Advanced National Seismic System (ANSS).

6.2 2007-2008 Activities

By its nature, data archiving is an ongoing activity. In 2007-2008, the NCEDC continued to expand its data holdings and enhance access to the data. Projects and activities of particular note include:

- In collaboration with the USGS Menlo Park, imported the entire NCSN earthquake catalog with phase and amplitude readings into the CISN database schema, performed quality-control tests on the catalog, and updated Web data distribution tools to use the NCSN catalog from the database.
- Developed procedures for replacing waveforms rapidly collected in real-time for earthquake event analysis with QC-ed waveforms from the BK and BP networks.
- Supported the NCEMC earthquake analysis by providing real-time access to earthquake parameters and waveforms from the NCEDC for the CISN `Jiggle` earthquake review software.
- Made significant progress on reading and archiving continuous NCSN seismograms from tapes for 2001-2005.
- In collaboration with USGS Menlo Park, provided QC procedures to evaluate the intermediate conversion of older 1990's NCSN waveform tapes into a format that could be processed and archived at the NCEDC.

6.3 BDSN/NHFN/MPBO Seismic Data

Archiving current BDSN (Section 1.), NHFN (Section 3.), and Mini-PBO (Section 3.) (all stations using the network code BK) seismic data is an ongoing task. These data are telemetered from 47 seismic data loggers in real-time to the BSL, where they are written to disk files, used for CISN real-time earthquake processing, and delivered in real-time to the DART (Data Available in Real Time) system on the NCEDC, where they are immediately available to anyone on the Internet. In September 2004, the NCEDC began to archive continuous high frequency data (80 Hz and 100 Hz) from all of the BDSN broadband, strong motion, and strainmeter sensors. Previously, 20 Hz and lower rate data channels were archived continuously, and high frequency data was archived only for events. In early 2006, the NCEDC started to receive all of the BK stations in real-time and make them available to users through the DART. All timeseries data from the Berkeley networks continue to be processed and archived by an NCEDC analyst using *calqc* in order to provide the highest quality and most complete data stream to the NCEDC.

NCSN Seismic Data

NCSN continuous waveform data are sent in real-time to the NCEDC via the internet, and are made available to users in real-time through the NCEDC DART. NCSN event waveform data, as well as data from all other real-time BSL and collaborating networks, are automatically collected by the NCEMC waveform archiver and stored at the NCEDC for event review and analysis and for distribution to users. All NCSN and NCEMC data are archived in MiniSEED format.

The NCEDC also maintains a list of historic teleseismic events recorded by the NCSN, since these events do not appear in the NCSN catalog.

A description of the successive improvements in the acquisition of NCSN data, leading to the acquisition of complete NCSN waveform data in early 2006, can be found in the 2005-06 BSL Annual Report. We have made significant progress this year in the NCSN continuous waveform archiving project by reading, converting and archiving NCSN seismograms from all NCSN tapes for 2003 through early 2006. Figure 3.23 shows the total data volume by year.

Parkfield High Resolution Seismic Network Data

The history of upgrades to the acquisition and archival of HRSN data can be found in the 2005-06 BSL Annual Report.

In early 2006, the NCEDC started to receive the HRSN 20 Hz data and a subset of the 250 Hz data in real-time for distribution through the DART. The NCEDC continued to archive continuous 250 Hz and 20 Hz data streams from the HRSN tapes written in Parkfield and processed at the NCEDC. In early 2007, the BSL established a radio telemetry link from the HRSN recording center at the California Department of Forestry (CDF) in Parkfield to Carr Hill, and started to telemeter all HRSN continuously to UCB. These data are fed into the NCSN backup Earthworm system at Carr Hill, and are also routed through the USGS Parkfield T1 circuit to USGS/MP and through the NCEMC T1 circuit to the BSL for real-time processing by the NCEMC earthquake processing system. The data are also made available to users through the NCEDC DART and are continuously archived at the NCEDC.

EarthScope USArray Transportable Array

EarthScope began installing broadband stations for the Transportable Array component of USArray in California in 2005. The NCEDC started acquiring telemetered continuous data from the Northern California and surrounding stations as they were installed, and is archiving these data to support users working with Northern California seismic data. These data are made available to users using the same data request methods as all other continuous data waveform data at the NCEDC. The Transportable Array stations have a limited operational timespan of 18 to 24 months, after which they will be relocated to new sites across the country. Data from these stations were delivered to the NCEDC as they were received by the BSL for distribution through the DART. The USArray station feed to the BSL was discontinued in late November 2007 when the stations were relocated to new sites outside of California.

EarthScope Plate Boundary Observatory (PBO) strain data

The NCEDC is one of two funded archives for PBO EarthScope borehole and laser strain data. Strain data are collected from all of the PBO strain sites and are processed by UNAVCO. MiniSEED data are delivered to the NCEDC using SeedLink, and raw and XML processed data are delivered to the NCEDC using Unidata's Local Data Manager (LDM). The MiniSEED data are inserted into the NCEDC DART and are subsequently archived from the DART. UNAVCO provides EarthScope funding to the NCEDC to help cover the processing, archiving, and distribution costs for these data.

EarthScope SAFOD

The NCEDC is an archive center for the SAFOD event data and will also process the continuous SAFOD data. Starting in July 2002, scientists from Duke University successfully installed a three component 32 level downhole-seismic array in the pilot hole at the EarthScope SAFOD site in collaboration with Steve Hickman (USGS), Mark Zoback (Stanford University), and the Oyo Geospace Engineering Resources International (GERI) Corporation. High frequency event recordings from this array have been provided by Duke University for archiving at the NCEDC. We converted data from the original SEG-2 format data files to MiniSEED, and have developed the SEED instrument responses for this data set. Continuous 4 KHz data from SAFOD are written to tape at SAFOD and are periodically sent to the BSL to be converted, archived, and forwarded to the IRIS DMC. SAFOD EarthScope funding to the NCEDC is to cover the processing, archiving, and distribution costs for these data. A small subset of the continuous SAFOD data channels are also incorporated into the NCSN, are available in real-time from the NCEDC DART, are archived at the NCEDC, and are forwarded to the IRIS DMC. In March 2008, SAFOD installed a Guralp broadband and accelerometer package in the Pilot Hole, which sends continuous data at 200 samples-per-second to the NCEDC.

UNR Broadband data

The University of Reno in Nevada (UNR) operates several broadband stations in western Nevada and eastern California that are important for Northern California earthquake processing and analysis. Starting in August 2000, the NCEDC has been receiving and archiving continuous broadband data from four UNR stations. The

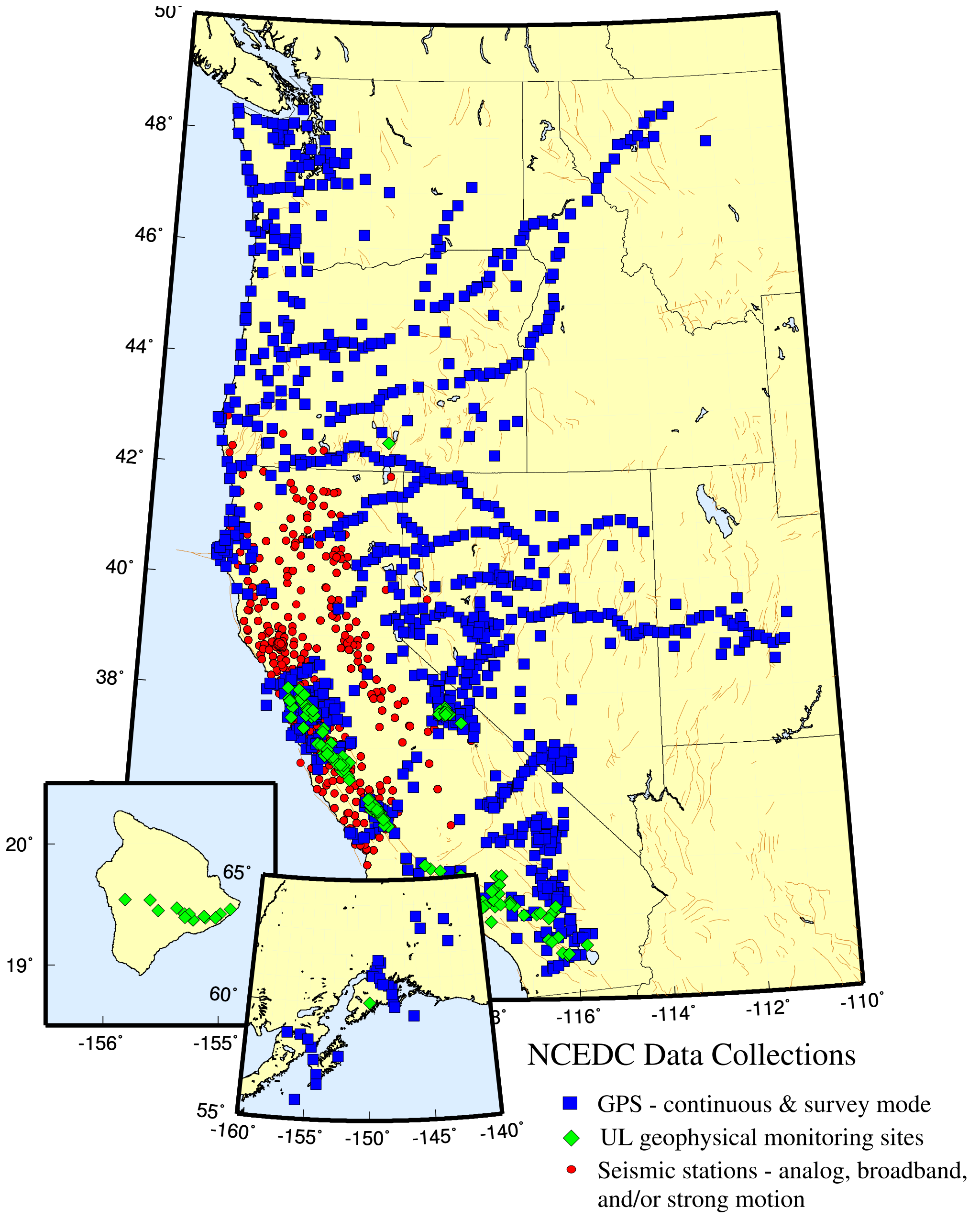

Figure 3.21: Map showing the location of stations whose data are archived at the NCEDC. Circles are seismic sites, squares are GPS sites, and diamonds are the locations of USGS low-frequency experiments.

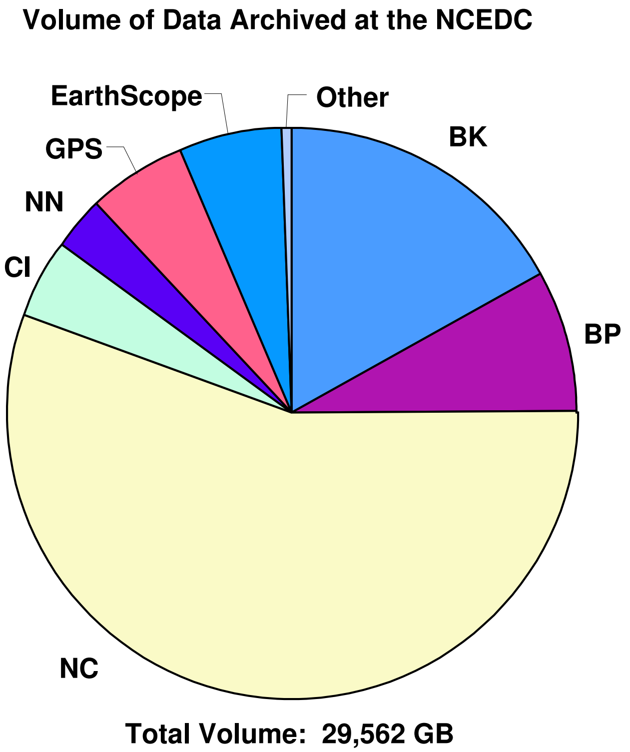

Figure 3.22: Chart showing the relative proportion of each data set at the NCEDC. (BK - Berkeley Digital Seismic Network; BP - Berkeley High-resolution Seismic Network in Parkfield; NC - Northern California Seismic Network and collaborators; CI - Southern California Seismic Network; NN - University of Nevada, Reno Seismic Network; GPS - various GPS datasets, including BARD; EarthScope - data from various EarthScope activities; Other - various small data sets

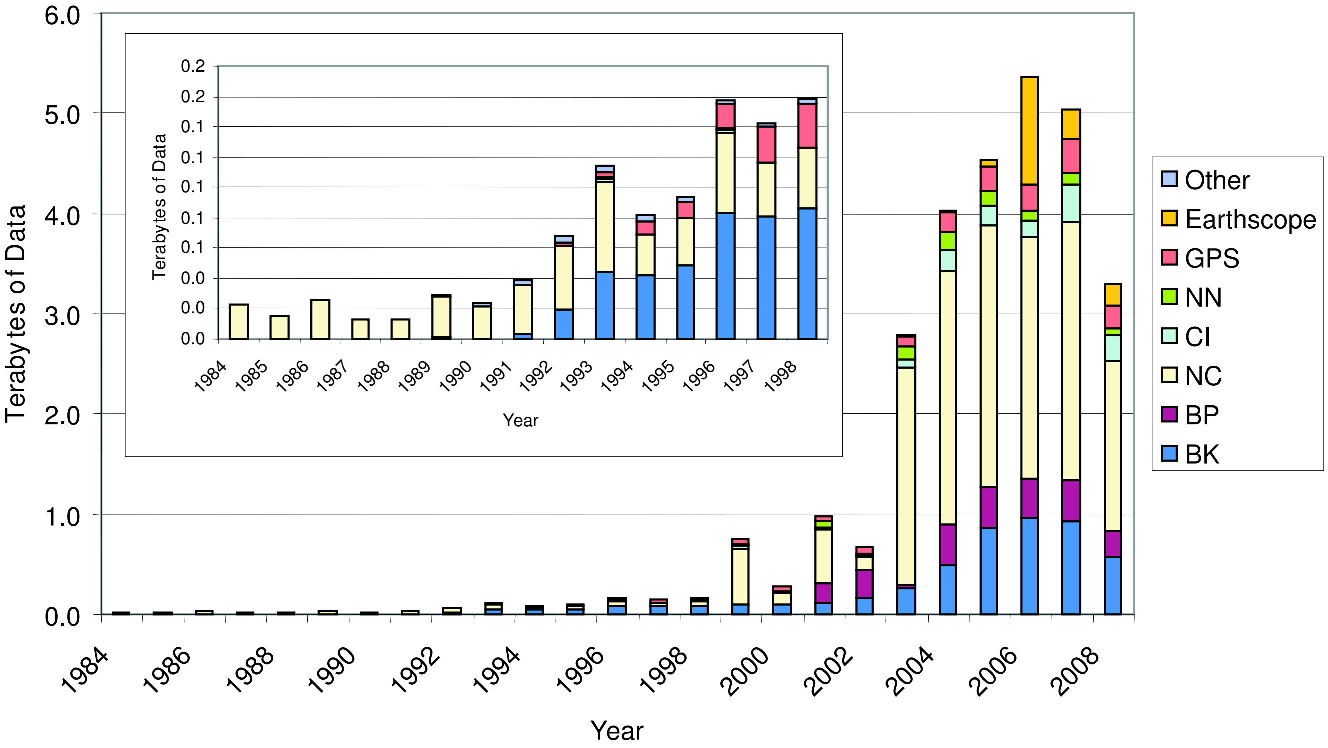

Figure 3.23: Figure showing the total volume of data archived at the NCEDC, broken down by data year.

Data Type	GBytes
BDSN/NHFN/MPBO (broadband, electric and magnetic field, strain) waveforms	5,026
NCSN seismograms	16,365
Parkfield HRSN seismograms	2,387
BARD GPS (RINEX and raw data)	1,704
UNR Nevada seismograms	880
SCSN seismograms	1,348
Calpine/Unocal Geysers region seismograms	38
EarthScope SAFOD seismograms	972
EarthScope USArray seismograms	271
EarthScope PBO strain waveforms	455
USGS low frequency geophysical waveforms	2
Misc data	114
Total size of archived data	29,562

Table 3.13: Volume of Data Archived at the NCEDC by network

data are transmitted in real-time from UNR to UC Berkeley, where they are made available for CISN real-time earthquake processing and for archiving. Initially, some of the stations were sampled at 20 Hz, but all stations are now sampled and archived continuously at 100 Hz.

The NCEDC installed Simple Wave Server (SWS) software at UNR, which provides an interface to UNR's recent collection of waveforms. The SWS is used by the NCEDC to retrieve waveforms from UNR that were missing at the NCEDC due to real-time telemetry outages between UNR and UC Berkeley.

In early 2006, the NCEDC started to archive continuous data from the UNR short-period stations that are contributed to the NCSN. Both the broadband and short-period UNR stations contributed to the CISN are available in real-time through the NCEDC DART.

Electro-Magnetic Data

The NCEDC continues to archive and process electric and magnetic field data acquired at several UC Berkeley sites. The BSL operates both magnetic and electric field sensors at PKD and SAO. Through a collaboration with Dr. Simon Klemperer at Standord University, we acquire magnetic and electric field channels at BSL sites JRSC and BRIB, and magnetic field channels at site MHDL. The three magnetic field channels and either two or four electric field channels are digitized at 40 Hz, 1 Hz, and 0.1 Hz, and are telemetered in real-time along with seismic data to the Berkeley Seismological Laboratory, where they are processed and archived at the NCEDC in a similar fashion to the seismic data.

Using programs developed by Dr. Martin Fullerkrug at the Stanford University STAR Laboratory (now at the University of Bath), the NCEDC has computed and archived magnetic activity and Schumann resonance analysis using the 40 Hz data from this dataset. The magnetic activity and Schumann resonance data can be accessed from the Web. This processing was halted in mid 2005 due to problems with the code and will be resumed when the problems have been identified and corrected.

The NCEDC also archives data from a low-frequency, long-baseline electric field project operated by Dr. Steve Park of UC Riverside at site PKD2. These data are acquired and archived in an identical manner to the other electric field data at the NCEDC.

GPS Data

The NCEDC continues to archive GPS data through the BARD (Bay Area Regional Deformation) network of continuously monitored GPS receivers in Northern California (Section 5.). The NCEDC GPS archive now includes 67 continuous sites in Northern California. There are approximately 50 core BARD sites owned and operated by UC Berkeley, USGS (Menlo Park and Cascade Volcano Observatory), LLNL, UC Davis, UC Santa Cruz, Trimble Navigation, and Stanford. Data are also archived from sites operated by other agencies including East Bay Municipal Utilities District, the City of Modesto, the National Geodetic Survey, and the Jet Propulsion Laboratory.

In addition to the standard 15 second or 30 second continuous GPS datastream, the NCEDC is now privately archiving high-rate 1 Hz continuous GPS data from the 14 stations in Parkfield and from 10 BARD stations. The high-rate Parkfield data are collected by UNAVCO as part of the PBO Nucleus. The Parkfield data are available via anonymous FTP from the NCEDC but are currently not included in the GPS Seamless Archive (GSAC), since the GSAC does not currently handle both high-rate and low-rate data from the same site and day.

The NCEDC continues to archive non-continuous survey GPS data. The initial dataset archived is the survey GPS data collected by the USGS Menlo Park for Northern California and other locations. The NCEDC is the principal archive for this dataset. Significant quality control efforts were implemented by the NCEDC to ensure that the raw data, scanned site log sheets, and RINEX data are archived for each survey. All of the USGS MP GPS data have been transferred to the NCEDC, and virtually all of the data from 1992 to the present has been archived and is available for distribution.

Geysers Seismic Data

The Calpine Corporation operated a micro-seismic monitoring network in the Geysers region of Northern California. Prior to 1999 this network was operated by Unocal. Through various agreements, both Unocal and Calpine have released triggered event waveform data from 1989 through 2000 along with preliminary event catalogs for the same time period for archiving and distribution through the NCEDC. This dataset represents over 296,000 events that were recorded by Calpine/Unocal Geysers network and are available via research accounts at the NCEDC.

The Lawrence Berkeley Laboratory (LBL), with funding from the California Energy Commission, currently operates a 22 station network in the Geysers region with an emphasis on monitoring seismicity related to well water injection. The earthquake locations and waveforms from this network are sent to the NCEDC, and the locations are forwarded to the NCSN so that they can be merged into the NCSN earthquake catalog. In August 2007, the NCSN installed an Earthworm system at the Geysers to receive continuous LBL Geysers data, and this system provides event waveforms in real-time for the NCEMC earthquake procssing and the NCEDC event archives. The event data from LBL Geysers event waveforms collected from April 2004 to August 2007 will be associated with events from the NCSN catalog and will be included with the existing waveforms for these events.

USGS Low Frequency Data

Over the last 30 years, the USGS at Menlo Park, in collaboration with other principal investigators, has collected an extensive low-frequency geophysical data set that contains over 1300 channels of tilt, tensor strain, dilatational strain, creep, magnetic field, and water level as well as auxiliary channels such as temperature, pore pressure, rain and snow accumulation, and wind speed. In collaboration with the USGS, we assembled the requisite information for the hardware representation of the stations and the instrument responses for many channels of this diverse dataset, and developed the required programs to populate and update the hardware database and generate the instrument responses. We developed the programs and procedures to automate the process of importing the raw waveform data and converting it to MiniSEED format. Since these data are delivered to the NCEDC on a daily basis and immediately archived, these data are not inserted into the NCEDC DART.

We have currently archived timeseries data from 887 data channels from 167 sites, and have instrument response information for 542 channels at 139 sites. The waveform archive is updated on a daily basis with data from 350 currently operating data channels. We will augment the raw data archive as additional instrument response information is assembled by the USGS for the channels and will work with the USGS to clearly define the attributes of the "processed" data channels.

SCSN/Statewide seismic data

In 2004, the NCEDC started to archive broadband and strong motion data from 15 SCSN (network CI) stations that are telemetered to the Northern California Management Center (NCEMC) of the California Integrated Seismic Network (CISN). These data are used in the prototype real-time state-wide earthquake processing system and also provide increased coverage for Northern California events. Since the data are telemetered directly from the stations in real-time to both the SCSN and to the NCEMC, the NCEDC archives the NCEMC's copy of the data to ensure that at least one copy of the data will be preserved.

In early 2006, the NCEDC started to continuously archive all of the selected SCSN short-period stations that are contributed to the NCSN. All of these data are available in real-time from the NCEDC DART.

Earthquake Catalogs

Northern California: The NCEDC provides searchable access to both the USGS and BSL earthquake catalogs for Northern and Central California. The "official" UC Berkeley earthquake catalog begins in 1910 and runs through 2003, and the "official" USGS catalog begins in 1966. Both of these catalogs are archived and available through the NCEDC, but the existence of 2 catalogs has caused confusion among both researchers and the public.

In late 2006, the NCEMC begun to archive and distribute a single unified Northern California earthquake catalog in real-time to the NCEDC through database replication from the NCEMC's real-time systems. The NCEDC developed and tested the required programs used to enter all previous NCSN catalog data into the NCEDC database. In 2008, we migrated all of the historic NCSN catalog, phase, and amplitude data from 1967 - 2006 into the NCEMC catalog. In addition, we spent considerable effort addressing the mapping of phase data in the BSL catalog to SEED channel names. We plan to merge the BSL catalog with the NCEMC catalog to form a single unified Northern California catalog from 1910 to the present. The BSL and the USGS have spent considerable effort over the past years to define procedures for merging the data from the two catalogs into a single Northern and Central California earthquake catalog in order to present a unified view of Northern California seismicity. The differences in time period, variations in data availability, and mismatches in regions of coverage all complicate the task.

Worldwide: The NCEDC, in conjunction with the Council of the National Seismic System (CNSS), produced and distributed a world-wide composite catalog of earthquakes based on the catalogs of the national and various U.S. regional networks for several years. Each network updates their earthquake catalog on a daily basis at the NCEDC, and the NCEDC constructs a composite world-wide earthquake catalog by combining the data, removing duplicate entries that may occur from multiple networks recording an event, and giving priority to the data from each network's *authoritative region.* The catalog, which includes data from 14 regional and national networks, is searchable using a Web interface at the NCEDC. The catalog is also freely available to anyone via ftp over the Internet.

With the demise of the CNSS and the development of the Advanced National Seismic System (ANSS), the NCEDC was asked to update its Web pages to present the composite catalog as a product of the ANSS. This conversion was completed in the fall of 2002. We continue to create, house, distribute, and provide a searchable web interface to the ANSS composite catalog, and to aid the regional networks in submitting data to the catalog.

6.4 NCEDC Operations

In 2005, the NCEDC relocated its archive and distribution system from McCone Hall to a new state-of-the-art computer facility in a new seismically braced building on the Berkeley campus. The facility provides seismically braced equipment racks, gigabit ethernet network, air conditioning, and power conditioning. The entire facility is powered by a UPS with generator backup.

The currently installed NCEDC facilities consist of a mass storage environment hosted by a Sun V240 host computer, a 100 slot LTO-2 tape library with two tape drives and a 20 TByte capacity, and 50 TBytes of RAID storage, all managed with the SAM-FS hierarchical storage management (HSM) software. A Sun system provides Web services and research account access to the NCEDC, a dual Sun 280R processor provides data import and export services, and a Sun V20Z computer is used for quality control procedures. Two AIT tape libraries are used to read NCSN continuous data tapes. A 64-bit Linux system hosts a database dedicated to providing data to external users. Two Sun Opteron processors provide additional data processing support for the NCEDC.

The hardware and software system is configured to automatically create multiple copies of each timeseries file. The NCEDC creates one copy of each file on an online RAID, a second copy on LTO2 tape which is stored online in the tape library, and a third copy on LTO2 tape which is stored offline and offsite. All NCEDC data are online and rapidly accessible by users.

The NCEDC operates two instances of its Oracle database, one for internal operations and one for external use for user data queries and data distribution programs. The databases are synchronized using multi-master replication.

Data Quality Control

The NCEDC developed a GUI-based state-driven system *calqc* to facilitate the quality control processing that is applied to the continuously archived data sets at the NCEDC.

The quality control procedures for these datasets include the following tasks:

- data extraction of a full day of data,
- quickcheck program to summarize the quality and stability of the stations' clocks,
- determination if there is missing data for any data channel,
- provided procedures to retrieve missing data from the stations and incorporate it into the day's data,
- optional creation of multi-day timeseries plots for state-of-health data channels,
- optional timing corrections for data,
- optional extraction of event-based waveforms from continuous data channels,
- optional repacking of MiniSEED data,
- creating waveform inventory entries in the NCEDC database,
- publishing the data for remote access on the NCEDC.

Calqc uses previously developed programs to perform each function, but it provides a graphical point-and-click interface to automate these procedures, and to provide the analyst with a record of when each process was started, whether it executed correctly, and whether the analyst has indicated that a step has been completed. *Calqc* is used to process all data from the BDSN network, and all continuous broadband data from the NCSN, UNR, SCSN, and HRSN networks that are archived by the NCEDC. The remainder of the continuously archived data are automatically archived without any analyst interaction.

The NCEDC is developing programs and procedures to replace waveforms collected for event analysis in near real-time with QC-ed waveforms from the UCB QC-ed waveform archive. This procedure will also be used to augment the NCSN event-based waveform collection from 1991 - 2006 with the appropriate waveforms from the UCB seismic networks.

6.5 Database Development

The NCEDC parametric database schema for storing earthquake event information was adopted by the CISN for use within the Northern and Southern California earthquake processing centers as well as the NCEDC and SCEDC. Through the efforts of the CISN Standards Group, this schema continues to be enhanced to address new requirements of the CISN.

The most significant database development this year has been the migration of the entire NCSN earthquake catalog, phase data, and amplitude readings into the NCEDC database. In collaboration with the NCSN, we developed the programs and procedures necessary to migrate the 1967-2006 NCSN catalog into the CISN parametric schema and have been performing quality control procedures on the data prior to entering the catalog into the database. In support of this project, the NCEDC developed the *dbselect* program which can search the database, retrieve earthquake information, and optionally recreate full Hypoinverse files. The *dbselect* program is now used in the NCEDC web-based catalog search interface.

The NCEDC continues to support the Northern California Earthquake Management Center (NCEMC) by providing information and resources vital to the NCEMC's role of rapid earthquake analysis and data dissemination. The NCEDC receives earthquake parametric data in real-time from the NCEMC real-time systems and provides real-time access to the NCEDC database for *jiggle*, the CISN event analysis tool. The NCEMC continues to support the maintenance and distribution of the hardware configurations and instrument responses of the UCB, USGS/MP NCSN, and other seismic stations used by the NCEMC. During 2002-2004, the NCEDC and NCSN jointly developed a system consisting of an extensive spreadsheet containing per-channel information that describes the hardware of each NCSN data channel and provides each channel with a SEED-compliant channel name. This spreadsheet, combined with a limited number of files that describe the central-site analog digitizer, FIR decimation filters, and general characteristics of digital acquisition systems, allows the NCSN to assemble its station history in a format that the NCEDC can use to populate the hardware tracking and instrument response database tables for the NCSN.

The NCEDC instrument response schema represents full multi-stage instrument responses (including filter coefficients) for the broadband data loggers. The hardware tracking schema represents the interconnection of instruments, amplifiers, filters, and data loggers over time, and is used to describe all of the UC Berkeley and USGS stations and channels archived at the NCEDC.

The NCEDC has developed XML import and export procedures to provide better maintenance of the hardware tracking information and resulting instrument responses for stations in our database. When changes are made to either existing hardware or to station configurations, we export the current view in XML format, use a GUI-based XML editor to easily update the information, and import the changes back into the database. When adding new stations or hardware, we can easily use information from existing hardware or stations as templates for the new information. This allows us to treat the database as the authoritative source of information, and to use off-the-shelf tools such as the XML editor and XML differencing programs as part of our database maintenance procedures.

All NCSN event waveforms originally collected with the USGS CUSP processing system have been converted to MiniSEED, and are available along with the UC Berkeley data and data from the other networks archived at the NCEDC in full SEED format.

Additional details on the joint catalog effort and database schema development may be found at `http://www.ncedc.org/db`

6.6 Data Distribution

The NCEDC continues to use the World Wide Web as a principal interface for users to request, search for, and receive data from the NCEDC. In fall 2005, the NCEDC acquired the domain name *ncedc.org*. The NCEDC's Web address is now `http://www.ncedc.org/`

Earthquake Catalogs

The NCEDC provides users with searchable access to Northern California earthquake catalogs and to the ANSS world-wide catalog via the web. Users can search the catalogs by time, magnitude, and geographic region, and can retrieve either hypocenter and magnitude information or a full set of earthquake parameters including phase readings, amplitudes, and codas. Moment tensor results are now being added to the NCEMC California earthquake catalog.

Station Metadata

In addition to the metadata returned through the various data request methods, the NCECD provides dataless SEED volumes and SEED RESP files for all data channels archived at the NCEDC. The NCEDC currently has full SEED instrument responses for 12,989 data channels from 1,909 stations in 20 networks. This includes stations from the California Geological Survey (CGS) strong motion network that will contribute seismic waveform data for significant earthquakes to the NCEDC and SCEDC.

SeismiQuery

We have ported and installed the IRIS *SeismiQuery* program at the NCEDC, which provides a common interface to query network, station, and channel attributes and query the availability of archived timeseries data. We have provided both IRIS and the SCEC Data Center with our modified version of *SeismiQuery*.

DART (Data Available in Real Time)

The DART (Data Available in Real Time) represents the first step in NCEDC's effort to make current and recent timeseries data from all networks, stations, and channels available to users in real-time. The NCEDC developed DART in December 2005 to provide a mechanism for users to obtain access to real-time data from the NCEDC. All real-time timeseries data streams delivered to the NCEDC are placed in MiniSEED files in a Web-accessible directory structure. The DART waveforms can be accessed by Web browsers or http command-line programs such as *wget*, a *FISSURES* waveform server, and a Berkelely-developed Simple Wave Server (SWS) which provides programmatic access to the DART data by specified SEED channel and time interval. We will be providing users with a client program to retrieve data from the SWS in the near future. The DART currently provide assess to the most recent 30 days of data.

We are using the Freeorb software, an enhanced version of the open-source orb software developed by the IRIS-funded Joint Seismic Project (JSP), as the primary method for delivering real-time data to the NCEDC and into the DART. The freeorb package implements an object ring buffer (ORB) and orbserver, which provides a reliable storage ring buffer and an interface for orb client programs to read, write, and query the orbserver. Orbserver clients running at the NCEDC computer connect to remote orbservers at the BSL and USGS/Menlo Park, retrieve the MiniSEED timeseries data records, and write them to daily channel files in the NCEDC DART. Strain data from the EarthScope PBO network are delivered to the NCEDC using SeedLink and are inserted into the DART using a similar SeedLink client program.

The NCEDC developed an automated data archiving system to archive data from the DART on a daily basis. It allows us to specify which stations should be automatically archived, and which stations should be handled by the NCEDC's Quality Control program *calqc*, which allows an analyst to review the waveforms, retrieve missing data from stations or waveservers that may have late-arriving, out-of-order data, and perform timing corrections on the waveform data. The majority of data channels are currently archived automatically from the DART.

NetDC

In a collaborative project with the IRIS DMC and other worldwide datacenters, the NCEDC helped develop and implement *NetDC*, a protocol which will provide a seamless user interface to multiple datacenters for geophysical network and station inventory, instrument responses, and data retrieval requests. The *NetDC* builds upon the foundation and concepts of the IRIS *BREQ_FAST* data request system. The *NetDC* system was put into production in January 2000 and is currently operational at several datacenters worldwide, including NCEDC, IRIS DMC, ORFEUS, Geoscope, and SCEDC. The *NetDC* system receives user requests via email, automatically routes the appropriate portion of the requests to the appropriate datacenter, optionally aggregates the responses from the various datacenters, and delivers the data (or ftp pointers to the data) to the users via email.

STP

In 2002, the NCEDC wrote a collaborative proposal with the SCEDC to the Southern California Earthquake Center, with the goal of unifying data access between the two data centers. As part of this project, the NCEDC and SCEDC are working to support a common set of 3 tools for accessing waveform and parametric data: *SeismiQuery*, *NetDC*, and *STP*.

The *Seismogram Transfer Program* or *STP* is a simple client-server program, developed at the SCEDC. Access to *STP* is either through a simple direct interface that is available for Sun or Linux platforms, or through a GUI Web interface. With the direct interface, the data are placed directly on a user's computer in several possible formats, with the byte-swap conversion performed automatically. With the Web interface, the selected and converted data are retrieved with a single ftp command. The *STP* interface also allows rapid access to parametric data such as hypocenters and phases.

The NCEDC has continued work on *STP*, working with the SCEDC on extensions and needed additions. We added support for the full SEED channel name (Station, Network, Channel, and Location), and are now able to return event-associated waveforms from the NCSN waveform archive.

EVT_FAST

In order to provide Web access to the NCSN waveform before the SEED conversion and instrument response for the NCSN has been completed, the NCEDC implemented *EVT_FAST*, an interim email-based waveform request system similar to the *BREQ_FAST* email request system. Users email *EVT_FAST* requests to the NCEDC and request NCSN waveform data based on the NCSN event ID. Initially, the NCSN waveform data was converted to either SAC ASCII, SAC binary, or AH format, and placed in the anonymous ftp directory for retrieval by the users. *EVT_FAST* event waveforms can now also be provided in MiniSEED format and are now named with their SEED channel names.

FISSURES

The *FISSURES* project developed from an initiative by IRIS to improve earth scientists' efficiency by developing a unified environment that can provide interactive or programmatic access to waveform data and the corresponding metadata for instrument response, as well as station and channel inventory information. *FISSURES* was developed using CORBA (Common Object Request Broker Architecture) as the architecture to implement a system-independent method for the exchange of this binary data. The IRIS DMC developed a series of services, referred to as the *Data Handling Interface (DHI)*, using the *FISSURES* architecture to provide waveform and metadata from the IRIS DMC.

The NCEDC has implemented the *FISSURES Data Handling Interface (DHI)* services at the NCEDC, which involves interfacing the DHI servers with the NCEDC database schema. These services interact with the NCEDC database and data storage system and can deliver NCEDC channel metadata as well as waveforms using the *FISSURES* interfaces. We have separate *FISSURES DHI* waveform servers to serve archived and DART data streams. Our *FISSURES* servers are registed with the IRIS *FISSURES naming services*, which ensures that all *FISSURES* users have transparent access to data from the NCEDC.

GSAC

Since 1997, the NCEDC has collaborated with UNAVCO and other members of the GPS community on the development of the *GPS Seamless Archive Centers (GSAC)* project. This project allows a user to access the most current version of GPS data and metadata from distributed archive locations. The NCEDC is participating at several levels in the *GSAC* project: as a primary provider of data collected from core BARD stations and USGS MP surveys, and as a wholesale collection point for other data collected in Northern California. We helped to define database schema and file formats for the *GSAC* project and have produced complete and incremental monumentation and data holdings files describing the data sets that are produced by the BARD project or archived at the NCEDC so that other members of the *GSAC* community can provide up-to-date information about our holdings. Currently, the NCEDC is the primary provider for over 138,000 data files from over 1400 continuous and survey-mode monuments. The data holdings records for these data have been incorporated into the *GSAC* retailer system, which became publicly available in late 2002.

In addition, the NCEDC is archiving and distributing high-rate 1 Hz GPS data from 10 BARD stations in addition to the normally sampled 15 second or 30 second data. These high-rate data are now publicly available to the entire community.

6.7 Acknowledgements

The NCEDC is a joint project of the BSL and the USGS Menlo Park and is funded primarily by the BSL and the USGS Cooperative Agreement 07HQAG0013. Additional funding for the processing and archiving of the EarthScope PBO and SAFOD data were proviced by EarthScope subawards EAR0350025-06 through UNAVCO and 18036080-28436-F through Stanford University.

Doug Neuhauser is the manager of the NCEDC. Stephane Zuzlewski, Rick McKenzie, Mario Aranha, Nicolas Houlie, Bob Uhrhammer, Jennifer Taggart,and Peggy Hellweg of the BSL and David Oppenheimer, Hal Macbeth, Lynn Dietz, and Fred Klein of the USGS Menlo Park contribute to the operation of the NCEDC. Doug Neuhauser and Peggy Hellweg contributed to the preparation of this section.

7. Data Acquisition and Quality Control

7.1 Introduction

Stations from the networks operated by the BSL transmit data continuously to the BSL facilities on the UC Berkeley campus for analysis and archival. In this section, we describe activities and facilities which pertain to the individual networks described in Sections 1., 3., and 4., including procedures for data acquisition and quality control, and sensor testing capabilities and procedures. Some of these activities are continuous from year to year and have been described in prior BSL annual reports. In this section, we describe changes or activities which are specific to 2007-2008.

7.2 Data Acquisition Facilities

Before 2005-2006, both the BSL staff monitoring routine data acquisition and the computers and facilities to acquire, process, and archive the data were located in McCone Hall. Since 2006, the computers and telemetry equipment associated with data acquisition reside in the new campus computer facility at 2195 Hearst Avenue. This building was constructed to current "emergency grade" seismic codes, and is expected to be operational even after a M 7 earthquake on the nearby Hayward Fault. The hardened campus computer facility within was designed with special attention for post-earthquake operations. The computer center contains state-of-the art seismic bracing, UPS power and air conditioning with generator backup, and extensive security and equipment monitoring.

With the move of many BSL and NCEDC operations servers to the campus computer center, the generator power and air conditioning resources in the BSL server room in 237 McCone better match our needs for the infrastructure remaining in McCone Hall. The BSL generator is maintained by Physical Plant Capital Services and is run without load twice monthly. During the past year, we noted problems with the UPS and replaced defunct batteries. In addition, during a spell of hot weather the cooling system failed, requiring repairs.

7.3 Data Acquisition

Central-site data acquisition for data from the BDSN/NHFN/MPBO networks is performed by two computer systems in the 2195 Hearst Avenue data center (Figure 3.24). These acquisition systems also collect data from the Parkfield-Hollister electromagnetic array and the BARD network. A third system is used primarily for data exchange with the USNSN and transmits data to the USNSN from HOPS, CMB, SAO, WDC, HUMO, MOD, MCCM, and YBH. Data acquisition for the HRSN was upgraded during the past year, to use the USGS T1 from Parkfield to Menlo Park. This is described in Section 4.. We also collected data from local USArray travelling array stations from the orb-server of the Anza Network Facility at the University of California San Diego until the array moved out of California in the late fall of 2007.

The BSL uses the program `comserv` developed by Quanterra for central data acquisition. This program receives data from a remote Quanterra data logger and redistributes the data to one or more comserv client programs. The comserv clients used by REDI include `datalog`, which writes the data to disk files for archival purposes, `cdafill`, which writes the data to the shared memory region for REDI analysis, and other programs such as the seismic alarm process, the DAC480 system, and the feed for the Memento Mori Web page (Figure 3.25).

The two computers performing data acquisition also serve as REDI processing systems and hold the databases now used by these systems for storing earthquake information. In order to facilitate REDI processing, each system maintains a shared memory region that contains the most recent 30 minutes of data for each channel used by the REDI analysis system. All REDI analysis routines first attempt to use data in the shared memory region and will only revert to retrieving data from disk files if the requested data is unavailable in the shared memory region.

Each BDSN data logger that uses frame relay telemetry is configured to enable data transmission simultaneously to two different computers over two different frame relay T1 circuits to UCB. However, the BSL normally actively enables and uses only one of these data streams from each station at any given time. The `comserv` client program `cs2m` receives data from a comserv and multicasts the data over a private ethernet. The program `mcast`, a modified version of Quanterra's `comserv` program, receives the multicast data from `cs2m`, and provides a comserv-like interface to local comserv clients. This allows each REDI system to have a comserv server for every station, and each of the two systems has a complete copy of all waveform data.

We have extended the multicasting approach to handle data received from other networks such as the NCSN and UNR. These data are received by Earthworm data exchange programs and are then converted to MiniSEED and multicast in the same manner as the BSL data. We use `mserv` on both REDI computers to receive the multicast data and handle it in an identical fashion to the BSL MiniSEED data.

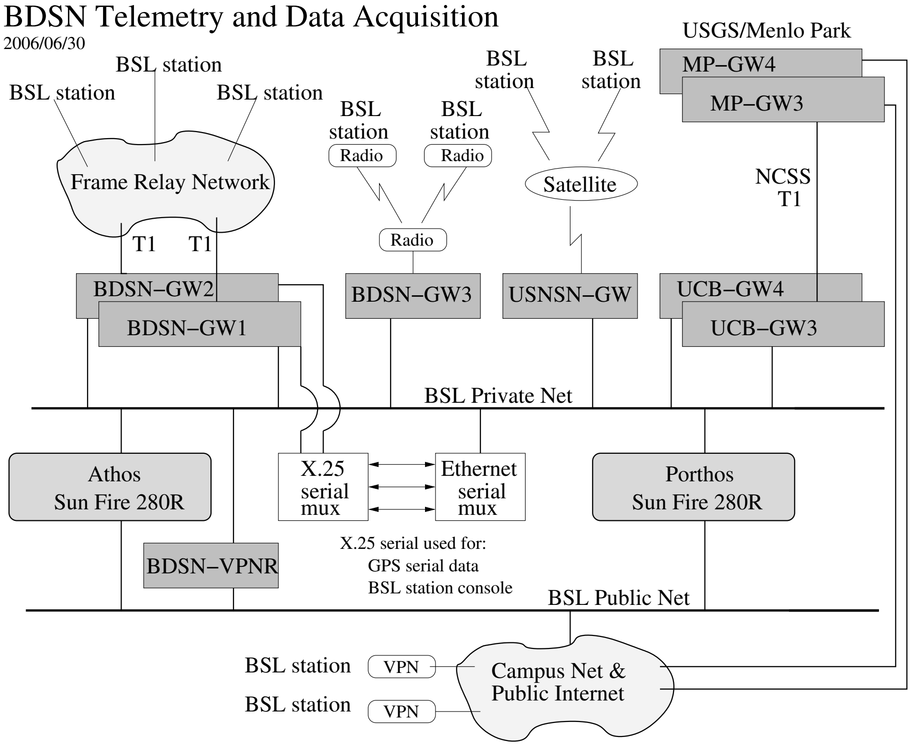

Figure 3.24: Data flow from the BDSN, NHFN, MPBO, HRSN, and BARD network into the BSL central processing facility.

In 2006, the BSL established a real-time data feed of all BSL waveforms between the BSL acquisition systems and the NCEDC computers using the open source Freeorb software. This allows the NCEDC to provide near-real-time access to all BSL waveform data through the NCEDC DART (Data Availabile in Real Time) system.

For several years now, we have been monitoring the seismic stations and telemetry using the program `seisnetwatch`. This program extracts current informaiton such as time quality, mass positions, and battery voltage and allows it to be displayed. If the parameter departs from the nominal range, the station is marked with yellow or red to indicate a possible problem.

7.4 Seismic Noise Analysis

BSL seismic data are routinely monitored for state-of-health. An automated analysis is computed regularly to characterize the seismic noise level recorded by each broadband seismometer.

PSD Noise Analysis

The estimation of the Power Spectral Density (PSD) of the ground motion recorded at a seismic station, as documented in the 2000-2001 BSL annual report (`http://seismo.berkeley.edu/annual_report/ar00_01/`), provides an objective measure of background seismic noise characteristics over a wide range of frequencies. When used routinely, the PSD algorithm also provides an objective measure of seasonal and secular variation in the noise characteristics and aids in the early diagnoses of instrumental problems. A PSD estimation algorithm was developed in the early 1990's at the BSL for characterizing the background seismic noise and as a tool for quality control. As presently implemented, the algorithm sends the results via email to the engineering and some research staff members and generates a bar graph output which compares all the BDSN broadband stations by components. We also use the weekly PSD results to monitor trends in the noise level at each station. Figures showing the analysis for the current year are produced. These cumulative PSD plots are generated for each station and show the noise level in 5 frequency bands for the broadband channels. These plots make it easier to spot certain problems, such as failure of a sensor. In addition to the station-based plots, a summary plot for each channel is produced, comparing all stations. These figures are presented as part of a noise analysis of the BDSN on the WWW at `http://www.seismo.berkeley.edu/seismo/bdsn/psd/`.

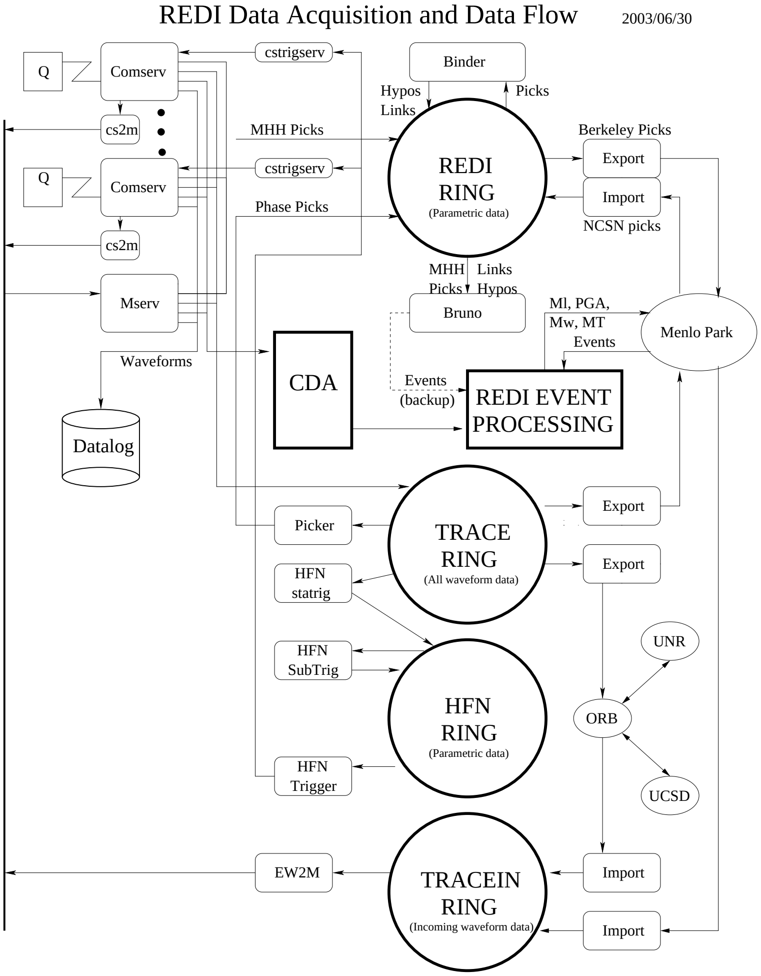

Figure 3.25: Dataflow in the REDI processing environment, showing waveform data coming in from the Quanterra data loggers (Q) into `comserv`. From comserv, data are logged to disk (via `datalog`), distributed to other computers (`mserv`), fed into the CDA for REDI processing, and spooled into a trace ring for export.

PDF PSD Noise Analysis

In addition to the PSD analysis developed by Bob Uhrhammer, the BSL has implemented the Ambient Noise Probability Density Function (PDF) analysis system developed by *McNamara and Buland* (2004). This system performs its noise analysis over all the data of a given time period (week or year), including earthquakes, calibration pulses, and cultural noise. This is in contrast to Bob Uhrhammer's PSD analysis, which looks at only the quietest portion of data within a day or week. Pete Lombard of the BSL extended the McNamara code to cover a larger frequency range and support the many different types of sensors employed by the BSL. Besides the originally supported broadband sensors, our PDF analysis now includes surface and bore-hole accelerometers, strain meters, and electric and magnetic field sensors. These enhancements to the PDF code, plus a number of bug fixes, were provided back to the McNamara team for incorporation in their work. The results of the PDF analysis are presented on the web at `http://www.ncedc.org/ncedc/PDF/`. One difficulty with using these plots for review of station quality is that it is necessary to look at data from each component separately. To provide an overview, we have developed summary figures for all components in two spectral bands, 30 - 60 s and 0.125 - 0.25 s.

7.5 Sensor Testing Facility

The BSL has an Instrumentation Test Facility in the Byerly Seismographic Vault in order to systematically determine and compare the characteristics of up to eight sensors at a time. The test equipment consists of an eight-channel Quanterra Q4120 high-resolution data logger and a custom interconnect panel that provides isolated power and preamplification, when required, to facilitate the connection and routing of signals from the sensors to the data logger with shielded signal lines. A GPS rebroadcaster has also been installed, so that all data loggers in the Byerly vault operate on the same time base. Upon acquisition of data at up to 200 samples-per-second (sps) from the instruments under test, PSD analysis, coherence analysis, and additional ad hoc analysis algorithms are used to characterize and compare the performance of each sensor. Tilt tests and seismic signals with a sufficient signal level above the background seismic noise are also used to verify the absolute calibration of the sensors. A simple vertical shake table is used to assess the linearity of a seismic sensor. The sensor testing facility of the BSL is described in detail in the BSL 2001-2002 Annual Report (available on-line at `http://www.seismo.berkeley.edu/`).

Several projects made use of the sensor testing facility in 2007-2008. Initial tests of the new STS-1 electronics (E300) took place in Byerly Vault (see Section 9.). In addition, the new pressure/temperature sensors were installed and data collected for calibration and assessment (see Section 9.). Finally, the facility will house initial tests of new STS-1-type sensors being developed jointly by Metrozet and the BSL.

7.6 Acknowledgements

Doug Neuhauser, Bob Uhrhammer, Peggy Hellweg, Pete Lombard, Rick McKenzie and Jennifer Taggart are involved in the data acquisition and quality control of BDSN/NHFN/MBPO data. Development of the sensor test facility and analysis system was a collaborative effort of Bob Uhrhammer, Tom McEvilly, John Friday, and Bill Karavas. IRIS and DTRA provided, in part, funding for and/or incentive to set up and operate the facility, and we thank them for their support. Bob Uhrhammer, Peggy Hellweg, Pete Lombard, Doug Neuhauser, and Barbara Romanowicz contributed to the preparation of this section. The STS-1 project is funded by the NSF through the IRIS/GSN program (IRIS Subaward Agreement number 388). This is a collaborative project with Tom VanZandt of Metrozet, LLC (Redondo Beach, CA).

7.7 References

Ekström, G. and M. Nettles, `http://www.seismology.harvard.edu/~ekstrom/Projects/WQC.html`, 2005.

Gardner, W. A., A unifying view of coherence in signal processing, Signal Processing, 29, p. 113-140, 1992.

Ingate, S. et al, Workshop Report from Broadband Seismometer Workshop, Lake Tahoe, CA, `http://www.iris.edu/stations/seisWorkshop04/report.htm`, 2004.

McNamara, D. and R. Buland, Ambient Noise Levels in the Continental United States *Bull. Seism. Soc. Am.*, 94, 4, 2004.

Scherbaum, Frank. Of Poles and Zeros: Fundamentals in Digital Seismology, Volume 15 of Modern Approaches in Geophysics, G. Nolet, Managing Editor, Kluwer Academic Press, Dordrecht, xi + 257 pp., 1996.

Tapley, W. C. and J. E. Tull, SAC - Seismic Analysis Code: Users Manual, *Lawrence Livermore National Laboratory*, Revision 4, 388 pp., March 20, 1992.

Wielandt, E. and G. Streckeisen, The leaf spring seismometer: design and performance, *Bull. Seis. Soc. Am., 72*, 2349-2367, 1982.

Wielandt, E. and Steim, J. M., A digital very broad band seismograph, *Annales Geophysicae*, 4 B(3), 227-232, 1986.

8. Northern California Earthquake Monitoring

8.1 Introduction

Routine analysis of the data produced by BSL networks begins as the waveforms are acquired by computers at UC Berkeley, and ranges from automatic processing for earthquake response to analyst review for earthquake catalogs and quality control.

Starting in the mid 1990s, the BSL invested in the development of the hardware and software necessary for an automated earthquake notification system (*Gee et al.*, 1996; 2003a) called the Rapid Earthquake Data Integration (REDI) project. This system provides rapid determination of earthquake parameters: near real-time locations and magnitudes of Northern and Central California earthquakes, estimates of the rupture characteristics and the distribution of ground shaking following significant earthquakes, and tools for the rapid assessment of damage and estimation of loss. In 1996, the BSL and the USGS began collaborating on a joint notification system for Northern and Central California earthquakes. This system merges the programs in Menlo Park and Berkeley into a single earthquake notification system, combining data from the NCSN and the BDSN. Today, the joint BSL and USGS system forms the Northern California Earthquake Management Center (NCEMC) of the California Integrated Seismic Network (Section 2.), and development is proceeding on the next generation of earthquake reporting software based on Southern California's Trinet system.

With partial support from the USGS, the BSL has also embarked on the development and assessment of a system to warn of imminent ground shaking in the seconds after an earthquake has initiated but before strong motion begins at sites that may be damaged (Research Study 26.).

8.2 Northern California Earthquake Management Center

Details of the Northern California processing system and the REDI project have been described in previous annual reports. In this section, we describe how the Northern California Earthquake Management Center fits within the CISN system.

Figure 3.8 in Section 2. illustrates the NCEMC as part of the the CISN communications ring. The NCEMC is a distributed center, with elements in Berkeley and in Menlo Park. The 35 mile separation between these two centers is in sharp contrast to the Southern California Earthquake Management Center, where the USGS Pasadena is located across the street from the Caltech Seismological Laboratory. As described in Section 2., the CISN partners are connected by a dedicated T1 communications link, with the capability of falling back to the Internet. In addition to the CISN ring, the BSL and the USGS Menlo Park have a second dedicated communications link to provide bandwidth for shipping waveform data and other information between their processing systems.

Figure 3.26 provides more detail on the current system at the NCEMC. At present, two Earthworm-Earlybird systems in Menlo Park feed two "standard" REDI processing systems at UC Berkeley. One of these systems is the production or paging system; the other is set up as a hot backup. The second system is frequently used to test new software developments before migrating them to the production environment. The Earthworm-Earlybird-REDI systems perform standard detection and location and estimate M_d, M_L, and M_w as well as processing ground motion data. The computation of ShakeMaps is also performed on two systems, one in Menlo Park and one in Berkeley. An additional system at the BSL performs finite-fault processing and computes higher level ShakeMaps.

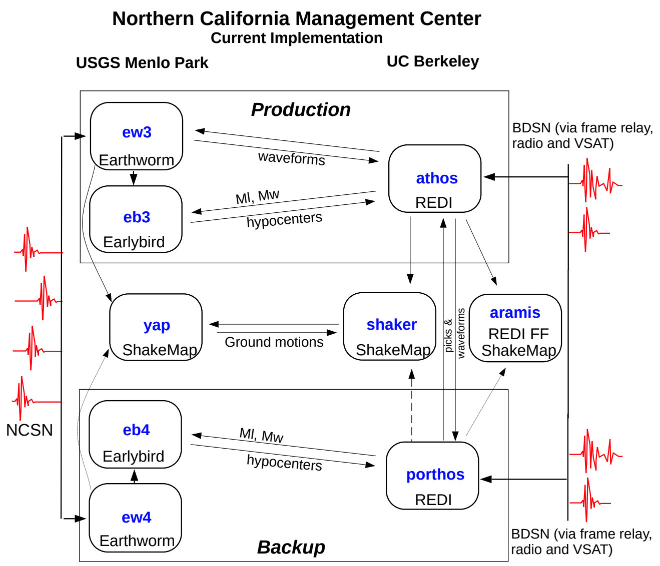

Figure 3.26: Detailed view of the current Northern California processing system, showing the two Earthworm-Earlybird-REDI systems, the two ShakeMap systems, and the finite-fault system.

The dense network and Earthworm-Earlybird processing environment of the NCSN provides rapid and accurate earthquake locations, low magnitude detection thresholds, and first-motion mechanisms for small quakes. The high dynamic range data loggers, digital telemetry, and broadband and strong-motion sensors of the BDSN along with the REDI analysis software provide reliable magnitude determination, moment tensor estimation, peak ground motions, and source rupture characteristics. Robust preliminary hypocenters are available about 25 seconds after the origin time, while preliminary coda magnitudes follow within 2-4 minutes. Estimates of local magnitude are generally available 30-120 seconds later, and other parameters, such as the peak ground acceleration and moment magnitude, follow within 1-4 minutes (Figure 3.27).

Earthquake information from the joint notification system is distributed by pager/cellphone, e-mail, and the WWW. The first two mechanisms "push" the information to recipients, while the current Web interface requires interested parties to actively seek the information. Consequently, paging and, to a lesser extent, e-mail are the preferred methods for emergency response notification. The *recenteqs* site has enjoyed enormous popularity since its introduction and provides a valuable resource for information whose bandwidth exceeds the limits of wireless systems and for access to information which is useful not only in the seconds immediately after an earthquake, but in the following hours and days as well.

8.3 2007-2008 Activities

System Development

As part of ongoing efforts to improve the monitoring systems in Northern California and to unify the processing systems within the CISN, the BSL and the USGS Menlo Park made progress in the development of the next generation of the Northern California joint notification system for the Northern California Seismic System (NCSS). Figure 3.26 illustrates the current organization of the system. Although this approach functions reasonably well, there are potential problems associated with the separation of critical system elements by ∼35 miles of San Francisco Bay.

Since FY01-02, we have been working to design and implement software for Northern California operations so that identical, complete systems operate independently at the USGS and UC Berkeley. When CISN started, independently developed systems for monitoring earthquakes operated in Southern and Northern California, Trinet and Earthworm/REDI, respectively. Each of these systems has its strengths and weaknesses, and choices had to be made. The current design for the new Northern California system draws strongly on the development of TriNet in Southern California (Figure 3.28), with modifications to allow for local differences (such as very different forms of data acquisition and variability in network distribution). In addition, the BSL and the USGS want to minimize use of proprietary software in the system. One exception is the database program. As part of the development of the Northern California Earthquake Data Center, the USGS and BSL have worked extensively with Oracle databases, and extending this to the real-time system is not viewed as a major issue.

During the last few years, BSL staff members, particularly Pete Lombard, have become extremely familiar with portions of the TriNet software. We have continued to adapt the software for Northern California, making adjustments and modifications along the way. For example, Pete Lombard has adapted the TriNet magnitude module to Northern California, where it is now running on a test system. Pete made a number of suggestions on how to improve the performance of the magnitude module and has worked closely with Caltech and the USGS/Pasadena on modifications. One of the biggest programming efforts in the past year has been to make the package leap second compliant.

The BSL and the USGS Menlo Park have implemented a system to exchange "reduced amplitude timeseries." One of the important innovations of the TriNet software development is the concept of continuous processing (*Kanamori et al.*, 1999). Waveform data are constantly processed to produce Wood Anderson synthetic amplitudes and peak ground motions. A program called `rad` produces a reduced timeseries, sampled every 5 secs, and stores it in a memory area called an "Amplitude Data Area" or ADA. Other modules can access the ADA to retrieve amplitudes to calculate magnitude and ShakeMaps as needed. The BSL and the USGS Menlo Park have collaborated to establish the tools for ADA-based exchange. As part of the software development in Northern California, a number of modules have been developed.

Event Review with `Jiggle`

`CUSP` was finally retired as the event review system in the NCEMC in late November, 2006. This program was initially developed in Southern California during the late 1970s - early 1980s and has been used to time earthquakes for a number of years in Northern California. However, the `CUSP` system became increasingly outdated, as it relied on obsolete hardware. The primary responsibility for the programming and development necessary to make the transition has rested on BSL staff. They implemented the `RequestCardGenerator` (a module that decides which channels to archive, given a particular earthquake), a waveform archiving module, and `Jiggle` (the earthquake timing interface) within the Northern California system. The entry of all parameteric earthquake data from real-time processing into the Oracle database and the preparation of station and instrument metadata for insertion into the database were important prerequisites for the transition. The NCEMC and SCEMC collaborated on modifications to `Jiggle` for use in Northern California, such as the computation of M_d.

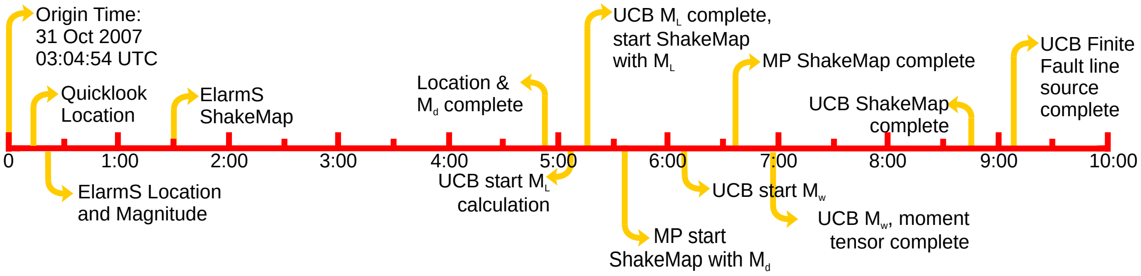

Figure 3.27: Illustration of the earthquake products timeline for the M_w 5.4 Alum Rock earthquake of October 30, 2007. Note that all processing was complete within 10 minutes of the origin time.

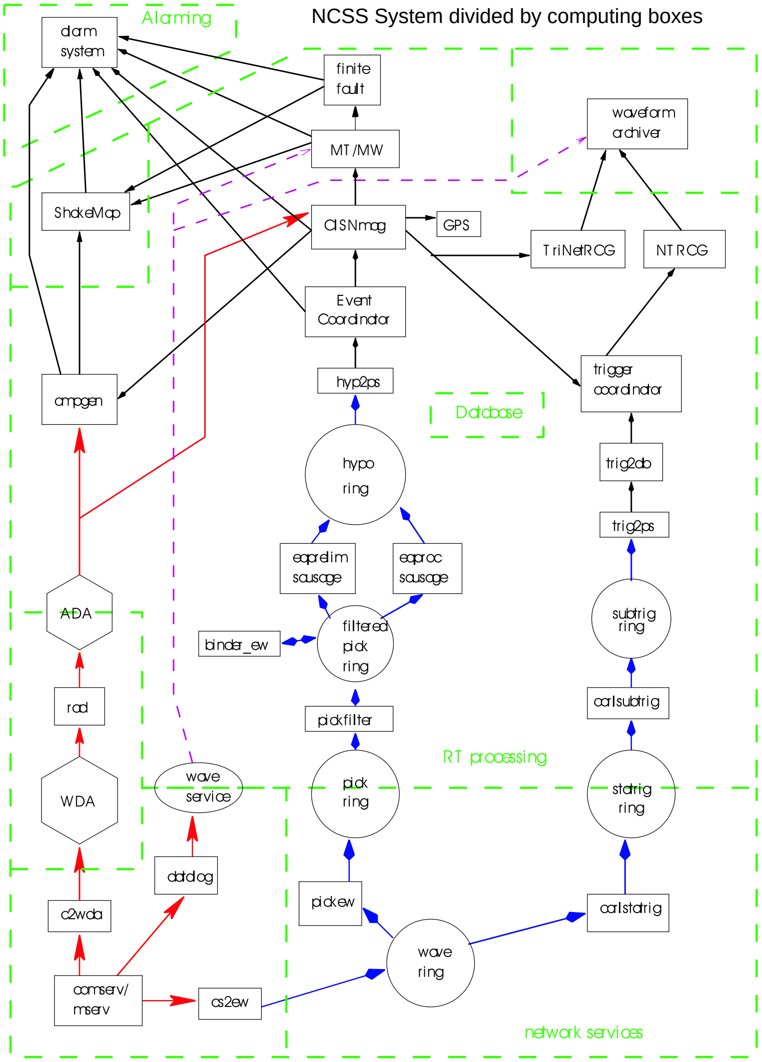

Figure 3.28: Schematic diagram of the planned NCSS system. The design combines elements of the Earthworm, TriNet, and REDI systems

M_L and M_w

The REDI system has routinely produced automatic estimates of moment magnitude (M_w) for many years. However, wary of complications caused by the publication of multiple magnitudes, these estimates were not routinely used as the “official” magnitude until after the

05/14/2002 Gilroy earthquake (M_w 4.9, M_L 5.1). Since then, solutions that meet a minimum quality criterion are automatically reported (a variance reduction of 40% or higher). This criterion appears to work very well and screens out events contaminated by teleseisms. Over the last few years, nearly all events over 4.5 have met this criterion, as have a number of events in the M3.5-4.5 range. As part of the effort to establish a statewide magnitude reporting hierarchy, we have looked more closely at the estimates of M_w (*Gee et al.*, 2003b; 2004) and the comparison between M_w and M_L.

Two methods of determining regional moment tensor (RMT) solutions were originally part of the REDI system - the complete waveform modeling technique (CW) of *Dreger and Romanowicz* (1994) and the surface wave inversion (SW) of *Romanowicz et al.* (1993). In FY05-06, processing for the SW algorithm was discontinued; however, CW moment tensors continue to be calculated, reviewed, and reported. Comparison between the results of the CW method and other regional moment tensor studies in Northern California and the western United States show excellent agreement in the estimate of seismic moment and M_w.

As we transition toward statewide reporting of earthquake information, a comparison of magnitudes calculated for Southern and Northern California becomes important. We have collected a set of events recorded well by digital broadband and and strong motion stations of the Northern California (NC), Berkeley, (BK) and Southern California (CI) networks. Research Study 34. reports on these activities. A new logA_o function has been developed that is valid throughout the state, and a corresponding set of corrections calculated for the collocated broadband and strong motion stations. Research Study 34. reports on the validation of these parameters for Northern and Southern California.

8.4 Routine Earthquake Analysis

In fiscal year 2007-2008, more than 26,000 earthquakes were detected and located by the automatic systems in Northern California. This compares with over 23,000 in 2006-2007, 30,000 in 2005-2006 and 38,800 in 2004-2005. Many of the large number of events in 2004-2005 are aftershocks of the 2004 Parkfield earthquake. The number of events continues to remain high, because we now receive and process data from a network of seismometers in the Geysers, a region with a high level of small magnitude seismicity. Of the more than 26,000 events, over 200 had preliminary magnitudes of three or greater. Thirty-two events had M_L greater than 4. The largest event recorded by the system was the Alum Rock earthquake which occurred on 31 October 2007 with M_w 5.4. Other earthquakes with magnitudes greater than 5 occurred off the coast of northernmost California.

As described in the 2003-2004 Annual Report, the BSL staff are no longer reading BDSN records for local and regional earthquakes (as of March 2004). This decision was in part intended to reduce duplication of effort between Berkeley and Menlo Park.

8.5 Moment Tensor and Finite Fault Analysis

The BSL continues to focus on the unique contributions that can be made from the broadband network. From July 2007 through June 2008, BSL analysts reviewed many earthquakes in Northern California and adjoining areas of magnitude 3.2 and higher. Reviewed moment tensor solutions were obtained for 39 of these events (through 6/30/2008). Figure 3.29 and Table 3.14 display the locations of earthquakes in the BSL moment tensor catalog and their mechanisms.

In the past, moment tensor information has been stored in a flat file, with only the fault planes and the moment recorded. The database associated with the CISN software system allows all the information to be stored that is necessary to recalculate the moment tensor. It includes the moment tensor components as well. During this year, we made an effort to enter information for past Northern California events into the database (see Research Study 36.). This project is nearly completed, thanks to the hard work of Angie Chung, Rick McKenzie, and Jennifer Taggart.

During this year, two earthquakes were large enough to allow finite fault inversions to be performed: the Alum Rock earthquake (October 31, 2007) (see Research Study 22.) and the Wells, NV earthquake of February 7, 2008 (see Research Study 24.).

8.6 Acknowledgements

Peggy Hellweg oversees the REDI system and directs the routine analysis. Peter Lombard and Doug Neuhauser contribute to the development of software. Rick McKenzie, Doug Dreger, Aimin Cao, Sean Ford, Aurelie Guilhem, Ayhi Kim, Ved Lekic, Angie Chung, and Jennifer Taggart contribute to the routine analysis of moment tensors. Peggy Hellweg, Doug Neuhauser, and Bob Uhrhammer contributed to the writing of this section. Partial support for the development and maintenance of the REDI system is provided by the USGS.

8.7 References

Dreger, D., and B. Romanowicz, Source characteristics of events in the San Francisco Bay region, *USGS Open File Report 94-176*, 301-309, 1994.

Gee, L., J. Polet, R. Uhrhammer, and K. Hutton, Earthquake Magnitudes in California, *Seism. Res. Lett., 75(2)*, 272, 2004.

Gee, L., D. Neuhauser, D. Dreger, M. Pasyanos, R. Uhrhammer, and B. Romanowicz, The Rapid Earth-

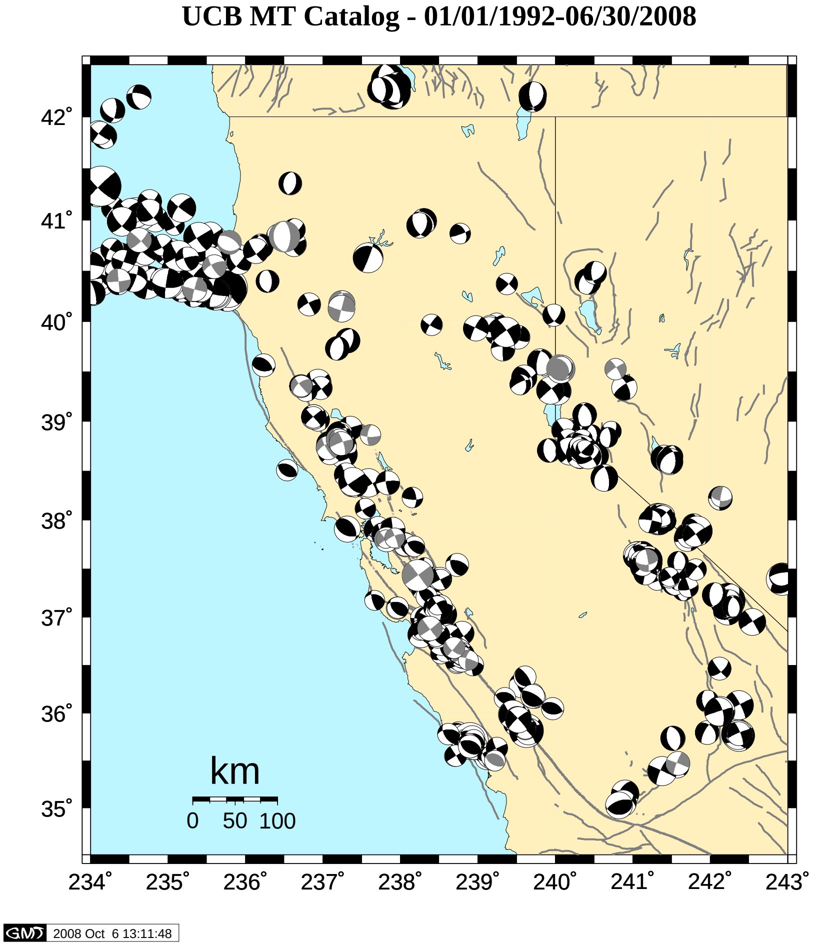

Figure 3.29: Map comparing reviewed moment tensor solutions determined by the BSL from past years (black) with those from the fiscal year 2007-2008 (grey).

quake Data Integration Project, *Handbook of Earthquake and Engineering Seismology*, IASPEI, 1261-1273, 2003a.

Gee, L., D. Dreger, G. Wurman, Y, Gung, B. Uhrhammer, and B. Romanowicz, A Decade of Regional Moment Tensor Analysis at UC Berkeley, *Eos Trans. AGU, 84(46)* , Fall Meet. Suppl., Abstract S52C-0148, 2003b.

Gee, L., D. Neuhauser, D. Dreger, M. Pasyanos, B. Romanowicz, and R. Uhrhammer, The Rapid Earthquake Data Integration System, *Bull. Seis. Soc. Am., 86,* 936-945,1996.

Pasyanos, M., D. Dreger, and B. Romanowicz, Toward real-time estimation of regional moment tensors, *Bull. Seis. Soc. Am., 86,* 1255-1269, 1996.

Romanowicz, B., D. Dreger, M. Pasyanos, and R. Uhrhammer, Monitoring of strain release in central and northern California using broadband data, *Geophys. Res. Lett., 20,* 1643-1646, 1993.

Location	Date	UTC Time	Lat.	Lon.	MT Depth	M_l	M_w	Mo	Str.	Dip	Rake
Aromas	7/2/2007	19:58:53	36.882	-121.622	8	4.5	4.3	3.06E+22	143	88	-174
Oakland	7/20/2007	11:42:22	37.8	-122.18	5	4.1	4.2	2.52E+22	321	89	168
Geysers	7/20/2007	17:50:20	38.81	-122.8	11	3.7	3.9	9.09E+21	61	75	-41
Chatsworth	8/9/2007	07:58:48	34.258	-118.635	8	4.4	4.4	5.86E+22	298	60	111
Oakland	8/15/2007	07:13:10	37.8052	-122.189	5	3.2	3.2	8.54E+20	140	88	-178
Petrolia	9/8/2007	08:16:28	40.3193	-124.654	14	4.3	4.3	3.30E+22	105	88	177
Clear Lake	9/17/2007	14:43:21	38.86	-122.388	8	3.6	3.6	2.73E+21	91	77	-23
Cuca	10/16/2007	08:53:44	34.356	-117.629	11	4	4	1.31E+22	295	58	114
Alum Rock	10/31/2007	03:04:54	37.4323	-121.776	11	5.6	5.4	1.85E+24	323	87	180
Ferndale	11/9/2007	03:37:11	40.5398	-124.404	21	4.1	4.1	1.80E+22	149	77	157
Pinnacles	11/28/2007	02:30:12	36.5998	-121.208	8	5.1	3.4	1.40E+21	49	78	-15
Geysers	12/1/2007	20:50:12	38.7333	-122.933	4	3.9	3.9	1.97E+22	149	77	152
Pinnacles	12/11/2007	08:04:45	36.554	-121.122	5	3.4	3.5	2.44E+21	287	80	23
Offshore of Mendocino	12/11/2007	19:17:20	40.415	-126.384	8	4.8	4.8	1.98E+23	271	88	-134
Redbluff	1/19/2008	17:18:46	40.175	-122.755	11	4.4	4.5	6.49E+22	352	68	-112
Redbluff	1/19/2008	23:13:05	40.125	-122.759	11	4.9	4.7	1.26E+23	14	90	-10
Nevada	2/7/2008	12:53:09	38.236	-117.855	5	3.28	3.6	2.79E+21	190	83	-148
Geysers	2/24/2008	05:32:10	38.817	-122.809	5	4.01	4	1.30E+22	50	63	-44
Willits	3/10/2008	05:14:27	39.355	-123.277	8	3.44	3.7	4.35E+21	140	86	151
Offshore of Oregon	3/15/2008	14:44:38	42.487	-126.663	18	5.6	5.6	3.48E+24	25	73	-91
Geysers	3/27/2008	21:04:36	38.817	-122.786	8	3.6	3.6	3.04E+21	244	84	23
Offshore of Mendocino	4/10/2008	14:17:35	40.404	-125.639	30	3.89	4.2	2.46E+22	175	89	-174
Eureka	4/21/2008	22:00:54	40.78	-124.208	21	4.2	4.2	2.38E+22	301	61	-79
Reno, NV	4/24/2008	22:47:04	39.525	-119.223	5	3.8	3.7	5.10E+21	236	81	-11
Reno, NV	4/24/2008	22:55:49	39.527	-119.929	5	4.2	4.3	3.81E+22	153	74	-166
Reno, NV	4/26/2008	06:40:11	39.524	-119.932	5	5.13	4.9	3.35E+23	60	85	25
Reno, NV	4/28/2008	11:33:18	39.533	-119.931	5	4.2	4.1	1.77E+22	315	87	-170
Templeton	4/29/2008	17:45:17	35.499	-120.783	8	3.6	3.6	2.95E+21	119	55	93
Willow Creek	4/30/2008	03:03:07	40.836	-123.497	30	5.4	5.4	1.46E+24	359	60	-88
Lake Isabella	5/1/2008	08:11:43	35.471	-118.42	8	4.1	4.1	1.96E+22	291	89	-172
Offshore of Mendocino	5/6/2008	17:18:32	43.171	-126.447	14	4.5	4.5	6.70E+22	123	83	165
Reno, NV	5/8/2008	05:55:01	39.542	-119.92	5	3.5	3.6	3.40E+21	118	82	-167
Ferndale	5/13/2008	04:07:39	40.801	-125.374	11	4.2	4.3	3,29e22	314	86	167
Geysers	5/30/2008	04:48:36	38.776	-122.764	5	3.9	4.1	2.01E+22	250	82	-14
Green Valley	6/4/2008	02:29:04	38.242	-122.184	8	3.9	3.9	8.27E+21	63	87	-12
Oakland	6/6/2008	09:02:54	37.816	-122.075	8	3.5	3.5	2.00E+21	339	84	-162
Reno, NV	6/8/2008	17:53:41	39.546	-119.918	5	3.6	3.7	3.66E+21	195	-54	56
Tres Pinos	6/19/2008	23:57:51	36.681	-121.308	8	3.76	3.8	5.45E+21	40	88	-24
Tom's Place	6/28/2008	14:44:10	37.586	-118.819	11	4.3	3.9	9.89E+21	351	83	-32

Table 3.14: Moment tensor solutions for significant events from July 1, 2007 through June 30, 2008 using a complete waveform fitting inversion. Epicentral information is from the UC Berkeley/USGS Northern California Earthquake Management Center. Moment is in dyne-cm and depth is in km.

9. Instrumentation Testing

9.1 Introduction

The BSL Instrumentation Testing Facility located in the Byerly Vault (BKS) has been busy this past year with the testing of several sensors. In July 2007, the sensitivity and noise performance of the 8-channel Quanterra Q4120 data logger was checked to verify that is operating within the factory specifications. The BSL staff has also been involved in projects to test new STS-1 electronics developed by Metrozet LLC and to test a new temperature, hygrometer, and pressure sensor package that is being developed in-house. We have also tested new and repaired broadband and strong motion sensors on an *ad hoc* basis prior to deployment in the field.

A new advanced electronics package, the Metrozet STS-1-E300, has been developed and tested as a modern replacement for the original Streckeisen STS-1 very-broadband seismometer "Feedback Electronics" boxes. The development and testing is a collaborative effort between Metrozet LLC and the BSL. The new electronics package matches the outstanding analog performance of the original Streckeisen circuitry while providing a number of enhancements to facilitate installation and operation of the STS-1 sensors. The enhancements include: digital control of all sensor parameters; digital control of centering motor operations; monitoring of all major state-of-health parameters, and a complete calibration capability. All control and diagnostic functions can be controlled either locally (via RS-232, USB or Ethernet) or remotely (via Ethernet).

A new temperature, humidity, and pressure (THP) sensor package is being developed in-house at BSL as a replacement for the existing and aging temperature and pressure sensors at the BDSN stations. Measurement of the temperature and pressure at a BDSN station is useful for reducing the components of the seismic background noise that are correlated with temperature and pressure. A hygrometer has also been added to the sensor package to enable measurement of the local atmospheric relative humidity, a parameter which is potentially useful for estimating and correcting for geodetic GPS tropospheric propagation delays.

9.2 Instrumentation Test Facility

The BSL sensor testing facility is described in detail in the BSL 2001-2002 Annual Report (available on-line at `http://www.seismo.berkeley.edu`).

Data Logger Calibration

In July 2007, the sensitivity and self-noise PSD for each data channel and inter-channel crosstalk of the 8 channel Quanterra Q4120 data logger was checked using a reference signal applied first simultaneously and then sequentially to all channels, with the non-driven channels resistively terminated. The relative sensitivities of the data logger channels were checked by applying a high-level (∼19.8 V peak-to-peak (P-P)) 1 Hz square wave signal simultaneously to all channels. The signal level on each channel was measured and the relative signal levels were compared to the sensitivities on the factory calibration sheet. The sensitivities of four of the channels have not changed by more than 0.01% from the factory calibration values. Of the remaining four channels, three changed by less than ±0.3%, and the fourth changed by -0.8%. Modulo 0.25% sensitivity changes are inherent in Q4120 at boot time because it steps the sensitivity in 0.25% increments and selects the sensitivity that has the lowest internal noise level. Sensitivity changes that are not near modulo 0.25% are likely due to a combination of modulo 0.25% increments and degradation of the components.

The self-noise of the Q4120 channels (with 1 kΩ resistance termination) was determined via Power Spectral Density (PSD) analysis. A composite plot of the Q4120 self-noise over the 20 microHz to 0.5 Hz band is shown in Figure 3.30, and a more detailed plot of the high-frequency (0.2-80 Hz self-noise PSD is shown in Figure 3.31. The minimum observed self-noise PSD is approximately 6 dB below the factory specification for a thermally stable environment in the 2-20 Hz band.

The inter-channel cross-talk of the data logger was checked by connecting each of the channels in sequence with the high amplitude (20 V P-P) 1 Hz square-wave signal while terminating the other seven channels with 1 kΩ resistors at the data logger input connectors. The Q4120 data logger contains two 4-channel digitizer modules (HH1-HH4 and HH5-HH8). The observed cross-talk signal level on all 8 channels is below the 2.34 μV quantization (least significant bit or LSB) level of the Q4120 data logger. The cross-talk signal level is thus more than 138.5 dB below the drive signal level. A check of the coherence between the channels was performed by driving each channel sequentially with a one minute duration 20V P-P 1 Hz square wave while terminating the remaining seven channels with 1 kΩ resistors across the signal input connectors of the data logger. Spectral phase coherence analysis of the signal between the inter-channel pair combinations did not detect any significant coherence.

Instrumentation Test Bed

The data logger is connected to the seismometer test bed breakout box via a ∼6 meter shielded signal ca-

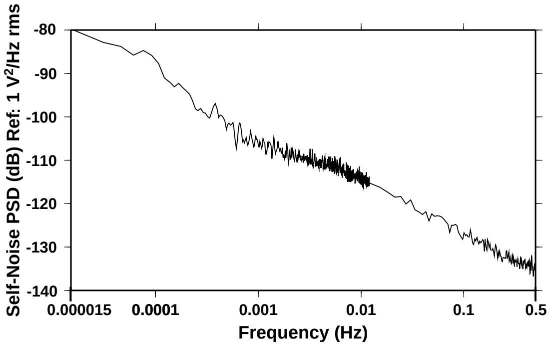

Figure 3.30: Self-Noise PSD of Q4120 data logger used in testing. A 1 kΩ resistance termination was placed across the data logger input. The plot is composite, derived from 1 sps noise data for frequencies below ∼ 0.01 Hz and 200 sps noise data at higher frequencies.

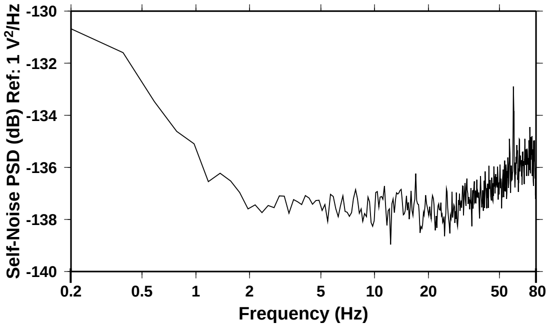

Figure 3.31: High-frequency self-noise PSD of Q4120 data logger used in testing. The data logger input was terminated with a 1 kΩ resistor. The median value of 32 noise sample PSD data are plotted, and the lowest self-noise PSD of ∼-137 dB is observed in the 2-30 Hz band. For comparison, the factory noise specification is that the terminated input noise level is typically -134.5 dB and it may exceed -137.5 dB at constant temperature.

ble. The above coherence test was repeated with the drive signal and terminating resistances connected at the breakout box, and some inter-channel pairs exhibited detectable phase coherence at 1 Hz and its odd harmonics and also at the 60 Hz power mains frequency, between adjacent signal pairs in the cable, which is consistent with capacitive coupling in the signal cable and with proximity of the signal cable to 60 Hz power wires in the vault. The largest observed cross-talk signal levels on the terminated channels were ∼120 dB below the 20V P-P 1 Hz square wave drive signal level which is sufficiently low that the cross-talk does not interfere with subsequent data analysis.

9.3 BDSN *Ad Hoc* Sensor Testing

During the past year, the following sensors were tested to verify that they were performing within the factory specifications prior to re-deployment in the field:

1) The 3 STS-1's from KCC (STS-1Z s/n 109112, STS-1H s/n 29212, and STS-1H s/n 29201) with Metrozet STS-1-E300-005 electronics,

2) The 3 STS-1's from SAO with their corresponding factory electronics boxes (STS-1Z s/n 109119, STS-1H s/n 48528, and STS-1H s/n 48529).

9.4 STS-1 Sensor Electronics Testing

From the perspective of the BSL, the critical task in developing new electronics for the STS-1 seismometers, the E300, is the evaluation of performance and the comparison between new and old systems. Several iterations of the E300 were evaluated during the design and development phase. Objective evaluation of the new electronic subsystem required a stable and repeatable test platform of seismometers, base plates, cables, connectors, and digitizer channels. Only when the system was stable, as evidenced by repeated calibration results, was the platform suitable for evaluation of the new electronics.

Seismometer Acquisition and Alignment

Having characterized and calibrated the data logger (as discussed above), it was necessary to establish a stable seismometer subsystem test bed. Nine different STS-1 instruments (six horizontal, and three vertical instruments) were set up and leveled, and the outputs to the Q4120 data logger were compared quantitatively.

The horizontal instruments were aligned along a single axis allowing comparisons and evaluations of their coherence. Misalignment of less than one degree across the six horizontal instruments caused unacceptable variances in signal coherence, and took a week to resolve by rotating individual instruments. Alignment of the vertical instruments was much easier. Only after all alignment incoherences were resolved, were the new electronics evaluated against the original factory electronics.

Each cable, connector, and base plates combination were marked, color coded, and assigned, as new and original electronics were mated with seismometers. The color coding endeavored to eliminate ambiguities and variables beyond the actual electronics. Each combination of seismometers and electronics was recorded for a minimum of 24 hours. In the end, over 100 combinations of original and new electronics and seismometers were evaluated under conditions that were documented.

When individually labeled and identified combinations of base plates, cables, seismometers, and electronics were characterized and deemed repeatable, the new Metrozet electronics were substituted. Initially, the prototype

Metrozet electronics were operated on only one seismometer, with three, four or five other seismometers simultaneously operating on Streckeisen's factory electronics. After verifying correct input and output signal levels, the single Metrozet electronics were rotated and verified amongst six seismometers. A second prototype Metrozet electronics package was likewise rotated through the seismometers, but this time powering two seismometers concurrently.

Sensor/Electronics Testing

Testing of the STS-1 sensor and electronics systems involved several components. STS-1 vertical- and horizontal-component sensors for testing were gathered from among the available BDSN sensors, from surplus sensors on loan from the Gräfenberg Array, and from UC San Diego. The sensors were systematically inspected and checked to ensure that they were operating correctly. The ones that performed best were selected for the testing procedures and installed in the test bed. In total, 16 broadband STS-1 sensors (7 vertical and 9 horizontal components) were utilized during the testing process. Nine of them are owned by the BSL; 5 were on loan from Gräfenberg and 2 from IGPP/UCSD. The horizontal-component sensors were aligned east.

Coherence and Power Spectral Density

An algorithm (*scn_psd*) to calculate the signal Power Spectral Density (PSD), the noise PSD, and the coherence between sensors has been developed, in-house at BSL, as a tool for quantifying the performance differences between the seismic sensors under test. Three continuous hours of 200 Hz data are used by the *scn_psd* algorithm. *scn_psd* parses the data into 32 non-overlapping segments, applies and corrects for the effects of a Hanning window, scales the data to ground motion, calculates the Fast Fourier Transform (FFT) and stores the resulting complex spectral values for each segment. At each frequency, the RMS signal PSD is calculated from the average of the complex spectral values, coherence is calculated from the averaged complex spectral cross product, and the RMS noise PSD is then determined from the product of the signal PSD and (1 - coherence). The method is described in detail in *Barzilai et al.* (1992). In all tests, the BKS STS-1's are used as the reference signals in the analysis. Two sample results of the algorithm are shown. Figure 3.32 shows the results for four seismometers in the case of a large seismic event, and Figure 3.33 shows the results for four seismometers in the case of background noise. In the presence of large seismic signals, the coherence is typically close to unity at all frequencies below the 5 Hz high-frequency corner of the BKS reference STS-1's. Note the relatively high noise PSD level on the horizontal components in the vicinity of 0.1 Hz. This is due to a slight misalignment of the sensitive axes of the horizontal components. Several time-consuming trial and error iterations in aligning the horizontal components are required to lower the horizontal component noise PSD.

Response Calibration

A pair of algorithms were developed in-house to determine the seismometer frequency response as characterized by the seismometer free period (T_s) and fraction of critical damping (h_s) and the high-frequency ("galvanometer") corner frequency (f_g) and fraction of critical damping (h_g). These algorithms were developed to take advantage of the step function and low-frequency swept sine and high-frequency stepped sine calibration stimuli generated by the E300 electronics boxes, applied to the STS-1 calibration coils, and also recorded on one channel of the data logger. Thus, we can compare the observed and calculated responses to a known calibration stimulus to precisely determine the frequency response of the seismometer. Note that these algorithms determine only the shape of the frequency response and not the sensitivity of the seismometer. The corresponding flat pass-band sensitivity of the seismometer is determined using the Metrozet-supplied STS-1 Scale Factor Calculator V1.0 Java software applet (available via `http://www.metrozet.com/TSA-100S.html`), which, when given the values of all the feedback components from the factory calibration sheet for a specific STS-1 with factory electronics, determines the corresponding sensitivity with the E300 electronics connected. This method, of course, assumes that the original factory determination of the STS-1 response parameters is accurate. An alternative method to determine the absolute sensitivity is to determine the response of the STS-1 to known micro-tilts, a procedure which is very tedious and not easily done with sufficient accuracy. We prefer to check the accuracy of the STS-1 sensitivity by comparison of large seismic ground motions inferred from the STS-1s, with the corresponding ground motions from co-sited broadband or strong motion sensors. An added advantage of comparison with the signals from the accelerometers is that their responses are flat to DC, and their calibration is easily checked by tilting them ±90 degrees along the horizontal sensitive axes to induce a ±1 g acceleration step.

The first algorithm, *td_tfp*, determines the transfer function parameters using an adaptive migrating grid search methodology to minimize the difference between the observed and calculated time series response to a known stimulus function. This routine determines the calculated response via direct integration of the seismometer equation of motion response to a known stimulus input using a fourth-order Runge-Kutta integration scheme. Also, the *td_tfp* algorithm was specifically developed to determine the seismometer T_s and h_s using, preferably, the low-frequency calibration stimulus or, alternatively, the step-function stimulus data.

The free period T_s and fraction of critical damping were determined via a grid search for the maximum variance reduction between the observed response and the theoretical response to stimulus signal input to the calibration coils. Sample outputs of the *td_tfp* are shown in Figures 3.34 and 3.35 and the calibration results for the BKS reference STS-1 sensors are listed in Table 4.

The second algorithm, *pd_tfp*, determines the transfer function parameters using a grid search methodology to minimize the difference between the observed and calculated phase response to a known stimulus function. *pd_tfp* determines the parameters from the frequency and slope of the phase response curve when the measured phase delay between the calculated and observed responses is $\pi/2$. Also, *pd_tfp* algorithm was specifically developed to determine f_g and h_g using high sampling rate data (e.g. ≥ 80 sps) and the stepped sine (0.5-40Hz) stimulus input to the calibration coils. A sample of the algorithm output is shown in Figure 3.36.

Both algorithms, *td_tfp* and *pd_tfp*, are capable of determining the transfer function parameters (T_s, h_s, f_g and h_g) to approximately one part per thousand or better when the response to the stimulus signal is 20+ dB above the seismic background noise level.

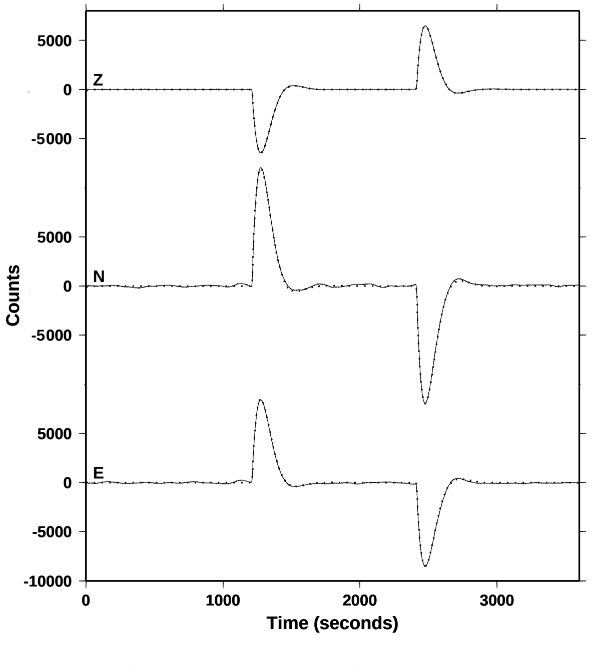

Figure 3.34: Calibration of BKS STS-1 seismometer low-frequency responses by time domain analysis of response of the seismometer to a step function calibration stimulus. Shown are the observed (solid lines) and calculated responses (dashed lines) to a 1200 second duration current step (equivalent to an acceleration step) input to the seismometer calibration coils.

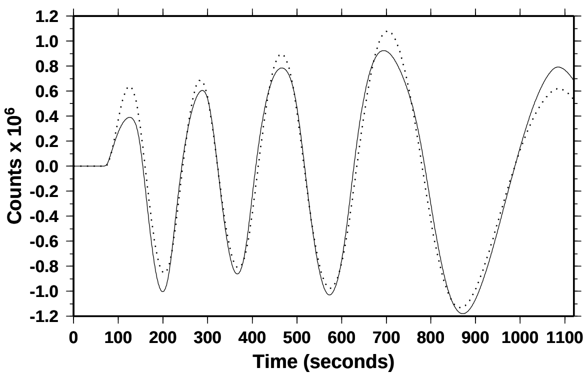

Figure 3.35: Calibration of HOPS STS-1 Z-component seismometer low-frequency response by time domain analysis of response of seismometer to a swept sine function calibration stimulus. Shown are the observed (solid line) and calculated (dashed line) responses to a 40-1100 second swept sine current (equivalent to a swept acceleration) input to the seismometer calibration coil.

9.5 Temperature, Humidity, Pressure Sensor Testing

During the past year, BSL staff have tested several generations of a new temperature, humidity, pressure (THP) sensor at the Instrumentation Test Facility and on the roof of McCone Hall. The new THP sensor package is being developed and upgraded to replace the temperature and pressure sensors currently installed at bdsn stations, which are aging and failing.

The pressure sensing element is a Honeywell SDX15A2-A which is temperature compensated. The specification sheet says that the sensor range of 0-15 psi in absolute pressure results in a 90mv (±1%) differential change on the outputs when the bridge is excited with 12V. The sensor is operated in a bridge circuit configuration and its sensitivity is:

$P(psi) = (V + 134.3)/9.995$

where: V is the bridge output in Volts and psi is pounds per square inch (1 psi = 6894.8 Pa).

The resistance thermal detector (RTD) is a Honeywell HEL-700 with a resistance of 1kΩ at 0° C. The RTD is operated in a circuit with offset and gain and its sensitivity is:

$T(°\text{ C}) = (V + 9.09)/.3463$

where: V is the output in Volts.

The humidity sensing element is a Honeywell HIH-4602C which is sensitive to the relative humidity. The sensor is operated in a circuit which results in a overall calibrated sensitivity of:

$\%RH = ((V + 9.29)/3.168 - Z)/S$

where: %RH is the percent relative humidity and V is the voltage output. S and Z are given in the factory calibration sheet as Z ~0.826 mV and S ~31.5 mv/%RH. Thus:

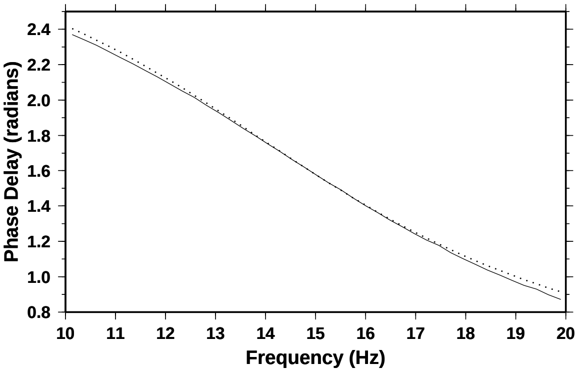

Figure 3.36: Calibration of HOPS STS-1 Z-component seismometer high-frequency response by phase domain analysis of response of seismometer to a stepped sine function calibration stimulus. Shown are the observed (solid line) and calculated (dashed line) responses to a 0.5-40 Hz stepped sine current (equivalent to a stepped acceleration) input to the seismometer calibration coil.

$\%RH = (V + 6.673)/0.09979$.

The factory specification sheet indicates that the response time is ∼50 seconds and the accuracy is ±3.5%RH. The absolute humidity (AH) is a function of temperature, and, given the temperature, AH can be derived from relative humidity (RH) via:

$AH(g/m^3) = (0.000002T^4 + 0.0002T^3 + 0.0095T^2 + 0.337T + 4.9034) * RH$

where: T is the temperature in ° C.

9.6 Acknowledgements

Development of the sensor test facility and analysis system was a collaborative effort of Bob Uhrhammer, Tom McEvilly, John Friday, and Bill Karavas. IRIS and DTRA provided, in part, funding for and/or incentive to set up and operate the facility, and we thank them for their support. Robert Uhrhammer, John, Friday, Jarrett Gardner, Bill Karavas and Barbara Romanowicz (all from BSL), Tom VanZandt (Metrozet LLC), Charles R. Hutt (Albuquerque Seismological Laboratory) and Erhard Wielandt (Institute of Geophysics, University of Stuttgart) contributed to this chapter. The STS-1 electronics upgrade project was funded by the NSF through the IRIS/GSN program, with complementary support from University funds to the BSL. We thank Jennifer Taggart and Aimin Cao for their help in preparing the figures.

9.7 References

Barzilai, A., T. VanZandt, and T. Kenny, Technique for measurement of the noise of a sensor in the presence of large background signals, *Rev. Sci., Instrum.*, 69, 2767-2772, 1998.

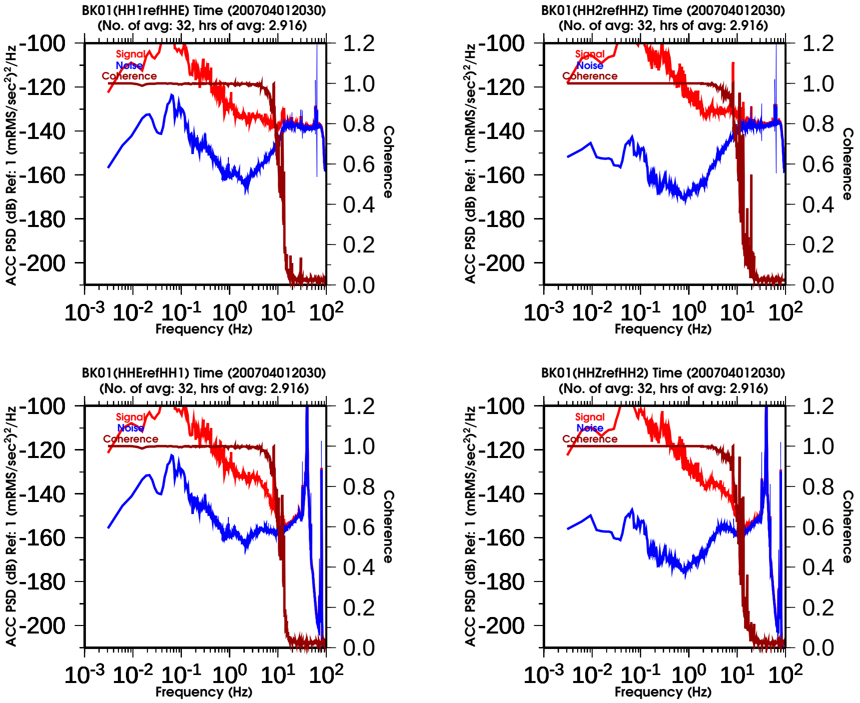

Figure 3.32: Results for two vertical component STS-1's (HHZ and HH2) and two horizontal component STS-1's (HHE and HH1) in the presence of a large seismic signal. The event is a M_w 8.1 earthquake which occurred 87.9 degrees WSW of Berkeley on 2007/04/01 at 20:39 UT. Shown are the signal PSD (red), the noise PSD (blue), and the coherence (brown) for each sensor.

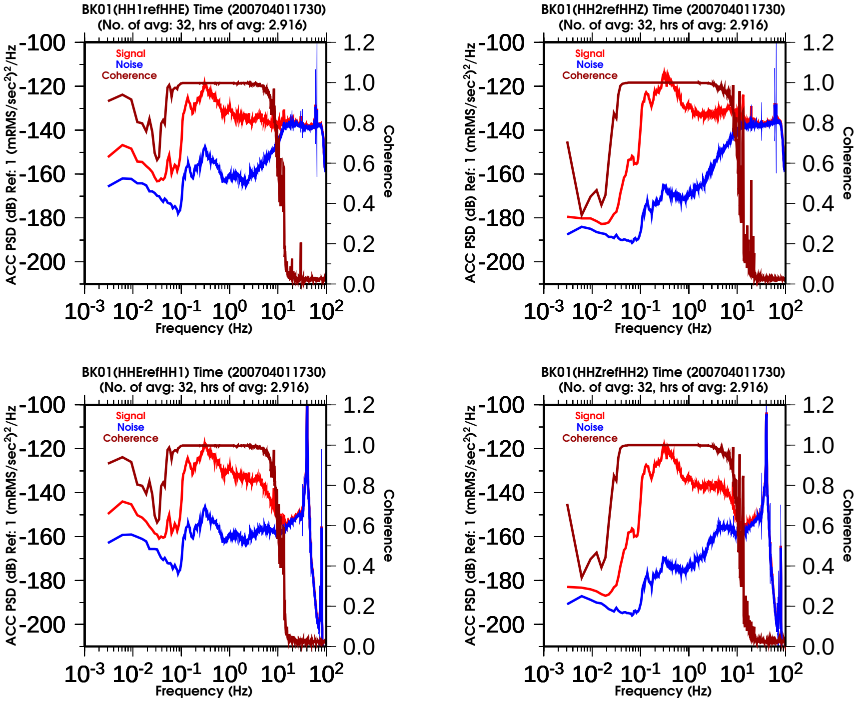

Figure 3.33: Results for four vertical component STS-1's (HHZ, HH4, HH5, and HH7) in the presence of background noise. The traces are the same as in Figure 3.32. The lower and upper frequencies at which the coherence degrades from near unity varies among the sensors. Coherence bandwidth is a measure of the performance of the sensors, and HH5 has the best performance of the four sensors.

10. Outreach and Educational Activities

10.1 Introduction

The BSL is involved in a variety of outreach activities ranging from lectures to lab tours and educational displays. Recorded information on current earthquake activity is updated regularly on our information tape (510-642-2160). Additional basic information on earthquakes and seismic hazards for northern and central California, as well as other information about seismology and our research, can be found on our extensive set of web pages at `http://seismo.berkeley.edu/`.

10.2 Highlights of 2007-2008

The Hayward Fault runs through the UCB campus. It last ruptured on October 21, 1868. Since then, new scientific insights put the average interval between large earthquakes on the Hayward Fault at 140 years; 2008 represents an important anniversary.

This year's Lawson Lecture highlighted local concerns. Dr. Roland Bürgmann of U.C. Berkeley presented "A tectonic time bomb in our backyard: Earthquake Potential of the Hayward Fault." He described the many advances, such as GPS monitoring and paleoseismological investigations, that allow us new insight into the forces that cause large movements along the fault. The Lawson Lectures are webcast at `http://seismo.berkeley.edu/news/lawsonlecture`.

The 1868 Earthquake Alliance is using the 140th anniversary as a unique opportunity to increase public awareness of seismic hazard posed by the Hayward Fault and other East Bay Faults, promote earthquake preparedness and mitigation, and to explore the ways in which the 1868 Hayward earthquake affected the personal lives, culture, economy and development of the greater San Francisco Bay Area (`http://1868alliance.org`). The BSL is contributing to the commemoration activities and participates in organization.

The 140th anniversary of the Hayward Earthquake is also the impetus for organizing the "Third Conference on Earthquake Hazards in the Eastern San Francisco Bay Region", which will take place October 22-26, 2008, at Cal State University East Bay (Hayward). The previous two conferences were held in 1982 and 1992. The BSL is a co-organizer of this conference, with Roland Bürgmann and Peggy Hellweg serving on the organizing committee. The meeting will include three days of technical sessions, a public forum, field trips and teacher education programs (`http://www.consrv.ca.gov/cgs/News/Pages/eastbayconference.aspx`).

10.3 On-Going Activities

Tours and Presentations

As in every year, tours and presentations formed an important part of BSL's public relations activities. Each month, several groups, ranging from middle-school students to scientists and engineers, tour our laboratory under the guidance of a graduate student or a member of the staff.

During 2007-2008 the BSL conducted several tours, both for local schools and groups from around the world. Peggy Hellweg led a group of Germans along the California Faults for the Bild der Wissenschaft magazine, starting in Los Angeles and ending in the San Francisco Bay Area. Several school classes at different grade levels received tours. BSL graduate students also visited local elementary, middle and high schools to talk about earthquakes and how we measure them. In addition to the tours, Drs. Allen, Dreger, Hellweg, Mayeda and Uhrhammer presented talks on earthquakes and related phenomena to public groups and the media.

Open House

The BSL again participated in *CalDay*. The attendance for the open house was exceptionally good this year. The visitors learned about UC Berkeley's role in earthquake monitoring, watched a streaming feed of earthquake data, jumped up and down to "make a quake," played with the earthquake machine, made P and S-waves with springs, learned about earthquake preparedness, and were given sample seismograms. The BSL repeated Roland Bürgmann's Lawson Lecture and also co-sponsored a lecture with the Earth and Planetary Scienc department on "Field Geology and Digital Mapping."

Educational Displays

The BSL continues to make REDI earthquake data available to certain schools, universities, colleges, and museums for educational displays. Participating organizations receive a REDI pager and the Qpager software to display the earthquake information. The Qpager program maps the previous seven days of seismicity, with each earthquake shown as a dot. The size of the dot indicates the magnitude of the event, while the color of the dot indicates its age. These educational displays have been installed at UC Berkeley (McCone Hall, Earthquake Engineering Research Center), California Academy of Sciences, CSU Fresno, CSU Northridge, CSU Sacramento, Caltech, College of the Redwoods, Fresno City College, Humboldt State University, San Diego State University, Sonoma State University, Stanford University

(Blume Engineering Center, Department of Geophysics), UC Davis, UC Santa Cruz, UC San Diego, and USC. For the past four years, middle schools of the San Francisco Unified School District have participated in the program.

In addition to the seismicity displays, the BSL provides local waveform feeds for helicorders at visitor centers associated with BDSN stations (CMB and MHC). Organizations such as LHS, KRON, and KPIX receive feeds from BKS via dedicated phone lines for display, while the USGS Menlo Park uses data from CMB for display in the lobby of the seismology building. The BSL has also loaned a seismometer and helicorder display to the San Leandro Unified School District for their use in science classes.

BSL Web Pages

We continue to maintain and update our presence on the Internet. The Web pages are intended to provide a source of earthquake information for the public. They also present information about the networks we operate, including station profiles. This benefits the research community as well. The BSL Web pages publicize seminar schedules, advertise courses, and describe our research, as well as our operations. They offer updates on recent earthquake activity, details on Bay Area seismicity and hazards, and links to other earthquake and earth science servers. We also use the web server to distribute information internally among BSL personnel, with such details as the computing and operational resources, rosters, and schedules for various purposes.

Earthquake Research Affiliates Program

The UC Berkeley Earthquake Research Affiliates (ERA) Program is an outreach project of the BSL, the Department of Earth and Planetary Science, and the Earthquake Engineering Research Center. The purpose is to promote the support of earthquake research while involving corporations and governmental agencies in academic investigation and education activities such as conferences and field trips. The ERA program provides an interface between the academic investigation and practical application of earthquake studies.

10.4 Acknowledgements

Peggy Hellweg oversees the outreach activities at the BSL. Barbara Romanowicz, Bob Uhrhammer, Rick McKenzie, Jennifer Taggart and many other faculty, staff, and students at the BSL contribute to the outreach activities. Rick McKenzie and Peggy Hellweg contributed to the preparation of this section.

Glossary of Common Acronyms

Table 3.15: Standard abbreviations used in this report.

Acronym	Definition
AMR	Accelerating Moment Release
ANSS	Advanced National Seismic System
BARD	Bay Area Regional Deformation
BAVU	Bay Area Velocity Unification
BDSN	Berkeley Digital Seismic Network
BSL	Berkeley Seismological Laboratory
CALREF	Canifornia Reference Frame
CDF	California Department of Forestry
CFS	Coulomb Failure Stress
CGS	California Geological Survey
CISN	California Integrated Seismic Network
CLVD	Compensated Linear Vector Dipole
CSMIP	California Strong Motion Instrumentation Program
CW	Complete Waveform
DART	Data Available in Real Time
DC	Double Couple
DNA07	Dynamic North America model of 2007
EM	Electromagnetic
ElarmS	Earthquake Alarm Systems
FA	Flexible Array
FACES	FlexArray along Cascadia Experiment for Segmentation
FAME	Flexible Array Mendocino Experiment
FFT	Fast Fourier Transform
FRAD	Frame Relay Access Device
GVF	Green Valley Fault
HF	Hayward Fault
HRSN	High Resolution Seismic Network
ICB	Inner Core Boundary
IG	Infragravity
IMS	International Monitoring System
InSAR	Interferometric Synthetic Aperture Radar
IRIS	Incorporated Research Institutions in Seismology
K-NET	Kyoshin Net, Japan
LBL	Lawrence Berkeley National Laboratory
LFEs	Low-frequency Earthquakes
LLNL	Lawrence Livermore National Laboratory
LP	Long Period
MBARI	Monterey Bay Aquarium Research Institute
MMI	Modified Mercalli Intensity
MORB	Mid Ocean Ridge Basalts

continued on next page

Table 3.15: *continued*

Acronym	Definition
MPBO	Mini-Plate Boundary Observatory
MT	Magnetotelluric
NCEDC	Northern California Earthquake Data Center
NCEMC	Northern California Earthquake Management Center
NCF	Noise Correlation Functions
NCSN	Northern California Seismic Network
NCSS	Northern California Seismic System
NHFN	Northern Hayward Fault Network
NSMP	National Strong Motion Program
NTS	Nevada Test Site
NVT	Non-volcanic Tremor
OES	California Governer's Office of Emergency Services
PBO	Plate Boundary Observatory
PDF	Probability Density Function
PGV	Peak Ground Velocity
PSD	Power Spectral Density
PVC	Permanent Virtual Circuit
QDDS/EIDS	Quake Data Distribution System/Earthquake Information Distribution System
RCF	Rodgers Creek Fault
REDI	Rapid Earthquake Data Integration
RES	Repeating Earthquake Sequence
RGF	Reference Green Function
RMS	Root Mean Squared
RMT	Regional Moment Tensor
S/N	Signal to Noise
SAF	San Andreas Fault
SAFOD	San Andreas Fault Observatory at Depth
SCEC	Southern California Earthquake Center
SCEMC	Southern California Earthquake Management Center
SCSN	Southern Canifornia Seismic Network
SFBA	San Francisco Bay Area
SMIP	Strong Motion Instrumentation Program
STA/LTA	Short Time Average/ Long Time Average
SW	Surface Wave Inversion
SWD	Spectral Wave Density
THP	Temperature, Humidity, Pressure
UNAVCO	University NAVSTAR Consortium
USGS/MP	United States Geological Survey/ Menlo Park
USNSN	United States National Seismic Network
UUSS	University of Utah Seismic Stations
VLP	Very Long Period

Appendix I Publications, Presentations, and Panels 2008-2008

Publications

Aagaard, B. T., T. M. Brocher, D. Dolenc, D. Dreger, R. W. Graves, S. Harmsen, S. Hartzell, S. Larsen, and M. L. Zoback, Ground-motion modeling of the 1906 San Francisco Earthquake, Part I: Validation using the 1989 Loma Prieta Earthquake, *Bull. Seism. Soc. Am., 98*, 989-1011, 2008.

Aagaard, B. T., T. M. Brocher, D. Dolenc, D. Dreger, R. W. Graves, S. Harmsen, S. Hartzell, S. Larsen, K. McCandless, S. Nilsson, N. A. Petersson, A. Rodgers, B. Sjoegreen, and M. L. Zoback, Ground-motion modeling of the 1906 San Francisco Earthquake, Part II: Ground-motion estimates for the 1906 Earthquake and scenario events, *Bull. Seism. Soc. Am., 98*, 1012-1046, 2008.

Allen, R.M., Earthquake hazard mitigation: New directions and opportunities, *Treatise on Geophysics*, G. Schubert (ed.), Vol 4 (H. Kanamori ed.), p607-648, Elsevier, 2007.

Benetatos, C., D. Dreger, and A. Kiratzi, Complex and segmented rupture associated with the 14 August 2003 Mw 6.2 Lefkada, Ionian Islands, Earthquake, *Bull. Seism. Soc. Am., 97*, 35-51, 2007.

Biggs, J., R. Bürgmann, J. Freymueller, Z. Lu, B. Parsons, I. Ryder, G. Schmalzle and T. Wright, The postseismic response to the 2002 M7.9 Denali Fault Earthquake: Constraints from InSAR, *Geophys. J. Int.* (in press).

Bolt, B.A., and D. S. Dreger, Nature of Earthquakes and Seismic Hazards, *Designing for Earthquakes*, FEMA Publication 454, 392p., 2008.

Brocher, T. M., K. Knudsen, M.L. Zoback, J. Perkins, M. Hellweg, W. Savage, and K. Bailey, The Hayward fault: Is it America's most dangerous?, *Catastrophe Risk Magazine*, April 2008.

Brudzinski, M.R. and R.M. Allen, Segmentation in episodic tremor and slip all along Cascadia, *Geology, 35* (10), 907-910, doi: 10.1130/G23740A.1, 2007.

Bürgmann, R., and G. Dresen, Rheology of the lower crust and upper mantle: Evidence from rock mechanics, geodesy and field observations, *Ann. Rev. Earth Plan. Sci., 36*, 531-567, doi:10.1146/annurev.earth.36.031207.124326, 2008

Cammarano F. and Romanowicz B., Radial profiles of seismic attenuation in the upper mantle based on physical models. *Geophys. J. Int.*, (in press).

Cannon, E. C., R. Bürgmann, A. J. Crone, M. N. Machette, and R. L. Dart, Map and data for Quaternary faults and fault systems on the Island of Hawaii, U .S. Geological Survey Open-File Report, 2007-1284 (`http:/pubs.usgs.gov/of/2007/1284/`), 1-81, 2007.

Cao, A. and B. Romanowicz, Test of the Innermost Inner Core Models Using Broadband PKIKP travel time residuals, *Geophys. Res. Lett., 34*, L08303, doi:10.1029/2007GL029384, 2007.

Chen, K.H., S. Toda, and R.J. Rau, A leaping, triggered sequence along a segmented fault: the 1951 Hualien - Taitung earthquake sequence in eastern Taiwan, *J. Geophys. Res., 113*, doi:10.1029/2007JB005048, 2008.

Cobden L., Goes S., Cammarano F., and Connolly J.D., Thermo-chemical interpretation of one dimensional seismic reference models for the upper mantle: evidence for bias due to heterogeneity, *Geophys. J. Int.*, (in press).

Dolenc, D., B. Romanowicz, P. McGill, and W. Wilcock, Observations of infragravity waves at the ocean-bottom broadband seismic stations Endeavour (KEBB) and Explorer (KXBB), *Geochem. Geophys. Geosys., 9(Q05007)*, doi:10.1029/2008GC001942, 2008.

Dreger, D., R. Nadeau, and A. Chung, Repeating Earthquake Finite-Source Models: Strong Asperities Revealed on the San Andreas Fault, *Geophys. Res. Lett., 34(L23302)*, doi:10.1029/2007GL031353, 2007.

Dziewonski, A. M. and B. Romanowicz, Overview of Volume I: Seismology and structure of the earth, *Treatise on Geophysics* G. Schubert (ed.), Vol. 1 (B. Romanowicz and A. Dziewonski, ed.), Elsevier, ISBN: 0-444-51928-9, 2007.

Ellsworth, W.L., P.E. Malin, K. Imanishi, S.W. Roecker, R. Nadeau, V. Oye, C.H. Thurber, F. Waldhauser, N.L. Boness, S.H. Hickman, and M.D. Zoback, Seismology Inside the Fault Zone: Applications to Fault-Zone Properties and Rupture Dynamics, *Scientific Drilling*, Special Issue No. 1, Part 4: The Physics of Earthquake Rupture, p. 84, doi:10.2204/iodp.sd.s01.04-2007, 2007.

Ford, S.R., D.S. Dreger, K. Mayeda, W.R. Walter, L. Malagnini, W.S. Phillips, Regional attenuation in northern California: A comparison of five 1-D methods, *Bull. Seismol. Soc. Am.*, August, 2008.

Freed, A.M., R. Bürgmann, and T.A. Herring, Far-reaching transient motions after Mojave earthquakes require broad mantle flow beneath a strong crust, *Geophys. Res. Lett., 34*, doi:10.1029/2007GL030959, 2007.

Funning, G., R. Bürgmann, A. Ferretti, F. Novali, and A. Fumagalli, Creep on the Rodgers Creek fault from PS-InSAR measurements, *Geophys. Res. Lett., 34*, doi:10.1029/2007GL030836, 2007.

Gasperikova, E., J.T. Smith, H.F. Morrison, A. Becker, and K. Kappler, UXO detection and identification based on intrinsic target polarizabilities - a case history, *Geophysics*, (in press).

Goldfinger, C., K. Grijalva, R. Bürgmann, A.E. Morey, J.E. Johnson, C.H. Nelson, J. Gutirrez-Pastor, A. Ericsson, E. Karabanov, J.D. Chaytor, J. Patton, and E. Gràcia, Late Holocene rupture of the Northern San Andreas fault and possible stress linkage to the Cascadia subduction zone, *Bull. Seism. Soc. Am., 98*, 861-889, 2008.

Kim, A. and D. Dreger, Rupture Process of the 2004 Parkfield Earthquake from Near-Fault Seismic Waveform and Geodetic Records, *J. Geophys. Res., 113(B07308)*, doi:10.1029/2007JB005115, 2008.

Malagnini, L. and K. Mayeda, High-stress strike-slip faults in the Apennines: An example from the 2002 San Giuliano earthquakes (Southern Italy), *Geophys. Res. Lett., 35*, doi:10.1029/2008GL034024, 2008.

Malagnini, L., L. Scognamiglio, A. Mercuri, A. Akinci, K. Mayeda, Source scaling for ground motion prediction in central Italy: Evidence for strong non-self-similar behavior, *Geophys. Res. Lett.*, (accepted).

Minson, S. and D. Dreger, Stable Inversions for Complete Moment Tensors, *Geophys. J. Int.*, 2007 (in press).

Minson, S. E., D. S. Dreger, R. Bürgmann, H. Kanamori, and K. M. Larson, Seismically and geodetically determined nondouble-couple source mechanisms from the 2000 Miyakejima volcanic earthquake swarm, *J. Geophys. Res., 112*, doi:10.1029/2006JB004847, 2007.

Morasca, P., K. Mayeda, R. Gök, W.S. Phillips, and L. Malagnini, 2-D coda and direct wave tomography in northern Italy, *Bull. Seism. Soc. Am., 98*, doi: 10.1785/0120070089, 2008.

Murphy, K.R., K. Mayeda, and W.R. Walter, Coda spectral peaking for Nevada nuclear test site explosions, *Seism. Res. Lett.*, in press, 2008.

Phillips, W.S., R.J. Stead, G.E. Randall, H.E. Hartse, and K. Mayeda, Source effects from broad area network calibration of regional distance coda waves, *Scattering of Short Period Waves in the Heterogeneous Earth*, H. Sato and M.C. Fehler, Editors, 2008 (in press).

Pollitz, F., P. Banerjee, K. Grijalva, B. Nagarajan, and R. Bürgmann, Effect of 3D viscoelastic structure on postseismic relaxation from the 2004 M = 9.2 Sumatra earthquake, *Geophys. J. Int., 172*, 189-204, 2008.

Olivieri, M., R.M. Allen, and G. Wurman, The potential for Earthquake Early Warning in Italy using ElarmS, *Bull. Seism. Soc. Am, 98*, 495-503, doi: 10.1785/0120070054, 2008.

Romanowicz, B. and B. Mitchell, Q in the Earth from crust to core, *Treatise of Geophysics, Vol. 1*, Elsevier, ISBN: 0-444-51928-9, 2007.

Romanowicz, B. Using seismic waves to image Earth's internal structure, *Nature, 451*, 266-268, 2008.

Ryder, I. and R. Burgmann, Spatial variations in creep rate on the central San Andreas Fault, *Geophys. J. Int.* (in press).

Rau, R.J. and K.H. Chen, Repeating earthquakes and seismic potential along the northern Longitudinal Valley fault of eastern Taiwan, *Geophys. Res. Lett., 34(L24301)*, doi:10.1029/2007GL031622, 2007.

Schutt, D. L., K. Dueker, and H. Yuan, Crust and upper mantle velocity structure of the Yellowstone hot spot and surroundings, *J. Geophys. Res.,113(B03310)*, doi:10.1029/2007JB005109, 2008.

Stachnik, J. C., K. Dueker, D. Schutt, and H. Y. Yuan, Imaging Yellowstone plume-lithosphere interactions from inversion of ballistic and diffusive Rayleigh wave dispersion and crustal thickness data, *Geochem. Geophys. Geosyst.*, doi:10.1029/2007GC001901(9), doi:10.1029/2008GC001992, 2008.

Taira, T., P.G. Silver, F. Niu, and R.M. Nadeau, Detecting seismogenic stress evolution and constraining fault-zone rheology in the San Andreas Fault following the 2004 Parkfield Earthquake, *J. Geophys. Res., 113(B03303)*, doi:10.1029/2007JB005151, 2008.

Templeton, D., R.M. Nadeau R., and Bürgmann, Behavior of Repeating Earthquake Sequences in Central California and the Implications for Subsurface Fault Creep, *Bull. Seism. Soc. Am., 98*, 52-65, 2008.

Tsang, L., R.M. Allen, and G. Wurman, Magnitude scaling relations from P-waves in southern California, *Geophys. Res. Lett., 34(L19304)*, doi:10.1029/2007GL031077, 2007.

Xue, M. and R.M. Allen, The Fate of the Juan de Fuca Plate: Implications for a Yellowstone plume head, *Earth Planet. Sci. Lett., 264*, 266-276, doi:10.1016/j.epsl.2007.09.047, 2007.

Yuan, H. Y., K. Dueker, and D. L. Schutt, Testing five of the simplest upper mantle anisotropic velocity parameterizations using teleseismic S and SKS data from the Billings, Montana PASSCAL array, *J. Geophys. Res., 113(B03304)*, doi:10.1029/2007JB005092, 2008.

Zollezi, F., P. Morasca, K. Mayeda, W.S. Phillips, and C. Eva, Attenuation tomography of the southern Apennines (Italy), *J. of Seism., 12*, doi10.1007/s10950-007-9079-6, 2007.

Presentations

Southern California Earthquake Center 2007 Meeting, Palm Springs, CA, September 9-12, 2007

Guilhem, A., R. Bürgmann, A. Freed, and T. Ali, Accelerating Moment Release in the Areas of High Stress?

Houlié, N. and B. Romanowicz, Asymmetric motion along the San Francisco Bay Area faults. Implication on the magnitude of future seismic events.

Ryder, I. and R. Bürgmann, A Decade of InSAR Observations on the Creeping Segment of the San Andreas Fault.

Annual Workshop of the Working Group "Seismic phenomena associated with volcanic activity" of the European Seismological Commission, Nesjavellir, Iceland, September 10-15, 2007

Hellweg, M., S. Ford, D. Templeton, S. J. Ohlendorf, S. Minson, and D. Dreger, Volcanoes and Geysers: Full Moment Tensors for these (and Other) Unusual Sources.

Wilhelm and Else Heraeus Seminar: Density, Temperature and Elastic Constants of Earth's Mantle II, Linderhof, Germany, September 11-16, 2007

Romanowicz, B., Elastic, anisotropic and anelastic structure of the upper mantle at the global and continental scale, (keynote speaker).

Monitoring Research Review, Denver, CO, September 26-28, 2007

Ford, S.R., D.S. Dreger, and W.R. Walter, Identifying isotropic events using an improved regional moment tensor inversion technique.

Ford, S.R., D.S. Dreger, K. Mayeda, W.R. Walter, L. Malagnini, and W.S. Phillips, Regional analysis of Lg attenuation: Comparison of 1D methods in Northern California and application to the Yellow Sea/Korean Peninsula.

Romanowicz, B., A. Cao, A. Kim, M. Panning, M. Pasyanos, and D. Dreger, Calibration of 3D upper mantle structure in Eurasia using regional and teleseismic full waveform data.

American Geophysical Union Fall Meeting, San Francisco, CA, December 10-14, 2007

Acevedo-Cabrera, A.L., M. Xue, and R.M. Allen. Seismic Tomography of western North America, *Eos Trans. AGU, 88*(52), Fall Meet. Suppl., Abstract S23B-1391, 2007.

Allen, R.M., G. Wurman, P. Hellweg, A. Kireev, and D. Neuhauser, Earthquake early warning across California: Performance of ElarmS on the existing seismic networks, *Eos Trans. AGU, 88*(52), Fall Meet. Suppl., Abstract S23E-01, 2007.

Brown, H. and R.M. Allen, Application of ElarmS to earthquakes in Japan, *Eos Trans. AGU, 88*(52), Fall Meet. Suppl., Abstract S13C-1443, 2007.

Bürgmann, R., G. Funning, I. Johanson, K. Johnson, and R.M. Nadeau, Imaging Rupture Asperities and Earthquake Potential of Partly Creeping Faults, *EOS Trans. AGU, 88*, Fall Meet. Suppl., Abstract S34C-03, 2007 (invited).

Cammarano, F. and B. Romanowicz, Constraints on Upper Mantle Temperature from Seismic Attenuation, *EOS Trans. AGU, 88*, Fall Meet. Suppl., Abstract U21A-0003, 2007.

Cammarano, F., B. Romanowicz, A. Deuss, and S. Goes, Insights on Compositional and Thermal Structure of the Earth's Upper Mantle Using Mineral Physics and Seismic Data. *EOS Trans. AGU, 88*, Fall Meet. Suppl., Abstract DI51B-01, 2007 (invited).

Cannata, A., M. Hellweg, R.M. Nadeau, and S. Gresta, Detection Method of Low-Frequency Earthquakes in the Non-Volcanic Tremor Beneath the San Andreas Fault, *Eos Trans. AGU, 88*(52), Fall Meet. Suppl., Abstract T21A-0356, 2007.

Cao, A., M. Panning, A. Kim, and B. Romanowicz, Non-linear 3D Born Shear Wave Tomography in Southeastern Asia, *EOS Trans. AGU, 88*, Fall Meet. Suppl., Abstract S31E-02, 2007.

Chen, K.H., R. Bürgmann, and R.M. Nadeau, Do repeating earthquakes talk to each other?, *EOS Trans. AGU, 88*(52), Fall Meet. Suppl., Abstract S33C-1469, 2007.

Chang, S., S. Van der Lee, M. P. Flanagan, H. Bedle, F. Marone, E. Matzel, M. Pasyanos, A. Rodgers, B. Romanowicz, and C. Schmid, Joint inversion for 3-dimensional S-velocity mantle structure along the Tethyan margin, *Eos Trans. AGU, 88(52)*, Fall Meet. Suppl., Abstract T23A-1202, 2007.

Cheng, X., F. Niu, P.G. Silver, and R.M. Nadeau, Seismic imaging of scatterer migration using waveform data of repeating earthquakes, *EOS Trans. AGU, 88*(52), Fall Meet. Suppl., Abstract T51C-0683, 2007.

Dreger, D., A. Morrish, and R.M. Nadeau, Finite-Source Modeling of Micro-earthquakes on the Parkfield Segment of the San Andreas Fault, *EOS Trans. AGU, 88*(52), Fall Meet. Suppl., Abstract S54A-08, 2007.

Dolenc, D., B. Romanowicz, P. McGill, and D. Neuhauser, Five Years of Data at the Monterey Ocean Bottom Broadband Seismic Station (MOBB), *Eos Trans. AGU, 88(52)*, Fall Meet. Suppl., Abstract S11D-06, 2007 (invited).

Dolenc, D., B. Romanowicz, P. McGill, and W. Wilcock, Observations of Infragravity Waves at the Ocean-Bottom Broadband Seismic Stations Endeavour (KEBB) and Explorer (KXBB), Eos Trans. AGU, 88(52), Fall Meet. Suppl., Abstract S23A-1106, 2007.

Dziewonski, A.M., B. Kustowski, V. Lekic, and B. Romanowicz, Seismic Tomography and Structure of the Transition Zone, *EOS Trans. AGU, 88*(52), Fall Meet. Suppl., Abstract V44B-01, 2007.

Evans, E., R. Bürgmann, and R.M. Nadeau, Linking Faults: Subsurface Creep on a Contiguous Fault Structure Connecting the Hayward and Calaveras Faults, *EOS Trans. AGU, 88*(52), Fall Meet. Suppl., Abstract S21A-0240, 2007.

Grijalva, K., E. Apel, and R. Bürgmann, Modeling stress changes following the 2004-2005 Sumatra earthquake sequence: Exploring triggering of the 2007 rupture and its relationship to the 1797 and 1833 events, *Eos Trans., AGU, 88* (52), Fall Meet. Suppl., Abstract U51A-0011, 2007.

Grijalva, K., R. Bürgmann, and C. Goldfinger, Stress interaction between the Cascadia subduction zone and the northern San Andreas fault, *Eos Trans., AGU, 88* (52), Fall Meet. Suppl., Abstract G13A-0911, 2007.

Guilhem, A., D.S. Dreger, and R.M. Nadeau, Scanning for Unusual Seismicity in the Mendocino Triple Junction Region, *EOS Trans. AGU, 88*(52), Fall Meet. Suppl., Abstract S43A-1047, 2007.

Hellweg, M., R. Uhrhammer, K. Hutton, A. Walter, P. Lombard, and E. Hauksson, Recalibrating ML for the California Integrated Seismic Network, *Eos Trans. AGU, 88*(52), Fall Meet. Suppl., Abstract S43A-1057, 2007.

Houlié, N., D. Dreger, A. Kim, and B. Romanowicz, The 28th September 2004 Parkfield earthquake revisited through high-rate GPS data inversion, *Eos Trans. AGU, 88*(52), Fall Meet. Suppl., Abstract G24A-02, 2007 (invited).

Houlié, N. and B. Romanowicz, Asymmetric motion along the San Franciso Bay Area faults. Implication on the magnitude of future seismic events, *Eos Trans. AGU, 88*(52), Fall Meet. Suppl., Abstract G21C-0678, 2007.

Kim, A., D. Dreger, and S. Larsen, 3D structure effects on local and near-regional seismic wave propagation in the San Francisco Bay Area *EOS Trans. AGU, 88*, Fall Meet. Suppl., S21A-0235

Komorowski, J-C.K., N. Houlié, J.P. Montagner, J. Dufek, Hidden Dykes detected on Ultra Long Period seismic signals at Piton de la Fournaise volcano - Constraints on the upper reservoir pressure state since 1992, *Eos Trans. AGU, 88*(52), Fall Meet. Suppl., Abstract V52B-07, 2007 (convener).

Lekic, V. and B. Romanowicz, Finite Frequency Upper Mantle Tomography Using the Spectral Element Method, *EOS Trans. AGU, 88*(52), Fall Meet. Suppl., Abstract S32A-05, 2007.

Lippman, J., A. Cao, and B. Romanowicz, Global Observations of Short Wavelength Topography on the Inner Core Boundary, *EOS Trans. AGU, 88*(52), Fall Meet. Suppl., Abstract DI31A-0251, 2007.

Nadeau, R.M. and A. Guilhem, Multi-scale Quasi-periodic Rate Changes of Nonvolcanic Tremor at Cholame, CA Following the 2004 Parkfield Mainshock, *EOS Trans. AGU, 88*(52), Fall Meet. Suppl., Abstract T12C-04, 2007.

Neuhauser, D.S., A. Kireev, G. Wurman, M. Hellweg, and R. Allen, A Real-Time CISN Test Bed for the ElarmS Early Warning Algorithm, *Eos Trans. AGU, 88*(52), Fall Meet. Suppl., Abstract S13C-144, 2007.

Olivieri, M., R. Basili, and R.M. Allen. ElarmS and the next large earthquake in Italy *Eos Trans. AGU, 88*(52), Fall Meet. Suppl., Abstract S13C-1441, 2007.

Porritt, R. and R.M. Allen. Observations of tremor using newly available seismic datasets in Cascadia, *Eos Trans. AGU, 88*(52), Fall Meet. Suppl., Abstract T21A-0348, 2007.

Ryder, I. and R. Burgmann, Variations in Creep Rate along the Central San Andreas Fault from InSAR and GPS Observations, *Eos Trans. AGU, 88*(52), Fall Meet. Suppl., Abstract G53A-01, 2007.

Romanowicz, B., F. Cammarano, L. Stixrude, C. Lithgow-Bertelloni, W. Xu, Constraints on Lateral Variations in Temperature and Composition in the Upper Mantle From Inversion of Long Period Seismic Waveforms, *Eos Trans. AGU, 88(52)*, Fall Meet. Suppl., Abstract MR52A-02, 2007 (invited).

Romanowicz, B. and A. Cao, Illuminating Slab Remnants in the Lower Mantle Using PKP Precursors, *Eos Trans. AGU, 88*(52), Fall Meet. Suppl., Abstract U21A-0006, 2007.

Silver, P.G., T. Taira, F. Niu, and R.M. Nadeau, Dynamic Weakening of the San Andreas Fault by the 2004 Sumatra-Andaman Earthquake, *EOS Trans. AGU, 88*, Fall Meet. Suppl., Abstract T53C-05, 2007.

Tsang, L.L.H., R.M. Allen, and G. Wurman, Calibration of ElarmS using earthquakes in southern California, *Eos Trans. AGU, 88*(52), Fall Meet. Suppl., Abstract S13C-1442, 2007.

Tran, A. and R.M. Allen. Patches of tremor around the Mendocino Triple Junction, *Eos Trans. AGU, 88*(52), Fall Meet. Suppl., Abstract T21A-0347, 2007.

Uhrhammer, R., W. Karavas, J. Friday, T. van Zandt, R. Hutt, E. Wielandt, and B. Romanowicz, New STS-1 Electronics: Development and Test Results, *Eos Trans. AGU, 88(52)*, Fall Meet. Suppl., Abstract S41A-0248, 2007.

Wurman, G., D.D. Oglesby, and R.M. Allen. Exploring the Relationship Between Early Rupture History and Final Earthquake Size, *Eos Trans. AGU, 88*(52), Fall Meet. Suppl., Abstract S14B-07, 2007.

Xue, M. and R.M. Allen. Imaging Mantle Convection Processes Beneath the Western USA Using the EarthScope Transportable Array, *Eos Trans. AGU, 88*(52), Fall Meet. Suppl., Abstract S43D-01, 2007.

Yuan, H. Y., F. Marone, K. Liu, S. Gao, and B. Romanowicz, 3D Radial and Azimuthal Anisotropic Structure in North America, *Eos Trans. AGU, 88*(52), Fall Meet. Suppl., Abstract T23A-1204, 2007.

Zeleznik, M., P.J. Maechling, G. Wurman, A. Kireev, K. Solanki, R. Allen, D. Neuhauser, E. Hauksson, P. Hellweg, G. Cua, T. Heaton, and T.H. Jordan, Development of the CISN Earthquake Early Warning Web Site: Establishing a Basis for Comparison of Algorithms, *Eos Trans. AGU, 88*(52), Fall Meet. Suppl., Abstract S13C-1446, 2007.

Joint BSL/IPG Workshop: "Seismology and Seismotectonics: BSL and IPGP research perspectives", Berkeley Seismological Laboratory, December 16-17, 2007

Cao, A., N Born and SEM based regional tomography.

Dreger, D., Repeating Earthquake Finite-Source Models: Strong Asperities Revealed on the San Andreas Fault.

Dreger, D., R Allen, G. Wurman - The M5.4 Alum Rock earthquake.

Houlié, N., Chasing EQ in Northern California using RT GPS.

Mayeda, K., A New Approach to Constrain Earthquake Source Scaling.

Nadeau, R.M., Change in Nonvolcanic Tremor Evolution in Central California Associated with the San Simeon M6.5 and Parkfield M6.0 Earthquakes.

Neuhauser, D., Real time data acquisition and processing at BSL.

USGS/NEHRP Northern California Earthquake Hazards Workshop, USGS Menlo Park, January 23-24, 2008

Allen, R.M., H. Brown, P. Hellweg, A. Kireev, and D. Neuhauser, CISN earthquake early warning: Testing of seismological algorithms.

Grijalva, K., R. Bürgmann, C. Goldfinger, Stress interaction between the Cascadia subduction zone and the northern San Andreas fault.

Hellweg, M., The Orinda Events: Complexity in Small Earthquakes.

Mayeda, K., Stable source estimates derived from local and regional coda envelopes.

Romanowicz, B., M. Hellweg, and D. Neuhauser, Operation of the Northern California Earthquake Management Center (NCEMC): Collaboration between UC Berkeley and the USGS Menlo Park, CA.

Uhrhammer, R., M. Hellweg, P. Lombard, K. Hutton, E. Hauksson, A. Walter, and D. Oppenheimer, Recalibrating M_L for CISN.

EarthScope Workshop on Aseismic Slip, Non-Volcanic Tremor, and Earthquakes, Sidney, British Columbia, February 25-28, 2008

Nadeau, R.M. and A. Guilhem, Evidence for Laterally Distributed Tremor Activity Across the San Andreas Fault Zone at Cholame, CA.

Workshop on Deformation Process and Earthquake Scaling, Hiroshima University, Hiroshima, Japan, March 3-4, 2008

Hellweg, M., Scaling and Complexity in small earthquakes.

International Workshop on Ocean floor observations, JAMSTEC, Tokyo, Japan, March 10-11, 2008

Romanowicz, B., Scientific Motivations for Seafloor Observatories, International Workshop on Ocean floor observations, (keynote lecture).

UNAVCO Science Workshop, Boulder, CO, March 11-13, 2008

Ryder, I., R. Bürgmann, Z. Shen, and A. Thomas, Postseismic motion following two recent major earthquakes in Tibet.

European Geophysical Union Meeting, April 2008

Cua, G., P. Maechling, R.M. Allen, E. Hauksson, T. Heaton, P. Hellweg, A. Kireev, D. Neuhauser, K. Solanki, S. Wiemer, J.Woessner, and M. Zeleznik, Comparison and testing of earthquake early warning algorithm performance.

Environmental and Engineering Geophysical Society Annual Meeting (SAGEEP), April 6-10, 2008

Kappler, K.N., An approach to UXO discrimination via polarizability curvematching and feature extraction applied to polarizability curves.

Annual Meeting of the Seismological Society of America, Santa Fe, NM, April 16-18, 2008

Allen, R.M., M. Xue, and S.H. Hung, Convective interactions beneath North America: An improved view using finite frequency kernels, *Seism. Res. Lett., 79*, 308, 2008 (invited).

Chung, A.I., D.S. Dreger, and R.M. Nadeau, Kinematic Source Parameters and Scaling of Micro-Repeating Earthquakes at Parkfield, *Seism. Res. Lett., 79*, 357, 2008.

Dolenc, D., R. Uhrhammer, and B. Romanowicz, Analysis of long-period noise at the Farallon Islands broadband seismic station FARB, *Seism. Res. Lett., 79*, 293, 2008.

Hellweg, M., A. Cannata, S. Gresta, S. Ford, and G. Di Grazia, Moment tensors for very long period signals at Etna Volcano, Italy, *Seism. Res. Lett., 79*, 320, 2008.

Hellweg, M, A. Chung, D. Dreger, A. Kim, and J. Boatwright, Mapping the rupture of the MW 5.4 Alum Rock earthquake. *Seism. Res. Lett. 79*, 353, 2008.

Hellweg, M., R.A. Uhrhammer, S. Ford, and J. Friday, Nonvolcanic tremor in Denali surface waves at broadband stations in Northern California: Instrumental causes? *Seism. Res. Lett., 79*, 327, 2008.

Malagnini, L. and K. Mayeda, Strong Coupling of Strike-Slip Faults: An Example from the San Giuliano Mainshocks (Southern Italy), *Seism. Res. Lett., 79*, 336, 2008.

Mayeda, K., L. Malagnini, and W.R. Walter, Earthquake Scaling for the Chi-Chi, Taiwan Sequence, *Seism. Res. Lett., 79* , 337, 2008.

Nadeau, R.M. and A. Guilhem, Evidence for Laterally distributed Tremor Activity across the San Andreas Fault Zone at Cholame CA, *Seism. Res. Lett., 79*, 291, 2008.

Oppenheimer, D., W. Bakun, R. Uhrhammer, J. Boatwright, and R. Simpson, Seismicity on the central and southern Calaveras fault and earthquake forecasts; Part 1 1910-present, *Seism. Res. Lett., 79,* 342-343, 2008.

Shelly, D.R., R.M. Nadeau, R. Burgmann, W.L. Ellsworth, J.M. Murray, T.F. Ryberg and C. Haberland, Repeating Nature and Relative Location of San Andreas Fault Tremors near Cholame, CA, *Seism. Res. Lett., 79*, 291, 2008.

American Geophysical Union Joint Meeting, Fort Lauderdale, FL, May 27-30, 2008

Allen, R., M. Bose, H. Brown, G. Cua, D. Given, E. Hauksson, T. Heaton, M. Hellweg, T. Jordan, A. Kireev, P. Maechling, D. Neuhauser, D. Oppenheimer, K. Solanki, and M. Zeleznik, Rapid telemetry and earthquake early warning, *Eos Trans. AGU, 89*(23), Jt. Assem. Suppl., Abstract G21A-01, 2008.

Houlié, N. and R.M. Allen. The Instantaneous Displacement (ID) Method: Application of rapid displacement estimates to earthquake early warning alerts, *Eos Trans. AGU, 89*(23), Jt. Assem. Suppl., Abstract G21A-02, 2008.

IRIS Annual Workshop, Stevenson, WA, June 4-6, 2008

Allen, R.M., M. Xue, and S.H. Hung, The fate of the Juan de Fuca plate.

Guilhem, A. and R.M. Nadeau, Influence of large earthquakes on the nonvolcanic tremor activity in the Parkfield-Cholame region , CA.

Taira, T., P.G. Silver, F. Niu, and R.M. Nadeau, Dynamically-induced weakening of the San Andreas Fault by the 2004 Sumatra-Andaman earthquake.

Shelly, D.R., R.M. Nadeau, R. Bürgmann, W.L. Ellsworth, J. Murphy, T.F. Ryberg, C. Haberland, and G. Fuis, Repeating Nature and Relative Location of San Andreas Fault Tremors Near Cholame, CA.

Yuan, H. Y., F. Marone, K. Liu, S. Gao, and B. Romanowicz, 3D Radial and Azimuthal Anisotropic Structure in North America.

ORFEUS Workshop, Utrecht University, Utrecht, Netherlands, June 19-20, 2008

Romanowicz, B., Elastic, anisotropic and anelastic tomography of the Earth's mantle: inferences on global dynamics.

Speaking Engagements

Allen, R.M., Toward earthquake early warning for California. SAFER (Seismic Early Warning for Europe) Meeting, Athens, Greece, June 2007.

Allen, R.M., Subduction, upwelling, earthquakes and tremor, all in the Pacific Northwest, UC Davis Geology and Geophysics Seminar, January 2008.

Allen, R.M., Earthquake early warning: Adding societal value to regional networks and station clusters, IRIS "Out of Africa" Workshop, Boston, MA, February 2008.

Allen, R.M., Detecting large earthquakes (and warning before ground shaking), Georgia Tech Department Seminar, March 2008.

Allen, R.M., Tremor across Cascadia: A view of megathrust processes? Georgia Tech Geophysics Seminar, March 2008.

Allen, R.M., Subduction, upwelling, earthquakes and tremor, all in the Pacific Northwest. Earthquake Hazards and Volcano Hazards joint seminar, USGS, Menlo Park, CA, May 2008.

Allen, R.M., First Jolt: New Science Behind Understanding Earthquakes. Presentation at the Annual Donors Dinner for the College of Letters and Sciences, UC Berkeley, May 2008.

Allen, R.M. and M. Hellweg, Berkeley Seismological Laboratory: A research Laboratory for active earthquake monitoring. Briefing to Floyd Kvamme, Co-Chair of President Bush's Council of Advisors on Science and Technology, USGS, Menlo Park, CA, May 2008.

Apel, E., Shells on a Sphere: Insights from Indian Plate motion, USGS Earthquake Seminar Series, Menlo Park, CA, August 22, 2007.

Bürgmann, R., Earthquakes in the San Francisco Bay Area, Deutsche Studienstiftung in North America, Meeting, Berkeley, CA, September 29, 2007.

Bürgmann, R., Active Tectonics and Non-Tectonics in the San Francisco Bay Area, Stanford University, Stanford, CA, November 11, 2007.

Bürgmann, R., A tectonic time bomb in our backyard: Earthquake potential of the Hayward fault, Lawson Lecture, UC Berkeley, Berkeley, CA, April 9, 2008.

Bürgmann, R., A tectonic time bomb in our backyard: Earthquake potential of the Hayward fault, CalDay, UC Berkeley, Berkeley, CA, April 12, 2008.

Bürgmann, R., Active Tectonics and Non-Tectonics of the San Francisco Bay Area (from "Aseismology"), Univ. Washington, Seattle, WA, May 29, 2008.

Bürgmann, R., What gives in the lower crust? Evidence from post-loading deformation and exhumed fault zones, CIG Workshop, Golden, CO, June 24, 2008.

Cammarano F., Insights on the compositional and thermal structure of the upper mantle from seismic data, Macquarie University, Sydney, Australia, February, 2008 (invited).

Chen, K.H., How do the repeating earthquakes at Parkfield talk to each other?, Institute of Earth Sciences, Academia Sinica, Taiwan, May 29, 2008 (invited).

Hellweg, M., Characteristics of tremor and other unusual seismic signals, presented at Hiroshima University, Hiroshima, Japan, February 19 - March 14, 2008.

Hellweg, M., Moment tensors of local and regional events, including isotropic components, presented at Hiroshima University, Hiroshima, Japan, February 19 - March 14, 2008.

Hellweg, M., Realtime Earthquake Monitoring at UCB and Waveform Analysis: Filtering and Polarization, presented at Hiroshima University, Hiroshima, Japan, February 19 - March 14, 2008.

Hellweg, M., Erdbeben im Garten: Einfhrung in die Seismotektonik und Seismizitt von Kalifornien, presented as part of the Bild der Wissenschaft Leserreise "Bewegte Erde", June 07-25, 2008.

Hellweg, M., Introduction to the Berkeley Seismological Laboratory, presented as part of the Bild der Wissenschaft Leserreise "Bewegte Erde", June 07-25, 2008.

Hellweg, M., Schornsteine der Subduktion: Der Mount St. Helens und die Vulkane des Kaskadengebirges, presented as part of the Bild der Wissenschaft Leserreise "Bewegte Erde", June 07-25, 2008.

Hellweg, M., Below Zero: Scaling and Complexity in Small Earthquakes, Seminar at the School of the Earth and Environment, University of Leeds, Leeds, UK, September 17, 2008.

Houlié, N., Deformation transitoire longue periode de la croute terrestre. Application au Piton de la Fournaise et au seisme de Parkfield, Observatoire Midi-Pyrenees, Toulouse, France, April 29, 2008.

Houlié, N., GPS Double Difference. Application to Volcanology and Seismology. A new hope for GPS seismology? , Departemento de Geofisica, Facultad de Ciencias Fisicas y Matematicas, Universidad de Chile, Chile, July 18th, 2008.

Houlié, N., GPS: past and future investigations., Departemento de Geofisica, Facultad de Ciencias Fisicas y Matematicas, Universidad de Chile, Chile, July 16th 2008.

Mayeda, K. and J. Bonner, Regional P-coda for stable estimates of body wave magnitude and yield: Extending the Ms:mb discriminant to smaller events, Air Force Research Laboratory, Hanscom Air Force Base, MA, September 24, 2007.

Mayeda, K., Earthquakes and Seismic Hazard in our Backyard, Head-Royce Middle School 6th grade class, Oakland, CA, also filmed by French TV travel show Echappèes Belles, March 10, 2008.

Mayeda, K., Stable source estimates derived from local and regional coda envelopes, UC Santa Cruz, Santa Cruz, CA, March 14th, 2008.

Mayeda, K., A new approach to constrain earthquake source scaling: On the path to improving MDAC, Air Force Technical Applications Center, Patrick Air Force Base, Satellite Beach, Florida, April 2, 2008.

Nadeau, R.M., Nonvolcanic Tremor and the M6.5 San Simeon and M6.0 Parkfield Earthquakes in Central California, Institut de Physique du Globe de Paris Departement de Sismologie seminar, Paris, France, June 24, 2008.

Romanowicz, B., The Earth's hum: bridging the gap between seismology and oceanography, US Geological Survey, Menlo Park, CA, October 2007.

Romanowicz, B., Seismological Constraints on the deep structure of continents, Smith Lecture, University of Michigan, Ann Arbor, MI, October 2007.

Romanowicz, B., Global and regional mantle tomography by inversion of time domain seismic waveforms, Institute of Geophysics, Chinese Academy of Sciences, Beijing, China, February 2008.

Romanowicz, B., Global and regional mantle tomography by inversion of time domain seismic waveforms, Chinese Earthquake Administration, Beijing, China, February 2008.

Romanowicz, B., The Earth's hum: bridging the gap between seismology and oceanography, Peking University, Department of Geophysics, Beijing, China, February 2008.

Romanowicz, B., Elastic and anelastic tomography of the Earth's mantle: Inferences on global dynamics, Earthquake Research Institute, University of Tokyo, Tokyo, Japan, March 2008.

Romanowicz, B., Elastic and anelastic tomography of the Earth's mantle: Inferences on global dynamics, IFREE, Yokohama, Japan (Institute for Research on the Earth and Environment), March 2008.

Romanowicz, B., The Earth's hum: bridging the gap between seismology and oceanography, Kyoto University, Kyoto, Japan, March 2008.

Romanowicz, B., Elastic and anelastic tomography of the Earth's mantle: Inferences on global dynamics, Rice University, Houston, Texas, March 26, 2008.

Romanowicz, B., Global Earth Structure in the context of global broadband seismic networks, Science Advisory Committee meeting for Geoscope, Paris, France, April 2008.

Ryder, I., Probing the deep rheology of Tibet using satellite imagery, Rosenstiel School of Marine and Atmospheric Science, University of Miami, May 7, 2008.

Uhrhammer, R., Earthquakes, Albany Rotary Club, Albany, CA, July 15, 2007.

Uhrhammer, R., Seismology, Berkeley Rotary Club, Berkeley, CA, September 15, 2007.

Uhrhammer, R., California Earthquakes, Redwood Empire DX Association, Petaluma, CA, April 9, 2008.

Panels and Professional Service

Richard M. Allen

Member, IRIS PASSCAL Standing Committee, December 2007-present
Organizer of the "ElarmS Users Workshop" May 5-16 2008, attendees from Korea, Germany, Switzerland, Puerto, Rico, and the Pacific Tsunami Warning Center
U.S. participant in the European Commission project "Seismic Early Warning Across Europe," June 2006 to June 2009

Roland Bürgmann

Associate Editor, Bulletin of the Seismological Society of America
Editorial Advisory Board, Eos
Editorial Board, Earth and Planetary Science Letters
Elected member, SSA Board Of Directors
Chair, EarthScope PBO Standing Committee
Member, UC Berkeley Graduate Fellowship Committee
Organizing Committee of Third Conference on Earthquake Hazards in the Eastern San Francisco Bay Area

Douglas S. Dreger

Member, COSMOS Board of Directors
Member, Golden Gate Bridge Instrumentation Committee
Reviewer of manuscripts for BSSA, GRL, JGR, and PRL.
Reviewer of proposals submitted to NSF and NNSA.
Associate Director, BSL, 2002-
Acting Director, BSL, Jan-July, 2008

Margaret Hellweg

Member, CISN Program Management Committee
Member, CISN Standards Committee
Member, CISN Steering Committee
Member, CISN Outreach Committee
Member, 1868 Commemoration Committee
Member, 1868 Commemoration Executive Committee
Member, Organizing Committee, Third Conference on East Bay Earthquake Hazards (October 21-25, 2008)
Member, Editorial Board of Journal of Volcanology and Geothermal Research
Chair, 1868 Committee for Developing Education and Outreach Materials and Programs
Contributed earthquake sounds to Bates, M., "Music from Underground Spaces (World Premier)" orchestra and electronica, California Symphony, May 4 and 6, 2008, Lesher Center for the Arts, Walnut Creek, CA

Douglas S. Neuhauser

Chair, Standards Group, California Integrated Seismic Network (CISN)
Acting Member, CISN Program Management Committee

Barbara Romanowicz

Reviewing Editor for Science
Seismology Coordinator, International Scientific Review of the IMS
Member, AGU Fellows Committee
Member, Advisory Committee for College de France, Paris, France
Member, Conseil d'Administration, Institut de Physique du Globe, Paris, France
Member, Conseil scientifique, Institut pour la Recherche et le Développement, France
Member, Advisory Committee, Geophysical Institute, University of Alaska, Fairbanks
Member, Scientific Review committee for the Geoforschungs Zentrum (GFZ), Potsdam, Germany (Spring 2008)
Member, National Earthquake Prediction Evaluation Council
Member, CISN Steering Committee
Member, NRC's Board on Earth Sciences and Resources (BESR)
Lead organizer, CIDER 2008 summer program in Santa Barbara
Co-organizer, Workshop on Ocean floor observatories, JAMSTEC, Tokyo, Japan, March 2008

Robert A. Uhrhammer

Member, International Association of Seismology and Physics of the Earths Interior, Working Group on Magnitudes
Member, California Integrated Seismic Network, Magnitude Working Group
Member, American National Seismic System, Technical Integration Committee, Working Group D, Seismic Instrumentation

Appendix II Seminar Speakers 2007-2008

HUAIYU YUAN
Berkeley Seismological Laboratory
UC Berkeley
"Yellowstone hotspot system: plume interaction with old cratonic continent"
Tuesday, August 28, 2007

BERNARD CHOUET
USGS Menlo Park
"Shallow magma transport pathway under Kilauea Caldera imaged from waveform inversions of very-long-period seismic data"
Tuesday, September 4, 2007

NATHAN SIMMONS
Lawrence Livermore National Laboratory
"Mantle Heterogeneity and Flow from Seismic and Geodynamic Constraints"
Tuesday September 11, 2007

SHUO MA
Stanford
"Dynamic Modeling of the 2004 Mw 6.0 Parkfield Earthquake"
Tuesday, September 18, 2007

DAVID SHELLY
UC Berkeley
Department of Earth and Planetary Science
"A new look at episodic transient slip through precise tremor locations in Japan: "fast" sub-events and tidal triggering"
Tuesday, September 25, 2007

THORNE LAY
UC Santa Cruz
"Seismic Migrations For Imaging "Rough" Upper and Lower Mantle Structure"
Tuesday, October 2, 2007

BILL ELLSWORTH
USGS Menlo Park
"Earthquake Science in the Source: Fault Rocks and Earthquakes in the Near Field in the San Andreas Fault Observatory at Depth"
Tuesday, October 9, 2007

DAVID SCHWARTZ
USGS Menlo Park
"A Tale of Two Earthquake Cycles: the San Francisco Bay Area, AD 1600-2007; the Denali Fault System, Alaska, AD 800-2007"
Tuesday, October 16

JOE DUFEK
UC Berkeley
Department of Earth and Planetary Science
"The growth and eruption of large silicic magma bodies"
Tuesday, October 23, 2007

JENNIFER JACKSON
Caltech
"Wave velocities of minerals at high-pressure and temperature: Geophysical implications"
Tuesday, October 30, 2007

LARRY HUTCHINGS
Lawrence Berkeley National Laboratory
"A Physically-based Strong Ground Motion Prediction Methodology Applied to the SFO Bay Bridge"
Tuesday, November 6, 2007

DAVID BOWMAN
CSU at Fullerton
"Getting Ready for a Big One: Accelerating Seismicity and Earthquake Predictability"
Tuesday, November 13, 2007

KEN CREAGER
University of Washington
"Episodic Tremor and Slip"
Tuesday, November 20, 2007

MEI XUE
Berkeley Seismological Laboratory
UC Berkeley
"High resolution imaging of the western USA: Interaction between the Yellowstone plume and Cascadia subduction?"
Tuesday, December 4, 2007

TAKA'AKI TIARA
University of Utah
"Stress-induced temporal changes in the seismogenic crust at the San Andreas Fault zone"
Tuesday, January 22, 2008

MEGHAN MILLER
Rice University
"The Caribbean: from the crust to the core"
Tuesday, January 29, 2008

KAREN FISCHER
Brown University
"Subduction zone structure, dynamics and melting processes: Lessons from Central America"
Tuesday, February 5, 2008

MARIE LUCE-CHEVALIER
Stanford University
"Determination, by 10Be cosmogenic dating, of slip-rates on the Karakorum Fault (Tibet) and paleoclimatic evolution since 200ka"
Tuesday, February 12, 2008

JESSE LAWRENCE
Stanford University
"The Quake Catcher Network & Distributed Computing Seismology"
Tuesday, February 19, 2008

LAURENT STEHLY
Berkeley Seismological Laboratory
UC Berkeley
"Surface waves tomography from observations of seismic ambient noise"
Tuesday, February 26, 2008

MARCO BOHNHOFF
Stanford University
"Seismotectonic Setting of the Aegean-Anatolian region"
Tuesday, March 4, 2008

JAY MELOSH
University of Arizona
"Landslides, Impact Craters and Earthquakes: The Paradoxical Behavior of Sliding Rock en Masse"
Tuesday, March 18, 2008

Lawson Lecture
ROLAND BÜRGMANN
Berkeley Seismological Laboratory
UC Berkeley
"A tectonic time bomb in our backyard: Earthquake potential of the Hayward fault"
Wednesday, April 9, 2008

WU-CHENG CHI
Academia Sinica, Taiwan
"Seismological, Oceanic, and Metrological Phenomena Observed by Ocean Bottom Seismographs: An Example from Taiwan"
Tuesday, April 22, 2008

THOMAS L. HOLZER
USGS Menlo Park
"Probabilistic mapping of liquefaction hazard in the San Francisco Bay Area"
Tuesday, April 29, 2008

REBECCA HARRINGTON
UCLA
"Volcanic hybrids that are brittle failure events"
Tuesday, May 6, 2008

BRIAN STUMP
Southern Methodist University
"Combining high frequency seismic and infrasound signals for characterizing propagation paths in both the atmosphere and the solid earth"
Tuesday, May 13, 2008

DAYANTHIE WEERARATNE
CSU Northridge
"Seismic and Rheological Behavior of the Asthenosphere Beneath Intraplate Seamount Chains in the South Pacific"
Tuesday, May 20, 2008

Berkeley Seismological Laboratory
Organizational Chart
2007-2008